I.R.Iran

ISSN:2423-5547
e-ISSN:2423-7469

Journal of Renewable Energy and Environment

Volume 9, Number 1, Winter 2022

Materials and Energy Research Center

Iranian Association of Chemical Engineers

ISSN: 2423-5547; e-ISSN: 2423-7469

Journal of Renewable Energy and Environment (JREE): Vol. 9, No. 1, (Winter 2022), 1-111

CONTENTS

AIMS AND SCOPE

Journal of Renewable Energy and Environment (JREE) publishes original papers, review articles, short communications and technical notes in the field of science and technology of renewable energies and environmental-related issues including:

- Generation
- Storage
- Conversion
- Distribution
- Management (economics, policies and planning)
- Environmental Sustainability

INSTRUCTIONS FOR AUTHORS

Submission of manuscript represents that it had neither been published nor submitted for publication elsewhere and is result of research carried out by author(s). Only the extended and upgraded articles presented in a conference and/or appeared in a symposium proceedings could be evaluated for publication.

Authors are required to include a list describing all the symbols and abbreviations in the paper. Use of the international system of measurement units is mandatory.

- On-line submission of manuscripts results in faster publication process and is recommended. Instructions are given in the JREE web sites: www.jree.ir
- References should be numbered in brackets and appear in sequence through the text. List of references should be given at the end of the paper. All journal articles listed in the References section must follow with article doi.
- Figure captions are to be indicated under the illustrations. They should sufficiently explain the figures.
- Illustrations should appear in their appropriate places in the text.
- Tables and diagrams should be submitted in a form suitable for reproduction.
- Photographs should be of high quality saved as jpg files.
- Tables' illustrations, figures and diagrams will be normally printed in single column width (8 cm). Exceptionally large ones may be printed across two columns (17 cm).

Journal of Renewable Energy and Environment

Journal Homepage: www.jree.ir

Materials and Energy Research Center

MERC

Research Article

Sensitivity Analysis for 3E Assessment of BIPV System Performance in Abadan in Southwestern Iran

Sepideh Rahmati Dehkordi [a], Mehdi Jahangiri [b*]

[a] *Department of Architecture and Urbanism, Central Tehran Branch, Islamic Azad University, Tehran, Iran.*
[b] *Department of Mechanical Engineering, Shahrekord Branch, Islamic Azad University, Shahrekord, Iran.*

PAPER INFO

Paper history:
Received: 16 December 2020
Revised in revised form: 07 February 2021
Scientific Accepted: 16 February 2021
Published: 22 August 2021

Keywords:
BIPV,
HOMER,
CO_2 Emission,
Photovoltaic,
3E Analysis

ABSTRACT

In Iran, due to the problems and constraints of fossil fuels and the need to maximize the use of solar potential, one of the best ways is the application of photovoltaic systems integrated with buildings. Due to the significant dependence of solar cell performance on the availability of radiation, it is necessary for architects to have an accurate assessment of the amount of electricity produced in different conditions. Therefore, in the present work, using HOMER software, the energy-econo-Enviro (3E) potential of a Building Integrated Photovoltaic (BIPV) in Abadan was studied. The effect of slope and azimuth of solar cells as well as cloudiness and system losses were investigated using sensitivity analysis. The results showed that the PV-grid system was the most economical option and after the azimuth angle of zero degree, the positive azimuth angle was the most economical. The results also showed that the slope of 30 degree and the angle of azimuth equal to zero was appropriate, for which the price per kWh of generated electricity was calculated to be $0.09. For the use of solar cells in the vertical wall of the building, the southwest direction was the most suitable and based on the results, it was suggested that the western wall of the building should be in the form of "inclined PVs with windows". The authors of this paper hope that the results of the present work can be used by architects and energy decision-makers as a guide in developing the BIPV use in Iran.

https://doi.org/10.30501/jree.2021.262420.1173

1. INTRODUCTION

About half of the world's energy consumption is allocated to buildings, which makes buildings the largest energy consumption source in the world and they are equally important sources of carbon dioxide emissions and play an important role in environmental pollution [1-3]. Therefore, it is necessary for architects to reduce the emission of environmental pollutants by constructing efficient buildings that require less energy for cooling, heating, and lighting [4].

The advantage of integrated photovoltaics over more common non-integrated systems is that the initial cost for the former can become negligible by purchasing cost-effective building materials and deactivating some of BIPV modules' functions [5]. Compared to other methods that use photovoltaics, some other unique features of BIPV in buildings include shielding against adverse weather conditions, light purification, prevention of heat loss, and non-requirement of space for installation of modules [6]. These advantages make BIPV one of the fastest growing systems in the photovoltaic industry.

To design and employ building elements such as walls, windows, and awnings, designers usually pay much more attention to the geographical latitude of the place and climate, neighborhoods, sizes, etc. For designing and combining photovoltaics with buildings, one should also be mindful of all the necessities and delicacies required for the design process [7]. In case of designing a building based solely on climatic conditions of a place and integrates the photovoltaic system with the building properly to ensure a suitable view, the architect should emphasize the element of residents' comfort in association with building conditions and make it a self-sufficient building [8-11].

One-third of BIPV projects belong renovation projects while the other two-thirds to new buildings. Half of the BIPV components are used in the facade, one third in the ceilings, and the rest in combination in the roof and facade [12]. In 2019, about 9 % of the global PV and construction markets were allocated to BIPV, which required much more attention to this issue [13]. According to the statistics given in Figure 1, Japan, France, and Italy are the leaders in the use of BIPV. At the end of 2018, the installed BIPV capacity for these countries was 3, 2.7, and 2.5 GW, respectively [14].

According to Figure 2 concerning the BIPV market forecast [15], the investment cost in this sector will reach about 11600 million dollars in 2027. In addition, the commercial and residential sectors will be accounting for a very large share of investments and the industrial sector will have a small share. In Iran and around the world, despite the enactment of laws to

*Corresponding Author's Email: jahangiri.m@iaushk.ac.ir (M. Jahangiri)
URL: https://www.jree.ir/article_135329.html

Please cite this article as: Rahmati Dehkordi, S. and Jahangiri, M., "Sensitivity analysis for 3E assessment of BIPV system performance in Abadan in southwestern Iran", ***Journal of Renewable Energy and Environment (JREE)***, Vol. 9, No. 1, (2022), 1-12. (https://doi.org/10.30501/jree.2021.262420.1173).

reduce buildings' energy waste, unawareness of housing professionals about new technologies and materials and, sometimes, wrong management policies in the field of construction have marginalized the use of BIPV technology in architecture [7]. Therefore, since most of Iran's regions enjoy significant radiation potential [16, 17], the use of BIPV in Iran is quite reasonable.

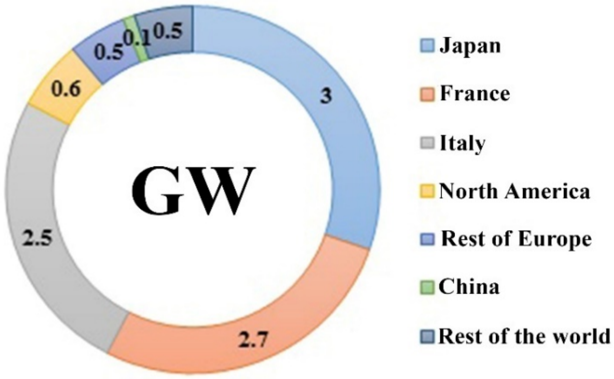

Figure 1. Leading countries in the use of BIPV [14]

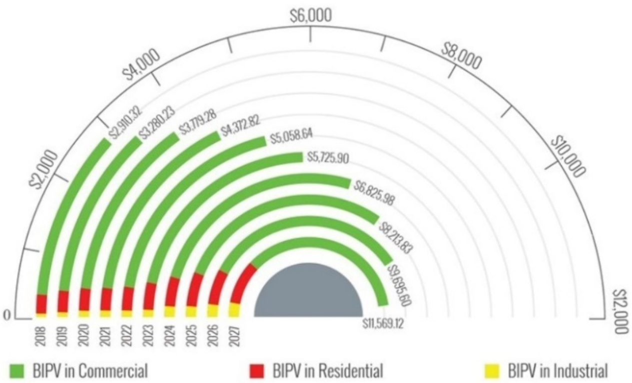

Figure 2. BIPV market forecast by 2027 [15]

The following is a review of recent research works on the use of BIPV in different countries. Given that the present work involves simulation, relevant studies have been considered.

Kuehner et al. (2017) [18] explored the possibility of developing BIPV in Switzerland. Hourly energy demand of the buildings was estimated using CitySim Pro software and then, by using HOMER Pro software, a number of procedures including optimization, performance evaluation, etc. were performed for different BIPV capacities. According to the results, full reliance on renewable energy is not yet realistic due to its random nature and that the use of daily and seasonal storage systems is also very important. With a Cost of Energy (COE) estimated at 0.183 $/kWh and a renewable energy fraction of 47 %, a scenario based on the simultaneous production of biomass through a BIPV-wind turbine battery was introduced as the most proper option.

Tadesse (2017) [19] evaluated the design of an off-grid BIPV system and carried out a feasibility analysis on it for the University of Bahir Dar in Ethiopia using HOMER software. The goal was to supply 76 kWh/day of electricity with a peak load of 12 kW. With a total NPC of $176815 and a COE of 0.558 $/kWh as the result of the most economical scenario under consideration, there will be an economic saving of $40185 over 25 years compared to using the national electricity grid.

Aelenei et al. (2018) [20] investigated the energy production potential for a building equipped with 12 kW solar cells on the facade and 12 kW solar cells on the roof in Portugal. They examined the effect of adding batteries while the systems under study were connected to the national electricity grid. The results showed that if a battery with a capacity of 13.5 kWh was used, the best economic result would ensue such that the total Net Present Cost (NPC), rate of return on investment, and the annual electricity sold to the grid were 1416.1 Euros, 8.1 years, and 12737 kWh, respectively.

Ramanan et al. (2019) [21] evaluated the performance of a grid-connected BIPV system for residential buildings in southern India. Using HOMER software, they investigated the effect of the slope of the solar modules and their azimuth angle. The results of the analysis showed that the optimal orientation for the installation of solar modules would be the facade and the eastern wall, while a sloping roof was recommended for the southern wall, because the annual energy rates produced for the 90 degree slope of solar cells in the south, east, and west directions were 1050 kWh, 1198 kWh, and 1150 kWh, respectively.

Zomer et al. (2020) [4] evaluated the performance of a BIPV in Brazil under partial shading from architectural perspectives. Three different PV types with different slopes and azimuth angles were studied. The simulations were performed using PVSyst commercial software. Comparisons between actual measured data and simulations pointed to the good agreement. Among the studied modes, the one with a bus station roof enjoying an installed capacity of 2.44 kW, an annual production of 1.503 kWh/kWp, and a performance factor of 92 % was the most appropriate configuration for the conditions under study.

Ni et al. (2020) [22] used the PVsyst and HOMER software to design and economically configure a BIPV system in China. In the first stage, using PVsyst software, according to the geographical location of the building and the operational characteristics of the load, suitable PV modules and the required area for the modules were selected. Then, using HOMER software, they looked into the total installation and operation costs, battery life, and so on. The results showed that using a system consisting of 6 kW PV cells with a total NPC of $22326 would achieve a solar power generation at a cost of 0.406 $/kWh. For this system, a battery with a lifetime of 20 years based on its performance was considered.

Based on the above findings and other implications, it can be realized that the environmental impact of using BIPV systems has not been studied or done. Therefore, for the first time, the present studied investigated the techno-econo-enviro performance of a BIPV system in Abadan city located in Khuzestan province in southwestern Iran. One-year analyses were performed through HOMER software and sensitivity analysis was applied to effective parameters. Although the present work is a case study, the proposed method can be used anywhere in the world for BIPV analysis, energy simulation, and calculations and performance comparisons of different configurations.

2. DIFFERENT TYPES OF BIPV

In the BIPV building, the architect can use six modes to ensure its full integration:"saw-toothed north light roof", "Atrium", "Vertical with windows", "inclined wall with windows", "inclined PVs with windows", and "fixed shadows for walls" for wall and roof [23]. These modes are shown in Figures 3 to 8.

The six modes shown in Figures 3 to 8 and their impact on building performance are briefly described [23]. The skylight on the roof greatly reduces the need for electricity during the day by providing indirect lighting, and if combined with photovoltaics, they can also meet the need for night lighting. In the BIPV building with the aim of integrating photovoltaics with the roof, the architect can design the roof in the form of toothed skylights integrated with photovoltaics or replace translucent photovoltaic panels with glass and skylights and atriums (Figures 3 and 4). In a photovoltaic system integrated with a façade, heat penetration is prevented, electricity is generated, and the view to the outside and the provision of natural light are achieved (Figures 5 and 6). Photovoltaic panels can be used in combination with the building as Shadowing, Louver or Light-shelf (Figures 7 and 8). In this case, by installing sloping and horizontal canopies, there is no direct radiation into the space, which reduces the load of cooling equipment and provides partial electricity required for cooling equipment.

Figure 3. Saw-toothed north light roof

Figure 4. Atrium

Figure 5. Vertical with windows

Figure 6. Inclined wall with windows

Figure 7. Inclined PVs with windows

Figure 8. Fixed shadows

3. THE CITY UNDER STUDY

As can be seen in Figure 9, in the hot and dry climate of Abadan, radiation on the walls and ceiling has a great role in increasing the cooling load of the building; therefore, architects must install photovoltaic panels so that the amount of radiation on the surface and the roof of the building would remain low. The purpose of this work is to prevent the penetration of radiation and heat into the building and to generate the electricity needed for cooling [4].

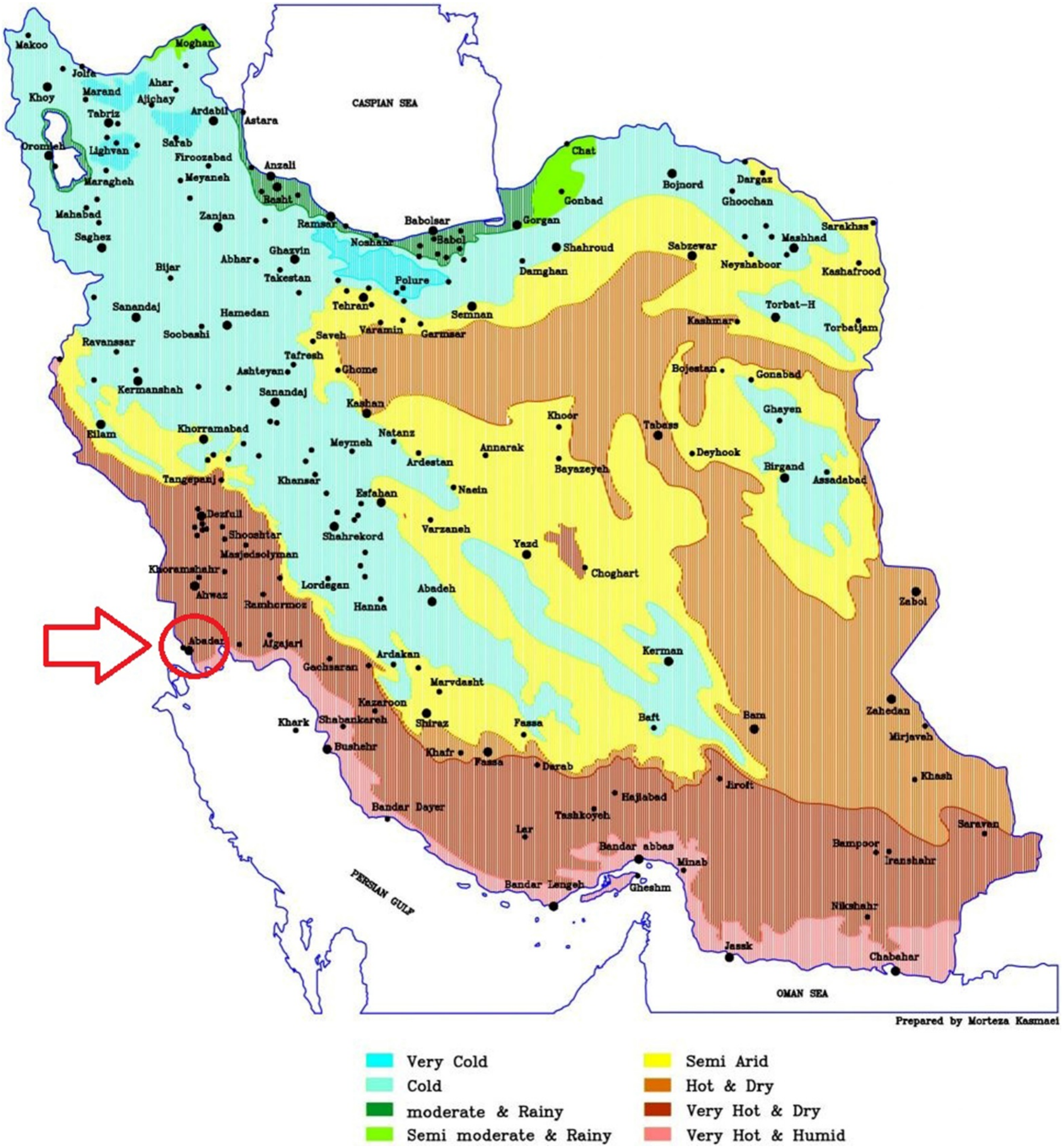

Figure 9. Climatic divisions of Iran and Abadan in particular [24]

4. METHODOLOGY

Analysis of photovoltaic panels and their smart application in buildings, as if there are no appendages and additional elements in the facade or roof, could illustrate some sensitive issues that must be considered in the building design [6]. Therefore, architects and designers need to be aware of the amount of energy received by PV cells in the study area, PV efficiency, and price of solar electricity per kWh as one of the building materials in different directions and slopes to the sun radiation [4].

Based on the above finding and due to the gap in the knowledge and skills of architects regarding the supply of all or part of the energy required for a BIPV building [6], the present work employed HOMER software to study the techno-econo-enviro in the electricity supply of a 5-storey BIPV in the city of Abadan. The reason behind choosing the present building which involves performing a feasibility study of BIPV construction in Abadan is that with a rise in the number of floors and height of the building, the ratio of facade to roof surface increases and, as a result, facade is a good option for installing photovoltaic cells. In other words, BIPV is more valuable for designing photovoltaic systems in urban centers with high density.

Climate data on solar radiation collected over an average of 20 years [25-27] have been extracted from the NASA site. The schematic of the simulation performed in the present work is shown in Figure 10. According to the figure, the BIPV building under study has the possibility of exchanging electricity with the national electricity grid, which converts the DC electricity generated by solar cells to the AC power consumed by an electric converter. The advantage of connecting the BIPV building under study to the grid power is reducing the cost of the photovoltaic system by selling the surplus electricity to the grid.

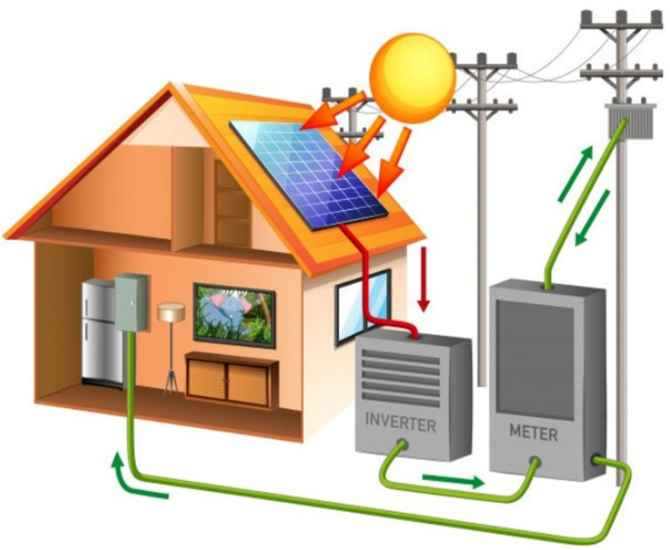

Figure 10. Schematic of the simulated system

HOMER software uses the following equations to calculate the amount of electricity generated by photovoltaic cells and to calculate the air clearness index [28-30] by taking the average monthly radiation data and the geographical location of the study area.

$$H_{oh} = \frac{24 \times 60}{\pi} G_{sc} \times d_r \times (\omega_s . \sin\varphi . \sin\delta + \cos\varphi . \cos\delta . \sin\omega_s) \tag{1}$$

$$d_r = 1 + 0.033 \cos\left(\frac{2\pi n}{365}\right) \tag{2}$$

$$\delta = 0.409 \sin\left(\frac{2\pi n}{365} - 1.35\right) \tag{3}$$

$$\omega_s = \operatorname{Arc}\cos\ (-\tan\varphi . \tan\delta) \tag{4}$$

$$\overline{k_T} = \frac{\overline{H}}{\overline{H_{oh}}} \tag{5}$$

$$P_{pv} = Y_{pv} \times f_{pv} \times \frac{\overline{H_T}}{\overline{H_{T,STC}}} \tag{6}$$

Regarding the performance of HOMER software, different configurations including the lowest total NPC should be ranked in the first place based on the total NPC parameter [31, 32]. Given the uncertainty involved, the mentioned software can perform sensitivity analysis for some parameters such as the intensity of radiation reaching the surface of photovoltaic cells as well as the extent of losses such as dust, wiring, shading, etc. Economic calculations in HOMER software are performed through the following equations [33-35].

$$NPC = \frac{C_{ann,total}}{CRF\ (i, R_{proj})} \tag{7}$$

$$CRF = \frac{i\,(1+i)^N}{(1+i)^N - 1} \tag{8}$$

$$i = \frac{i' - f}{1 + f} \tag{9}$$

$$COE = \frac{C_{ann,total}}{E_{Load\ served}} \tag{10}$$

If net electricity is calculated on a monthly basis, HOMER software calculates the total annual energy cost through the following equation [36]:

$$C_{grid.energy} = \sum_{i}^{rates}\sum_{j}^{12}\begin{cases} E_{net\ grid\ purchases.i.j} \cdot c_{power.i} & \text{if } E_{net\ grid\ purchases.i.j} \geq 0 \\ E_{net\ grid\ purchases.i.j} \cdot c_{sellback.i} & \text{if } E_{net\ grid\ purchases.i.j} < 0 \end{cases} \tag{11}$$

The above equation involves buying/selling electricity from/to the national electricity grid on a monthly basis for a period of one year. The formula has two conditions that are based on whether the purchasing of electricity from the grid is positive (or zero) or negative. The reason for this is that the purchasing price of electricity from the grid is different from the selling price of electricity to the grid.

According to Figures 3 to 8, to investigate the effect of solar cell slope on the generated electricity, six angles of 15, 30, 45, 60, 75, and 90 degrees were considered. Also, since different weather conditions and losses must be considered, in the present work, three values of 50 %, 70 % and 90 % were considered for the derating factor parameter. The azimuth angles for solar cells were considered at -90, -45, 0, 45, and 90 degrees so that the most appropriate orientation could be selected and the potential of different walls be investigated.

5. REQUIRED DATA

The performed simulation flowchart is shown in Figure 11. As can be seen, the data required for the simulation are presented as input to the simulation and optimization sections as well as to the sensitivity analysis. Required data include power consumption profile (Figure 12), solar radiation data (Figure 13), constraints and search space (Table 1), and prices and characteristics of the equipment used (Table 1). According to Figure 12, the maximum electrical load required in different months occurs within the duration of 18 PM to 22 PM. The average annual load is 21 kWh/day with a peak value of 2.7 kW. According to Figure 13, the maximum, minimum, and average amounts of radiation were 7.4 kWh/m^2-day (June), 3 kWh/m^2-day (December), and 5.4 kWh/m^2-day, respectively. The average annual air clearness index could be equal to 0.624 based on the geographical location of the studied station (latitude 30.4 E, longitude 48.30 E, and time zone GMT + 03: 30).

Other software inputs in the present work include the annual interest rate of 18 % [37, 38], project lifetime of 25 years [39, 40], emission fines equal to zero [41, 42], and electricity exchange price with the national electricity grids at three off-peak times (23 PM to 8 AM), normal times (8 AM to 16 PM), and peak times (16 PM to 23 PM) being equal to 0.05, 0.07, and 0.12 $/kWh [43, 44], respectively.

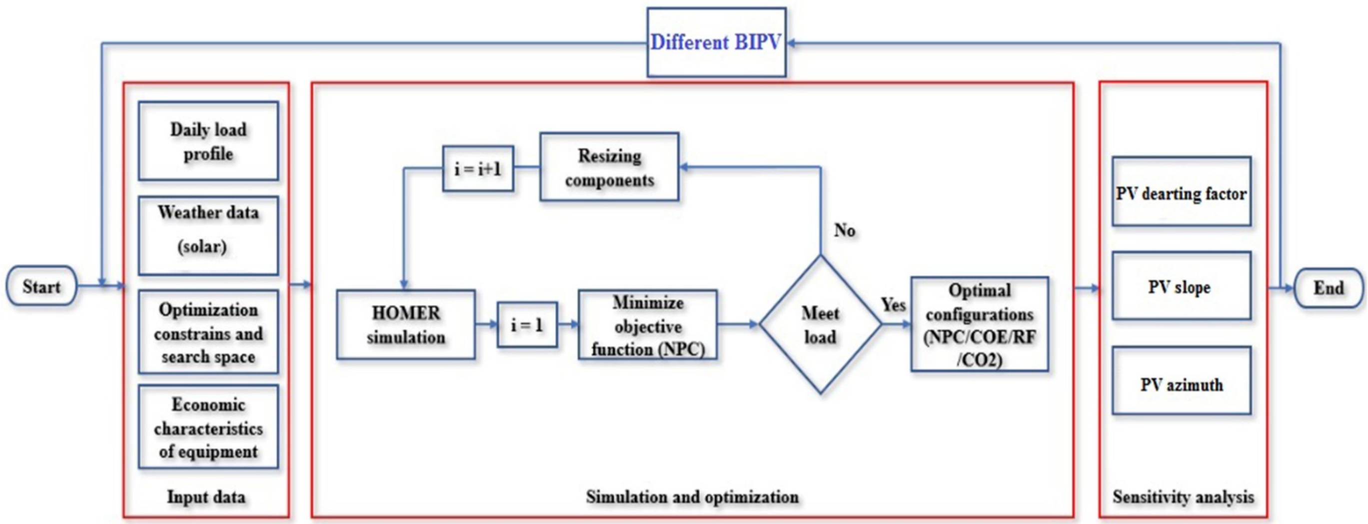

Figure 11. Optimization flowchart for the present work by HOMER software

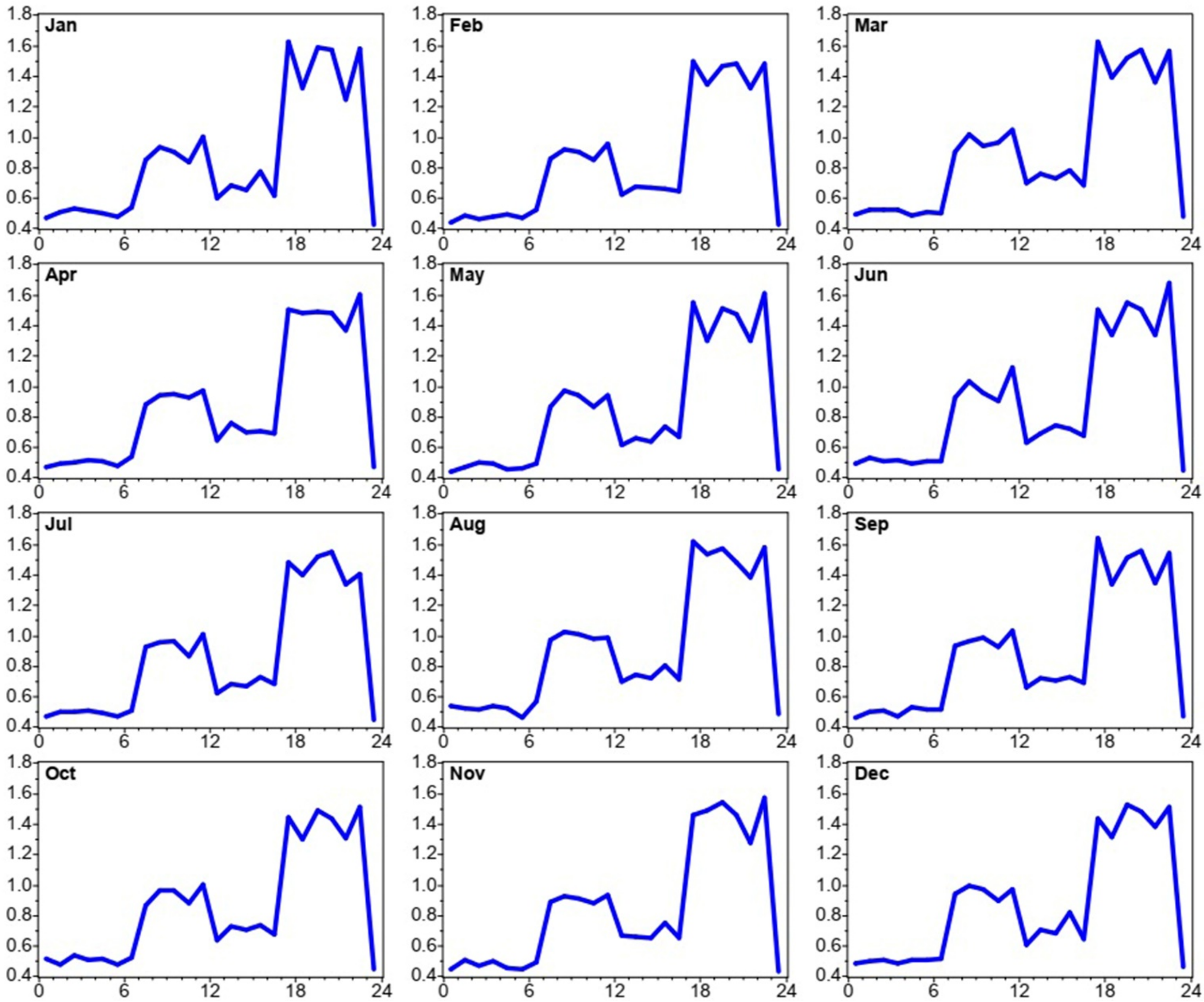

Figure 12. Profile of the average required electricity per kW over a year

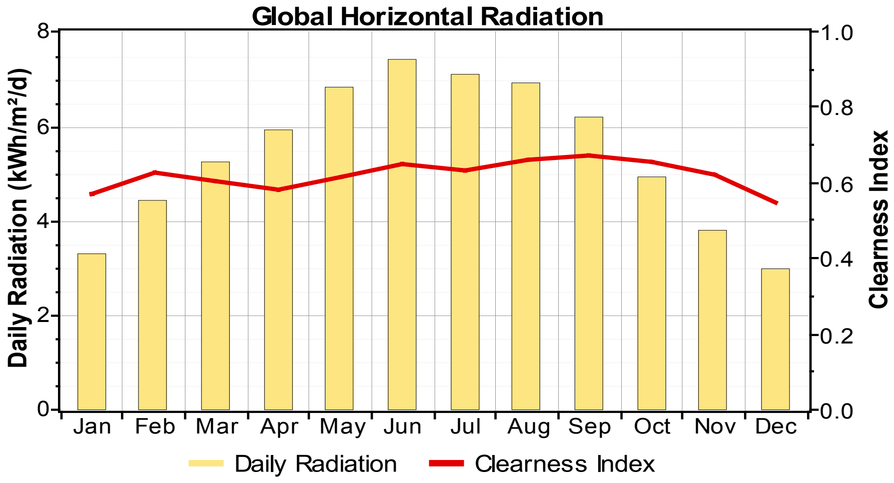

Figure 13. Average monthly radiation and air clearness index for Abadan

Table 1. Information of the BIPV system under study

Equipment	Cost ($)			Size (kW)	Other information
	Capital	Replacement	O & M		
PV [45]	1000	1000	5	5-50	Lifetime: 25 years Ground reflectance: 20 %
Battery T-105 [46]	174	174	5	0-20	Nominal Voltage: 6 Nominal capacity: 225 Ah
Converter [47]	200	200	10	0-20	Lifetime: 10 years Efficiency: 90 %

6. RESULTS AND DISCUSSION

The results of simulations and sensitivity analysis on the COE parameter are shown in Figures 14a to 14c for derating factors of 90 %, 70 % and 50 %, respectively. The results illustrated that for all cases, use of a solar cell-national grid is the most optimal and economical option. Based on the comparison between Figures 14a to 14c, it can be seen that upon increasing the derating factor, which corresponds to greater radiation reaching the surface of PV or less losses in the BIPV system, the amount of COE decreases significantly. The outcome showed that the most suitable direction for the azimuth angle would be the zero degree angle, i.e., the direction of the solar cells to the south. It can also be seen that positive angles of azimuth (orientation of solar cells to the west) have better results than the negative counterpart (orientation of solar cells to the east). This result is justified by the fact that the use of national electricity grid on the west side of the building is more significant than that on the east side.

The lowest price of solar power generated per kWh based on the results for a slope of 30 degree, zero azimuth angle, and derating factor of 90 % was 0.09 $/kWh. This price ranged between the prices of the national electricity tariff at peak load and normal load times and was 25 % less than that at the time of peak load, which is very significant. Also, based on the results for different slopes of solar cells, it is seen that the angle of 30 degree could be more suitable than other angles because it would lead to the lowest amount of COE for the optimal azimuth angle of zero degree. The results of a 15 degree slope of solar cells have values very close to the optimal angle of 30 degree.

For derating factors equal to 90 %, 70 % and 50 %, the minimum COE values were 0.09, 0.125 and 143 $/kWh, respectively. For the vertical placement of solar cells on the wall of the building (slope equal to 90 degree), the most suitable azimuth angle to the southwest (angle + 45 degree) could bring about greater cost effectiveness and the appropriate azimuth angle might be determined better upon further reducing the derating factor. In other words, for less radiation or more cloudy conditions or more system losses, it is recommended the solar cells be placed in the study station to reduce costs to the southwest.

Given that the city under study is very hot and the thermal loss of solar cells is considerable and that Abadan has been facing dust and fine dust problems in recent years, the derating factor is considered equal to 70 % for further research.

Figure 15 shows the amount of net electricity purchasing from the grid. The results demonstrate that the lowest electricity purchased from the grid, equivalent to the highest electricity sales to the grid, was 1915 kWh/year at the azimuth angle of zero and the slope of the solar cells was equal to 30 degree. If solar cells were used as applications in vertical walls, then the optimum mode increased by about 90 % compared to the optimal mode of purchasing power from the grid, i.e., an angle of 30 degree and zero azimuth. Based on Figure 15, it was only at the azimuth angle of zero degree that the 30 degree slope of the solar cells had the lowest power purchase from the grid, and at other azimuth angles, the 15 degree slope was more appropriate. In other words, in a case involving the special form of the building, it is not possible to use solar cells in the south, and it is recommended that the slope of the solar cells to receive the maximum amount of radiation or the minimum net electricity purchase from the grid is 15 degree. The latter mode is equivalent to using the "inclined wall with windows" mode (shown in Figure 6) for the station in question.

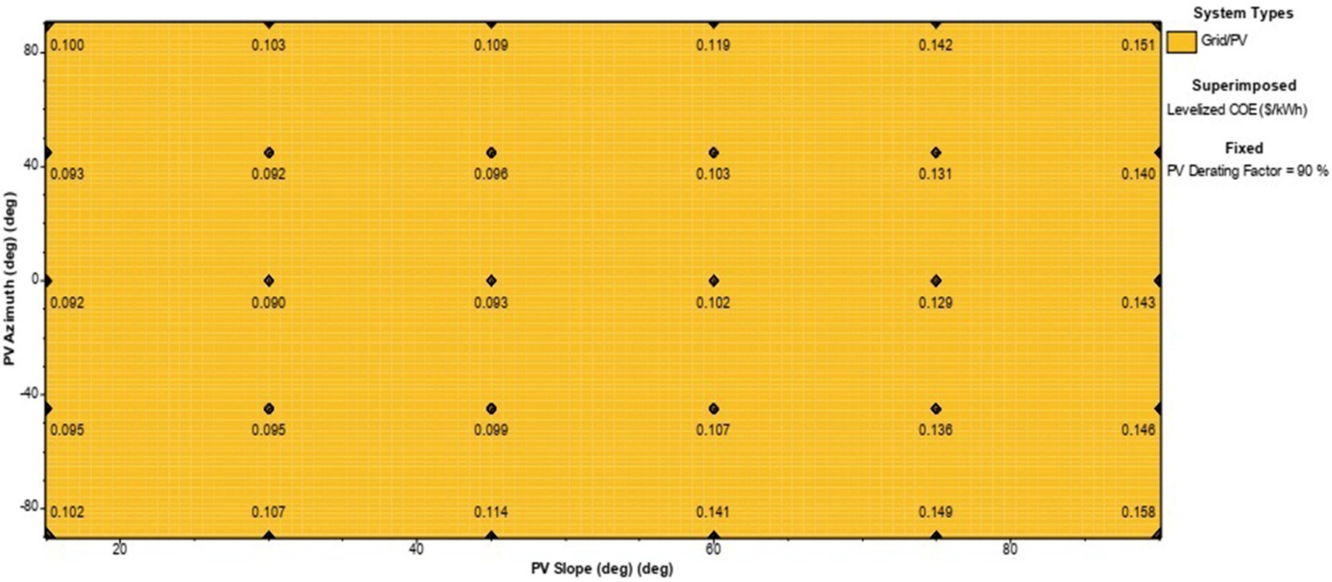

(a)

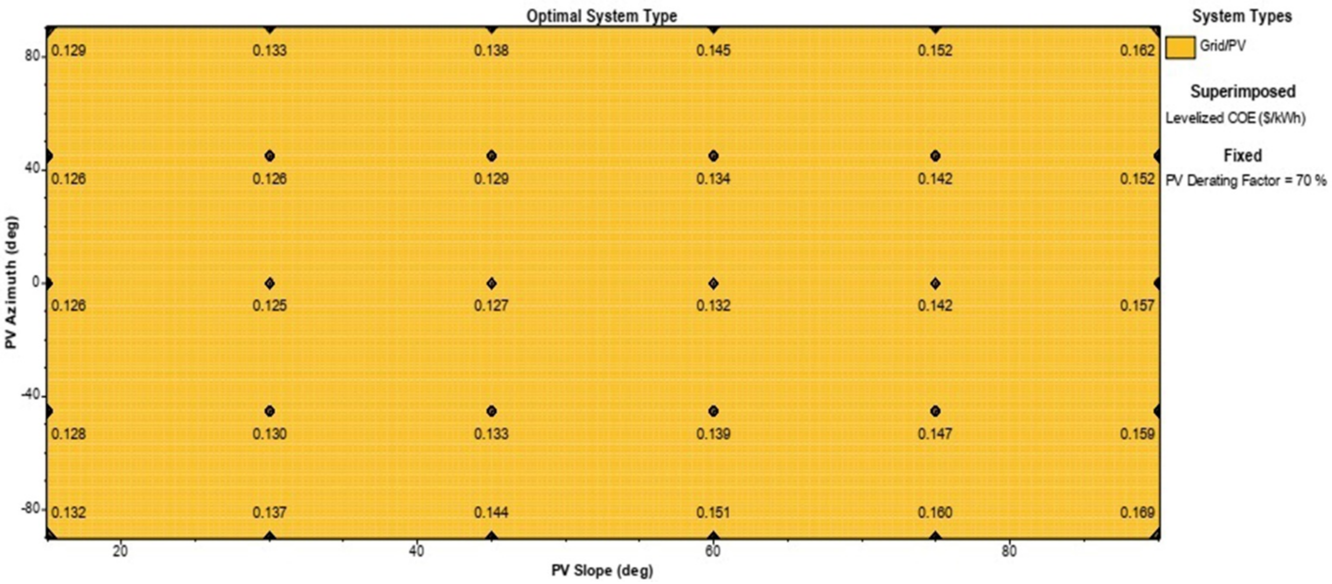

(b)

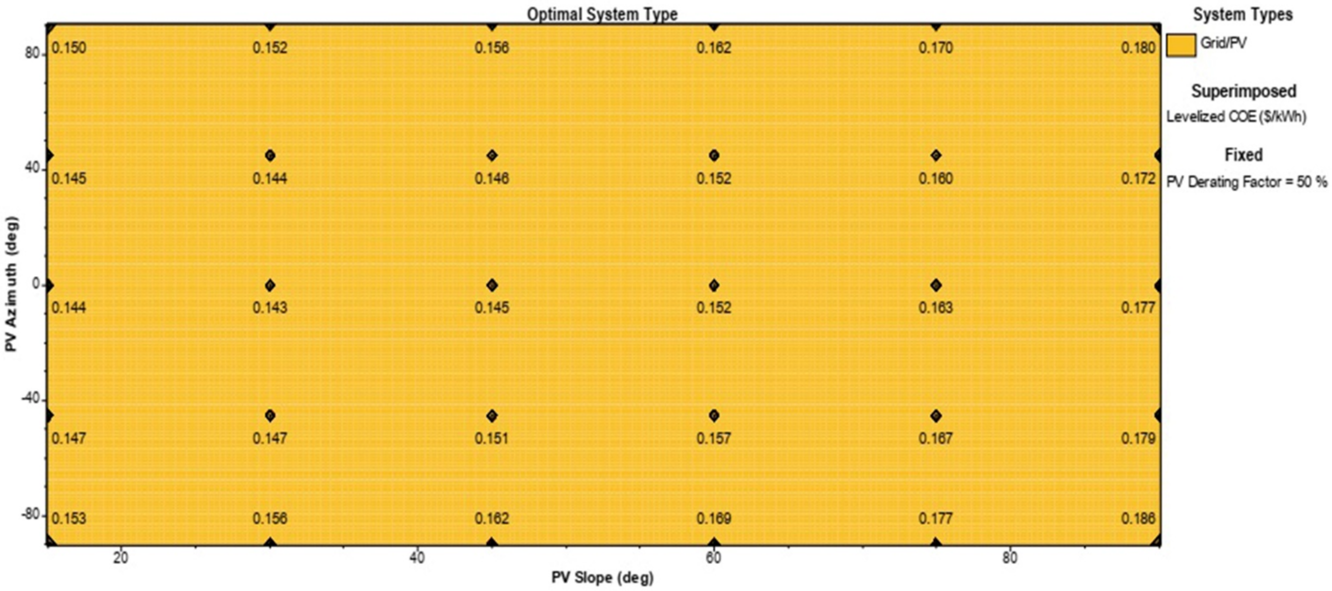

(c)

Figure 14. Sensitivity analysis for the optimal systems on the COE parameter and derating factors of: a) 90 %, b) 70 %, c) 50 %

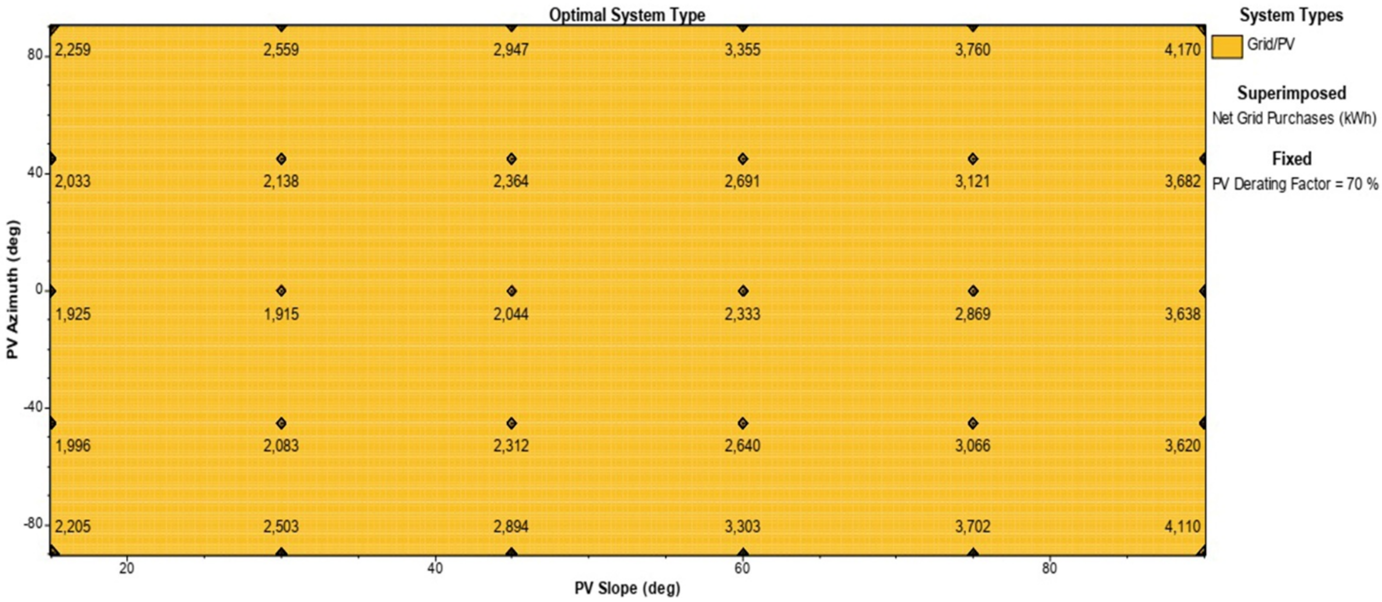

Figure 15. Sensitivity analysis for the optimal systems on the net grid purchase parameter and the derating factor of 70 %

Figure 16 shows the amount of electricity generated by solar cells at different slope angles and azimuth angles of -90 to +90. According to the results, the highest amount of electricity generated in the azimuth angle was zero and the slope was 30 degree with an amount of 7634 kWh/year. At azimuth angles of +45 and -45, with respective values of 7622 and 7362 kWh/year, the same slope of 30 degree had the highest amount of electricity produced by solar cells. However, at azimuth angles of +90 and -90 with a slope of 15 degree, the electricity generated by solar cells was about 5 % higher than that at an angle of 30 degree. For the 90 degree slope of the solar cells, i.e., the position of the solar cells on the vertical walls, it can be seen that the angle of azimuth at -90 degree, i.e., the eastern wall, generated much more electricity than that at the angle of azimuth +90 degrees, i.e., the western wall. In other words, it is recommended that the western wall of the building be made inclined for the station under study so that a greater amount of electricity could be generated if solar energy was used.

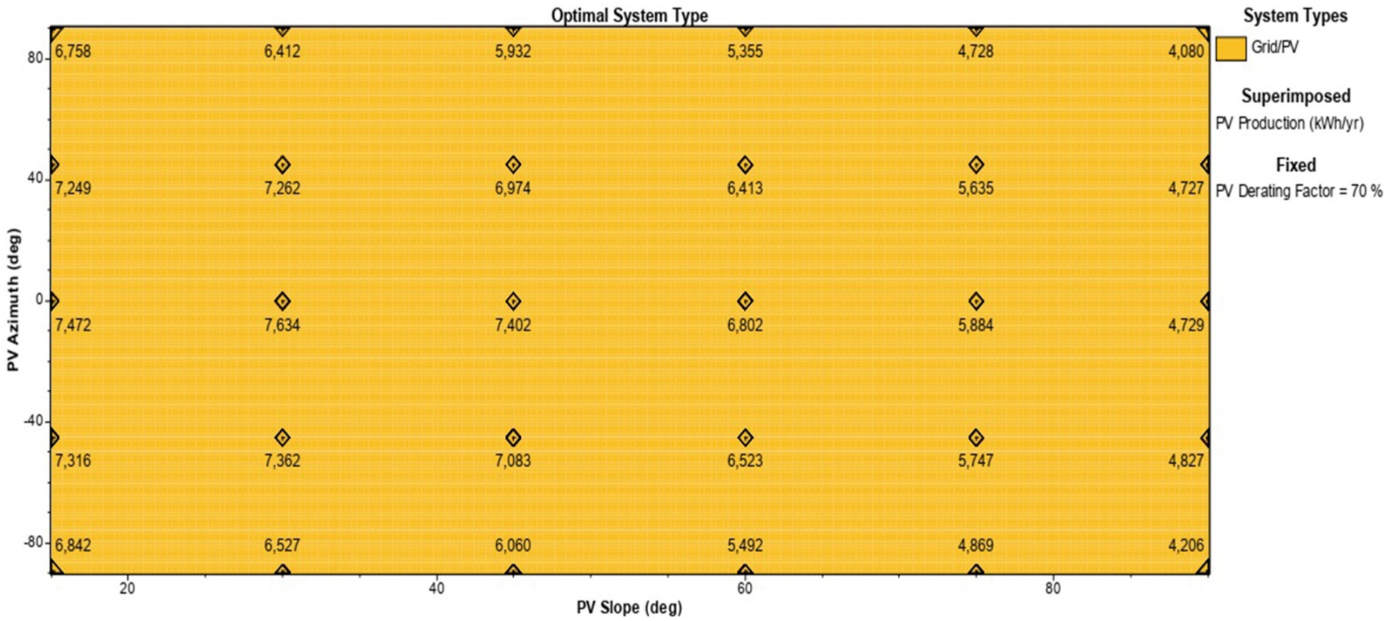

Figure 16. Sensitivity analysis for the optimal systems on the PV production parameter, derating factor: 70 %

Figure 17 shows the amount of CO_2 emissions for different scenarios with azimuth angle and slope of solar cells. Given that one of the most important advantages of BIPV buildings is their environmental friendliness, it is necessary to study this parameter. According to the findings, the scenarios with the lowest amount of pollutant production included the azimuth angle of zero degree and slope angle of solar cells equal to 30 degree (1210 kg/year emission of pollutants), the azimuth angle of zero degree, and the slope angle of solar cells equal to 15 degree (1217 kg/year pollutant production), and azimuth angle of -45 degree, and the slope angle of solar cells equal to 15 degree (1261 kg/year pollutant production). In general, it can be said that upon an increase in the slope of solar cells and in the azimuth angle, the production of pollutants will increase.

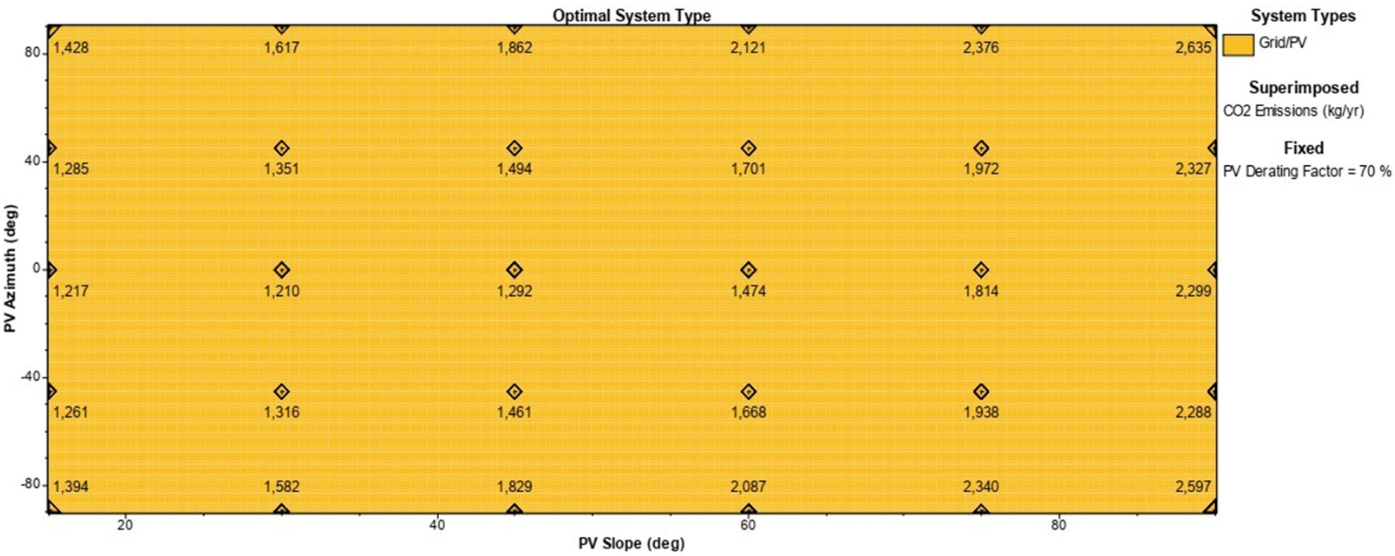

Figure 17. Sensitivity analysis for the optimal systems on the CO_2 emission parameter and derating factor of 70 %

7. CONCLUSIONS

Today, the use of photovoltaic systems in combination with buildings has become of great importance and attractiveness among designers and architects. Therefore, the performance of these buildings and also their design must be correct and flawless so that after the installation of photovoltaics, the photovoltaic system or the building itself would not cause any problems. According to the above, in the present work, for the first time, techno-econo-enviro evaluation and sensitivity analysis on the variable parameters of a BIPV in Abadan were carried out. Sensitivity analysis was performed on PV slope, PV azimuth, and derating factor parameters and their effect on COE, Net grid purchases, PV production, and CO_2 emission parameters was investigated. The analysis was performed using HOMER software and the main results are as follows:

- Using solar cell with the national electricity grid was the most economical option in all cases.
- From an economic point of view, zero azimuth angle, positive azimuth angle, and negative azimuth angle were the most appropriate, in order.
- The minimum COE was equal to 0.09 $/kWh; at a slope of 30 degree, the azimuth angle was zero and the derating factor was equal to 90 %.
- To place solar cells on vertical walls, the southwestern azimuth angle was the most economically appropriate scenario.
- According to the climatic conditions of the study city, the derating factor parameter equal to 70 % is recommended.
- The lowest amount of electricity purchased from the network with a rate of 1915 kWh/year was related to the slope of 30 degree and the azimuth angle of zero.
- If the south of the building was not reachable or operable, a slope of 15 degree would be recommended, being equivalent to using the “inclined wall with windows” mode.
- It is recommended that the western wall of the building be built in the “inclined” mode.
- The minimum pollutant produced due to the use of the national electricity grid was 1210 kg/year.

8. ACKNOWLEDGEMENT

The authors would like to thank all the organizations that provided data for this work.

NOMENCLATURE

i	Annual interest rate (%)
f	Annual inflation rate (%)
i'	Nominal interest rate (%)
CRF	Capacity Recovery Factor
R_{proj}	Lifetime of project (year)
k_t	Clearness index
$\overline{H_{T,STC}}$	Incident radiation on the cell’s surface under standard conditions (1 kW/m^2)
G_{sc}	Solar constant (0.082 MJ/m^2-min)
Y_{PV}	Output power of solar cell under standard conditions (kW)
f_{PV}	Derating factor (%)
$\overline{H_T}$	Incident radiation on the cell’s surface on a monthly basis (kW/m^2)
H_{oh}	Extraterrestrial radiation (MJ/m^2-day)
P_{PV}	Output power of PV cells (kW)
d_r	Inverse relative distance earth-sun
$C_{ann,total}$	Total annual cost ($)
H	Monthly average daily radiation on a horizontal plane (MJ/m^2-day)
$C_{grid, energy}$	Total annual energy charge (kWh)
$E_{net grid purchases}$	The net grid purchases (grid purchases minus grid sales) (kWh)
GMT	Greenwich Mean Time
C_{power}	The grid power price ($/kWh)
N	Useful life-time (year)
$C_{sell back}$	The sellback rate ($/kWh)
PV	Photovoltaic
NPC	Net Present Cost ($)
COE	Levelized Cost of Electricity ($/kWh)
BIPV	Building Integrated Photovoltaic
$E_{load served}$	Real electrical load by system (kWh/year)
Greek letters	
ω_s	Sunset hour angle (Radian)
n	Number of day during the year
φ	Latitude (Radian)
δ	Declination of sun (Radian)

REFERENCES

1. Kalbasi, R., Izadi, F. and Talebizadehsardari, P., "Improving performance of AHU using exhaust air potential by applying exergy analysis", ***Journal of Thermal Analysis and Calorimetry***, Vol. 139, (2020), 2913-2923. (https://doi.org/10.1007/s10973-019-09198-1).
2. Li, Z., Du, C., Ahmadi, D., Kalbasi, R. and Rostami, S., "Numerical modeling of a hybrid PCM‐based wall for energy usage reduction in the warmest and coldest months", ***Journal of Thermal Analysis and Calorimetry***, Vol. 144, (2020), 1985-1998. (https://doi.org/10.1007/s10973-020-09861-y).
3. Nariman, A., Kalbasi, R. and Rostami, S., "Sensitivity of AHU power consumption to PCM implementation in the wall-considering the solar

radiation", ***Journal of Thermal Analysis and Calorimetry***, Vol. 143, (2020), 2789-2800. (https://doi.org/10.1007/s10973-020-10068-4).

4. Zomer, C., Custódio, I., Antoniolli, A. and Rüther, R., "Performance assessment of partially shaded building-integrated photovoltaic (BIPV) systems in a positive-energy solar energy laboratory building: Architecture perspectives", ***Solar Energy***, Vol. 211, (2020), 879-896. (https://doi.org/10.1016/j.solener.2020.10.026).
5. Building Integrated Photovoltaics for Norway. (http://bipvno.no), (Accessed: 27 Nov. 2020).
6. Tabakovic, M., Fechner, H., Van Sark, W., Louwen, A., Georghiou, G., Makrides, G., Loucaidou, E., Ioannidou, M., Weiss, I., Arancon, S. and Betz, S., "Status and outlook for building integrated photovoltaics (BIPV) in relation to educational needs in the BIPV sector", ***Energy Procedia***, Vol. 111, (2017), 993-999. (https://doi.org/10.1016/j.egypro.2017.03.262).
7. Bonomo, P., Chatzipanagi, A. and Frontini, F., "Overview and analysis of current BIPV products: New criteria for supporting the technological transfer in the building sector", ***VITRUVIO-International Journal of Architectural Technology and Sustainability***, Vol. 1, (2015), 67-85. (https://doi.org/10.4995/vitruvio-ijats.2015.4476).
8. Haugjord, A., "Building integrated photovoltaics with thermal energy storage: A techno-economic performance assessment under grid constraints", Master's Thesis, University of Agder, (2020). (https://uia.brage.unit.no/uia-xmlui/bitstream/handle/11250/2679376/Alexander%20Haugjord.pdf?sequence=1).
9. Kalbasi, R., Shahsavar, A. and Afrand, M., "Incorporating novel heat recovery units into an AHU for energy demand reduction-exergy analysis" ***Journal of Thermal Analysis and Calorimetry***, Vol. 139, (2020), 2821-2830. (https://doi.org/10.1007/s10973-019-09060-4).
10. Nguyen, Q., Naghieh, A., Kalbasi, R., Akbari, M., Karimipour, A. and Tlili, I., "Efficacy of incorporating PCMs into the commercial wall on the energy-saving annual thermal analysis", ***Journal of Thermal Analysis and Calorimetry***, Vol. 143, (2020), 2179-2187. (https://doi.org/10.1007/s10973-020-09713-9).
11. Kalbasi, R., Shahsavar, A. and Afrand, M., "Reducing AHU energy consumption by a new layout of using heat recovery units", ***Journal of Thermal Analysis and Calorimetry***, Vol. 139, (2020), 2811-2820. (https://doi.org/10.1007/s10973-019-09070-2).
12. Delponte, E., Marchi, F., Frontini, F., Polo, C., Fath, K. and Batey, M., "BIPV in EU28, from niche to mass market: an assessment of current projects and the potential for growth through product innovation", ***Proceedings of 31st European Photovoltaic Solar Energy Conference Exhibition***, (2015), 3046-3050. (https://doi.org/10.4229/EUPVSEC20152015-7DO.15.4).
13. BIPV market and stakeholderanalysis and needs, PVSites, (http://www.pvsites.eu), (Accessed: 27 Nov. 2020).
14. Updated on BIPV market and stakeholder analysis, BIPV boost, Public reports. (https://bipvboost.eu/public-reports), (Accessed: 27 Nov. 2020).
15. Worldwide BIPV Market, 24-7 press release. (https://www.24-7pressrelease.com/press-release/455396/worldwide-bipv-market-to-reach-57-billion-in-2023-says-new-n-tech-report), (Accessed: 29 Nov. 2020).
16. Jahangiri, M., Ghaderi, R., Haghani, A. and Nematollahi, O., "Finding the best locations for establishment of solar-wind power stations in Middle-East using GIS: A review", ***Renewable and Sustainable Energy Reviews***, Vol. 66, (2016), 38-52. (https://doi.org/10.1016/j.rser.2016.07.069).
17. Kalbasi, R., Jahangiri, M., Nariman, A. and Yari, M., "Optimal design and parametric assessment of grid-connected solar power plants in Iran, a Review", ***Journal of Solar Energy Research***, Vol. 4, (2019), 142-162. (https://doi.org/10.22059/jser.2019.282276.1114).
18. Kuehner, A.L., Mdeihli, N., Coccolo, S., Perera, A.T.D., Mohajeri, N. and Scartezzini, J.L., "Extending building integrated photovoltaics (BIPV) using distributed energy hubs. A case study in Cartigny, Switzerland", ***Energy Procedia***, Vol. 122, (2017), 487-492. (https://doi.org/10.1016/j.egypro.2017.07.299).
19. Tadesse, M., "Design and feasibility analysis of Building Integrated PV (BIPV) system: Case study in Bahir Dar university lecture halls building", ***American Journal of Mechanical Engineering***, Vol. 5, (2017), 24-32. (https://doi.org/10.12691/ajme-5-1-5).
20. Aelenei, D., Lopes, R.A., Aelenei, L. and Gonçalves, H., "Investigating the potential for energy flexibility in an office building with a vertical BIPV and a PV roof system", ***Renewable Energy***, Vol. 137, (2019), 189-197. (https://doi.org/10.1016/j.renene.2018.07.140).
21. Ramanan, P., Kalidasa Murugavel, K., Karthick, A. and Sudhakar, K., "Performance evaluation of building-integrated photovoltaic systems for residential buildings in southern India", ***Building Services Engineering Research and Technology***, Vol. 41, (2019), 492-506. (https://doi.org/10.1177/0143624419881740).
22. Ni, Z., Jiang, J., Cai, X., Hu, L., Shi, G., Cao, H., Lu, W. and Wu, Z., "System design and economic configuration of building integrated photovoltaic", ***Proceedings of 37th European Photovoltaic Solar Energy Conference and Exhibition***, (2020), 1891-1895. (https://www.eupvsec-planner.com/presentations/c49007/system_design_and_economic_configuration_of_building_integrated_photovoltaic.htm).
23. Thomas, R. ed., Photovoltaics and architecture, Taylor & Francis, (2003). (https://www.amazon.com/Photovoltaics-Architecture-Randall-Thomas/dp/0415231825).
24. Climate of Iran, Iran Traveling Center. (https://www.irantravelingcenter.com/climate-of-iran), (Accessed: 24 Nov. 2020).
25. Jahangiri, M., Haghani, A., Heidarian, S., Alidadi Shamsabadi, A. and Pomares, L.M., "Electrification of a tourist village using hybrid renewable energy systems, Sarakhiyeh in Iran", ***Journal of Solar Energy Research***, Vol. 3, (2018), 201-211. (https://jser.ut.ac.ir/article_68643.html).
26. Jahangiri, M., Soulouknga, M.H., Bardei, F.K., Alidadi Shamsabadi, A., Akinlabi, E.T., Sichilalu, S.M. and Mostafaeipour, A., "Techno-econo-environmental optimal operation of grid-wind-solar electricity generation with hydrogen storage system for domestic scale, case study in Chad", ***International Journal of Hydrogen Energy***, Vol. 44, (2019), 28613-28628. (https://doi.org/10.1016/j.ijhydene.2019.09.130).
27. Jahangiri, M., Alidadi Shamsabadi, A., Mostafaeipour, A., Rezaei, M., Yousefi, Y. and Pomares, L.M., "Using fuzzy MCDM technique to find the best location in Qatar for exploiting wind and solar energy to generate hydrogen and electricity", ***International Journal of Hydrogen Energy***, Vol. 45, (2020), 13862-13875. (https://doi.org/10.1016/j.ijhydene.2020.03.101).
28. Jahangiri, M., Nematollahi, O., Haghani, A., Raiesi, H.A. and Alidadi Shamsabadi, A., "An optimization of energy cost of clean hybrid solar-wind power plants in Iran", ***International Journal of Green Energy***, Vol. 16, No. 15, (2019), 1422-1435. (https://doi.org/10.1080/15435075.2019.1671415).
29. Rezaei, M., Khalilpour, K.R. and Jahangiri, M., "Multi-criteria location identification for wind/solar based hydrogen generation: The case of capital cities of a developing country", ***International Journal of Hydrogen Energy***, Vol. 45, (2020), 33151-33168. (https://doi.org/10.1016/j.ijhydene.2020.09.138).
30. Jahangiri, M., Alidadi Shamsabadi, A., Riahi, R., Raeiszadeh, F. and Dehkordi, P.F., "Levelized cost of electricity for wind-solar power systems in Japan, a review", ***Journal of Power Technologies***, Vol. 100, (2020), 188-210. (http://papers.itc.pw.edu.pl/index.php/JPT/article/view/1359).
31. Pahlavan, S., Jahangiri, M., Alidadi Shamsabadi, A. and Rahimi Ariae, A., "Assessment of PV-based CHP system: The effect of heat recovery factor and fuel type", ***Journal of Energy Management and Technology***, Vol. 3, (2019), 40-47. (https://doi.org/10.22109/jemt.2018.137207.1106).
32. Mostafaeipour, A., Jahangiri, M., Haghani, A., Dehshiri, S.J.H., Dehshiri, S.S.H., Sedaghat, A., Saghaei, H., Akinlabi, E.T., Sichilalu, S.M., Chowdhury, M.S. and Techato, K., "Statistical evaluation of using the new generation of wind turbines in South Africa", ***Energy Reports***, Vol. 6, (2020), 2816-2827. (https://doi.org/10.1016/j.egyr.2020.09.035).
33. Jahangiri, M., Rizi, R.A. and Alidadi Shamsabadi, A., "Feasibility study on simultaneous generation of electricity and heat using renewable energies in Zarrin Shahr, Iran", ***Sustainable Cities and Society***, Vol. 38, (2018), 647-661. (https://doi.org/10.1016/j.scs.2018.01.043).
34. Jahangiri, M., Haghani, A., Alidadi Shamsabadi, A., Mostafaeipour, A. and Pomares, L.M., "Feasibility study on the provision of electricity and hydrogen for domestic purposes in the south of Iran using grid-connected renewable energy plants", ***Energy Strategy Reviews***, Vol. 23, (2019), 23-32. (https://doi.org/10.1016/j.esr.2018.12.003).
35. Jahangiri, M., Haghani, A., Mostafaeipour, A., Khosravi, A. and Raeisi, H.A., "Assessment of solar-wind power plants in Afghanistan: A review". ***Renewable and Sustainable Energy Reviews***, Vol. 99, (2019), 169-190. (https://doi.org/10.1016/j.rser.2018.10.003).

36. Mostafaeipour, A., Rezaei, M., Jahangiri, M. and Qolipour, M., "Feasibility analysis of a new tree-shaped wind turbine for urban application: A case study", ***Energy & Environment***, Vol. 31, (2020), 1230-1256 . (https://doi.org/10.1177%2F0958305X19888878).

37. Ebrahimi, S., Jahangiri, M., Raiesi, H.A. and Rahimi Ariae, A., "Optimal planning of on-grid hybrid microgrid for remote island using HOMER software, Kish in Iran", ***International Journal of Energetica***, Vol. 3, (2018), 13-21. (https://doi.org/10.47238/ijeca.v3i2.77).

38. Jahangiri, M., Khosravi, A., Raiesi, H.A. and Mostafaeipour, A., "Analysis of standalone PV-based hybrid systems for power generation in rural area", ***Proceedings of International Conference on Fundamental Research in Electrical Engineering***, (2017), 1-10. (https://civilica.com/doc/672922).

39. Mostafaeipour, A., Sedaghat, A., Hedayatpour, M. and Jahangiri, M., "Location planning for production of bioethanol fuel from agricultural residues in the south of Caspian Sea", ***Environmental Development***, Vol. 33, (2020), 100500. (https://doi.org/10.1016/j.envdev.2020.100500).

40. Vahdatpour, S., Behzadfar, S., Siampour, L., Veisi, E. and Jahangiri, M., "Evaluation of off-grid hybrid renewable systems in the four climate regions of Iran", ***Journal of Renewable Energy and Environment (JREE)***, Vol. 4, (2017), 61-70. (https://doi.org/10.30501/jree.2017.70107).

41. Jahangiri, M., Nematollahi, O., Sedaghat, A. and Saghafian, M., "Techno-economical assessment of renewable energies integrated with fuel cell for off grid electrification: A case study for developing countries", ***Journal of Renewable and Sustainable Energy***, Vol. 7, (2015), 023123. (https://doi.org/10.1063/1.4918592).

42. Zaniani, J.R., Dehkordi, R.H., Bibak, A., Bayat, P. and Jahangiri, M., "Examining the possibility of using solar energy to provide warm water using RETScreen4 software (Case study: Nasr primary school of Pirbalut)", ***Current World Environment***, Vol. 10 (Special Issue), (2015), 835. (http://doi.org/10.12944/CWE.10.Special-Issue1.101).

43. Moein, M., Pahlavan, S., Jahangiri, M. and Alidadi Shamsabadi, A., "Finding the minimum distance from the national electricity grid for the cost-effective use of diesel generator-based hybrid renewable systems in Iran", ***Journal of Renewable Energy and Environment (JREE)***, Vol. 5, (2018), 8-22. (https://doi.org/10.30501/jree.2018.88377).

44. Rahimi Ariae, A., Jahangiri, M., Fakhr, M.H. and Alidadi Shamsabadi, A., "Simulation of biogas utilization effect on the economic efficiency and greenhouse gas emission: A case study in Isfahan, Iran", ***International Journal of Renewable Energy Development***, Vol. 8, (2019), 149-160. (https://doi.org/10.14710/ijred.8.2.149-160).

45. Rezk, H., Alghassab, M. and Ziedan, H.A., "An optimal sizing of stand-alone hybrid PV-fuel cell-battery to desalinate seawater at saudi NEOM city", ***Processes***, Vol. 8, (2020), 382. (https://doi.org/10.3390/pr8040382).

46. Jahangiri, M., Haghani, A., Heidarian, S., Mostafaeipour, A., Raiesi, H.A. and Alidadi Shamsabadi, A., "Sensitivity analysis of using solar cells in regional electricity power supply of off-grid power systems in Iran", ***Journal of Engineering, Design and Technology***, Vol. 18, (2020), 1849-1866. (https://doi.org/10.1108/JEDT-10-2019-0268).

47. Ghaderian, A., Jahangiri, M. and Saghaei, H., "Emergency power supply for NICU of a hospital by solar-wind-based system, a step towards sustainable development", ***Journal of Solar Energy Research***, Vol. 5, (2020), 506-515. (https://doi.org/10.22059/jser.2020.306423.1166).

JREE: Vol. 9, No. 1, (Winter 2022) 13-22

Journal of Renewable Energy and Environment

Journal Homepage: www.jree.ir

Materials and Energy Research Center

MERC

Research Article

Investigation and Ranking of the Effect of Biodiesel Produced from Safflower Oil by the Hydrodynamic Method in Diesel Generator Engine Using TOPSIS Method

Marziyeh Gharibian [a], Bahram Hosseinzadeh Samani [a*], Alireza Shirneshan [b,c], Sajad Rostami [a]

[a] *Department of Mechanical Engineering of Biosystems, Shahrekord University, Shahrekord, Chaharmahal and Bakhtiari, Iran.*
[b] *Department of Mechanical Engineering, Najafabad Branch, Islamic Azad University, Najafabad, Iran.*
[c] *Aerospace and Energy Conversion Research Center, Najafabad Branch, Islamic Azad University, Najafabad, Iran.*

PAPER INFO

Paper history:
Received: 27 February 2021
Revised in revised form: 10 April 2021
Scientific Accepted: 15 April 2021
Published: 30 October 2021

Keywords:
Biodiesel,
Hydrodynamic Reactor,
Diesel Generator,
Performance Indices,
Pollution Indicators

ABSTRACT

To investigate the possibility of using fuel for plant origin in a diesel generator, safflower methyl ester was prepared and used as a biodiesel. In this research, biodiesel was produced through a transesterification reaction using a hydrodynamic reactor, which increased the reaction efficiency and reduced fuel production time. Upon increasing the reaction time from 30 seconds to 60 seconds, the reaction performance increased by 5.5 %. Then, its important features complied with ASTM D-6751 standard. The performance and pollution indices of the diesel generator engine were tested with compounds B0, B20, B50, B80 and B100. The results of short-term engine tests showed that by increasing the share of biodiesel to 20 %, CO emissions were reduced by 21 % compared to pure diesel fuel, but the amount of NO_X increased by 0.82 % compared to diesel. Also, the use of 20 % volume of biodiesel in the fuel composition increased the thermal efficiency of braking, braking power, and braking torque of fuel, compared to diesel. Also, the specific fuel consumption of B20 was reduced by 2 %, which is very important economically. Finally, the TOPSIS analysis illustrated that B50 fuel outperformed pure diesel fuel and other listed fuel combinations.

https://doi.org/10.30501/jree.2021.272074.1186

1. INTRODUCTION

With the rising population around the world, the use of fossil fuels, mainly in the transportation sector, has been soaring. Diesel engines are now considered an essential part of the propulsion of various vehicles. Today, however, diesel engines are considered as one of the main consumers of fossil fuels and hence, one of the important causes of noise and environmental pollution [1]. Today, because of the fast depleting nature of non-renewable fuel sources and the rise of greenhouse gas emissions owing to the combustion of these fuels, finding that can be cost-effective, renewable, and efficient with less greenhouse gas emissions is of particular importance [2]. Alternative fuels must come from cheap, renewable, affordable, and environmentally friendly sources. One of the most predominant sources of alternative fuels is biofuels. These fuels are used as liquid or gas in the transportation sector [3]. Biofuels generated from existing sources such as wood waste, plant species, municipal solid waste, aquatic plants, algae, and animal waste produce lower gas emission than fossil fuels [4].

Biodiesel is one of the most suitable substitute fuels that can be a good alternative to diesel fuel [5]. It is a renewable fuel with high combustion efficiency, less pollutant gases with degradability in the environment, and suitable lubrication properties [6, 7]. Biodiesels are also characterized by a large amount of cetane, less smoke, less sulfur, and non-toxicity compared to diesel; therefore, it is more popular than diesel [8].

To use vegetable oils and animal fats directly as a source of energy in internal combustion engines and to ensure proper combustion conditions, it is necessary to break the molecular structure of these sources into simpler and balanced components because, otherwise, it will damage engine components [9, 10]. To this end, molecules of oil or fat compounds play a part in the reaction with alcohol, including ethanol or methanol, in the presence of an acidic or alkaline reactant, and the OH group in the used alcohol replaces the hydrocarbon chain in the oil. As a result, esters form with a new molecular structure, called fatty acid methyl esters, which are very similar to Diesel No. 2 [11]. So far, various methods have been proposed for biodiesel production including microemulsion, pyrolysis, and transesterification. The biodiesel obtained by microemulsion or pyrolysis method, because of its low cetane number, could yield incomplete fuel combustion and not be suitable [12]. Among the biodiesel production methods, the transesterification method is the best

*Corresponding Author's Email: b.hosseinzadehsamani@gmail.com (B. Hosseinzadeh Samani)
URL: https://www.jree.ir/article_138922.html

Please cite this article as: Gharibian, M., Hosseinzadeh Samani, B., Shirneshan, A.R. and Rostami, S., "Investigation and ranking of the effect of biodiesel produced from safflower oil by the hydrodynamic method in diesel generator engine using TOPSIS method", ***Journal of Renewable Energy and Environment (JREE)***, Vol. 9, No. 1, (2022), 13-22. (https://doi.org/10.30501/jree.2021.272074.1186).

common method and it aims to reduce oil viscosity when triglyceride and alcohol react with each other [13]. In biodiesel production, with the help of conventional reactors, such problems as long production time, high production cost, low production efficiency, etc. need to be addressed in the design and construction of biodiesel production systems to make biodiesel fuel production more efficient and economical. In recent years, many types of research have been conducted on the development of various technologies for intensifying biodiesel production in order to eliminate or reduce some of the problems related to biodiesel production using conventional methods. These technologies include new reactors or a combination of reactors that intensify reactions such as turbulence, heat transfer, and mass transfer between two liquid phases in the biodiesel production process [14]. The use of hydrodynamic cavitation is one of these new technologies that has received much attention in recent years [15]. Biodiesel production with the assistance of hydrodynamic technology is a method with high potential on an industrial scale which is easier to develop than other methods [16]. The use of hydrodynamic cavitation has good energy efficiency and shortens the reaction time by consuming less energy than conventional mechanical methods. In this method, energy equivalent to half of the mechanical method is required which is a combination of two reaction phases using variable pressure. Cavitation is generated by fluid flow under controlled conditions through simple geometries such as venturi tubes and perforated plates. Given that the pressure of the fluid approaches the vapor pressure, large cavities form in the fluid, which subsequently fluctuate, causing the pressure and temperature to rise. As a result, immiscible liquids mix better and the transesterification process is enhanced [17]. In a study on biodiesel production from safflower seed oil by potassium hydroxide catalyst, Hosseinzadeh et al. (2013) reported that upon using hydrodynamic cavitation, biodiesel was obtained in optimum conditions [15].

The sharpest contrast between biodiesel and diesel compounds is their oxygen content. The oxygen content of diesel is zero, whereas biodiesel contains 10 to 12 % weight of oxygen, which reduces the emission of pollutants such as Particulate Matter (PM), Unburned Hydro-Carbons (UHC), and Carbon Monoxide (CO). Also, a high biodiesel cetane number can help shorten the ignition delay in a diesel engine [18]. Biodiesel is a long-chain fatty acid methyl or ethyl ester that is produced from biosources such as oils or fats from animals and vegetables and can be used instead of diesel in compression combustion engines without the need for major modifications [19].

In a study, El Morsi et al. (2019) examined biodiesel produced from a combination of kitchen waste oils, jatropha, palm, and algae using a transesterification process in single-cylinder diesel engines at 10 and 20 % by volume. The results showed that CO, CO_2, HC, and smoke emissions were lower for B10 and B20 than diesel, but NO_X increased slightly for all Bx's compared to diesel [20]. Nedayali and Shirneshan (2016) evaluated the effect of mixtures of biodiesel and diesel on engine performance characteristics (braking power, braking torque, braking thermal efficiency, and BSFC) in a diesel-electric motor. The results of this study exhibited an increase in braking power, braking torque, braking thermal efficiency, and a decrease in BSFC at higher engine loads for all fuel mixtures [21].

Safflower plant, scientifically called (*Carthamus Tinctorius L*), is an annual herbaceous plant whose flowers are yellow to red depending on the type of plant and each has 20 to 100 flowers and each produces a seed. The presence of wild species scattered throughout the country shows the good adaptation of this plant to the climatic conditions of Iran. Relative tolerance to soil salinity and air dryness, low moisture requirement, and high-quality oil are the noticeable features of safflower. In general, safflower seeds, depending on their genotype, contain 25 to 45 % oil, of which more than 90 % of fatty acids are unsaturated such as linoleic and oleic acid. Safflower with strong and long roots can absorb and consume water from the depths of the earth, and the prickly leaves and thorny organs create the least evaporation in the plant [22].

In the present study, safflower seed, which is native to Iran, was used for biodiesel production due to the mentioned advantages. Hydrodynamic cavitation reactors require less energy, lower sensitivity, lower production cost, and lower temperature than conventional reactors used to convert oil to biodiesel in the transesterification process [23, 24]. In short, much research has been done to investigate the emission and performance parameters of the engine with biodiesel fuel, but almost no research has been done to investigate the parameters of the engine with biodiesel from safflower oil using the hydrodynamic cavitation reactor. In this study, biodiesel was produced continuously using safflower oil and hydrodynamic cavitation reactor, and considering its various mixtures with diesel No. 2 common in Iran in the diesel generator engine, it was used to evaluate the engine performance indicators such as braking power, braking torque, BSFC, braking thermal efficiency, and exhaust gas temperature and engine pollution indicators, e.g., nitrogen oxides and carbon monoxide emissions, and the results were compared with pure diesel fuel.

2. EXPERIMENTAL

2.1. Raw materials and detectors

In the present study, the transesterification method was used. The required oil for biodiesel production was obtained from safflower seeds. The alcohol used was high purity methanol (99 %) and the catalyst used in the biodiesel production process was potassium hydroxide (KOH- 99.8 %). n-Hexane (96 %) and phenolphthalein (98 %) were also used as solvent aid and detector, respectively.

2.2. Extraction and preparation of oil

Safflower seeds were placed in an oven at 65 °C for 24 hours until their moisture content reached about 7 %. The grains were then ground using a laboratory mill. Soxhlet apparatus and normal hexane solution were employed to extract the oil. For this purpose, in 5 steps, oil was extracted each time a certain amount of ground grains (100 g) was placed in the Soxhlet machine and by controlling the solvent temperature, residence time, and solvent volume. Finally, the obtained oil was passed through a filter to remove solid particles [25]. Finally, 140 grams of oil was obtained, which showed a return of 28 % of oil.

2.3. Determining the acidity of safflower oil

Since fatty acids are weak acids, it is necessary to use strong alkalis such as potassium hydroxide to titrate them. If the percentage of free fatty acids is higher than 0.5 %, the ester exchange method cannot be used directly and a pre-refining step must be performed, which is the esterification step. To assess the acidity of the sample, 20 g of the oil tested in Erlenmeyer was weighed as 300 ml and then, 50 ml of solvent was added and stirred until the oil sample was completely dissolved. 2 ml of phenolphthalein was added and titrated with 0.1 mol/l potassium hydroxide until it turned a solid constant pink color. The solution was shaken vigorously during titration so that the pink color lasted for 30 seconds. Formulas (1) and (2) were employed to calculate the acid number and percentage of free fatty acids, respectively.

$$\text{Acid number} = \frac{PC \times NP \times 56.1}{W} \quad (1)$$

$$\text{Percentage of free fatty acids} = \frac{PC \times NP \times 28.2}{W} \quad (2)$$

where PC is the average of potassium consumed (ml), NP is the normality of the potassium solution (mol/L), and W is the weight of the oil. For transesterification testing, the oil acidity must be greater than 3 %.

2.4. Characteristics of biodiesel fatty acids produced from safflower

The characteristics of biodiesel are undeniably affected by the type of fatty acids. Recognition of these characteristics is very effective in determining the characteristics of biodiesel fuels [26]. Biodiesel is composed of some fatty acid monoesters, and the presence of the weight percentage of each one of them in biodiesel fuel affects its thermophysical properties. In other words, the properties of biodiesel fuel depend on the monoesters of its constituent fatty acids, the most important of which are the esters of palmitic, stearic, oleic, and linoleic fatty acids that directly affect the combustion process and engine performance [27]. Short-chain saturated fatty acids such as stearic and palmitic have a greater effect on engine power output, and long-chain unsaturated fatty acids such as oleic and linoleic have less significant effect on engine power. Therefore, biodiesel fuel from the oils with more saturated and less unsaturated fatty acids can increase power production by the engine [28]. Safflower oil is a good source for biodiesel owing to its high fatty acids. Some physical and chemical characteristics of safflower oil are shown in Table 1 [22].

Table 1. Physical and chemical characteristics of safflower oil

Properties	Normal limits	Unit
Viscosity at 40 °C	28.3	mm^2/s
Density at 15 °C	0.92	kg/m^3
Flash point	226	°C
Acid number	0.4-10	mg KOH/g Oil
Base number	186-194	-
Ionic number	130-150	-
Percentage of non-soapy ingredients	0.3-1.3	(wt %)
C18: 2 (Linoleic acid)	71-75	(wt %)
C18: 1 (Oleic acid)	16-20	(wt %)
C16: 0 (Palmitic acid)	6-8	(wt %)
C18: 0 (Stearic acid)	2-3	(wt %)

2.5. Hydrodynamic cavitation setup

The laboratory system required in this study was designed such that KOH and methanol would be first mixed with a magnetic stirrer model MR3001 made by the German company Heidolph and combined with safflower oil. The resulting solution was then injected into the hydrodynamic cavitation reactor by the Hydolf 5206 peristaltic pump. The reactor used in this study consisted of a transparent polycarbonate stator to observe the process, a stainless-steel perforated rotor to produce bubbles, and an electric motor to generate propulsion. The specifications of the reactor components are given in Table 2.

Table 2. Characteristics of the hydrodynamic reactor

Parameter	Value
Rotor length (m)	0.08
Rotor density (g/l)	905
Rotor diameter (m)	0.09
Number of holes	40
Stator diameter (m)	0.097
Electric-motor power (W)	75
Hole diameter (m)	0.004
Stator length (m)	0.09
Electric-motor rotational speed (rpm)	3200

2.6. Transesterification

To increase the reaction rate, the catalyst molecules must be homogeneously available to the oil and methyl hydrate molecules. For this reason, to increase the solubility of the catalyst used, potassium hydroxide and methanol were first combined with a magnetic stirrer and then, introduced into the methanol reservoir. Simply put, the catalyst and methanol were prepared before the transesterification reaction. In the next step, the desired solution is transferred into the chamber along with safflower oil. In this case, the combined solution rotates between the rotor and the stator using centrifugal force, and the rotation speed of the rotor ranges between 1000 and 3000 rpm. The holes in the rotor cause a sudden decrease in pressure, yielding a hole in the solution. As a result, at lower temperatures, the mass transfer between safflower oil and methanol increases. Following the completion of the transesterification reaction, methyl ester (biodiesel), glycerin, and some excess alcohols were the reaction products.

The glycerin phase was denser than the biodiesel phase and precipitated after a while. After precipitating glycerol, this phase was separated using a separating funnel [29]. The reason for choosing this method is its simplicity and low cost. After the settling step, the resulting biodiesel was washed 3 times with water containing 1 % by volume of phosphoric acid (H_3PO_4) to remove excess products such as glycerol, catalyst, and soap formed. Transparency of laundry wastewater remains a good measure of the completion of the work. Finally, after biodiesel purification, vacuum distillation was used to dry it [30]. The production steps of biodiesel using the hydrodynamic reactor are shown in Figure 1.

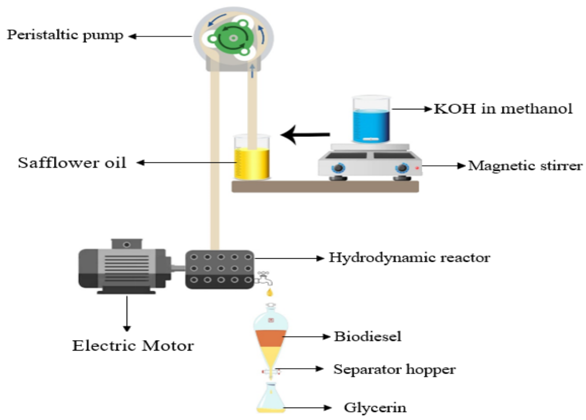

Figure 1. Schematic diagram of the hydrodynamic device

2.7. Calculation of methyl ester conversion and biodiesel performance

The weight of the biodiesel phase of each sample was measured after separation using a digital scale. Then, the exact amount of fatty acid esters was determined using gas chromatography (Claus 580 GC model, Perkin Elmer Co, USA) according to ASTM D6751 standard. Equation (3) was used to calculate the FAME performance [31, 32].

$$\text{FAME}\ \% = \frac{\sum A - A_{IS}}{A_{IS}} \times \frac{M_{IS}}{M} \times 100 \tag{3}$$

where $\sum A$ = The sum of the levels below the peaks; (μV×sec), A_{IS} = The sub-peak level corresponding to the internal standard; (μV×sec), C_{IS} = Internal standard solution concentration; (mg/ml), V_{IS}= Volume of use of internal standard solution; (ml) and M = Biodiesel weight for decomposition in GC (mg).

2.8. Diesel engine generator

The diesel generator engine used in this research consists of two parts: the engine and the generator. The engine part includes a 4-stroke, 12-cylinder, and direct injection engine equipped with a supercharger. This engine is a model (3412C TA) with a maximum engine power of 537 kW at 1800 rpm. The generator part is made by Caterpillar Company, which is connected to the central processor that can display the amount of output voltage, power, and motor speed on the control panel by processing data. The specifications of the diesel generator engine listed in Table 3 are shown.

Table 3. Specifications of the diesel generator engine

Engine type	**Diesel power generator CAT3412**
Cylinder number	12
Bore (mm)	137
Stroke (mm)	154
Cooling system	Water-cooled
Rated engine speed (rpm)	1800
Aspiration	Turbocharged-After cooled
Governor	Mechanical
Compression ratio	13:01
Starting motor	24 V/7 Kw

3. METHOD

3.1. Methodology

To assess the performance and pollution of diesel generator engine using biodiesel produced from safflower oil with the help of hydrodynamic cavitation and compare it with conventional diesel fuel, different ratios of biodiesel were combined with diesel as independent variables by volume. These compounds contain 0 %, 20 %, 50 %, 80 % and 100 % biodiesels based on volume, which are called B0, B20, B50, B80 and B100, respectively. Each fuel was tested at full dynamometer load and a constant speed of 1530 rpm and their effects on dependent variables such as engine pollution indices such as NO_X and CO emissions and engine performance indices such as Braking power, braking torque, BSFC, exhaust gas temperature, and braking thermal efficiency were investigated. This experiment was analyzed in a completely randomized design with three replications. The mean comparison test was performed by the LSD method. SPSS software was employed for statistical analysis.

3.2. Multi-index decision-making method

TOPSIS is a multi-criteria decision-making method used to select the best option based on the number of criteria [33].

The steps to solve the problem using the TOPSIS method are as follows [34]:

Step One: After forming a decision matrix to evaluate the options based on the number of criteria, the dimensionless matrix is formed by Equation (4) using the vector method.

$$n_{ij} = \frac{r_{ij}}{\sqrt{\sum_{i=1}^{m} r_{ij}^2}} \tag{4}$$

Step Two: At this stage of the TOPSIS method, the normal matrix created must be balanced. For this purpose, by using Equations (5) and (6), the weight of each criterion is multiplied in all subsets of that criterion and the weight of the criteria must be determined in advance.

$$W_i = \frac{r_i}{\sum_{i=1}^{n} r_i} \tag{5}$$

$$\sum_{i=1}^{n} W_i = 1 \tag{6}$$

$$V_{ij} = r_{ij} \times W_{n\times m} = \begin{matrix} V_{11} & V_{1j} & V_{1n} \\ \vdots & \vdots & \vdots \\ V_{m1} & V_{mj} & V_{mn} \end{matrix} \tag{7}$$

Step Three: Positive Ideal Point (PIS) and Negative Ideal Point (NIS) are calculated next. At this step, for each index, a positive ideal and a negative ideal were obtained through Relations (8) and (9), respectively.

$$\text{PIS} = \{(\max V_{ij} | j \in J), (\min V_{ij} | j \in J) | i = 1, 2, \dots, 3\} = \{V_1^+, V_2^+, \dots, V_j^+, \dots, V_n^+\} \tag{8}$$

$$\text{NIS} = \{(\max V_{ij} | j \in J), (\min V_{ij} | j \in J) | i = 1, 2, \dots, 3\} = \{V_1^-, V_2^-, \dots, V_j^-, \dots, V_n^-\} \tag{9}$$

Step Four: At this step, the relative proximity of each option to the ideal solution was calculated. The Euclidean distance of each method from the positive and negative ideals was calculated through Formulas (10) and (11), respectively.

$$d_{i+} = \{\sum j^n = 1^{(V_{ij} - V_j^+)^2}\}^{0.5}; \quad i = 1, 2, \dots, m \tag{10}$$

$$d_{i-} = \{\sum j^n = 1^{(V_{ij} - V_j^-)^2}\}^{0.5}; \quad i = 1, 2, \dots, m \tag{11}$$

Step Five: This step is to evaluate the ideal solution. At this point, the relative proximity of each method to the ideal solution was calculated using Equation 12 for this purpose.

$$C_i = \frac{d_{i-}}{((d_{i+}) + (d_{i-}))}; \quad 0 \le c_i \le 1; \quad i = 1, 2, \dots, m \tag{12}$$

Step Six: Ranking based on the value of C_i is done between zero and one. The closer this value is to one, the closer the solution is to the ideal answer and the better the solution is.

4. RESULTS AND DISCUSSION

4.1. Characteristics of produced biodiesel

The biodiesel characteristics of vegetable oils depend significantly on the fatty acid chains in the feed used. For methyl ester to be introduced as biodiesel, some of its characteristics must meet reference standards. Some characteristics of biodiesel achieved from SFO sing the hydrodynamic reactor including density, viscosity, acid content, flash point, iodine content, free glycerin, and cetane number according to ASTM standard D6751 were measured and the outcomes were compared with EN 14214 (Table 4). The results indicate that most of the characteristics comply with the ASTM standard.

In the process of producing biodiesel using a hydrodynamic reactor, the reaction time was increased from 30 seconds to 60 seconds, which led to a 5.5 % increase in the process. As a result, reaction time is a major factor in biodiesel production in this way. Also, the efficiency of methyl ester produced by the mentioned method was higher than the conventional method. The analysis of data showed that by increasing the distance between the stator and the rotor, the amount of solution mixing was reduced, which attenuated the performance of the biodiesel production process. The optimum yield of biodiesel production from safflower oil was 11.89 %, for which the distance between the stator and the rotor was 53.1 cm, reaction time was 63.88 seconds, catalyst concentration was 0.94 %, and the molar ratio of alcohol to oil was 1: 8.36.

Table 4. Some physicochemical characterization of biodiesel from SFO

Properties	Unit	EN 14214	ASTM D6751	Methyl ester
Ester content	% (m/m)	< 96.5	-	95.9
Density at 15 °C	g/cm^3	0.86–0.9	-	0.87
Kinematic viscosity at 40 °C	mm/s	3.5–5.0	1.9–6.0	4.52
Iodine number	g Iodine/100 g oil	< 120	-	117.47
Cetane number	-	> 51	> 47	48
Flash point	°C	> 101	> 130	157
Acid number	mgKOH/g	< 0.5	< 0.5	0.37
Free glycerin	% mass	0.02	-	0.017
Total glycerin	% mass	0. 24	-	0.25

4.2. NO_X emission

Figure 2 shows the changes in nitrogen oxides of biodiesel fuel compounds with the coefficient of determination (R^2=0.9575) and standard error (SE=6.7954). As shown earlier, the incremental percentage of NO_X emissions from B0 is minimal in B20 and maximal in B100. Following an increase in the amount of biodiesel in fuel content, the amount of NO_X increases as well. Therefore, the amount of NO_X in B100 compared to B0 increases by 14.5 %. Nitrogen Oxide (NO) is obtained by the combustion of hydrocarbons inside the engine combustion chamber. As smoke leaves the engine and communicates with the air, much more oxygen becomes available to NO, allowing for the production of nitrogen dioxide (NO_2). Therefore, high temperature and oxygen are the two principal factors in the formation of nitrogen oxides [33]. Since biodiesel fuel contains 10-12 % oxygen, it is not available [34] because it increases nitrogen oxides in two ways. First, as the share of biodiesel in the compound increases, the oxygen content of the compound also increases and more oxygen goes into contact with nitrogen, which leads to the production of nitrogen oxides. Second, as the oxygen content of the fuel increases, the ignition temperature decreases and the ignition time delay decreases. Therefore, it produces high temperatures due to combustion, thus providing a good opportunity for oxygen and nitrogen to react and produce nitrogen monoxide (NO) [35]. Most researchers have found that using biodiesel and diesel simultaneously increases NO_X due to the presence of much more oxygen in biodiesel than diesel [18, 36]. Hassanian et al. (2005) reported the same results for the effect of biodiesel percentage on NOx emission [37].

4.3. Carbon monoxide emissions (CO)

Figure 3 indicates the emission of CO pollutants from different percentages of biodiesel with a determination coefficient (R^2=0.8571) and a standard error (SE=0.000667). The results illustrated that the emission of CO pollutants in biodiesel fuels was significantly lower than pure diesel. Therefore, the amount of CO emission in B100 fuel compared to B0 fuel was reduced by 45.5 %. CO is a colorless, odorless gas that is dangerous to humans and animals, even at very low concentrations. CO is produced when the amount of oxygen in the combustion of organic matter is low. CO production and the presence of oxygen in an internal combustion engine are inversely related [20, 38]. As a result, less carbon monoxide is produced during combustion. Also, the ratio of carbon to hydrogen in biodiesel is lower than diesel [39, 40]. Therefore, this fact can be another reason for reducing CO emissions. Hosseinzadeh et al. reported the effect of biodiesel produced from safflower oil by ultrasonic waves on a diesel generator engine and reported that following an increase in percentage of biodiesel in fuel mixtures, CO emission decreased [41].

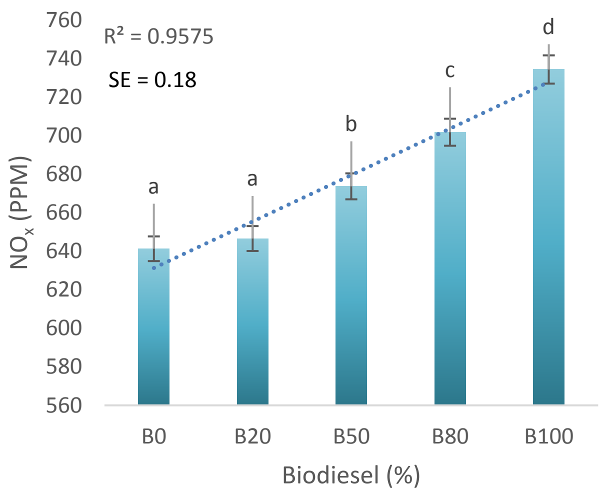

Figure 2. The effect of increasing biodiesel on NO_X emissions

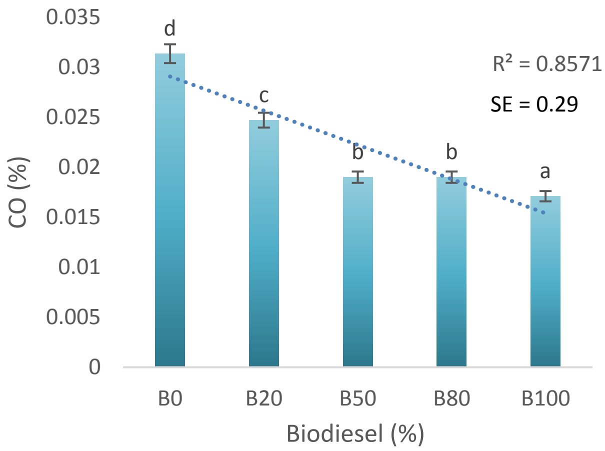

Figure 3. The effect of increasing biodiesel on CO emissions

4.4. Brake power

Figure 4 shows the braking power changes with the increasing value of Bx for different fuel combinations with the determination coefficient (R^2=0.8295) and standard error (SE=1.105037). Changes in engine braking power relative to different percentages of biodiesel are a quadratic function that is maximum at point B50 and minimum at point B100 (Equation 4). The results illustrated that upon increasing biodiesel content in fuel from B0 to B50, the braking power increased, and with increasing the percentage of biodiesel from B50 to B100, the braking power decreased. The reason for the increase in power in B50 is high fuel consumption and the presence of oxygen content, which causes a more complete combustion [42]. The reason for the decrease in power upon an increase in biodiesel content is the low thermal value of biodiesel [43]. Also, the viscosity of biodiesel is higher than diesel, which leads to incomplete automation of fuel in the combustion chamber and decreases the braking power of the engine [44]. Pure biodiesel at full load compared to pure diesel had a 3.7 % reduction in power owing to a decrease in the fuel thermal value. Murillo et al. reported that at full load, biodiesel power was reduced by 14.4 % compared to diesel fuel. They also concluded that the biodiesel calorific value was 13.5 % lower than diesel [45]. Xue et al. noted in a review study that the use of a low percentage of biodiesel in combination with diesel slightly reduced power and this reduction was not significant for the driver [18].

$$y = -1.5045X^2 + 8.102X + 92.701 \tag{13}$$

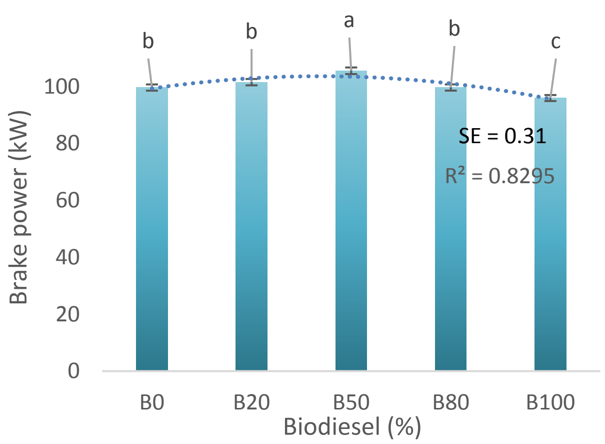

Figure 4. Effect of biodiesel content in fuel on the engine braking power

4.5. Brake torque

Figure 5 illustrates the variation of braking torque with the increasing biodiesel content for different fuel combinations with the coefficient of determination (R^2=0.7556) and standard error (SE=7.389837). The variation of braking torque to different percentages of biodiesel is a quadratic function which is maximum at point B50 and minimum at point B100 (Equation 5). The results illustrated an increase in braking torque with an increasing index value of Bx to B50 and then, with increasing the percentage of biodiesel, the amount of braking torque decreased. The energy release process for B100 is relatively slow due to its high cetane number, which lowers the pressure peak. The low thermal value of biodiesel also reduces the effective medium pressure. Based on the literature review, as the force applied to the surface of the piston decreased, the torque exerted by this force on the crankshaft is also reduced [46]. Therefore, the engine torque using pure biodiesel is less than pure diesel. In other words, oxygen of biodiesel content in the fuel improved the combustion process and complete combustion. As a result, more energy is released, increasing the average pressure inside the combustion chamber [47], which increases the power and torque produced for B50. Pure biodiesel at full load compared to pure diesel decreased by 5.27 % and B50 showed a 4.34 % increase in torque. Lin et al. reported that the maximum and minimum power and torque differences between diesel and eight types of vegetable oil methyl esters were 1.49 and 0.64, 1.39 and 1.25 percent, respectively. This is owing to high viscosity, high specific fuel consumption, high oxygen content, and high biodiesel ignition [48]. Shirneshan et al. reported in a study that the braking torque increased as the engine load increased because increasing the temperature of combustion led to more complete combustion at higher loads [49].

$$y = -7.5097X^2 + 36.424X + 589.15 \tag{14}$$

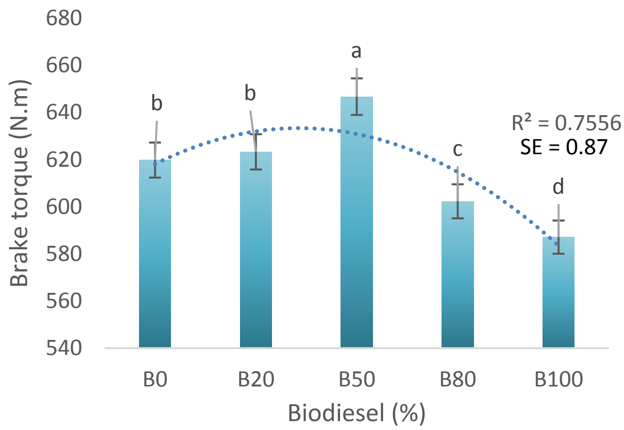

Figure 5. Effect of biodiesel content in fuel on the diesel engine output torque

4.6. Brake Special Fuel Consumption (BSFC)

The values of BSFC at full load for different percentages of biodiesel with the coefficient of determination (R^2=0.9948) and standard error (SE=9.853518) are shown in Figure 6. Changes in brake-specific fuel consumption relative to different percentages of biodiesel are a quadratic function that is minimum at point B20 and maximum at point B100 (Equation 6). As the share of biodiesel in fuel mixtures increases, the specific fuel consumption increases because biodiesel has a higher density and lower thermal value than B0 [50]. The results of the experiments show that high density cannot compensate for the low thermal value; as a result, by increasing biodiesel content in fuel, to produce the equal power as in pure diesel, it is necessary to use much more fuel per unit time by the engine, or in other words, fuel consumption increases to create the previous power [50]. In addition to these parameters, viscosity, injection pressure, and atomization ratio also have large effects on BSFC [48, 52]. The highest increase in specific brake fuel consumption is related to B100 fuel, which increases fuel consumption by 69.45 % compared to diesel. Also, the greatest reduction in BSFC is related to B20 and B50 fuels, for which due to the high biodiesel content, the braking power is improved and the low thermal value of biodiesel is compensated [47, 53]. In this way, the consumption of special fuel by 2 % is reduced compared to pure diesel and this issue is very important in terms of optimal fuel consumption. Labeckas and Slavinskas claimed that BSFC for biodiesel compounds was higher than B0 and they reported that this increase could result from the thermal value of rapeseed oil, which is about 12.5 % lower than that of diesel [51].

$$y = 17.359X^2 - 57.958X + 300.79 \tag{15}$$

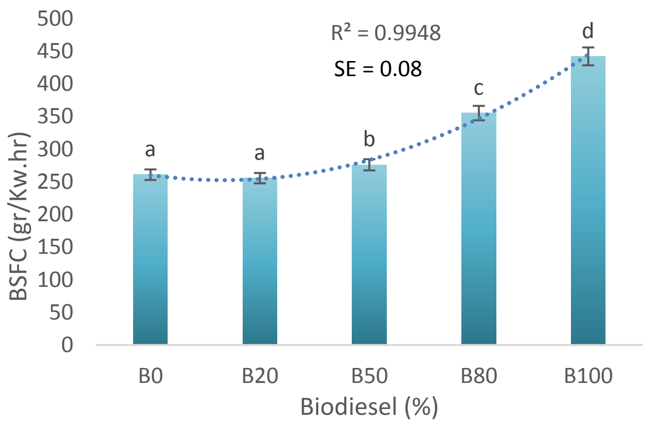

Figure 6. The effect of increasing biodiesel on BSFC

4.7. Brake thermal efficiency

The braking thermal efficiency of a diesel engine is the efficiency in which the chemical energy of the fuel is converted into useful work [54]. The braking thermal efficiency values of diesel fuels B0, B20, B50, B80 and B100 are shown in Figure 7 with the determination coefficient (R^2=0.8871) and standard error (SE=0.773479). Changes in braking thermal efficiency concerning different percentages of biodiesel are a quadratic function that occurs at point B20 with the best braking heat efficiency of the engine at full load and also with minimal braking thermal efficiency at point B100 (Equation 7). Braking thermal efficiency is inversely related to braking specific fuel consumption and fuel thermal value. Thus, the main reason for the reduction in the braking thermal efficiency of B100 fuel compared to other fuel mixtures is higher BSFC and lower HLHV of biodiesel. The results indicated that the BTE of the engine for B20 and B50 fuels is 21.21 % and 7.7 % higher than that for B0, respectively. According to some researchers, the improvement of brake thermal efficiency for these fuels results from more efficient combustion and increased lubrication of these fuel compounds compared to diesel [47, 53]. Shirneshan et al. reported in a study that for all fuel mixtures, upon increasing load, the braking heat efficiency increased due to the reduction of heat loss and the increase in power generated with increasing load [49]. Buyukkaya also tested rapeseed biodiesel compounds with diesel in the engine and concluded that BTE increased with an increase in the amount of biodiesel in the fuel composition, and the probable reason for the increase in BTE biodiesel at full load was its lubrication and the greater amount of oxygen [37].

$$Y = -1.706X^2 + 7.1287X + 23.162 \tag{16}$$

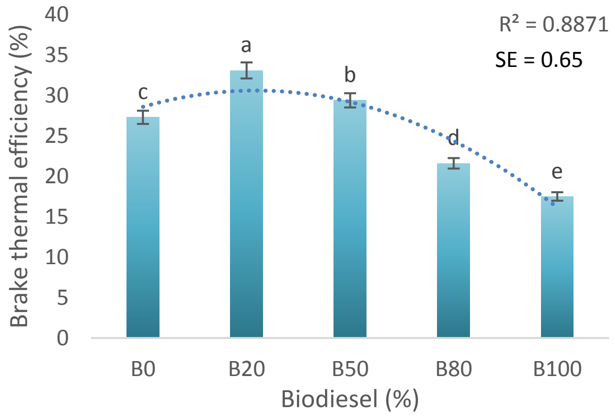

Figure 7. The effect of increasing biodiesel on braking thermal efficiency

4.8. Exhaust gas temperature

Figure 8 indicates the exhaust temperature changes for pure diesel fuel (B0), mixtures of diesel and biodiesel fuel, and pure biodiesel fuel (B100) with the determination coefficient (R^2=0.994) and standard error (SE=11.99893). As biodiesel content in fuel increases, the exhaust gas temperature decreases so that the highest exhaust gas temperature is related to diesel fuel and the lowest temperature is related to B100. Upon increasing biodiesel content, the pressure of the cylinder decreases and as a result, the exhaust gas temperature decreases. The exhaust gas temperature changes with the change in the combustion time delay. Long delays cause combustion delays and as a result, the temperature of the exhaust gases increases [55]. Also, a lower cetane number prolongs the time delay. For this reason, the exhaust gas temperature for B0 fuel is higher than other biodiesel fuel compounds due to its lower cetane number. Aydin and Binder reported that the highest exhaust gas temperatures were observed at 2500 rpm and full load for diesel fuel, which reached 469 °C, while the corresponding values for B20 were 395 °C under the same conditions [44].

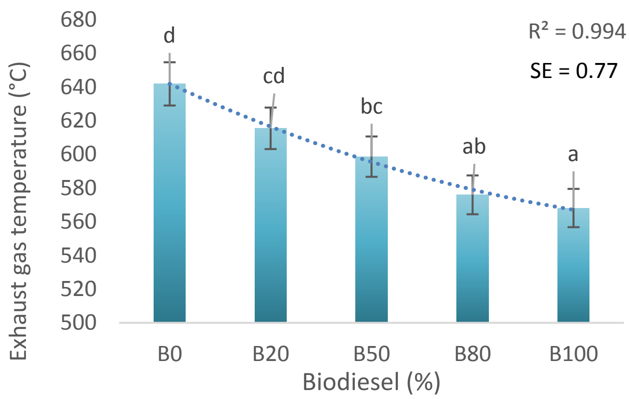

Figure 8. Effect of increasing biodiesel on exhaust gases

4.9. Comparison between the proposed combinations of fuels and pure diesel fuel

To select the most suitable fuel combination from 5 combinations (B0, B20, B50, B80 and B100), a multi-criteria decision method (TOPSIS) was used. According to the steps mentioned in the TOPSIS method, the decision matrix (Table 5), the scaleless matrix (Table 6), the normal weight matrix (Table 7), the PIS and NIS values (Table 8), and the distance from the positive and negative ideal solutions (Table 9) were calculated.

The final rankings of the five compared fuel combinations (B0, B20, B50, B80, and B100) in this study are shown in Figure 9. The results show that B50 fuel is better than pure diesel fuel and other listed fuel combinations.

Table 5. Decision-making matrix

Biodiesel blends	Power (kW)	Torque (N.m)	BSFC (g/kWh)	CO % (vol)	NOx (ppm)	BTE % (vol)	EGT (°C)
B0	99.63551	619.7808	260.8026	0.03135	641.294	27.30035	641.749
B20	101.5263	623.2578	255.4732	0.0247	646.5878	33.09792	615.3804
B50	105.5298	646.6796	275.9305	0.019	673.6998	29.39732	598.579
B80	99.64799	602.2808	355.1309	0.019	701.7747	21.6091	575.924
B100	95.95	587.1	441.94	0.0171	734.35	17.5085	568.1

Table 6. The dimensionless decision matrix

Biodiesel blends	Power (kW)	Torque (N.m)	BSFC (g/kWh)	CO % (vol)	NOx (ppm)	BTE % (vol)	EGT (°C)
B0	0.4433	0.4498	0.3579	0.61396	0.4214	0.4628	0.4778
B20	0.4517	0.4523	0.3506	0.4837	0.4249	0.5611	0.4582
B50	0.4695	0.4693	0.3787	0.3720	0.4427	0.4984	0.4457
B80	0.4433	0.4371	0.4874	0.3720	0.4612	0.3663	0.4288
B100	0.4269	0.4261	0.6065	0.3348	0.4826	0.2968	0.4230

Table 7. The weighted dimensionless decision matrix

Biodiesel blends	Power (kW)	Torque (N.m)	BSFC (g/kWh)	CO % (vol)	NOx (ppm)	BTE % (vol)	EGT (°C)
B0	0.0071	0.00751	0.1071	0.1988	0.0109	0.1370	0.0105
B20	0.0072	0.0075	0.1049	0.1566	0.0110	0.1661	0.0101
B50	0.0075	0.0078	0.1133	0.1204	0.0114	0.1475	0.0098
B80	0.0071	0.0073	0.1459	0.1204	0.0119	0.1084	0.0094
B100	0.0068	0.0071	0.1816	0.1084	0.0125	0.0878	0.0093

Table 8. PIS and NIS values for each dependent variable of five fuel types

	Power (kW)	Torque (N.m)	BSFC (g/kWh)	CO % (vol)	NOx (ppm)	BTE % (vol)	EGT (°C)
PIS	0.0075	0.0078	0.1049	0.1204	0.0109	0.1661	0.0094
NIS	0.0071	0.0073	0.1459	0.1988	0.0119	0.1084	0.0105

Table 9. Distance from the positive and negative ideal solutions

Biodiesel blends	D+	D-
B0	0.0835	0.0481
B20	0.0361	0.0823
B50	0.0203	0.0933
B80	0.0707	0.0783
B100	0.1101	0.0993

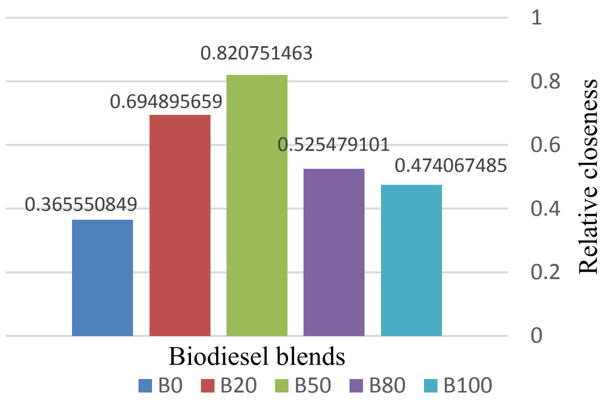

Figure 9. Final ranking of five fuel combinations (B0, B20, B50, B80 and B100)

5. CONCLUSIONS

Despite many types of research in the field of performance parameters and pollution of biodiesel fuel combustion engine, no research has been done so far on the parameters of biodiesel engine of safflower oil with transesterification reaction with the help of hydrodynamic cavitation reactor. According to the experiments conducted in this study, the efficiency of biodiesel produced by a hydrodynamic cavitation reactor was higher than that by conventional and ultrasonic reactors. After biodiesel production, performance characteristics and pollution of different percentages in combination with diesel fuel in the diesel generator engine were studied at the laboratory. The results showed that upon increasing the percentage of biodiesel in the fuel composition, the emission of nitrogen oxides increased due to the high combustion temperature and the emission of carbon monoxide decreased due to the high oxygen content of biodiesel compared to diesel fuel. Following an increase in the volume percentage of biodiesel to 50 % in the combination of fuel, braking power and braking torque increased and, then, decreased due to high fuel consumption and the presence of oxygen content in biodiesel. With the increase in the percentage of biodiesel fuel in fuel mixtures, the consumption of special brake fuels had an upward trend due to the high density and low calorific value of biodiesel. Also, braking thermal efficiency was inversely related to braking specific fuel consumption and fuel calorific value. Exhaust gas temperature decreased by increasing the percentage of biodiesel in the fuel mixture due to the reduction of cylinder pressure and ignition time delay. By using TOPSIS, the comparison between the proposed fuel compositions and the pure diesel fuel demonstrated that the fuel mixtures containing 20 % and 50 % biodiesel in terms of performance characteristics and pollution could be identified as potentially confirmed alternatives for use in diesel generators.

6. ACKNOWLEDGEMENT

The authors are grateful to the Research Council of Shahrekord University for their financial support for conducting this study (grant No.: 96GRN1M1796).

REFERENCES

1. Caliskan, H., "Environmental and enviroeconomic researches on diesel engines with diesel and biodiesel fuels", ***Journal of Cleaner Production***, Vol. 154, (2017), 125-129. (https://doi.org/10.1016/j.jclepro.2017.03.168).
2. Brennan, L. and Owende, P., "Biofuels from microalgae-A review of technologies for production, processing, and extractions of biofuels and co-products", ***Renewable and Sustainable Energy Reviews***, Vol. 14, No. 2, (2010), 557-577. (https://doi.org/10.1016/j.rser.2009.10.009).
3. Demirbas, A., "Biodiesel for future transportation energy needs", ***Energy Sources***, Vol. 32, No. 16, (2010), 1490-1508. (https://doi.org/10.1080/15567030903078335).
4. Demirbas, A., "Progress and recent trends in biodiesel fuels", ***Energy Conversion and Management***, Vol. 50, No. 1, (2009), 14-34. (https://doi.org/10.1016/j.enconman.2008.09.001).
5. Aransiola, E.F., Ojumu, T.V., Oyekola, O., Madzimbamuto, T. and Ikhu-Omoregbe, D., "A review of current technology for biodiesel production: State of the art", ***Biomass and Bioenergy***, Vol. 61, (2014), 276-297. (https://doi.org/10.1016/j.biombioe.2013.11.014).
6. Makareviciene, V., Skorupskaite, V., Levisauskas, D., Andruleviciute, V. and Kazancev, K., "The optimization of biodiesel fuel production from microalgae oil using response surface methodology", ***International Journal of Green Energy***, Vol. 11, No. 5, (2014), 527-541. (https://doi.org/10.1080/15435075.2013.777911).
7. Shahid, E.M. and Jamal, Y., "Production of biodiesel: A technical review", ***Renewable and Sustainable Energy Reviews***, Vol. 19, No. 9, (2011), 4732-4745. (https://doi.org/10.1016/j.rser.2011.07.079).
8. Atadashi, I., Aroua, M.K,. Aziz, A.A. and Sulaiman, N.M.N., "Production of biodiesel using high free fatty acid feedstocks", ***Renewable and Sustainable Energy Reviews***, Vol. 16, No. 5, (2012), 3275-3285. (https://doi.org/10.1016/j.rser.2012.02.063).
9. Ito, T., Sakurai, Y., Kakuta, Y., Sugano, M. and Hirano, K., "Biodiesel production from waste animal fats using pyrolysis method", ***Fuel Processing Technology***, Vol. 94, No. 1, (2012), 47-52. (https://doi.org/10.1016/j.fuproc.2011.10.004).
10. Rashtizadeh, E., Farzaneh, F. and Ghandi, M., "A comparative study of KOH loaded on double aluminosilicate layers, microporous and mesoporous materials as catalyst for biodiesel production via transesterification of soybean oil", ***Fuel***, Vol. 89, No. 11, (2010), 3393-3398. (https://doi.org/10.1016/j.fuel.2010.05.039).
11. Abbaszaadeh, A., Ghobadian, B., Omidkhah, M.R. and Najafi, G., "Current biodiesel production technologies: A comparative review", ***Energy Conversion and Management***, Vol. 63, (2012), 138-148. (https://doi.org/10.1016/j.enconman.2012.02.027).
12. Saifuddin, N., Samiuddin, A. and Kumaran, P., "A review on processing technology for biodiesel production", ***Trends in Applied Sciences Research***, Vol. 10, No. 1, (2015), 1. (https://doi.org/10.3923/tasr.2015.1.37).
13. Lin, L., Cunshan, Z., Vittayapadung, S., Shen, X. and Dong, M., "Opportunities and challenges for biodiesel fuel", ***Applied Energy***, Vol. 88, No. 4, (2011), 1020-1031. (https://doi.org/10.1016/j.apenergy.2010.09.029).
14. Qiu, Z., Zhao, L. and Weatherley, L., "Process intensification technologies in continuous biodiesel production", ***Chemical Engineering and Processing: Process Intensification***, Vol. 49, No. 4, (2010), 323-330. (https://doi.org/10.1016/j.cep.2010.03.005).
15. Hosseinzadeh Samani, B., Behruzian, M., Najafi, G., Fayyazi, E., Ghobadian, B., Behruzian, A., Mofijur, M., Mazlan, M. and Yue, J., "The rotor-stator type hydrodynamic cavitation reactor approach for enhanced biodiesel fuel production", ***Fuel***, Vol. 283, (2021), 118821. (https://doi.org/10.1016/j.fuel.2020.118821).
16. Ji, J., Wang, J., Li, Y., Yu, Y. and Xu, Z., "Preparation of biodiesel with the help of ultrasonic and hydrodynamic cavitation", ***Ultrasonics***, Vol. 44, (2006), e411-e414. (https://doi.org/10.1016/j.ultras.2006.05.020).
17. Raheman, H. and Ghadge, S., "Performance of diesel engine with biodiesel at varying compression ratio and ignition timing", ***Fuel***, Vol. 87, No. 12, (2008), 2659-2666. (https://doi.org/10.1016/j.fuel.2008.03.006).
18. Xue, J., Grift, T.E. and Hansen, A.C., "Effect of biodiesel on engine performances and emissions", ***Renewable and Sustainable Energy Reviews***, Vol. 15, No. 2, (2011), 1098-1116. (https://doi.org/10.1016/j.rser.2010.11.016).
19. Pal, A., Verma, A., Kachhwaha, S.S. and Maji, S., "Biodiesel production through hydrodynamic cavitation and performance testing", ***Renewable Energy***, Vol. 35, No. 3, (2010), 619-624. (https://doi.org/10.1016/j.renene.2009.08.027).
20. Abed, K., Gad, M., El Morsi, A., Sayed, M. and AbuElyazeed, S., "Effect of biodiesel fuels on diesel engine emissions", ***Egyptian Journal of Petroleum***, Vol. 28, No. 2, (2019), 183-188. (https://doi.org/10.1016/j.ejpe.2019.03.001).
21. Nedayali, A. and Shirneshan, A.R., "Experimental study of the effects of biodiesel on the performance of a diesel power generator", ***Energy & Environment***, Vol. 27, No. 5, (2016), 553-565. (https://doi.org/10.1177/0958305X15627550).
22. Duz, M.Z., Saydut, A. and Ozturk, G., "Alkali catalyzed transesterification of safflower seed oil assisted by microwave irradiation", ***Fuel Processing Technology***, Vol. 92, No. 3, (2011), 308-313. (https://doi.org/10.1016/j.fuproc.2010.09.020).
23. Gogate, P.R., Tayal, R.K. and Pandit, A.B., "Cavitation: A technology on the horizon", ***Current Science***, Vol. 91, (2006), 35-46. (https://www.jstor.org/stable/24094173?seq=1).
24. Tabatabaei, M., Aghbashlo, M., Dehhaghi, M., Shariat Panahi, H., Molla Hosseini, A., Hosseini, M. and Soufiyan, M., "Reactor technologies for biodiesel production and processing: A review", ***Progress in Energy and Combustion Science***, Vol. 74, (2019), 239-303. (https://doi.org/10.1016/j.pecs.2019.06.001).
25. Tahvildari, K. and Amani, M., "Preparation of biodiesel from saffllower oil and study of ITS 20 % mixure whit diesel fuel", ***Applide Researches***

in Chemistry, Vol. 4, (2010). (https://www.sid.ir/en/Journal/ViewPaper.aspx?ID=190122).

26. Knothe, G. and Steidley, K.R., "Kinematic viscosity of biodiesel components (fatty acid alkyl esters) and related compounds at low temperatures", ***Fuel***, Vol. 86, No. 16, (2007), 2560-2567. (https://doi.org/10.1016/j.fuel.2007.02.006).

27. El Diwani, G., Attia, N. and Hawash, S., "Development and evaluation of biodiesel fuel and by-products from jatropha oil", ***International Journal of Environmental Science & Technology***, Vol. 6, No. 2, (2009), 219-224. (https://link.springer.com/article/10.1007/BF03327625).

28. Sheng, C. and Azevedo, J., "Estimating the higher heating value of biomass fuels from basic analysis data", ***Biomass and Bioenergy***, Vol. 28, No. 5, (2005), 499-507. (https://doi.org/10.1016/j.biombioe.2004.11.008).

29. Fayyazi, E., Ghobadian, B., van de Bovenkamp, H.H., Najafi, G., Hosseinzadeh Samani, B., Heeres, H. and Yue, J., "Optimization of biodiesel production over chicken eggshell-derived CaO catalyst in a continuous centrifugal contactor separator" ***Industrial & Engineering Chemistry Research***, Vol. 57, No. 38, (2018), 12742-12755. (https://doi.org/10.1021/acs.iecr.8b02678).

30. Farvardin, M., Hosseinzadeh Samani, B., Rostami, S., Abbaszadeh-Mayvan, A., Najafi, G. and Fayyazi, E., "Enhancement of biodiesel production from waste cooking oil: Ultrasonic-hydrodynamic combined cavitation system", ***Energy Sources, Part A: Recovery, Utilization, and Environmental Effects***, Vol. 41, (2019), 1-15. (https://doi.org/10.1080/15567036.2019.1657524).

31. Rahimi, M., Mohammadi, F., Basiri, M., Parsamoghadam, M. and Masahi, M., "Transesterification of soybean oil in four-way micromixers for biodiesel production using a cosolvent", ***Journal of the Taiwan Institute of Chemical Engineers***, Vol. 64, (2016), 203-210. (https://doi.org/10.1016/j.jtice.2016.04.023).

32. Wang, Y., Ou, S., Liu, P., Xue, F. and Tang, S., "Comparison of two different processes to synthesize biodiesel by waste cooking oil", ***Journal of Molecular Catalysis A: Chemical***, Vol. 252, No. 2, (2006), 107-112. (https://doi.org/10.1016/j.molcata.2006.02.047).

33. Wang, T.-C. and Chang, T.-H., "Application of TOPSIS in evaluating initial training aircraft under a fuzzy environment", ***Expert Systems with Applications***. Vol. 33, No. 4, (2007), 870-880. (https://doi.org/10.1016/j.eswa.2006.07.003).

34. Fathi, M.R., Matin, H.Z., Zarchi, M.K. and Azizollahi, S., "The application of fuzzy TOPSIS approach to personnel selection for Padir Company, Iran", ***Journal of Management Research***, Vol. 3, No. 2, (2011), 1-14. (https://doi.org/10.5296/jmr.v3i2.663).

35. Ushakov, S., Valland, H. and Æsøy, V., "Combustion and emissions characteristics of fish oil fuel in a heavy-duty diesel engine", ***Energy Conversion and Management***, Vol. 65, (2013), 228-238. (https://doi.org/10.1016/j.enconman.2012.08.009).

36. Tyson, K.S., "Biodiesel handling and use guidelines", US Department of Energy, Energy Efficiency and Renewable Energy; (2006). (https://afdc.energy.gov/files/u/publication/biodiesel_handling_use_guide.pdf).

37. Pinto, A.C., Guarieiro, L.L., Rezende, M.J., Ribeiro, N.M., Torres, E.A., Lopes, W.A., Pereira, P. and Andrade, J.B., "Biodiesel: An overview", ***Journal of the Brazilian Chemical Society***, Vol. 16, No. 6B, (2005), 1313-1330. (https://doi.org/10.1590/S0103-50532005000800003).

38. Buyukkaya, E., "Effects of biodiesel on a DI diesel engine performance, emission and combustion characteristics", ***Fuel***, Vol. 89, No. 10, (2010), 3099-3105. (https://doi.org/10.1016/j.fuel.2010.05.034).

39. Allami, H.A., Tabasizadeh, M., Rohani, A., Nayebzadeh, H. and Farzad, A., "Effect of ultrasonic irradiation on the properties and performance of biodiesel produced from date seed oil used in the diesel engine", ***Ultrasonics Sonochemistry***, Vol, 60, (2020), 104672. (https://doi.org/10.1016/j.ultsonch.2019.104672).

40. Köse, H. and Acaroğlu, M., "The effect of hydrogen addition to Cynara biodiesel on engine performance and emissions in diesel engine", ***Energy Sources, Part A: Recovery, Utilization, and Environmental Effects***, Vol. 42, (2020), 1-20. (https://doi.org/10.1080/15567036.2020.1765904).

41. Gad, M., El-Araby, R., Abed, K., Ibiari, E.I., El Morsi, A.K. and El-Diwani, G.I., "Performance and emissions characteristics of CI engine fueled with palm oil/palm oil methyl ester blended with diesel fuel", ***Egyptian Journal of Petroleum***, Vol. 27, No. 2, (2018), 215-219. (https://doi.org/10.1016/j.ejpe.2017.05.009).

42. Behçet, R., "Performance and emission study of waste anchovy fish biodiesel in a diesel engine", ***Fuel Processing Technology***, Vol. 92, No. 6, (2011), 1187-1194. (https://doi.org/10.1016/j.fuproc.2011.01.012).

43. Hosseinzadeh Samani, B., Ansari Samani, M., Shirneshan, A.R., Fayyazi, E., Najafi, E. and Rostami, S., "Evaluation of an enhanced ultrasonic-assisted biodiesel synthesized using safflower oil in a diesel power generator", ***Biofuels***, Vol. 11, No. 4, (2020), 523-532. (https://doi.org/10.1080/17597269.2019.1646542).

44. Shirneshan, A.R., Almassi, M., Ghobadian, B. and Najafi, G.H., "Investigating the effects of biodiesel from waste cooking oil and engine operating conditions on the diesel engine performance by response surface methodology", ***Iranian Journal of Science and Technology-Transactions of Mechanical Engineering***, Vol, 38, No. M2, (2014), 289-301. (https://doi.org/10.22099/IJSTM.2014.2496).

45. Lapuerta, M., Armas, O. and Rodriguez-Fernandez, J., "Effect of biodiesel fuels on diesel engine emissions", ***Progress in Energy and Combustion Science***, Vol. 34, No. 2, (2008), 198-223. (https://doi.org/10.1016/j.pecs.2007.07.001).

46. Aydin, H. and Bayindir, H., "Performance and emission analysis of cottonseed oil methyl ester in a diesel engine", ***Renewable Energy***, Vol. 35, No. 3, (2010), 588-592. (https://doi.org/10.1016/j.renene.2009.08.009).

47. Murillo, S., Miguez, J., Porteiro, J., Granada, E. and Mora´n, J.C., "Performance and exhaust emissions in the use of biodiesel in outboard diesel engines", ***Fuel***, Vol. 86, No. 12-13, (2007), 1765-1771. (https://doi.org/10.1016/j.fuel.2006.11.031).

48. Ghobadian, B., Rahimi, H., Nikbakht, A. and Yusaf, T.F., "Diesel engine performance and exhaust emission analysis using waste cooking biodiesel fuel with an artificial neural network", ***Renewable Energy***, Vol. 34, No. 4, (2009), 976-982. (https://doi.org/10.1016/j.renene.2008.08.008).

49. Ramadhas, A., Muraleedharan, C. and Jayaraj, S., "Performance and emission evaluation of a diesel engine fueled with methyl esters of rubber seed oil", ***Renewable Energy***, Vol. 30, No. 12, (2005), 1789-1800. (https://doi.org/10.1016/j.renene.2005.01.009).

50. Lin, B.-F., Huang, J.-H. and Huang, D.-Y., "Experimental study of the effects of vegetable oil methyl ester on DI diesel engine performance characteristics and pollutant emissions", ***Fuel***, Vol. 88, No. 9, (2009), 1779-1785. (https://doi.org/10.1016/j.fuel.2009.04.006).

51. Shirneshan, A.R., Hosseinzadeh Samani, B. and Nedayali, A., "Artificial neural network model to predict the performance of a diesel power generator fueled with biodiesel", ***The Journal of Engine Research***, Vol. 42, No. 42, (2016), 43-50. (https://iranjournals.nlai.ir/handle/123456789/649544).

52. Luján, J., Bermúdez, V., Tormos, B. and Pla, B., "Comparative analysis of a DI diesel engine fuelled with biodiesel blends during the European MVEG-A cycle: Performance and emissions (II)", ***Biomass and Bioenergy***, Vol. 33, No. 6-7, (2009), 948-956. (https://doi.org/10.1016/j.biombioe.2009.02.003).

53. Labeckas, G. and Slavinskas, S., "The effect of rapeseed oil methyl ester on direct injection diesel engine performance and exhaust emissions", ***Energy Conversion and Management***, Vol. 47, No. 13-14, (2006), 1954-1967. (https://doi.org/10.1016/j.enconman.2005.09.003).

54. Song, J. and Zhang, C., "An experimental study on the performance and exhaust emissions of a diesel engine fuelled with soybean oil methyl ester", ***Proceedings of the Institution of Mechanical Engineers, Part D: Journal of Automobile Engineering***, Vol. 222, No. 12, (2008), 2487-2496. (https://doi.org/10.1243/09544070JAUTO932).

55. Canakci, M., Ozsezen, A.N., Arcaklioglu, E. and Erdil, A., "Prediction of performance and exhaust emissions of a diesel engine fueled with biodiesel produced from waste frying palm oil", ***Expert Systems with Applications***, Vol. 36, No. 5, (2009), 9268-9280. (https://doi.org/10.1016/j.eswa.2008.12.005).

Journal of Renewable Energy and Environment

Journal Homepage: www.jree.ir

Materials and Energy Research Center

MERC

Research Article

Assessment of Effect of Different Parameters on Temperature Distribution in Chemical Looping Combustor: Experimental and Numerical Approaches

Mohamed A. Barakat, Tamer Mohamed Ismail, Sayed Ibrahim Abdel-Mageed, Khaled Ramzy*

Department of Mechanical Engineering, Faculty of Engineering, Suez Canal University, Ismailia, Egypt.

PAPER INFO

Paper history:
Received: 26 January 2021
Revised in revised form: 15 March 2021
Scientific Accepted: 12 April 2021
Published: 07 November 2021

Keywords:
CO_2 Capture,
Chemical Looping Combustion,
Solid Fuel,
Gaseous Fuel,
Nickel Powder,
Modelling

ABSTRACT

The greenhouse problem has a significant effect on our communities, health, and climate. So, the capturing techniques for CO_2 remain the focus of attention these days. In this work, a Chemical Looping Combustor (CLC) was designed and fabricated with the major geometric sizes at the Faculty of Engineering, Suez Canal University. The system involves two interconnected fluidized beds. Nickel powder with 150 µm diameter as well as brown coal and liquefied petroleum gas were used as oxygen carrier, solid fuel, and gaseous fuel, respectively. The temperature distributions along the fuel reactor for LPG flow rates of 11 and 18 LPM with and without using nickel powder as well as using preheated reactor were discussed and evaluated. The effects of brown coal diameter change with and without using nickel powder were studied. The CO and CO_2 concentrations at combustion gases with and without using nickel powder were conducted for LPG and brown coal fuels. A mathematical model was used to simulate the combustion in CLC using combustion and energy code. The obtained results showed that using nickel powder improved the combustion process and in case of using LPG, the flame color changed to blue which is the color of the complete combustion flame. The CO was reduced by 48.4 % and CO_2 was augmented by 66.5 %. In case of using brown coal as solid fuel, CO was reduced by 53.7 % and CO_2 was increased by 71.9 %. Finally, there is good agreement between the experimental and numerical results based on the determination coefficient.

https://doi.org/10.30501/jree.2021.269946.1182

1. INTRODUCTION

Recently, the greenhouse effect has been the focus of attention of many scientists. Close to the years 1910-1940 and from 1970 to 2000, the earth's surface temperature increased by 0.35 °C and 0.55 °C, respectively. Based on the data recorded by global climate change organizations, the last decade has been the warmest [1]. The effect of the global warming problem is not limited to increasing the earth's surface temperature; however, as a result of this problem, scientists expect a steady increase in ice melting and increase in sea level above the normal. Many scientists today agree that an industrial greenhouse effect is the main cause of global warming such as combustion of fossil fuels and emissions of CO_2 [2]. Consequently, it is necessary to separate and store the CO_2 produced from combustion processes. A possible solution is to produce a pure stream of CO_2 from fossil fuels combustion and store it. This concept can be used as a long-term interim solution until the renewable energy sources can replace the traditional combustion systems. One of the newest technologies in this respect is called chemical looping combustion. It is a novel combustion process for gaseous or solid fuels, producing a pure stream of CO_2 [3].

Carbon capture and storage technology can be used to reduce the emitted carbon dioxide into the atmosphere in many fields of industry and power generation. If this technology is successfully used in different industrial areas and power plants, 57 % of CO_2 emissions can be reduced [4]. Driven by the global trend to reduce carbon dioxide in industrial emissions, many scientists investigated different methods of carbon dioxide capture in industrial application. However, the main problem is that carbon dioxide capture is very expensive and exceeds the cost of capturing one ton of carbon dioxide at 12 dollars. Carbon dioxide capturing at power plants reduces their efficiency by 10 ± 2 % [5].

Chemical looping combustion is the unmixed combustion technique because the fuel and the air do not have a direct reaction. Combustion occurs without air contact with fuel, where oxygen is separated from the air by a metal powder, called oxygen-carriers; therefore, the process of combustion is carried out by oxygen only and carbon dioxide can be captured with high efficiency. In chemical looping combustion, oxygen-carrier particles are run between two reactors, as shown in Figure 1.

In the first reactor, air flows from the bottom where the oxidation of particles occurs. This reactor is usually called an

*Corresponding Author's Email: kh.ramzy2005@eng.suez.edu.eg (Kh. Ramzy)
URL: https://www.jree.ir/article_139804.html

Please cite this article as: Barakat, M.A., Ismail, T.M., Abdel-Mageed, S.I. and Ramzy, Kh., "Assessment of effect of different parameters on temperature distribution in chemical looping combustor: Experimental and numerical approaches", ***Journal of Renewable Energy and Environment (JREE)***, Vol. 9, No. 1, (2022), 23-36. (https://doi.org/10.30501/jree.2021.269946.1182).

air-reactor. Then, the metal powder is transported through a ring seal to the second reactor where the fuel is inserted and this reactor is called the fuel-reactor [6-7]. The fuel and the available oxygen in the oxygen-carrier particles react according to Equation 1.

$$(2n+m)Me_xO_{y+1} + C_nH_{2m} \rightarrow (2n+m)Me_xO_y` + nCO_2 + mH_2O \quad (1)$$

Oxygen-carrier is reduced in fuel reactor and the metal powder is transferred to the air reactor to be oxidized, as shown in Equation 2.

$$2Me_xO_y + O_2 \rightarrow 2Me_xO_{y+1} \quad (2)$$

where Me_xO_{y+1} is the oxidized metal-powder and Me_xO_y is the reduced metal powder. Therefore, the objective of this process is to transport oxygen to the fuel reactor without any direct loss of efficiency and without nitrogen-dilute gas in the reaction results. Following the condensation of water and cleaning of the exhaust from impurities such as So_x, a pure stream of CO_2 is ready to be transported to a suitable location for storage [8-9]. Lewis and Gilliland put forward the principle of chemical looping combustion first [10-11].

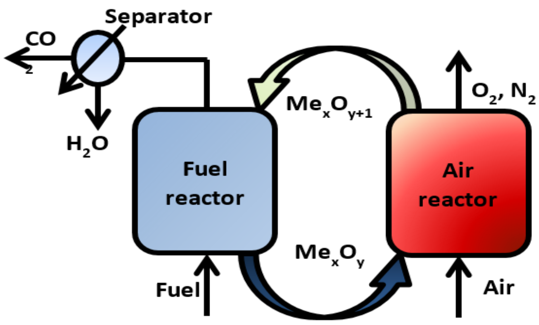

Figure 1. Schematic diagram of the chemical looping combustion process

Chemical looping combustion was first coined by Ishida et al. [11] and they recognized the concept of CLC system to capture CO_2 from fossil fuels. Lyngfelt et al. presented the first chemical looping combustion design based on the circulating fluidized bed principle [6]. More different materials have been investigated as oxygen carrier materials for use in CLC technology, especially the active oxides of iron, nickel, copper, and manganese [12]. In the beginning of the year 2011, it was reported that operation for more than 4000 h was completed in 12 different units [13] using gaseous fuels. Through the last few years, solid fuel has received a greater focus than liquid fuels, but the latter have been tested in relatively small lab units [14]. Until the year 2012, reports on nearly 120 hours of operation with three different oxygen carriers have been submitted [15] and more studies have been performed on solid fuel [16]. Due to the chemical looping combustion importance, it is important to make a comparison between different types of fuel.

Therefore, the main objectives of the present study are to design and fabricate a chemical looping combustor; to compare the combustion of gaseous and solid fuels in the chemical looping combustor' to investigate the temperature distribution along the fuel reactor using gaseous and solid fuels before and after applying CLC technology. The CO and CO_2 concentrations in combustion gases with and without using nickel powder were given for LPG and brown coal fuels. The temperature distribution along the fuel reactor for LPG flow rates of 11 and 18 LPM with and without using nickel powder as well as using preheated reactor will be discussed and evaluated.

Also, this study presents the experimental results of temperature distribution along the fuel reactor for brown coal of different diameters with and without using nickel powder. In addition, a mathematical model was developed to simulate the combustion in CLC using combustion and energy code. This code investigates the concentration of gases in emissions and temperature distribution in both gas and solid phases. The experimental and simulated results were validated according to the statistical methods such as the coefficient of determination R^2 as follows.

2. EXPERIMENTAL SETUP

2.1. Design of CLC reactor

This section presents the design of the CLC combustor with its main parts and dimensions. The chemical looping combustor was designed and fabricated at the combustion lab, Faculty of Engineering, Suez Canal University. The CLC system consists of the air reactor with a height of 2.67 m and an internal diameter of 0.09 m. The air reactor is connected to the fuel reactor with a height of 1.25 m and an internal diameter of 0.2 m. The particles flow upward in the air reactor with the inlet air and can be collected by the cyclone at the top of the CLC system. Two butterfly valves are used for measuring solid circulation flux. A photograph and a schematic diagram of the chemical looping combustor system with its main geometric sizes are shown in Figure 2.

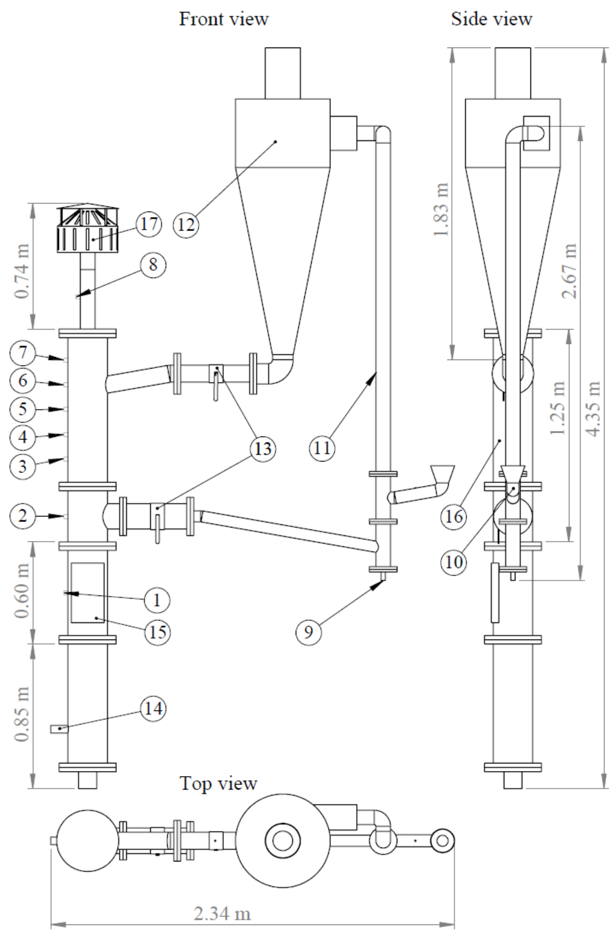

(a)

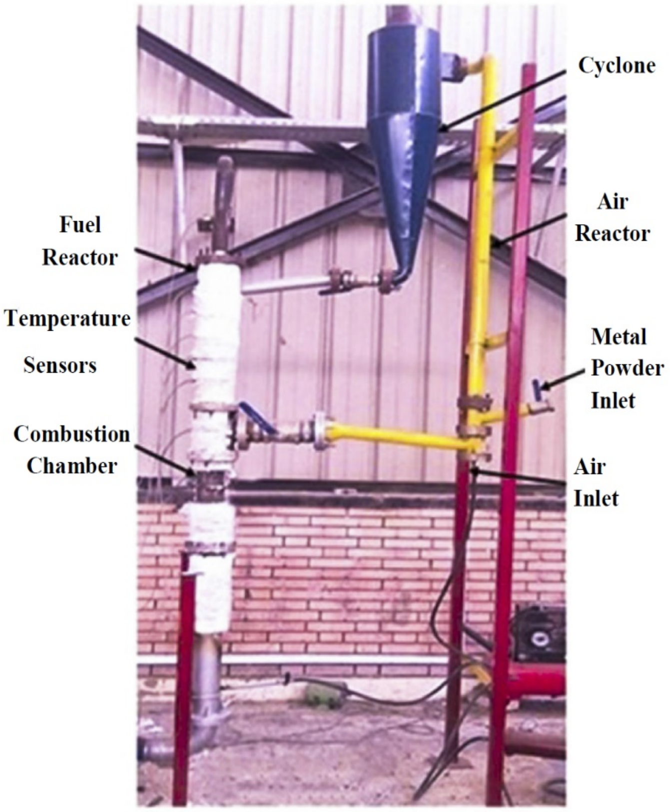

(b)

Figure 2. (a) Schematic diagram and (b) photograph of chemical looping combustion (CLC) system, where T is thermocouple sensors, 1- air inlet, 2- metal powder inlet, 3- air reactor, 4- cyclone, 5- butterfly valves, 6- burner, 7- combustion chamber, 8- fuel reactor and 9- chimney

2.2. Oxygen carrier selection

The selection of oxygen carrier is one of the most important aspects for designing the CLC system. There are many important factors to be considered when choosing an oxygen carrier. These factors include high reactivity in both cases of reduction by fuel gas and oxidation by oxygen in the air, oxygen transfer capacity, cost, environmental impacts, thermodynamic properties, and melting point. Researchers found that some oxide systems of the transition metals, Fe, Cu, Co, Mn, and Ni could be used as oxygen carriers [17, 18]. There are many experimental investigations of different oxygen carriers.

Nakano et al. [19] performed an experimental work using Fe_2O_3 with Al_2O_3 and Fe_2O_3 with Ni as support using a thermogravimetric analyzer. In addition, they presented a CLC reactor and a fixed bed reactor with gas chromatography [20]. Mattisson and Lyngfelt investigated iron ore, Fe_2O_3/Al_2O_3, and Fe_2O_3/MgO in fixed bed [21].

Also, different oxides of nickel, copper, cobalt, and manganese supported by aluminum oxide were studied by Mattisson et al. [22] for methane. From the previous studies, it can be noticed that the reaction rates during oxidation and reduction varied in a wide range depending upon the metal oxide used as well as reaction parameters. In general, nickel-based carriers appear to have the highest reduction reactivity compared to iron; manganese and copper based carriers have not been studied to the same extent. Therefore, nickel was used as metal powder in the CLC system under investigation.

2.3. Uncertainty analysis

Uncertainty in measurement is the doubt regarding the result of any measurement [23]. The analysis of experimental uncertainty was done and evaluated according to Holman [24] and Ismail et al. [25]. The minimum experimental error was equal to the ratio between its least count and the minimum recorded value of the measured output. All values were smaller than the obtained data and found to be within the allowable range of the measurements. Table 1 shows the uncertainty analysis for the measured parameters during experiments.

Table 1. Uncertainty analysis of the measured parameters

Parameter	Range	Accuracy	Uncertainty
Thermocouple K-type			
Temperature	0 °C to 1300 °C	± 2.2 °C or ± 0.25 %	± 0.043 %
Compact combustion analyzer			
Carbon dioxide	0-60 %	± 0.3	± 0.013 %
Carbon monoxide	0-2000 ppm And 4000 ppm max for 15 min	± 10 ppm ± 5 %	± 0.09 %
Rotameter			
Volume flow rate	1.2-18 LPM	-	± 2.7 %

2.4. Experimental setup for using gaseous fuel

In order to determine the effect of using CLC technology, the fuel should be combusted traditionally and the results before and after applying CLC technology need to be compared. The lower and upper explosive limits for gaseous fuel should be measured based on the system conditions. The minimum concentration of a particular combustible gas or vapor necessary to support its combustion in air is defined as the Lower Explosive Limit (LEL) for that gas. Below this level, the mixture is too "lean" to burn. The maximum concentration of a gas or vapor that burns in the air is defined as the Upper Explosive Limit (UEL). Above this level, the mixture is too “rich” to burn. In this study, Liquid Petroleum Gas (LPG) was used as gaseous fuel consisting of 60 % Propane (C_3H_8) and 40 % butane (C_4H_{10}), with a heating value equal to 46.1 MJ/kg [26]. The lower and upper explosive limits and stoichiometry percentage of Propane and Butane are shown in Table 2.

Table 2. Lower and upper explosive limits and stoichiometry percentage

Gas	LEL	UEL	Stoichiometry
Propane	2.1 %	9.5 %	4.016 %
Butane	1.8 %	8.4 %	3.135 %
All concentrations in percentage by volume			

A half HP blower with an airflow rate of 480 LPM was used as an air source for traditional combustion. Flammability limits of mixtures of several combustible gases can be measured using Le Chatelier's mixing rule for combustible volume fractions Xi using the following Equations [27].

$$LEL_{mix} = \frac{1}{\Sigma \frac{Xi}{LEL\,i}} \tag{3}$$

$$\text{UEL}_{\text{mix}} = \frac{1}{\Sigma \frac{X\,i}{UEL\,i}} \quad (4)$$

$$\text{Stoichiometry}_{\text{mix}} = \frac{1}{\Sigma \frac{X\,i}{stoich\,i}} \quad (5)$$

From the calculation above and at the air flow rate of 480 LPM, the minimum amount of fuel (Q_{min}), the maximum amount of fuel (Q_{max}), and the best ratio between the air and fuel used (Q_{stoich}) are shown in Table 3.

Table 3. Lower and upper explosive limits and stoichiometry percentage for LPG at the air flow rate of 480 LPM

Gas	Q_{min} (LPM)	Q_{max} (LPM)	Q_{stoich} (LPM)
LPG	9.64	47.629	17.98

The Q_{stoich} fuel ratio was used in experiments because due to its higher temperature than Q_{min} and lower toxic exhaust than Q_{max}. For stoichiometric combustion, Q_{fuel} =18 LPM and this flow rate consists of 40 % Butane and 60 % Propane.

$$C_3H_8 + 5\,O_2 \rightarrow 3\,CO_2 + 4\,H_2O \quad (6)$$

$$C_4H_{10} + 6.5\,O_2 \rightarrow 4\,CO_2 + 5\,H_2O \quad (7)$$

According to Equations (6) and (7), it can be noticed that 38.822×10^{-3} and 34.207×10^{-3} mole O_2 / sec are required for Propane and Butane, respectively. In order to calculate the required amount of nickel powder flow rate, the amount of needed oxygen to burn LPG components should be 73.029×10^{-3} mole/sec to burn the LPG flow rate of 18 LPM.

2.5. Experimental setup for use in solid fuel

A batch system was used by burning 300 g of brown coal with proximate analysis, as shown in Table 4. In order to calculate the required amount of nickel powder flow rate, the amount of needed oxygen to burn 300 g of brown coal experiments should be calculated. The proximate analysis for 300 g of brown coal used in experiments is shown in Table 5. From the mass percentage of the volatile matter components shown in Table 6, the required oxygen for burning combustible volatile matter can be calculated.

Table 4. Proximate analysis for brown coal

Element	Mass percent (%)
Fixed carbon (C)	39
Moisture (H_2O)	15
Volatile matter	29
Ash	17

Table 5. Proximate analysis for 300 g of brown coal

Element	Mass percent (%)	Mass for 300 g (g)	g/mole	Number of moles
Fixed carbon (C)	39	117	12	9.75
Moisture (H_2O)	15	45	18	2.5
Volatile matter	29	87	-	-
Ash	17	51	-	-

Table 6. Mass percentage for 87 g of volatile matter components

Element	Mass percent (%)	g	g/mole	Number of moles
H_2	20	17.4	2	8.7
CO	14	12.18	28	0.435
CH_4	15	13.05	16	0.82
S	1	0.87	32	0.027
N_2	5	4.35	28	0.16
O_2	24	20.88	32	0.65
CO_2	9	7.83	44	0.18
H_2O	12	10.44	18	0.58

The combustion equations of volatile matter elements are as follows:

$$8.7\,H_2 + 4.35\,O_2 \rightarrow 8.7\,H_2O \quad (8)$$

$$0.435\,CO + 0.2175\,O_2 \rightarrow 0.435\,CO_2 \quad (9)$$

$$0.82\,CH_4 + 1.64\,O_2 \rightarrow 0.82\,CO_2 + 1.64\,H_2O \quad (10)$$

$$0.027\,S + 0.027\,O_2 \rightarrow 0.027\,SO_2 \quad (11)$$

$$0.16\,N_2 + 0.32\,O_2 \rightarrow 0.32\,NO_2 \quad (12)$$

$$9.75\,C + 9.75\,O_2 \rightarrow 9.75\,CO_2 \quad (13)$$

$$32.609\,Ni + 16.3045\,O_2 \rightarrow 32.609\,NiO \quad (14)$$

According to Equations (9-13), the required oxygen for burning combustible volatile matter is equal to 6.5545 mole of O_2 and 9.75 moles of oxygen required for burning 117 g of fixed carbon. From this calculation, all the required moles of O_2 are equal to 16.3045 moles to burn 300 g of brown coal. From Equation (14), it can be noticed that 1913.82 g nickel is needed for burning 300 g of coal. From experiments, it can be noted that complete combustion with 300 g of coal takes 10 to 12 minutes. Assuming that combustion rate is constant, 2.66 to 3.2 g of nickel per the second path are required through the combustion chamber.

3. MATHEMATICAL MODELLING OF THE FUEL REACTOR

The mathematical model gives a simulation of combustion in CLC using combustion and energy code. CFD techniques offer the capacity of studying a system under conditions over its limits. In the combustion process, the simulation uses less advanced technology to study the solid, gas phase and temperature distribution of matter, thus greatly saving the calculation requirements. The mathematical model is built based on the conservation of a coupled transport equation and the equation of state of the fluid system. For obtaining a time- and grid-independent solution, the presented simulations were performed with a time step of 2 × 10^{-3} s and a space step of 0.1 mm. The combustion process was launched by the gas burner. More details of the current model can be found in the supplementary materials. The previously described mathematical model was evaluated based on the coefficient of determination, R^2. This statistical value can be used to test the linear relationship between the calculated and measured values; its value should be as close to unity as possible and is given by the following equation [28]:

$$R^2 = 1 - \frac{\text{Error between experimentaland predicted results}}{\text{Experimental result deviation}} \tag{15}$$

$$R^2 = 1 - \frac{\sum(E_m - E_c)^2}{\sum(E_m - \bar{E}_m)} \tag{16}$$

where E_m and E_c are the measured and calculated values, respectively. The term $\bar{E}_m$ in Equation (16) is the average measured value which can be defined as follows [28]:

$$\bar{E}_m = \frac{\sum_{i=1}^{n_p} E_m}{n_p} \tag{17}$$

where n_p is the number of experimental points.

4. RESULTS AND DISCUSSION

4.1. Gaseous fuel (LPG)

This section provides the results of temperature distribution along the fuel reactor of LPG as a gaseous fuel. The temperature was measured using K-type thermocouple with a data acquisition system. Also, this section gives the concentration measurements of CO and CO_2 in combustion exhaust in three different cases.

4.1.1. Experimental and simulated results for LPG without nickel powder

After preparing CLC reactor along the fuel reactor, a volume flow rate less than the stoichiometric was measured and recorded, as shown in Figure 3. This figure shows that the maximum recorded temperature was 576 °C at T_1 and the temperature gradually decreased to 288 °C at T_8. The simulated results of temperature distribution are shown in Figure 4. After preparing the CLC reactor and adjusting the volume flow rate to 18 LPM, the temperature distribution along the fuel reactor was measured and plotted, as shown in Figure 5. From the figure evaluation, it can be noticed that the maximum-recorded temperature was 824 °C and recorded by T_1. The temperature distribution starts decreasing gradually along the fuel reactor to reach 417 °C at T_8. The simulated results of temperature distribution along the fuel reactor for the LPG volume flow rate of 18 LPM are shown in Figure 6.

The red region in the simulated results represents the highest temperature and blue region represents the lowest temperature in the domain. It is clearly seen in these figures that the high-temperature region occurs in the bottom of the reactor and decreases gradually along the reactor length.

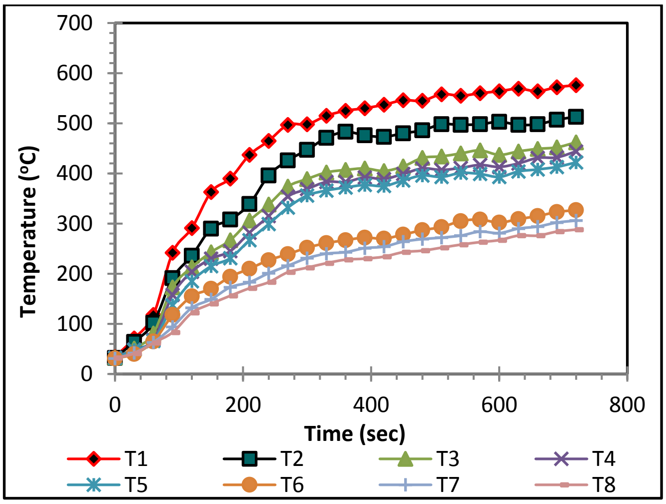

Figure 3. Experimental results of temperature distribution along the fuel reactor for LPG (Q = 11 LPM), without using nickel powder

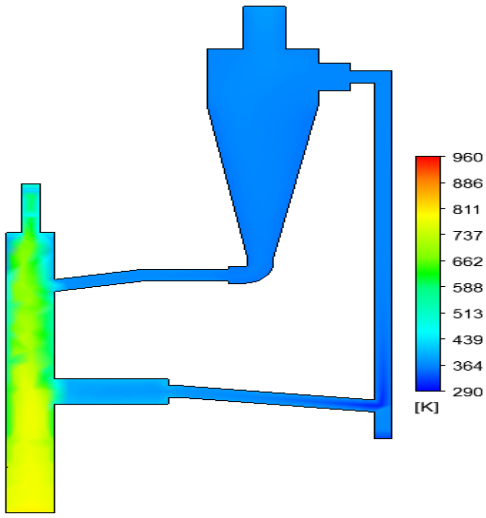

Figure 4. Simulated results of temperature distribution for LPG (Q = 11 LPM) without using nickel powder

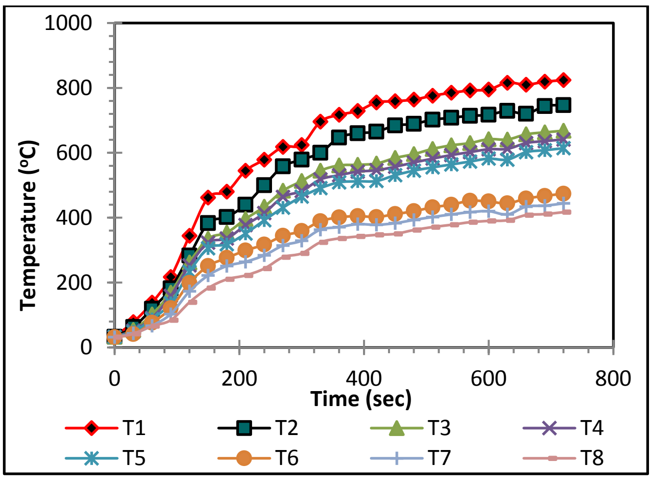

Figure 5. Experimental temperature distribution along the fuel reactor for LPG without using nickel powder

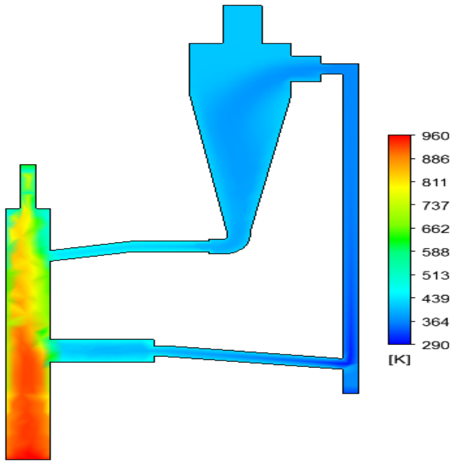

Figure 6. Simulated results of temperature distribution for LPG without using nickel powder

4.1.2. Comparison between experimental and simulated results for different flow rates of LPG

The comparison between the temperature distribution in the combustion chamber (T_1) for LPG flow rates of 11 and 18 LPM is shown in Figure 7. In the experiments, the proportion of gases emitted before and after the use of nickel powder is compared; therefore, the perfect LPG volume flow rate should be chosen to be used in all subsequent experiments. The simulated results of temperature distribution and different values of flow rates for LPG are shown in Figure 8. It was observed that the flow rate of 18 LPM was perfect and the temperature at the beginning of the experiments was less than the requirement of the reduction process of nickel powder. Therefore, it is necessary to preheat the reactor before starting the combustion process for obtaining high temperature. The experimental results of temperature distribution along the preheated fuel reactor for 18 LPM of LPG are shown in Figure 9. From this figure, it is clear that there is a high-temperature distribution along the fuel reactor at the beginning of the experiment and this is sufficient for nickel reduction, and the maximum recorded temperature was 1079 °C. For this reason, all the following experiments for gaseous fuel were carried out with 18 LPM after preheating the reactor. Also, the simulated results of the LPG volume flow rate of 18 LPM with preheated reactor are shown in Figure 10. From the analysis of these figures, it can be concluded that the temperature distribution is very crucial which occurs by different colors in the model domain.

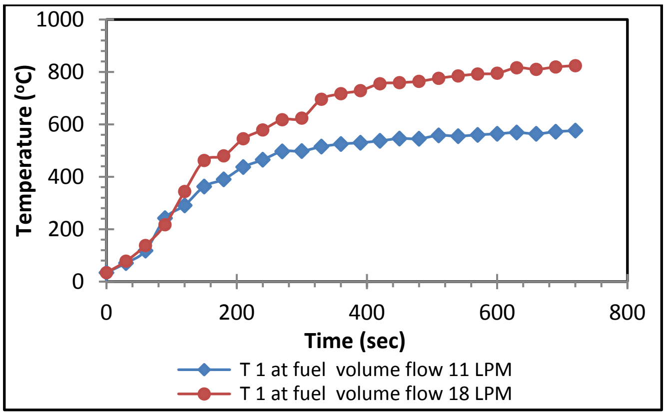

Figure 7. Comparison between the temperature distribution in the combustion chamber (T_1) at different LPG volume flow rates (Q = 11 and 18 LPM)

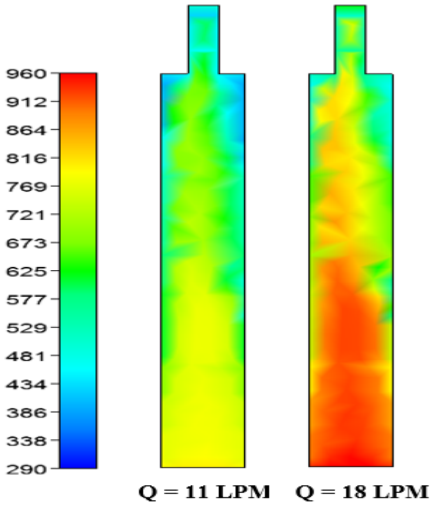

Figure 8. Simulated results of temperatures along the fuel reactor for different LPG volume flow rates (Q = 11 and 18 LPM)

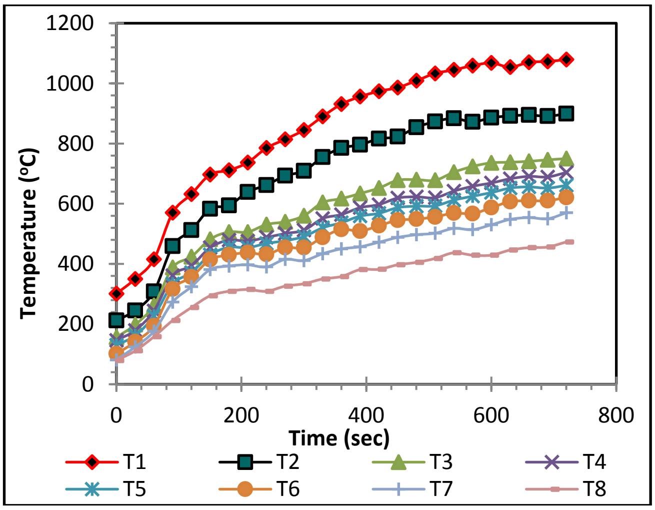

Figure 9. Experimental temperature distribution along the fuel reactor for LPG, preheated reactor without using nickel powder

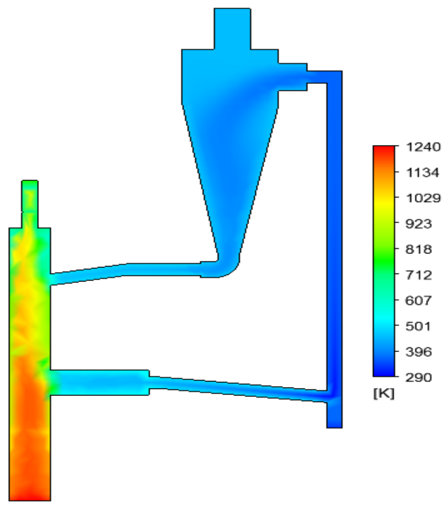

Figure 10. Simulated results of temperature distribution with LPG and preheated reactor without using nickel powder

4.1.3. Validation for using LPG without nickel powder

Figure 11 shows a comparison between experimental and simulated results of temperature distribution for preheated fuel reactor using LPG with a flow rate of 18 LPM without using nickel powder. Based on the analysis of this figure, it is clear that the values for experimental results and simulated results are different. This is due to the adiabatic system and the laminar flow. Therefore, there is no leakage of heat in the numerical system; in contrast, there is a leakage in the heat in the practical experiments. Moreover, the accuracy in measuring instruments is not ideal. The coefficient of determination (R^2) for the experimental and simulated results values of the LPG equals 80.83 %.

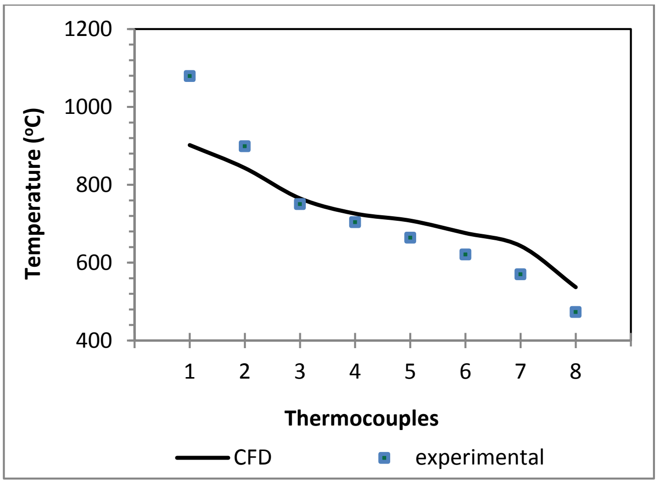

Figure 11. Experimental and simulated results of temperature distribution for LPG and preheated reactor without using nickel powder

4.1.4. Experimental concentrations of CO and CO_2 for gaseous fuel

Table 7 shows the operating conditions of carbon monoxide and carbon dioxide concentrations measurement for different cases with using gaseous fuel (LPG).

Table 7. Operating conditions of CO and CO_2 concentrations of measurement experiments using LPG

Case	Combustion method	The reactor used in combustion	The used amount of nickel
Gaseous fuel (18 LPM of LPG)			
Case # 1	Conventional combustion	The fuel reactor after separating it from the air reactor	without using nickel powder
Case # 2	CLC combustion technology	CLC system (fuel reactor and air reactor)	90 g
Case # 3			135 g and 45 g supplementation

Case # 1: Gaseous fuel, without nickel powder

In the experimental work, the concentration of carbon monoxide and carbon dioxide in the combustion exhaust emissions was measured using the gas analyzer. Figure 12 shows the concentrations of CO and CO_2 emissions for gaseous fuel without using metal powder. From the analysis of this figure, it is clear that the concentration of carbon monoxide increased continuously until the end of the experiment. In contrast, the concentration of carbon dioxide was reduced significantly throughout the experiment. The average values of the exhaust gases reading for CO and CO_2 during the experiment were 1289 ppm and 32.5 %, respectively. In other words, incomplete combustion occurs during this experiment.

Case # 2: Gaseous fuel using 90 g nickel powder

In this case, in order to improve the combustion process, 90 g of nickel powder was used in the experimental work. The nickel powder was used as an oxygen carrier for complete combustion in the system under investigation. The results are shown in Figure 13. From this figure, it is clear that at the beginning, the CO concentration decreases until 400 s and it begins to increase; otherwise, the CO_2 concentration increases until 400 s and it begins to decrease. In other words, the combustion process was enhanced during this experiment. The average experimental exhaust gases reading for CO and CO_2 were 678.5 ppm and 48 %, respectively. The results also showed the effect of using oxygen carriers on combustion gases where the average ratio of the carbon monoxide was lower than that in Case #1.

Case #3: Gaseous fuel using 135 g nickel powder with supplementation

In this case, gaseous fuel was used using 135 g nickel powder and 45 g was added in the experiment. The additional amount of nickel powder was added to study the effect of nickel powder supply on the combustion process. The additional amount of nickel powder was added after five minutes, which is the time in which CO and CO_2 curves began to change its direction in the previous experiment. Figure 14 represents the concentrations of CO and CO_2 emissions for this case. From the analysis of this figure, it can be noticed that the average exhausts gases reading for CO and CO_2 were 655 ppm and 54.1 %, respectively. According to previously obtained data, it can be concluded that there is a significant difference in the readings of the combustion gases before and after using nickel powder.

The average carbon monoxide before using nickel powder was about 1289 ppm, and after using nickel powder, it decreased to 655 ppm, meaning that using metal powder decreases the rate of CO with an average value of 49.1 %. In addition, for carbon dioxide, the average value before using nickel powder was about 32.5 % and after using nickel powder, it was 54.1 %, meaning that using metal powder improves the rate of CO_2 by 66.5 % and improves the combustion process.

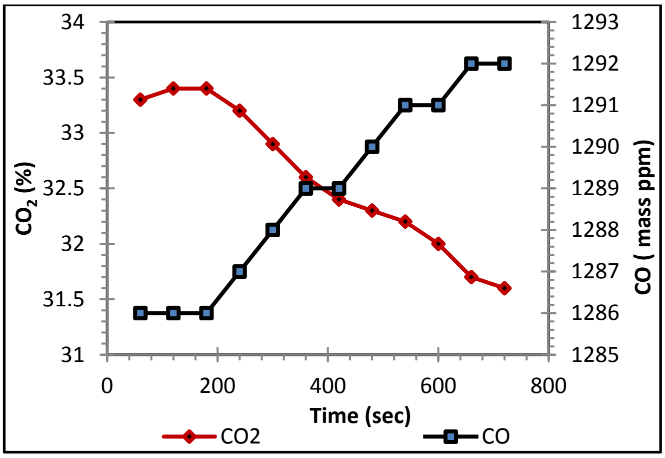

Figure 12. Concentrations of CO and CO_2 emissions for gaseous fuel without using metal powder

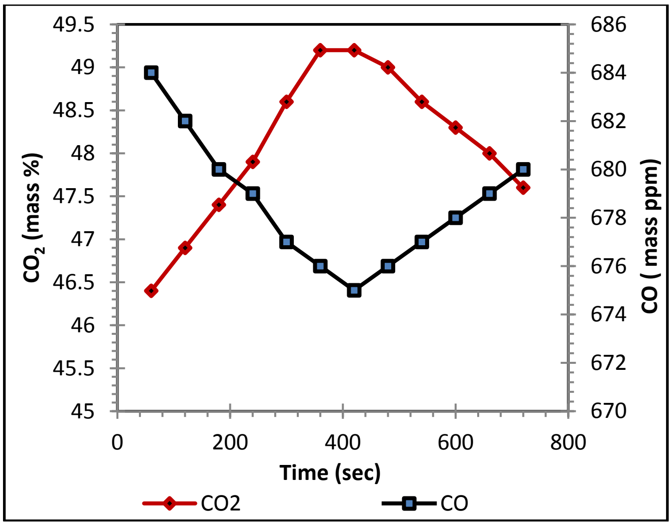

Figure 13. Concentrations of CO and CO_2 emissions for gaseous fuel using 90 g nickel powder

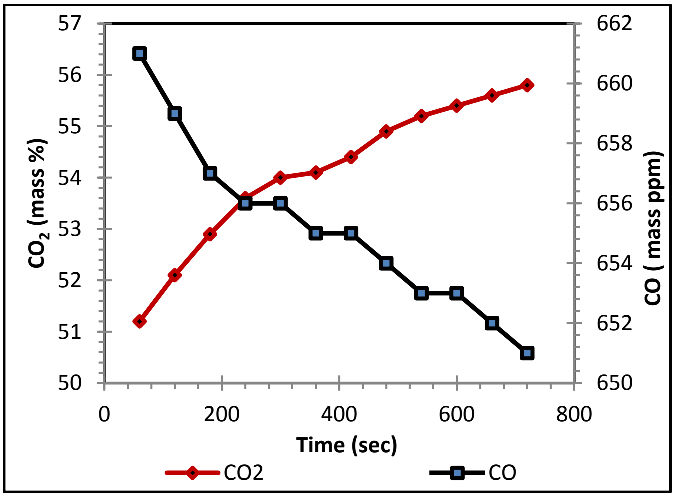

Figure 14. Concentrations of CO and CO_2 emissions for gaseous fuel using 135 g nickel powder with 45 g supplementation after five minutes

4.1.5. The effect of using nickel powder for gaseous fuel

As discussed in the previous section, nickel powder improved the combustion process. Thus, the temperature distribution along the fuel reactor was measured and recorded using experimental and numerical methods, as shown in Figures 15 and 16, respectively. From these figures, it is clear that there is an increase in the temperature after using oxygen carriers and the maximum recorded temperature is 1154 °C and measured by T_1. A comparison between the temperature distribution for LPG fuel with and without using nickel powder is shown in Figure 17. This figure shows that the nickel powder increases the temperature distribution along the fuel reactor. Also, the flame color is essential to a better understanding of the complete or incomplete combustion process. Figure 18 shows the flame color with and without using nickel powder. From the photograph in Figure 18 (a), it is clear that the flame color is yellow and this is one of the common colors for incomplete combustion, indicating that after using nickel powder, complete combustion is very close. On the contrary, the flame color is blue when using nickel powder, meaning that when burning LPG with using nickel powder, the complete combustion process occurs, as shown in Figure 18 (b).

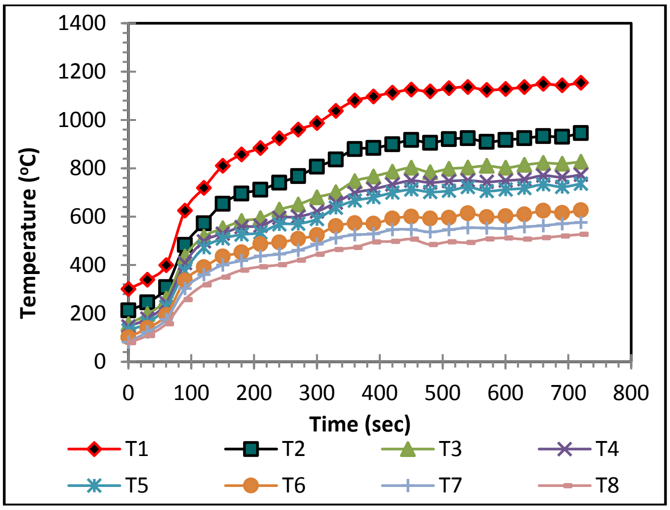

Figure 15. Experimental temperature distribution along the fuel reactor for LPG using nickel powder

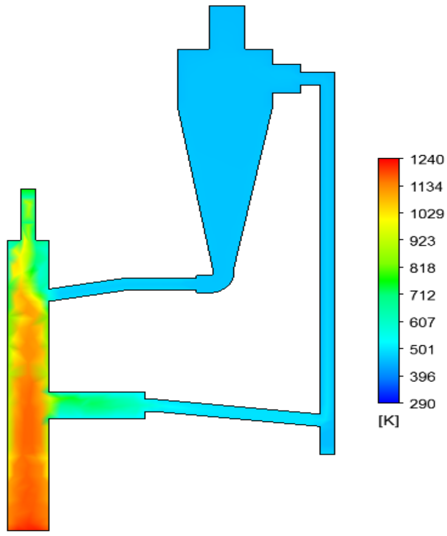

Figure 16. Simulated results of temperature distribution along the fuel reactor for LPG using nickel powder

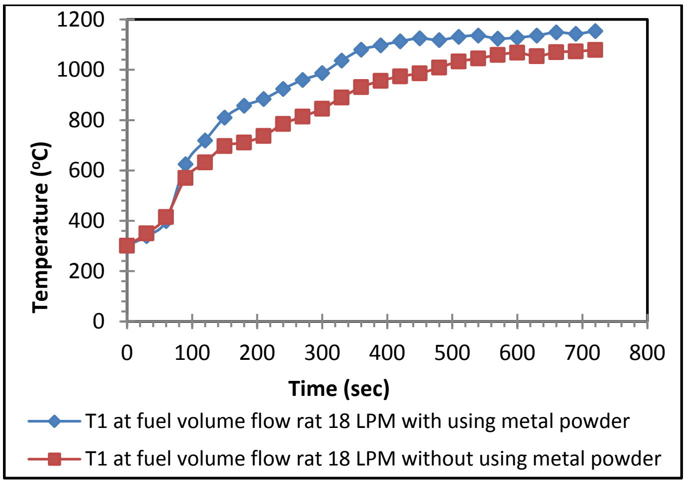

Figure 17. Comparison between the temperature distribution for LPG fuel with and without using nickel powder

(a) Without using nickel powder

(b) With using nickel powder

Figure 18. The flame color of gaseous fuel with and without using nickel powder

4.2. Solid fuel (brown coal)

4.2.1. Experimental and simulated results for different brown coal diameters, without using nickel powder

For brown coal (1-2 cm diameter), the results are shown in Figure 19. The maximum recorded temperature was 422 ºC at T_1 and the temperature gradually decreased to 115 ºC at T_8. Figure 20 shows the results of temperature distribution along the fuel reactor for brown coal (2-3 cm diameter) without using nickel powder. From the analysis of this figure, it can be noticed that the maximum recorded temperature was 531 ºC at T_1 and the temperature gradually decreased to 129 ºC at T_8. Also, Figure 21 shows the experimental results of temperature distribution along the fuel reactor for brown coal (3-4 cm diameter) without using nickel powder. The maximum recorded temperature was 678 ºC at T_1 and the temperature gradually decreased to 159 ºC at T8. Figure 22 shows the temperature distribution along the fuel reactor for brown coal (4-5 cm diameter) without using nickel powder. From this figure, it is clear that the maximum recorded temperature was 840 ºC at T_1 and the temperature decreased gradually to 209 ºC at T_8. For brown coal (5-6 cm diameter), the results are shown in Figure 23. The maximum recorded temperature was 567 ºC at T_1 and the temperature gradually decreased to 218 ºC at T_8. The simulated results of temperature distribution for different brown coal diameters without using nickel powder are shown in Figure 24.

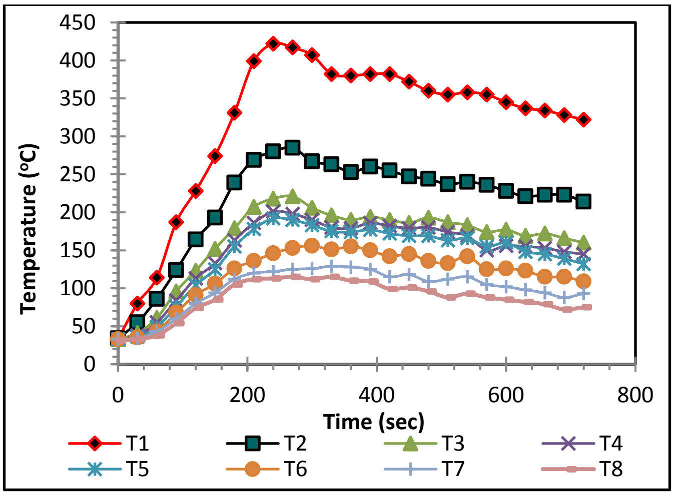

Figure 19. Experimental results of temperature distribution along the fuel reactor for brown coal (1-2 cm diameter) without using nickel powder

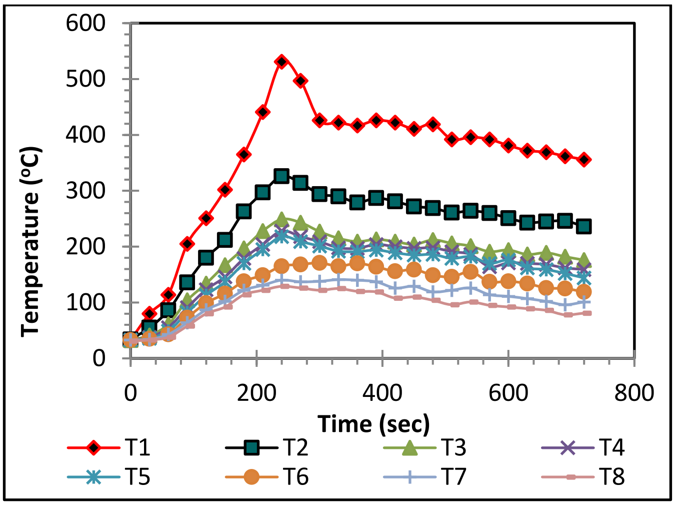

Figure 20. Experimental results of temperature distribution along the fuel reactor for brown coal (2-3 cm diameter) without using nickel powder

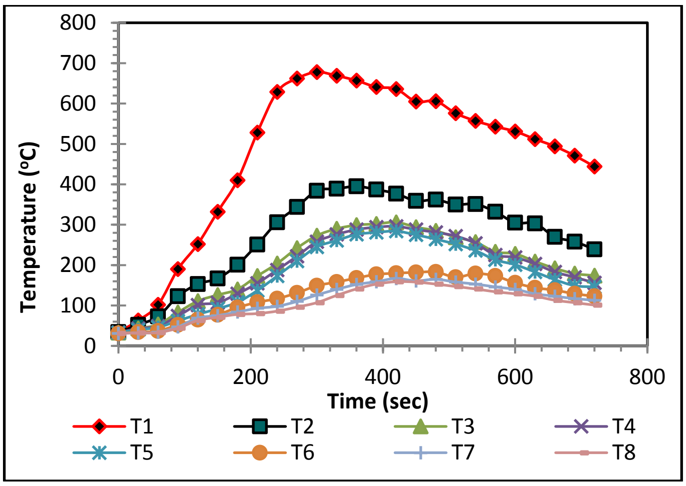

Figure 21. Experimental results of temperature distribution along the fuel reactor for brown coal (3-4 cm diameter) without using nickel powder

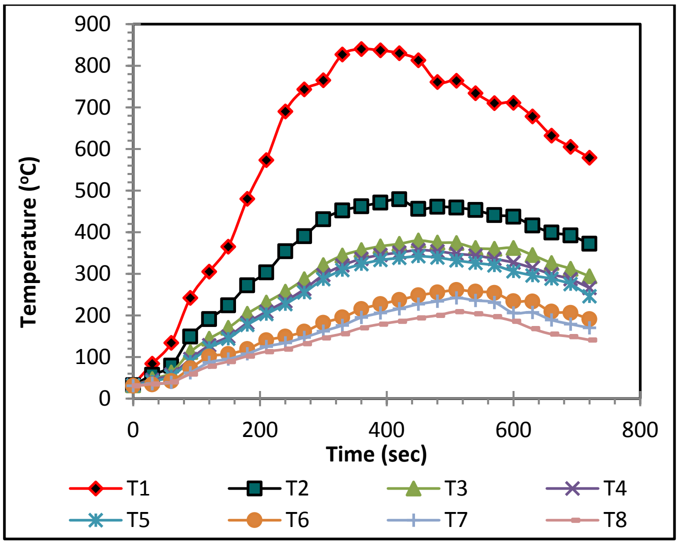

Figure 22. Experimental temperature distribution along the fuel reactor for brown coal (4-5 cm diameter) without using nickel powder

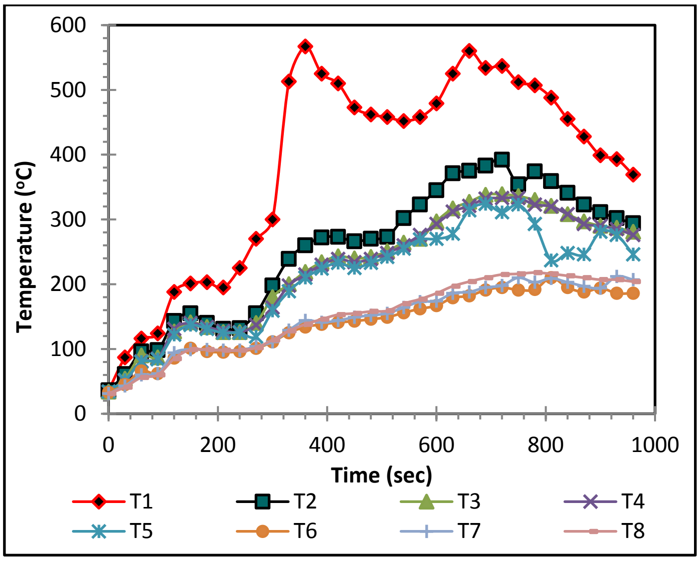

Figure 23. Experimental results of temperature distribution along the fuel reactor for brown coal (5-6 cm diameter) without using nickel powder

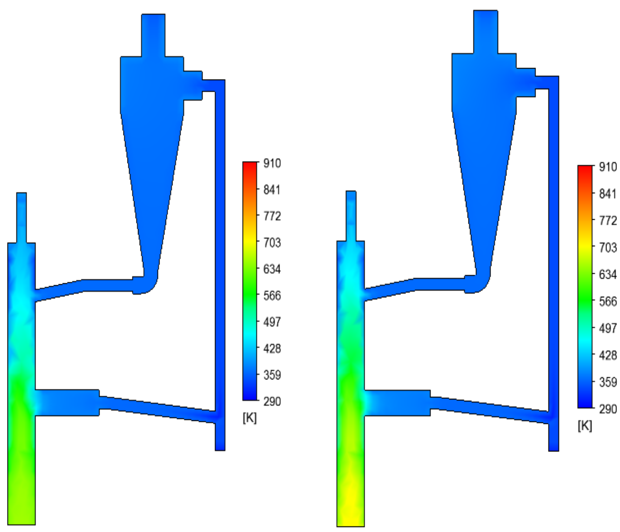

(a) Diameter from 1-2 cm (b) Diameter from 2-3 cm

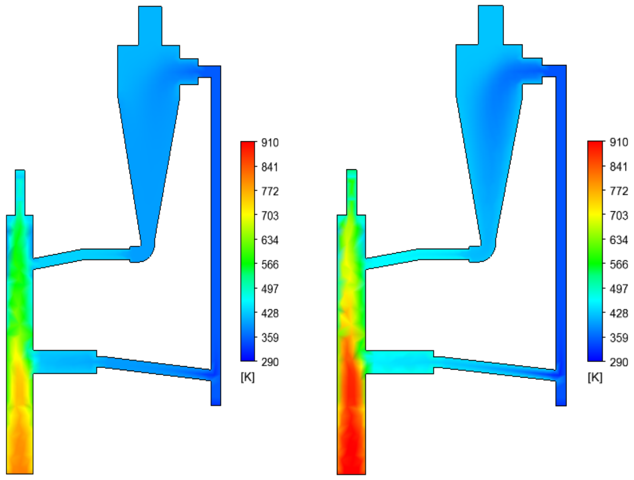

(c) Diameter from 3-4 cm (d) Diameter from 4-5 cm

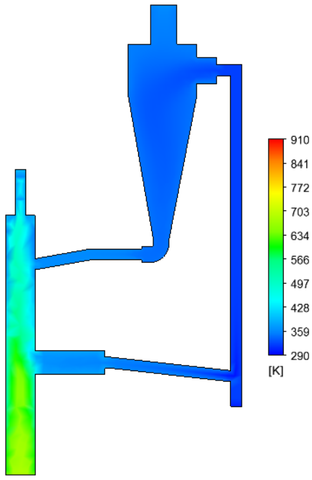

(e) Diameter from 5-6 cm

Figure 24. Simulated results of temperature distribution for different brown coal diameters without using nickel powder

4.2.2. Comparison between experimental and simulated results for different brown coal diameters

A comparison between the experimental results of temperature distribution in the combustion chamber (T_1) for different brown coal diameters is shown in Figure 25. From this figure, it is clear that the brown coal with a diameter (4-5 cm) gives the highest value of temperature distribution among the other diameters. Figure 26 shows the simulated results of temperature distribution along the fuel reactor for different diameters of brown coal. Also, the red region for the brown coal diameter of (4-5 cm) extends to a larger area, compared with the other diameters. It was observed that 4-5 cm diameter would be perfect and the temperature at the beginning of these experiments was less than the requirement of the reduction process of nickel powder.

Therefore, it is necessary to preheat the fuel reactor before starting the combustion process. The temperature at the beginning of the experiment is sufficient for nickel powder reduction. The experimental results of the temperature distribution with the preheated reactor are shown in Figure 27. From the analysis, it can be concluded that there was a significant increase in the temperature gradient and the maximum recorded temperature in this experiment was 973 °C at T_1. For this reason, all experiments for solid fuel were carried out with a 4-5 cm diameter and after preheating the fuel reactor. Figure 28 shows the simulated temperature distribution along the fuel reactor for brown coal (4-5 cm diameter) upon preheating the fuel reactor.

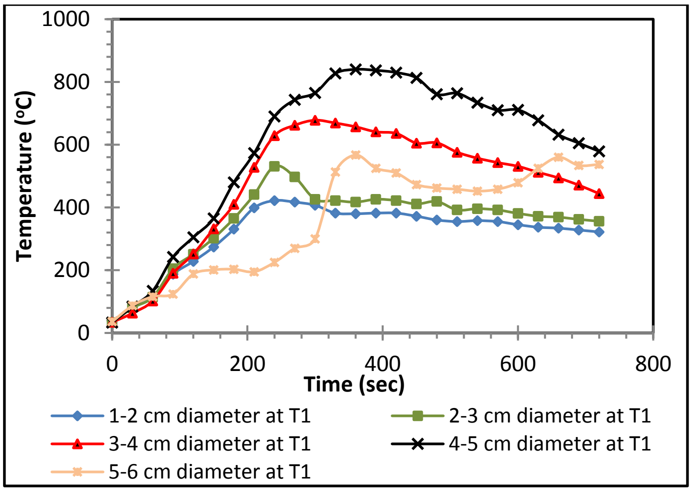

Figure 25. Comparison between the temperature distributions in the combustion chamber (T1) for different brown coal diameters

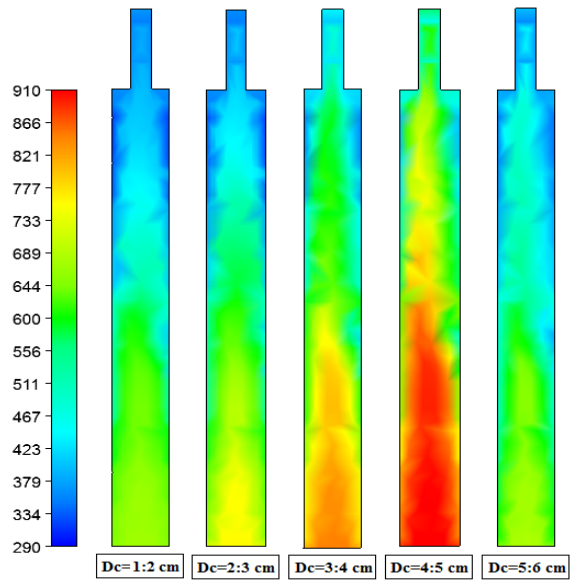

Figure 26. Simulated results of temperature distribution along the fuel reactor with different diameters of brown coal

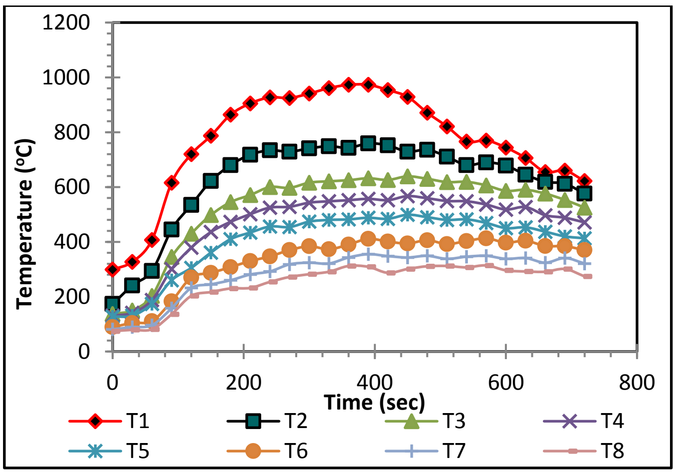

Figure 27. Experimental temperature distribution along the fuel reactor for brown coal (4-5 cm diameter) preheated reactor without using nickel powder

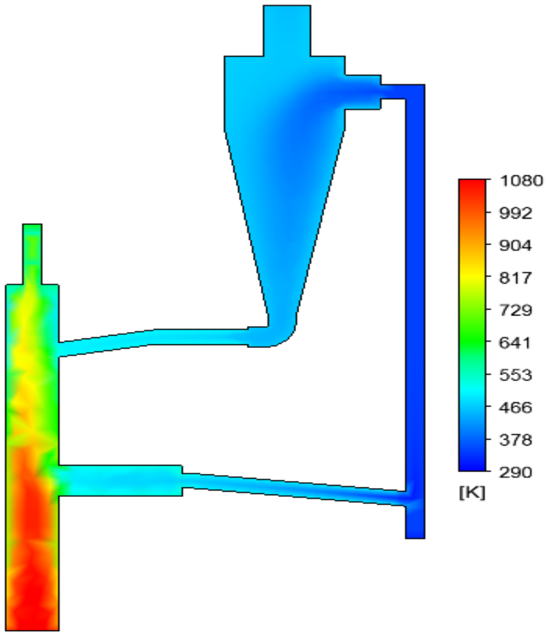

Figure 28. Simulated results of temperature distribution for brown coal (4-5 cm diameter), preheated reactor without using nickel powder

4.2.3. Validation for using brown coal without nickel powder

Figure 29 shows a comparison between experimental and simulated results for preheated fuel reactor using brown coal without using nickel powder. The brown coal has a diameter of 4-5 cm. From the analysis of this figure, it can be concluded that the values for the experimental results are consistent with those for the simulated results. The coefficient of determination (R^2) for the experimental and simulated results values of the brown coal equals 82.9 %.

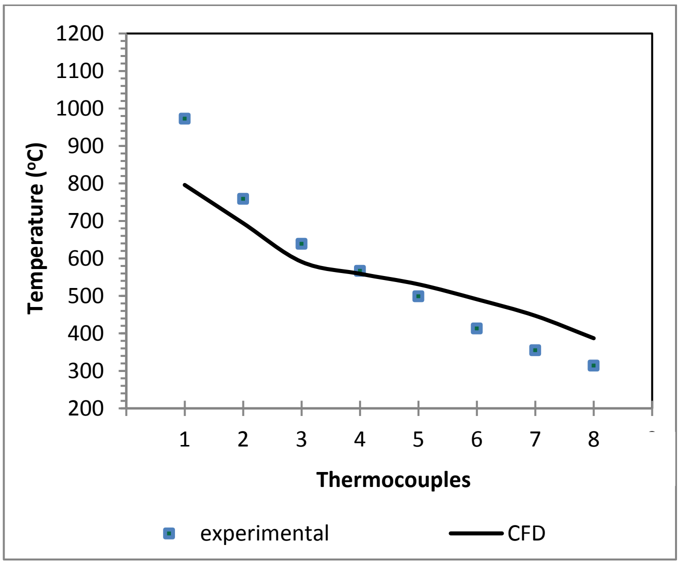

Figure 29. Experimental and simulated results of temperature distribution for brown coal, preheated reactor without using nickel powder

4.2.4. Experimental concentrations of CO and CO_2 for solid fuel

Table 8 shows the operating conditions of carbon monoxide and carbon dioxide Concentrations measurement for different cases with using solid fuel (brown coal).

Table 8. Operating conditions of CO and CO_2 concentrations of measurement experiments using brown coal fuel

Case	Combustion method	The reactor used in combustion	The used amount of nickel
Solid fuel (4-5 cm diameter of brown coal)			
Case # 1	Conventional combustion	The fuel reactor after separating it from the air reactor	without using nickel powder
Case # 2	CLC combustion technology	CLC system (fuel reactor and air reactor)	40 g
Case # 3			60 g and 20 g supplementation

Case # 1: Solid fuel, without using nickel powder

The concentration measurements of CO and CO_2 for solid fuel are discussed in three cases. In this case, the measurements were done without using nickel powder and the behavior of CO and CO_2 concentration is shown in Figure 30. This figure shows that the concentration of carbon monoxide increased continuously until the end of the experiment. In contrast, the concentration of carbon dioxide decreased significantly throughout the experiment, and the average exhaust gases reading for CO and CO_2 was 2591 ppm and 18.5 %, respectively.

Case # 2: Solid fuel, using 40 g nickel powder

In this case, 40 g of nickel powder was added to the fuel reactor. The concentrations of CO and CO_2 emissions were measured, as plotted in Figure 31. From the analysis of this figure, it can be concluded that using nickel powder as oxygen carrier improved the combustion process and the average exhaust gases reading of CO and CO_2 emissions were 1517 ppm and 26.8 %, respectively.

Case # 3: Solid fuel, using 60 g of nickel powder with supplementation

The effect of adding nickel powder with supplementation was studied in this case. In this experiment, 60 g of nickel was used at the beginning of the experiment and 20 g supplementation after six minutes. This time duration is the time at which the behavior of the curve begins to change its direction, as shown in Figure 32. From the analysis, it is clear that the CO_2 curve begins to increase significantly from the beginning to the end of the experiment. The average exhaust gases reading of the experiment for CO and CO_2 emissions was 1200 ppm and 31.8 %, respectively. According to the previously recorded data, there is a significant difference in the readings of the combustion gases before and after using nickel powder. The average carbon monoxide before and after using nickel powder was 2591 ppm and 1200 ppm respectively, meaning that using metal powder reduced the average rate of CO by 53.7 %. Also, the average carbon dioxide before and after using nickel powder was 18.5 % and 31.8 %, respectively, and this means that using metal powder improves the average rate of CO_2 by 71.9 %.

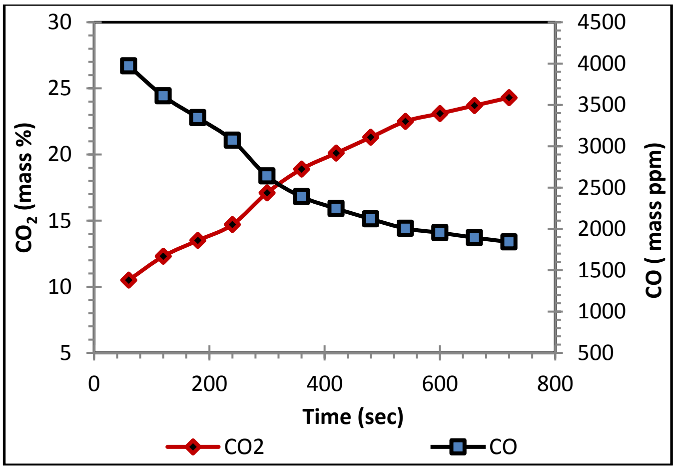

Figure 30. Concentrations of CO and CO_2 emissions for solid fuel without using metal powder

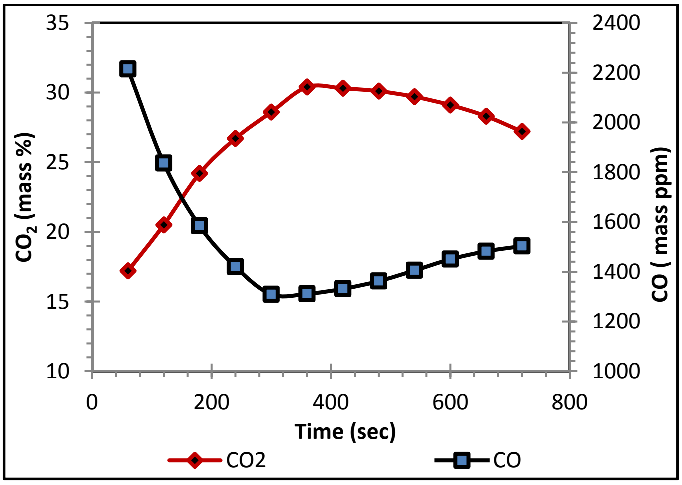

Figure 31. Concentrations of CO and CO_2 emissions using solid fuel with 40 g nickel powder

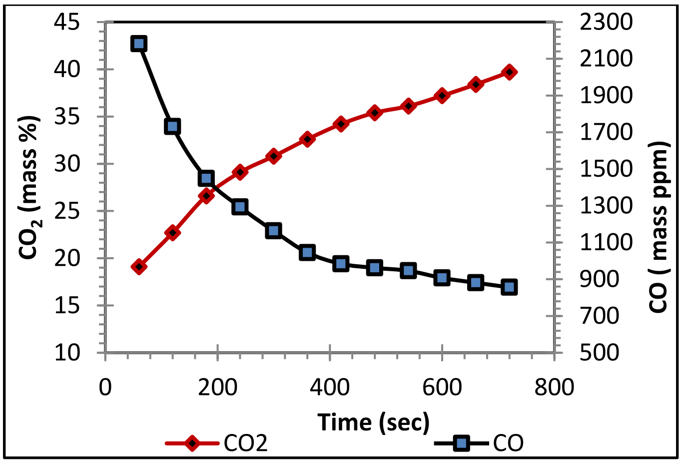

Figure 32. Concentrations of CO and CO_2 emissions using solid fuel with 60 g nickel powder and 20 g supplementation after six minutes

4.2.5. The effect of using nickel powder for brown coal fuel

The temperature distribution along the fuel reactor was measured and recorded using experimental and numerical methods, as shown in Figures 33 and 34, respectively. From these figures, it is clear that using oxygen carriers increases the temperature distribution. The maximum recorded temperature was 1037 ºC at T1. The comparison between the temperature distribution for brown coal (4-5 cm diameter) with and without using nickel powder is shown in Figure 35. Also, it is clear that there is a significant increase in temperature which yields increase in the CO_2 percentage and the approach to the complete combustion process.

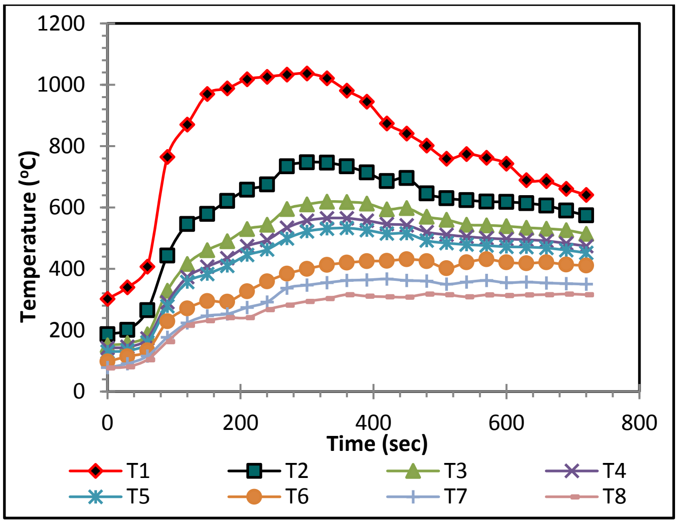

Figure 33. Temperature distribution along the fuel reactor for brown coal (4-5 cm diameter), a preheated reactor with nickel powder

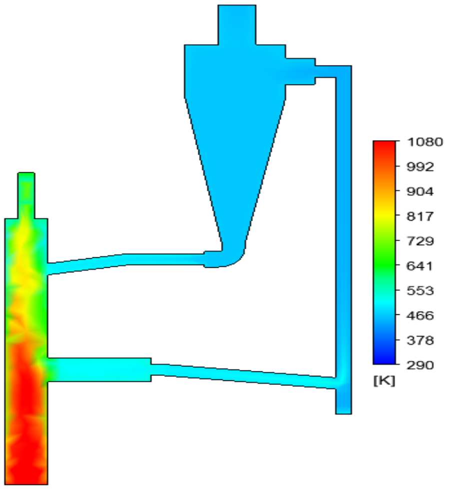

Figure 34. Simulated results of temperature distribution for brown coal (4-5 cm diameter), a preheated reactor with nickel powder

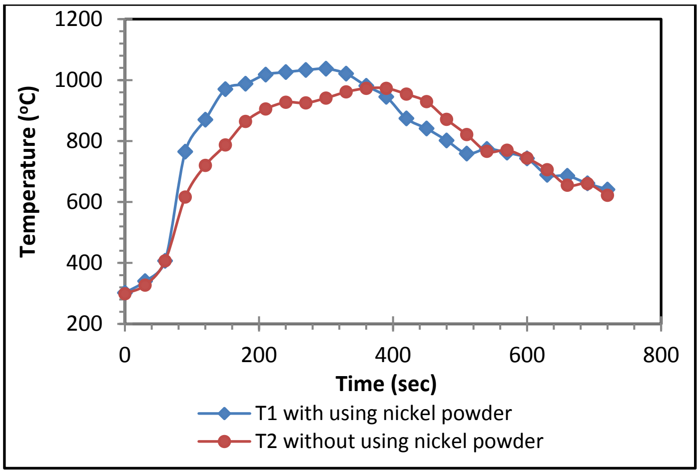

Figure 35. Comparison between the temperature distribution for brown coal (4-5 cm diameter) with and without using nickel powder

5. CONCLUSIONS

Chemical looping combustion is one of the most effective techniques that does not waste energy during the separation process of CO_2. In this study, a Chemical Looping Combustor (CLC) was designed and fabricated using nickel powder, brown coal and liquefied petroleum gas as an oxygen carrier. The temperature distribution along the fuel reactor using gaseous and solid fuels before and after applying CLC technology was investigated. The CO and CO_2 concentrations at combustion gases with and without using nickel powder were conducted for LPG and brown coal fuels. The temperature distributions along the fuel reactor for LPG flow rates of 11 and 18 LPM with and without using nickel powder as well as using preheated reactor were discussed and evaluated.

Also, the experimental results of temperature distribution along the fuel reactor for brown coal of different diameters with and without using nickel powder were studied. In addition a mathematical model was developed to simulate the combustion in CLC using combustion and energy code for both gas and solid phases. The experimental and simulated results were validated according to the coefficient of determination R^2. The results showed that the chemical looping combustion technique could be used for gaseous and solid fuels. Using nickel powder improved the combustion process and in case of using LPG, the color of the flame changed to blue which is the color of the complete combustion flame. The CO was reduced by 49.1 % and CO_2 increased by 66.5 %. In case of using brown coal as solid fuel, CO was reduced by 53.7 % and CO_2 was augmented by 71.9 %. Finally, there was good agreement between the experimental and simulated results based on the determination coefficient.

6. ACKNOWLEDGEMENT

The authors thank the combustion laboratory workers, Department of Mechanical Engineering, Faculty of Engineering, Suez Canal University, for technical guidance and support towards the preparation of this work.

REFERENCES

1. Karl, R. and Trenberth, K., "Modern global climate change", ***Science***, Vol. 302, (2003), 1719-1723. (https://doi.org/10.1126/science.1090228).
2. Chan., E.Y., "Climate change is the world's greatest threat–In Celsius or Fahrenheit", ***Journal of Environmental Psychology***, Vol. 60, (2018), 21-26. (https://doi.org/10.1016/j.jenvp.2018.09.002).
3. Pelletier, C., Rogaume, Y., Dieckhoff, L., Bardeau, G., Pons, M.-N. and Dufour, A., "Effect of combustion technology and biogenic CO_2 impact factor on global warming potential of wood-to-heat chains", ***Applied Energy***, Vol. 235, (2019), 1381-1388. (https://doi.org/10.1016/j.apenergy.2018.11.060).
4. IPCC, ***IPCC special report: Carbon dioxide capture and storage***, (2005). (Accessed: 10 July 2016) (https://www.ipcc.ch/report/carbon-dioxide-capture-and-storage/).
5. Cho, P., Mattisson, T. and Lyngfelt, A., "Comparison of iron-, nickel-, copper and manganese-based oxygen carriers for chemical-looping combustion", ***Fuel***, Vol. 83, (2004), 1215-1225. (https://doi.org/10.1016/j.fuel.2003.11.013).
6. Lyngfelt, A., Leckner, B. and Mattisson, T., "A fluidized-bed combustion process with inherent CO_2 separation; Application of chemical looping combustion", ***Chemical Engineering Science***, Vol. 56, (2001), 3101-3113. (https://doi.org/10.1016/S0009-2509(01)00007-0).
7. Ma, J., Zhao, H., Tian, X., Wei, Y., Zhang, Y. and Zheng, C., "Continuous operation of interconnected fluidized bed reactor for chemical looping combustion of CH_4 using hematite as oxygen carrier",

Energy Fuels, Vol. 29, (2015), 3257-3267. (https://doi.org/10.1021/ef502881x).

8. Linderholm, C. and Schmitz, M., "Chemical-looping combustion of solid fuels in a 100 kW dual circulating fluidized bed system using iron ore as oxygen carrier", ***Journal of Environmental Chemical Engineering***, Vol. 4, (2016), 1029-1039. (https://doi.org/10.1016/j.jece.2016.01.006).

9. Pérez-Vega, R., Abad, A., García-Labiano, F., Gayán, P., Luis, F. and Adánez, J., "Coal combustion in a 50 kWth chemical looping combustion unit: Seeking operating conditions to maximize CO_2 capture and combustion efficiency", ***International Journal of Greenhouse Gas Control***, Vol. 50, (2016), 80-92. (https://doi.org/10.1016/j.ijggc.2016.04.006).

10. Lewis, W.K., Gilliland, E.R. and Sweeney, W.P., "Gasification of carbon metal oxides in a fluidized power bed", ***Chemical Engineering Progress***, Vol. 47, (1951), 251-256. (https://doi.org/10.1021/ie50474a017).

11. Ishida, M. and Jin, H., "A novel combustor based on chemical-looping combustion reactions and its reactions kinetics", ***Journal of Chemical Engineering of Japan***, Vol. 27, (1994), 296-301. (https://doi.org/10.1252/jcej.27.296).

12. Lyngfelt, A. and Mattisson, T., "Materials for chemical-looping combustion", ***Process Engineering for CCS Power Plants***, (2011), 475-504. (https://www.worldcat.org/title/process-engineering-for-ccs-power-plants/oclc/740976968).

13. Lyngfelt, A., "Oxygen carriers for chemical looping combustion - 4000 h of operational experience", ***Oil & Gas Science and Technology***, Vol. 66, (2011), 161-172. (https://doi.org/10.2516/ogst/2010038).

14. Hoteit, A., Forret, A., Pelletant, W., Roesler, J. and Gauthier, T., "Chemical-looping combustion with different types of liquid fuels", ***Oil & Gas Science and Technology***, Vol. 66, (2011), 193-199. (https://doi.org/10.2516/ogst/2010022).

15. Moldenhauer, P., Ryd´en, M., Mattisson, T. and Lyngfelt, A., "Chemical-looping combustion and chemical-looping with oxygen uncoupling of kerosene with Mn- and Cu-based oxygen carriers in a circulating fluidized-bed 300 W laboratory reactor", ***Fuel Processing Technology***, Vol. 104, (2012), 378-389. (https://doi.org/10.1016/j.fuproc.2012.06.013).

16. Leion, H., Mattisson, T. and Lyngfelt, A., "The use of petroleum coke as fuel in chemical-looping combustion", ***Fuel***, Vol. 86, (2007), 1947-1958. (https://doi.org/10.1016/j.fuel.2006.11.037).

17. Jerndal, E., Mattisson, T. and Lyngfelt, A., "Thermal analysis of chemical-looping combustion", ***Chemical Engineering Research and Design***, Vol. 84, (2006), 795-806. (https://doi.org/10.1205/cherd05020).

18. Ishida, M., Jin, H. and Okamoto, T., "A fundamental study of a new kind of medium material for chemical-looping combustion", ***Energy Fuel***, Vol. 10, (1996), 958-963. (https://doi.org/10.1021/ef950173n).

19. Nakano, Y., Iwamoto, S., Maeda, T., Ishida, M. and Akehata, T., "Characteristics of reduction and oxidation cycle process by use of a Fe_2O_3 medium", ***Iron Steel J Jpn***, Vol. 72, (1986), 1521-1528.

20. Jin, H. and Ishida, M., "Reactivity study on natural-gas-fuelled chemical looping combustion by a fixed-bed reactor", ***Industrial & Engineering Chemistry Research***, Vol. 41, (2002), 4004-4007. (https://doi.org/10.1021/ie020184l).

21. Mattisson, T., Lyngfelt, A. and Cho, P., "The use of iron oxide as oxygen carrier in chemical-looping combustion of methane with inherent separation of CO_2", ***Fuel***, Vol. 80, (2001), 1953-1962. (https://doi.org/10.1016/S0016-2361(01)00051-5).

22. Mattisson, T., Järdnäs, A. and Lyngfelt, A., "Reactivity of some metal oxide supported on alumina with alternating methane and oxygen application for chemical-looping combustion", ***Energy Fuels***, Vol. 17, (2003), 643–651. (https://doi.org/10.1021/ef020151i).

23. Coleman, H.W. and Glenn Steele, W., Experimentation and uncertainty analysis for engineers, Wiley, New York, (1999). (https://www.wiley.com/en-us/Experimentation%2C+Validation%2C+and+Uncertainty+Analysis+for+Engineers%2C+4th+Edition-p-9781119417514).

24. Holman, J.P., Experimental method for engineers, 6th ed., McGraw-Hill, Singapore, (1994). (https://www.amazon.com/Experimental-Methods-Engineers-J-Holman/dp/0070296669).

25. Ismail, T.M., Ramzy,K., Abelwhab, M.N., Elnaghi, B.E., Abd El-Salam, M. and Ismail, M.I., "Performance of hybrid compression ignition engine using hydroxy (HHO) from dry cell", ***Energy Conversion and Management***, Vol. 155, (2018), 287-300. (https://doi.org/10.1016/j.enconman.2017.10.076).

26. Yaws, C.L. and Braker, W., "Flammability characteristics of combustible gases and vapors", Matheson gas data book, New York: Parsippany, NJ: Matheson Tri-Gas, Vol. 443, (2001). (https://www.worldcat.org/title/matheson-gas-data-book/oclc/46685585).

27. Koshiba, Y., Hasegawa, T., Kim, B. and Ohtani, H., "Flammability limits, explosion pressures, and applicability of Le Chatelier"s rule to binary alkane–nitrous oxide mixtures", ***Journal of Loss Prevention in the Process Industries***, Vol. 45, (2017), 1-8. (https://ynu.repo.nii.ac.jp/?action=repository_action_common_download&item_id=9396&item_no=1&attribute_id=20&file_no=1).

28. Maindonald, J. and Braun, J., Data analysis and graphics using R: An example-based approach, Cambridge University Press, (2006). (https://www.amazon.com/Data-Analysis-Graphics-Using-Example-Based/dp/0521762936).

JREE: Vol. 9, No. 1, (Winter 2022) 37-52

Journal of Renewable
Energy and Environment

Journal Homepage: www.jree.ir

Materials and Energy
Research Center

MERC

Review Article

Trends of Progress in Setting up Biorefineries in Developing Countries: A Review of Bioethanol Exploration in Nigeria

Toyese Oyegoke [a,b*], Emo Obadiah [a], Francis Adah [c], John E. Oguche [a], Geoffrey T. Timothy [d], Ismail A. Mantu [e], Abubakar D. Ado [a]

[a] Department of Chemical Engineering, Ahmadu Bello University, Zaria, Nigeria.
[b] Laboratoire de Chimie, École Normale Supérieure de Lyon, Lyon, France.
[c] Department of Water Resources & Environmental Engineering, Ahmadu Bello University, Zaria, Nigeria.
[d] Department of Biochemistry, Federal University, Dutsinma, Nigeria.
[e] Department of Political Science, Federal University, Dutsinma, Nigeria.

PAPER INFO

Paper history:
Received: 27 March 2021
Revised in revised form: 14 June 2021
Scientific Accepted: 19 July 2021
Published: 20 November 2021

Keywords:
Biofuels,
Biomass,
Biorefinery,
Bioethanol,
Renewable Fuels,
Nigeria

ABSTRACT

In recent times, limitations and adverse effects of fossil fuels have significantly attracted researchers' attention to green fuels worldwide, especially in developed nations. As a way of assessing this actualization of biorefineries establishment in developing nations, this report surveys the works done by various researches towards this great course in terms of promoting and gaining the attention of both government and private investors about the technical and economic feasibility of embracing the use of biofuels, a case of bioethanol in Nigeria. Different classes of feedstocks were reviewed for the laboratory-scale, process scale-up, pilot plant, and techno-economic studies regarding ascertaining the technical and economic feasibility of local setup of a functional biorefinery in Nigeria, which would be beneficial environmentally and economically. The literature survey unveiled that the Bioethanol yield obtained from sugarcane-juice (72.7 %), banana-stems (84.0 %), and cassava (92.0 %) were found to be of highest potential amongst other sugar-based, lignocellulosic, and starch-based feedstock, respectively. The survey further unveils that the volume of process scale-up and economic feasibility studies does not correlate well with the laboratory-scale studies. The bulk of the research works on bioethanol has given preferential attention to laboratory studies. Only a few studies have looked into the commercialization (i.e., scale-up) of the laboratory findings and the economic implications. Presently, only sugarcane and a few cassavas are reported in the literature so far. It is, therefore, necessary for further studies to give attention to the investigation of the commercializing locally developed technologies and the exploration of their economic benefits.

https://doi.org/10.30501/jree.2021.278037.1197

1. INTRODUCTION

Biofuel as a fuel derived from biological carbon fixation leads to the release of energy and can also be obtained from converting various lignocellulosic wastes into liquid, solid, and gaseous fuels. Today, biofuels have received much interest from the public and the scientific community [1-3]. This new-found interest buildup is attributed to certain factors such as environmental pollution caused by fossil fuels, increased oil price, and the urgent need for improved security in the world energy sector, African energy sectors, and the quest for green technology [4-6]. Some fuels obtained from solid biomass include bioethanol, bio-methanol, biodiesel, biohydrogen, and biomethane, in which some are liquid while others are gaseous fuels [7].

The world is facing global warming, which is majorly brought about by incomplete combustion and emission of harmful gases from fossil fuel consumption [8], which are non-biodegradable. Bioethanol, an alternative to fossil fuel, has high octane number, high heating value, and complete combustion in automobiles due to its rich oxygen content, leading to less poisonous gas emission [9, 10].

Over time, fossil fuels are experiencing drastic depreciation (in value) and relevance to the global scene. The demand and prices of hydrocarbon deposits are shrinking down daily, especially in developed nations. Most fossil fuel-dependent economies and oil-producing countries are gearing up policy frameworks to seek a more reliable alternative to fossil fuels. Efforts are in motion to explore bioethanol through a series of government policies to attain a paradigm shift from a nonrenewable energy source to a renewable one [11]. Nigeria is well known for being a petroleum-producing economy that is far lagging in policies and actions to gradually divorce fossil fuels for biofuels [12]. Lack of legislative-driven policies and strong political will are a few among the many rationales behind the slowdown in diverting the Nigerian state from fossil fuels to biofuels [13].

*Corresponding Author's Email: oyegoketoyese@gmail.com (T. Oyegoke)
URL: https://www.jree.ir/article_140459.html

Please cite this article as: Oyegoke, T., Obadiah, E., Adah, F., Oguche, J.E., Timothy, G.T., Mantu, I.A. and Ado, A.D., "Trends of progress in setting up biorefineries in developing countries: A review of bioethanol exploration in Nigeria", ***Journal of Renewable Energy and Environment (JREE)***, Vol. 9, No. 1, (2022), 37-52. (https://doi.org/10.30501/jree.2021.278037.1197).

2. BACKGROUND INFORMATION ON BIOETHANOL

Bioethanol is a substitute for fossil fuels and can be produced by fermenting sugar components from plant matter; ethanol can be produced synthetically and naturally through yeasts. About 51.3 billion liters of ethanol were produced worldwide in 2006, and ethanol production would increase in the future [14]. On a global scale, the challenges of rapid fuel exhaustion, fuel prices, and climate change have resulted in algal biomass gaining prominence in recent years. Algae are excellent resources for sustainable and renewable energy production with zero competition in the food market and do not need freshwater resources to thrive. With these recent developments in the promotion of algae used in biofuel production, there has been a growing interest in using algal biomass in an optimum manner for the production of other products like pharmaceuticals, cosmetics, wastewater treatment, and inhuman and animal fee.

Bioethanol is presently the most common biofuel, similar to about 73 % of the 135.3 billion liters of biofuel produced in 2016. The United States (USA) is the largest producer, 59 %, followed by Brazil, which produces 27 % global production [15]. Bioethanol can be used as a purely gasoline substitute or in a mixture of gasoline. The use of bioethanol in internal combustion engines has many benefits over gasoline. Presently, commercial bioethanol is of almost entirely first-generation because food crops are used as feedstock: sugarcane in Brazil, corn in the USA, and wheat and sugar beet in the European Union. The major drawback for the first-generation bioethanol is the competition over the use of arable land to cultivate food crops between biofuel feedstocks, thus increasing food prices [16].

A survey of the literature indicates that the Nigeria government has been investing largely in the importation of 300-350 million of bioethanol liters worth of 1.2 trillion Naira (i.e., 2.7 billion US dollars) on an annual basis to meet the national demand [17-19], which was primarily imported from US, Brazil, and other European countries. In recent time, the concern about the enormous amount of fund invested in importing bioethanol has strengthened the drives for different state governments in Nigeria and the federal government to give attention to the establishment of Nigeria-based biorefinery which would complement the use of petroleum fuels and would equally save the huge annual sum incurred on the importation of the bioethanol [20, 21]. Some of the concerned state governments that have taken steps towards the actualization of biorefinery in Nigeria include Kebbi, Kogi, Osun, and the Plateau States. All these states have proposed launching cassava-based bioethanol plants, including Nigerian National Petroleum Corporation (NNPC), except Kebbi State Government, which expressed an interest in setting up additional sugarcane-based bioethanol plants [22-27]. Nigeria is therefore seeking an efficient way for diversifying its energy mix [21] to reduce its overdependency upon the use of fossil fuels. The search for ways of inventing a local technology for the processing of Nigeria biomass into this fuel via the use of the local resource is also in progress. The government of Nigeria looks forward to the actualization of the dream of saving a huge cost of annual bioethanol importation and establishing functionally developed biorefineries across Nigerian communities.

3. OVERVIEW OF DIFFERENT PRODUCTION METHODS

3.1. Classification of bioethanol based on generation

This section briefly discusses various bioethanol classes based on the origin or generation of materials used either as biomass or waste. Bioethanol is classified into three categories based on generations known as the first, second, and third generations.

(a) **First-generation bioethanol:** The class of bioethanol generation consists of edible crops mainly. Examples include corn, barley, sugarcane, potato wastes, and wheat [28-30]. To a great extent, first-generation bioethanol hinges on energy crops like maize and sugarcane [30, 31]. Unlike the second-generation bioethanol, first-generation bioethanol does not demand saccharification since the sugars from these energy crops are easily accessible, making the production process simpler than second- and third-generation bioethanol [32].

(b) **Second-generation bioethanol:** This generation of bioethanol is produced using lignocellulosic materials. The lignocellulosic biomass consists of cellulose, hemicellulose, and lignin. They have advantages over first-generation bioethanol since they do not compete with food crops and are obtained from agricultural wastes such as corn stover, elephant grass, rice husk, corn cob, wheat straw, and sugarcane bagasse [30]. Since they contain a considerable amount of cellulose, they can be an excellent alternative to first-generation bioethanol. However, they require a saccharification process that increases production cost; hence, commercial-scale production is not widely feasible [29, 33-35]. Second-generation biofuel is cellulosic ethanol produced via a biochemical route, in which enzymes and other microorganisms are used to convert cellulose and hemicellulose components of the feedstocks to sugars before they are fermented to produce ethanol [36, 37].

(c) **Third-generation bioethanol:** They are primarily derived from algal biomass. Algal biomass has a very different growth yield than classical lignocellulosic biomass [38, 39]. Several algae species have been examined including fast-growing species: *Chlamydomonas reinhardtii, Dunaliella salina,* and various chlorella species [40]. Third-generation bioethanol does not compete with food, has a fast growth rate, and can be increased in wastewater and land unsuitable for agriculture than first- and second-generation bioethanol [39, 41].

Table 1. Several studies on the sugar-based bioethanol production (Note: Conventional approach=One-factor-at-a-time)

Ref.	Feedstock/Material used	Enzymes used for fermentation	Bioethanol yield, g/g %	Study approach
[42]	Raffia	*n.r.*	2.03	Conventional approach
[42]	Palm wine	*n.r.*	4.00	Conventional approach
[43]	Calabash (*Crescentia cujete*) pulp juice	*Saccharomyces cerevisiae*	6.19	RSM - CCD design approach
[44]	Sugar molasses	*Saccharomyces cerevisiae* (DIST/IPF/90)	10.50	Conventional approach
[45]	Sugarcane juice (SJ)	*Saccharomyces cerevisiae*	19.30	Factorial design approach

3.2. Classification of bioethanol based on feedstock

This section deals with the classification of bioethanol based on the raw materials used for conversion into bioethanol. Any materials that can be converted into sugar and further to bioethanol can be categorized as feedstock for bioethanol. The primary requirement of raw materials as a suitable raw material for conversion into bioethanol is its availability. However, one of the challenges encountered in bioethanol production from some raw materials like starch [46-48] and cellulosic-based [49-55] feedstock is the depolymerization of biomass into fermentable sugar before conversion into bioethanol, otherwise known as hydrolysis, which is often preceded by pretreatment. Bioethanol can be classified based on feedstock as sugar, starch, and lignocellulosic-based feedstocks (as shown in Figure 1).

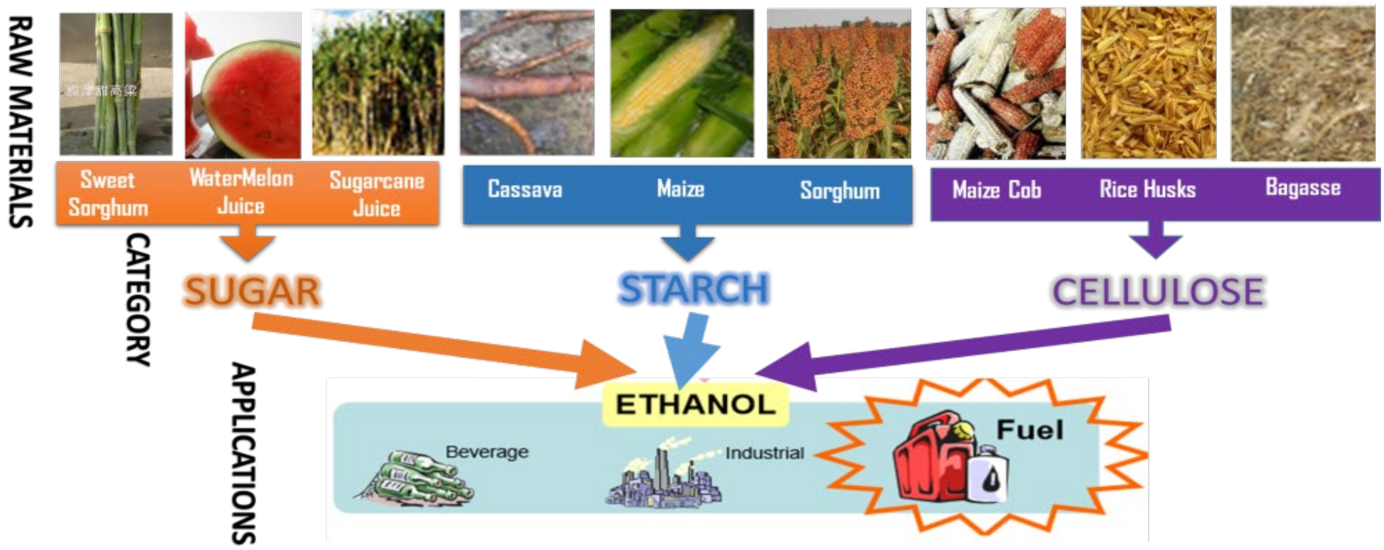

Figure 1. Raw materials, categories & applications of bioethanol [14, 56-58]

(a) **Sugar-based bioethanol:** These feedstocks for bioethanol are obtained from sugar raw materials. It requires fewer processes than starch-based bioethanol feedstock, which does not involve saccharification; hence, sugars are readily available [32]. Examples of sugar-based bioethanol feedstocks include sweet sorghum, sugarcane, molasses, and sugar beets. Essentially, they involve simple processes such as extraction (milling) to produce their high sugar components converted to bioethanol [59].

Among several studies conducted on the use of sugar-based feedstock (with details presented in Table 1), some of the feedstocks considered entail raffia [42], palm wine [42], calabash pulp juice [43], sugar molasse [44], and sugarcane juice [42, 45], among which the report on the use of sugarcane juice was found to have shown the highest yield (19.30 %), while the raffia showed the most negligible yield with 2.03 %. Moreover, a higher yield was reported by Nwufo et al. [42] which could be primarily attributed to the extended time of 12 days given for the fermentation process, unlike that of Suleiman et al. [45] which was only allowed to last the maximum of 96 hours found to be much shorter than the allowable time employed in the report of Nwufo et al. [42]. Suleiman et al. [45] reported that a lower temperature of about 30 ^{o}C would significantly promote the fermentation process than the higher temperature. The literature survey indicated that the bioethanol yield from sugarcane juice was the highest amongst other sugar-based biomasses, with a 72.7 % yield.

(b) **Lignocellulosic bioethanol:** These feedstocks are widely used to produce bioethanol and are primarily deposited as waste in developing countries like Nigeria. Lignocellulosic biomass as organic matter is widely available on a renewable basis, with some including energy crops, aquatic plants, agricultural waste, wood waste, and other wastes [34-36, 51, 52]. Unlike sugar and starch-based bioethanol feedstocks, accounting for 40-70 % of the total costs, lignocellulosic feedstocks only present about 30% of the total production costs [60]. Also, lignocellulosic feedstock does not compete with food. However, they have challenges in the conversion process due to the highly recalcitrant nature of lignin in the feedstocks, thus requiring complex pretreatment processes that may increase the overall cost of production [61, 62]. Examples are corn stover, algae, sugarcane bagasse, wheat straw, elephant grass, and rice husk [36, 58, 61].

Other studies on the use of cellulosic biomasses are summarized in Table 2 in which the cassava peels [49, 62-66], sweet potato peels [49, 51, 53], yam peels [62, 64], rice straw [55, 61, 67], rice husk [68-71], and much other biomasses are considered. The use of cassava peels, banana stem, rice husk, and elephant grass stem for the production of bioethanol has been proven from the reported research works to be of high yield, confirming the materials to be an excellent potential resource that facilitates the commercialization of bioethanol in developing nations, especially in Africa where these resource materials are widely and randomly disposed within the surroundings as waste for animals to feed on or allowed to decompose and pollute the environment. It also provides food security as the feedstocks are not sources of food.

A survey of the literature reveals that the rate of conversion of differentsubstrates such as yam peel [62], cassava peels [66], rice straw [61], rice husk [68], corn stover [12] and many other biomasses into bioethanol in the presence of specific enzymes like *saccharomyces cerevisiae* varies from one substrate to another. These findings indicate the significance of selecting appropriate enzymes of a specific substrate or feedstock during bioethanol fuel production from the use of biomass. Banana stem, rice husk, and elephant grass stem produced much more bioethanol than other lignocellulosic biomasses yielding 84.0 %, 80.0 %, and 78.0 %, respectively. The survey indicates that banana stem displays the highest yield among other lignocellulosic feedstock forms investigated in the literature.

(c) **Starch-based bioethanol:** These feedstocks for bioethanol are obtained from starchy materials. Starch-based raw materials require liquefaction and saccharification to hydrolyze carbohydrates into the corresponding sugar monomers [15, 72]. Production of bioethanol from starch involves three stages: hydrolysis, fermentation, and product purification [59]. Starch-based bioethanol feedstocks include wheat, barley, corn, wheat, cassava triticale potato, and rice [73].

Table 2. Several studies on the cellulosic-based bioethanol production (Note: *calculated , **glucose)

Ref.	Feedstock/Material used	Organism(s) used for fermentation	Bioethanol yield, g/g % (*computed)	Study approach
[74]	Banana pseudo-stem	*Saccharomyces cerevisiae*	84.00	Conventional approach
[53]	Cassava	*C. tropicalis* (IMI 398401)	23.80	Conventional approach
[66]	Cassava peel	*Saccharomyces cerevisiae*	16.00	Conventional approach
[65]	Cassava peels	Yeast	40.00	Conventional approach
[75]	Cassava peels	*Saccharomyces cerevisiae*	17.52	Not reported
[63]	Cassava peels	*Rhizopus nigricans, Aspergillus niger, Saccharomyces cerevisiae, Spirogyra Africana*	41.00	Conventional approach
[51]	Cassava peels	*Zymomonas mobilis, Saccharomyces cerevisiae*	23.00	Conventional approach
[51]	Cassava peels	*Gloeophyllum sepiarium* and *Pleurotuso streatus*	26.00	Conventional approach
[62]	Cassava peels	*Saccharomyces cerevisiae*	11.30	Conventional approach
[54]	Cocoyam peels	*Co-culture of Aspergillus niger* and *Saccharomyces cerevisiae*	*7.00 (4.2 g-bioethanol)	Conventional approach
[54]	Cocoyam peels	*Mono Aspergillus niger* and *Saccharomyces cerevisiae*	*9.40 (5.65 g-bioethanol)	Conventional approach
[12]	Corn stover (CS)	*Saccharomyces cerevisiae*	*11.30 (143.15 mg-bioethanol/1 L-CS)	Conventional approach
[76]	Elephant grass stem	*Aspergillus niger* and *Saccharomyces cerevisiae*	78.00	Conventional approach
[77]	Groundnut shell waste (GSW)	*Saccharomyces cerevisiae* and *Aspergillus niger*	*24.14(80 mL-bioethanol/420 g-GSW)	Conventional approach
[78]	Orange peels, cassava peels, and banana peels	*Aspergillus niger* and *Bacillus cereus*	*12.44 (12.44 g-bioethanol)	Conventional approach
[50]	Orange waste	*Escherichia coli* and *saccharomyces cerevisiae*	40.00	Conventional approach
[52]	Pineapple peels	*Saccharomyces cerevisiae*	5.82	RSM designed methodology
[64]	Potato peels,	*Saccharomyces cerevisiae*	4.02	Not reported
[68]	Rice husk (RH)	Saccharomyces cerevisiae	*80.00 (48 g-bioethanol)	Not reported
[69]	Rice husk	*Trichoderma harzianum*	6.25	Not reported
[69]	Rice husk	*Aspergillus niger*	6.99	Not reported
[70]	Rice husk	*Saccharomyces cerevisiae* and *Aspergillus niger*	*25.35 (32.13 g-bioethanol/mL-RH)	Conventional approach
[71]	Rice husk pretreated with $FeCl_3$ using SHF	*Trichoderma reesei,* cellulase, *Saccharomyces cerevisiae*	3.01	Conventional approach
[71]	Rice husk pretreated with $FeCl_3$ using SSF	*Trichoderma reesei,* cellulase, *Saccharomyces cerevisiae*	3.80	Conventional approach
[79]	Rice stalks treated with hydrogen peroxide	*Co-culture of Aspergillus niger* and *Saccharomyces cerevisiae*	3.91	Conventional approach
[79]	Rice stalks treated with sulfuric acid	*Co-culture of Aspergillus niger* and *Saccharomyces cerevisiae*	5.06	Conventional approach
[55]	Rice straw	*Trichoderma viride*	*8.11 (16.21 g-bioethanol)	Conventional approach
[61]	Rice straw	*Saccharomyces cerevisiae*	49.50	Conventional approach
[80]	Spent mushroom	*Saccharomyces cerevisiae*	**23.55 (0.51 mg/L)	Conventional approach
[45]	Sugarcane bagasse	*Aspergillus niger*	14.50	2^4 factorial design method
[66]	Sugarcane bagasse	*Saccharomyces cerevisiae*	9.03	Conventional approach
[53]	Sweet potato peels	*C. tropicalis* (IMI 398401)	47.99	Conventional approach
[53]	Sweet potato peels	*C. tropicalis* (IMI 398401)	47.99	Conventional approach
[49]	Sweet potato peels	*Saccharomyces cerevisiae*	31.00	Conventional approach

[49]	Sweet potatoes peels	*Zymomonas mobilis* and *Saccharomyces cerevisiae*	12.00	Conventional approach
[49]	Sweet potatoes peels	*Gloeophyllum sepiarium* and *Pleurotuso streatus*	12.00	Conventional approach
[80]	Wastepaper	*Saccharomyces cerevisiae*	**40.03 (0.51 mg-bioethanol/L)	Conventional approach
[64]	Yam peels	*Saccharomyces cerevisiae*	1.68	Not reported
[62]	yam peels	*Saccharomyces cerevisiae*	27.08	Conventional approach

Table 3. Several studies on the starch-based bioethanol production

Ref.	Feedstock/Material used	Enzyme used for fermentation	Bioethanol yield, g/g %	Study approach
[47]	Cassava flours	Yeast	52.00	Conventional approach
[81]	Cassava starch	*Saccharomyces cerevisiae*	5.85	Not reported
[64]	Cassava effluent	*Zymomonas mobilis and Saccharomyces cerevisiae*	16.50	Not reported
[82]	Cassava starch	*Saccharomyces cerevisiae*	92.00	Not reported
[83]	A mixture of cassava, yam, and potato	*Zymomonas mobilis*	8.36	Conventional approach
[83]	A mixture of cassava, yam, and potato	*Saccharomyces cerevisiae*	6.64	Conventional approach
[83]	Yam	*Zymomonas mobilis*	6.03	Conventional approach
[83]	Potato	*Zymomonas mobilis*	5.17	Conventional approach
[83]	Cassava	*Saccharomyces cerevisiae*	6.77	Conventional approach
[83]	Yam	*Saccharomyces cerevisiae*	7.39	Conventional approach
[83]	Potato	*Saccharomyces cerevisiae*	5.51	Conventional approach
[83]	Cassava	*Zymomonas mobilis*	6.86	Conventional approach
[48]	Cassava tubers + *koji* and yeast cells	*Aspergillus awamori* IAM8928 and *Saccharomyces cerevisiae* IR2	7.05	Analytical approach
[48]	Cassava tubers + gelatinized	*Aspergillus awamori* IAM8928 and *Saccharomyces cerevisiae* IR2	6.50	Analytical approach
[84]	Cassava wastewater	Yeast	8.69	RSM - CCD Design Approach
[85]	Cassava flour	*L Novoenzym, Aspergillus niger* and *Saccharomyces cerevisiae*	20.49	Conventional approach
[85]	Cassava starch	*L Novoenzym, Aspergillus niger* and *Saccharomyces cerevisiae*	14.04	Conventional approach
[86]	Cassava pulp	Yeast	82.40	Conventional approach
[87]	Yam tuber [89]s	*Saccharomyces cerevisiae* LC 269108	5.61	Conventional approach
[48]	Cassava tubers	*Aspergillus niger*	30.00	Conventional approach
[89]	Cassava mill effluents (cme)	*Saccharomyces cerevisiae*	48.55	Conventional approach
[89]	Cassava mill effluents + Empty fruit bunch	*Saccharomyces cerevisiae*	31.34	Conventional approach
[89]	Cassava mill effluents + chaff	*Saccharomyces cerevisiae*	68.56	Conventional approach
[89]	Cassava mill effluents + cassavapeel	*Saccharomyces cerevisiae*	28.65	Conventional approach

A further survey of literature has unveiled several works that have paid attention to the exploration of starch-based materials in the search for better technology for the production of bioethanol that would result in a higher yield which would facilitate complementing the use of existing fossil fuels in meeting the energy/fuels demand in developing nations like Nigeria. Among the feedstocks studied in the literature [47, 48, 64, 81-85, 87, 89-91], Cassava, a starch-based feedstock [82, 89, 91] has been experimentally proven to have shown a higher yield (92.0 %) for the production of bioethanol among its class of feedstocks studied in the literature. However, some of this feedstock would compete with the human food source.

4. IMPORTANT FEATURES OF BIOETHANOL OVER PETROL FUEL

Some of the essential features attracting the world towards embracing the use of bioethanol include the following:

(a) **Better octane-rating:** One of the advantages of bioethanol over petrol is that the octane rating of bioethanol is higher than that of gasoline; this allows an increase in the compression ratio of an engine for increased thermal efficiency. Balat [92-94] also emphasized that bioethanol, as an alternative to fossil fuel, had high octane number, high heating value, and complete combustion in automobiles due to its high oxygen content and less toxic gas emission [12].

(b) **Less pollution:** Petrol fuel used in automobiles today, despite meeting the demand needed for automobile functioning, has certain disadvantages including releasing sulfur oxides into the atmosphere, thereby contributing to the greenhouse effect. It is, therefore, vital that the advantages of bioethanol over petrol fuel be outlined. Another advantage of bioethanol over petrol fuel is that it does not emit dark smoke, which is an oxide of Sulfur and does not contribute to air type of environmental pollution [14, 20, 95].

5. FEEDSTOCK AVAILABILITY AND QUANTITY IN NIGERIA

Although the Nigerian state stands out among agricultural-oriented African countries with many biofuel-rich crops such as sugarcane, maize is mainly grown and cultivated in Nigeria. However, it is a severe worrisome decibel for most of these crops to be effectively utilized for biofuel production and consumable foodstuff without necessarily hiking the prices and affordability of these crops. Hence, there is a need to strike out a balance between its commercial and economic benefits [96]. There is no precise effort to hint the Nigerian government, policymakers, and stakeholders on which approach would perfectly enhance Nigeria's biofuel production. Researchers have failed to suggest a viable policy to arrest the possible foreseen widening gap between crop utilization for food production and biofuel production regarding the possible price escalation [97].

Several crops are used as a biofuel source; particularly, energy crops including sugar cane, sunflower, Barbados nut, soya bean, and maize are grown with less cost and low maintenance harvest. As mentioned earlier, Nigeria, nationally recognized as highly involved in agricultural production, is rich in feedstocks, especially as waste products both from industrial and domestic uses. Although not quantified, Nwofe's report [50] emphasizes that a high volume of waste is generated in Nigeria daily. Research in Nigeria shows that the bio-energy reserve as of the year 2005 stands as follows: 1,3071,464 hectares for fuelwood, 61 million tons per year for animal waste, and 83 million tons for crop residues [98], which indicate the abundance of bio-energy resource in the country.

Fruit wastes have also been identified as a significant feedstock for bioethanol production: one of such feedstock is the orange peel. The abundance of this feedstock in Nigeria results from its enormous consumption daily [80]. Instead of covering the land with these solid wastes, it would instead benefit the country to convert the orange peels into a helpful resource by producing bioethanol and reducing land pollution. Another feedstock that is much available in Nigeria, which is also fruit, is pineapple peel. This is because Nigeria is the seventh-largest pineapple producer globally and the leading producer in Africa [99]. Therefore, it would be advantageous to use the peels disposed of as waste to produce economically viable ethanol.

Interestingly, wastepaper and spent mushrooms have been identified as potential feedstocks for bioethanol production. Spent mushroom which refers to the substrate left after the mushroom is cultivated and harvested [100]. Paper and paper products consist of about 35 % of the weight of municipal solid waste [56]. Also, an extensive collection of Irish potato peels, maize cob, plantain peels, rice husk, sweet potato peels, rotten waste tomatoes, and yam peels can essentially be found in Zamfara/Plateau, Katsina, Cross River, Kano, Kaduna, Bauchi, and Yobe states in Nigeria, according to the report of the NBS [100, 101] for agricultural items production and cost.

Deductions from the literature survey indicate that Nigeria is blessed with a vast land fertile to cultivate the potentially available feedstocks to produce first- and second-generation bioethanol production. Some first-generation bioethanol feedstocks available in Nigeria include potatoes, yam, sugarcane, cassava, wheat, rice, sorghum, and many others [100, 101]. Nigeria's Energy Commission of Nigeria (ECN) and NNPC recommend using cassava, sorghum, and sugarcane to produce bioethanol due to the significant yield annually reported for Nigeria's crop production. On the other hand, the second-generation bioethanol production is currently receiving significant attention for consideration due to its inedibility nature, making it uncompetitive with the food market or supply. Instead, it further facilitates better management of our agricultural, municipal, and domestic wastes daily disposed and poorly managed in most communities in Nigeria. However, investment in the production of feedstock and the establishment of processing plants for the production of third-generation bioethanol is not gaining significant expected attention in Nigeria. Only a few efforts are put into exploring its economic potentials for actualizing the establishment of a feasible biorefinery in Nigeria.

6. FUEL CONSUMPTION IN NIGERIA

Nigeria is known to be one of the world's major petroleum-producing countries globally and exports petroleum for a refining process; the country depends on developed countries for refined products by exporting the products [46]. 5.06 quadrillion kilojoules (or 4.8 quadrillion British thermal units) remains the total primary energy consumption in Nigeria as of the year 2014. Traditional biomass and waste constitute 74 %, while oil, natural gas, and hydropower comprise 13 %, 12 %, and 1 %, respectively [46]. The recent report from Knoema on the energy consumption in Nigeria indicates that it has risen to 6.25 quadrillion kilojoules (or 5.93 quadrillions British thermal unit) as of the year 2018 [102].

According to the report by Nigeria Bureau of Statistics (2016-2019), the volume of Premium Motor Spirit (PMS or petrol) consumption in Nigeria (as shown in Figure 2a) has maintained an average of 1.5 billion liters within a range of 1 billion to 2.5 billion liters of PMS. It was shown that the tremendous volume of bioethanol was needed to complement the imported PMS to fulfill the requirement of E10 provided in Nigeria's energy policy for the use or sales of PMS/petrol in Nigeria. Moreover, the price of PMS has stood at the average of 140 Naira per liter except for the usual rise report in 2018, from November 2017 to March 2018 (as shown in Figure 2b), similar to the unexpected rise experienced in the late 2020 and present times. Therefore, the promotion of bioethanol production in Nigeria would go a long way to complement PMS use, which Nigeria residents majorly use for power and transport and promote cleaner air and a safe environment with a lower release of greenhouse gases.

The adoption of bioethanol (a biofuel) worldwide is significantly rising, not leaving any class of nations developed or developing (as shown in Figure 3), including private and public sectors. Embracing and promoting the use of biofuels for their environmental friendliness is very advantageous. Unlike the risk that the present use of fossil fuels is significantly posing to the health and safety in our environment due to the gases released, the carbon monoxide is commonly released during the incomplete process of combustion which the fossil fuels do undergo as a result of their lower octane rating when compared to the biofuels with higher rating.

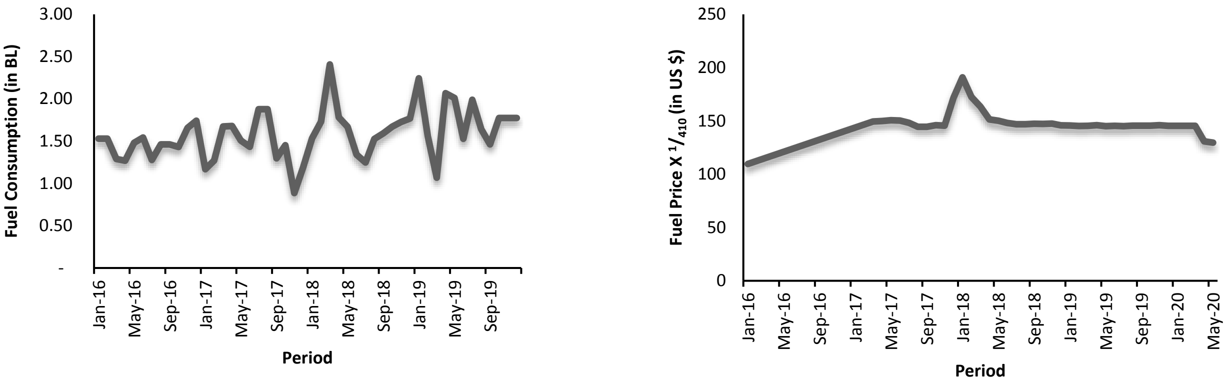

(a) (b)

Figure 2. (a) Fuel (PMS) consumption (expressed on Billion Liters i.e., BL) in Nigeria, (b) Fuel (PMS) price fluctuation in Nigeria expressed in Liter per Naira (1 US dollar = 410 Naira) from 2016-2020 NBS report

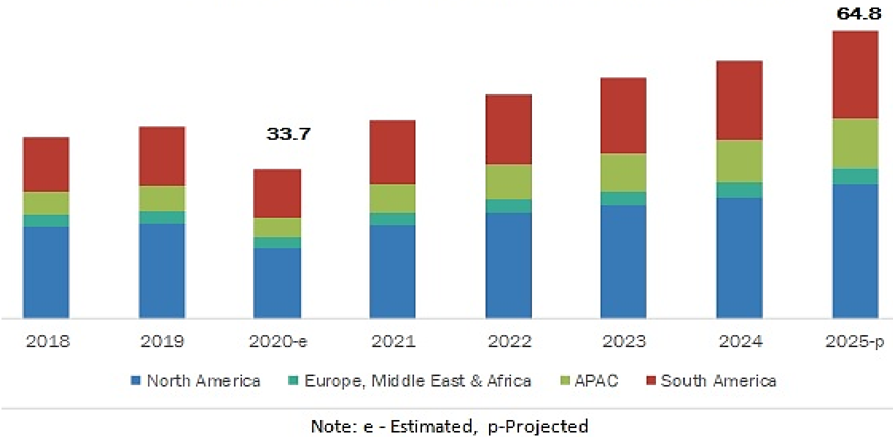

Figure 3. Global bioethanol fuel market (in USD billion) by different regions (2018-2025), where APAC is Asia-Pacific [Data Source: 2020 Bioethanol Market Global Forecast to 2025 | MarketsandMarkets.com]

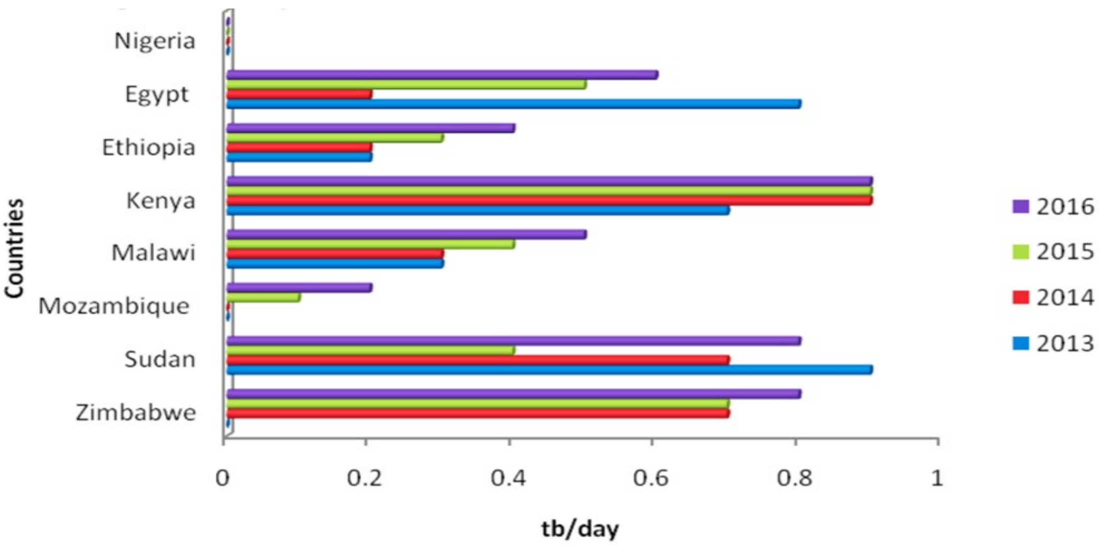

Figure 4. Fuel ethanol production in Africa from 2013 to 2016 [Data Source: 2017 Statistical Review of World Energy]

The 2017 Statistical Review of World Energy report shows that only a few African countries are presently part of this initiative, where most countries are mainly producing biofuels from the USA, Brazil, European Union, Asia, and other American continent countries. A few African countries currently into biofuels production primarily include Zimbabwe, Sudan, Malawi, Kenya, Egypt, Mozambique, and Ethiopia. Countries like Nigeria were found to have shown zero or insignificant production in line with the report (shown in Figure 4) of the 2017 Statistical Review of World Energy.

The report of Ogundari et al. [46] projected that the domestic demand for petrol (otherwise known as PMS) would have risen to two million tons and above as of the year 2019, as shown in Figure 5. As the energy demand has gradually risen in Nigeria for its residents to meet the demand for power and transport functions, the government needs to diversify its energy mix through a deliberate integration of biofuels production.

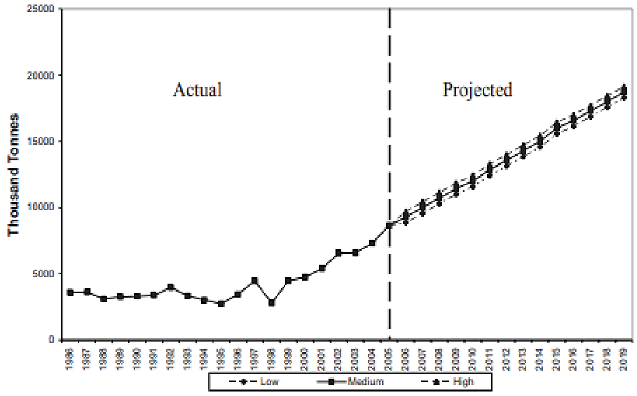

Figure 5. Domestic consumption of petrol in Nigeria (Actual & Projected values) [Source: Ogundari et al., [46]]

The report of Ogundari et al. [46] projected that the domestic demand for petrol (otherwise known as PMS) would have risen to two million tons and above as of the year 2019, as shown in Figure 5. As the energy demand has gradually risen in Nigeria for its residents to meet the demand for power and transport functions, the government needs to diversify its energy mix through a deliberate integration of biofuels production.

7. PROCESS SIMULATION, SCALE-UP, AND COMMERCIALIZATION OF BIOETHANOL FUEL IN NIGERIA

Process modeling and simulation involve developing representations of actual processes on a different platform that could facilitate the study and research of such processes [103, 104]. In recent time, the use of computer in the modeling of thermochemical, chemical, and biochemical processes is gaining significant attention among the industrialists and researchers in the study of chemical and biochemical process systems being a means that is an effective and efficient approach to studying reality via the use of process simulation, which would promote a better understanding of process plant and troubleshooting or retrofitting an existing planting process [103-105]. Deductions made from such studies would enable research works to understand better the preliminary technical and economic implications of commercializing such processes, which in most cases has already been confirmed to be feasibile from the laboratory studies findings [56, 57, 103-105].

A literature survey indicates that several research works have established the technical feasibility of setting up some functional bioethanol plants. However, some research papers have focused on using sugar-based materials while others focused on using cellulosic and starch-based materials. Some of these studies provide a report on the implication of utilizing cellulosic material like sugarcane-bagasse [56, 57] (in Figure 7), sorghum-bagasse [95] (in Figure 8), rice-husk (in Figure 9), and maize-cob [106, 107] for the production of bioethanol fuel through the process simulation approach. Other works that have employed the use of like approach are the use of sugar-based materials like molasses [14], sugarcane juice [88, 108] (in Figure 6), and many others.

Table 4. Report of the process scale-up studies

Ref.	Objectives of the work	Feedstock/Material used (Production capacity)	Study approach	Thermodynamics model used [Software used]	Key findings
[14]	Model and implement a cost-effective method of converting cane molasses, a by-product of sugar production in sugar refineries, into a liquid fuel known as bioethanol.	Sugarcane molasses (86 million liters of bioethanol per annum)	Process modeling and simulation	Non-Random Two liquid (NRTL) [Aspen HYSYS]	The parametric study found that the minimum number of trays in the distillation column for maximum purity was 40.
[95]	Model, simulate and study the financial implications of establishing or building a plant for transforming sorghum bagasse into bioethanol in Nigeria.	Sorghum bagasse (9408 kg/h of fuel-grade bioethanol)	Process modeling and simulation	NRTL [Aspen HYSYS, MATLAB, Ms-Excel 2013]	9,408 kg of fuel-grade bioethanol produced from 50,000 kg of sorghum bagasse was expensive relative to other existing bioethanol plant reports.
[88]	This study provides a pilot scale for bioethanol production from bioresources (sugarcane) through the fermentation process.	Sugarcane (100 L/day of bioethanol)	Process modeling and simulation	NRTL [SuperPro Designer]	A qualitative analysis of the fermenter and distillate using an infrared spectroscope revealed that ethanol accounted for approximately 67 % of ethanol.
[58]	Examine the cost-effectiveness of setting up a bioethanol plant in Nigeria, using waste (sugarcane bagasse) as a raw material.	Sugarcane bagasse (143 million liters/annum of fuel grade bioethanol)	Process modeling and simulation	NRTL [Aspen HYSYS, MATLAB, Ms-Excel]	The project's benefit is highly sensitive to the change(s) in sugar cane and government subsidy cost but not sensitive to the change(s) in minimum wages and taxes.
[57]	The model simulates bioethanol production from a combined cellulose and sugar feedstock and verifies the feedstock's feasibility and economic viability.	Sugarcane juice and bagasse (148 million liters/yr of bioethanol)	Process modeling and simulation	NRTL [Aspen HYSYS]	The energy efficiency of the proposed bioethanol plant was 63 %.

[56]	Examine the economic viability and sensitivity of selected variables to the bioethanol plant project's sustainability when cane juice and bagasse are used in Nigeria.	Sugarcane juice and bagasse (148 million liters/yr of bioethanol)	Process modeling and simulation	NRTL [MATLAB R2017a, Ms-Excel 2016]	According to the study's conditions, the study suggests that the proposed plant would be economically viable and profitable in Nigeria.
[106]	To comparatively investigate the material requirement, production yield, and total equipment cost involved in the rice-husk and maize-cob transformation into the bio-ethanol fuel for large-scale production using a process modeling and simulation study to promote the potential investors' interest.	Rice husk and maize -cob (9.94 kg/h and 7.32 kg/h of fuel-grade bioethanol)	Process modeling and simulation	NRTL [Aspen HYSYS, MATLAB and Microsoft Excel]	The study shows that rice husks show a high yield, while maize cob makes the production less capital-intensive.

The details of the works done so far that have advanced the scaling up and establishing the bioethanol plant in Nigeria are presented in Table 4. Studies indicate that no studies have been reported on starch-based feedstock use among the works done so far. Instead, most reports have been mainly on sugar and cellulosic-based feedstock like rice husk, maize cob, sugarcane bagasse, sorghum bagasse, molasses, and many other related feedstocks.

Most of the process scale-up studies reported in the literature have primarily been shown to have employed the thermodynamics model known as the Non-Random Two liquid (NRTL) model. Likewise, most of the studies that have majorly used Aspen HYSYS, while the report of Misau et al. [88, 108] employed SuperPro Designer simulator possessed good features and capacities similar to that of the Aspen HYSYS simulator. Some of the process flow diagrams reported for the studies of bioethanol production for the use of sugarcane juice [88, 108], sugarcane juice-bagasse [56, 57], sorghum bagasse [95, 109] and rice husk [106] to investigate the feasibility of commercial bioethanol in Nigeria. In most of the reports, the NRTL model has been reported to have the best fit to equilibrium due to the components involved in a bioethanol production process attributed to its polarity (like water and ethanol), and the vapor phase behavior can be compared to that of the ideal gas due to the low operating pressures, i.e., 1-5 atm as reported in the literature [14, 95]. Process modeling and pilot studies have reported using sugarcane juice and bagasse, indicating that it is technically feasible to set up such refineries in Nigeria.

8. ECONOMIC SIGNIFICANCE OF PROMOTING BIOETHANOL FUEL IN NIGERIA

Not only was the technical feasibility of scaling up the plant for its establishment in Nigeria carried out, but also many other studies focused on the economic feasibility of establishing this bioethanol plant in Nigeria. The report of the various research work findings is summarized in Table 5, reporting the nature of feedstocks used as well as the estimated capital and operating costs including the economic benefit of the projected deduced from studies.

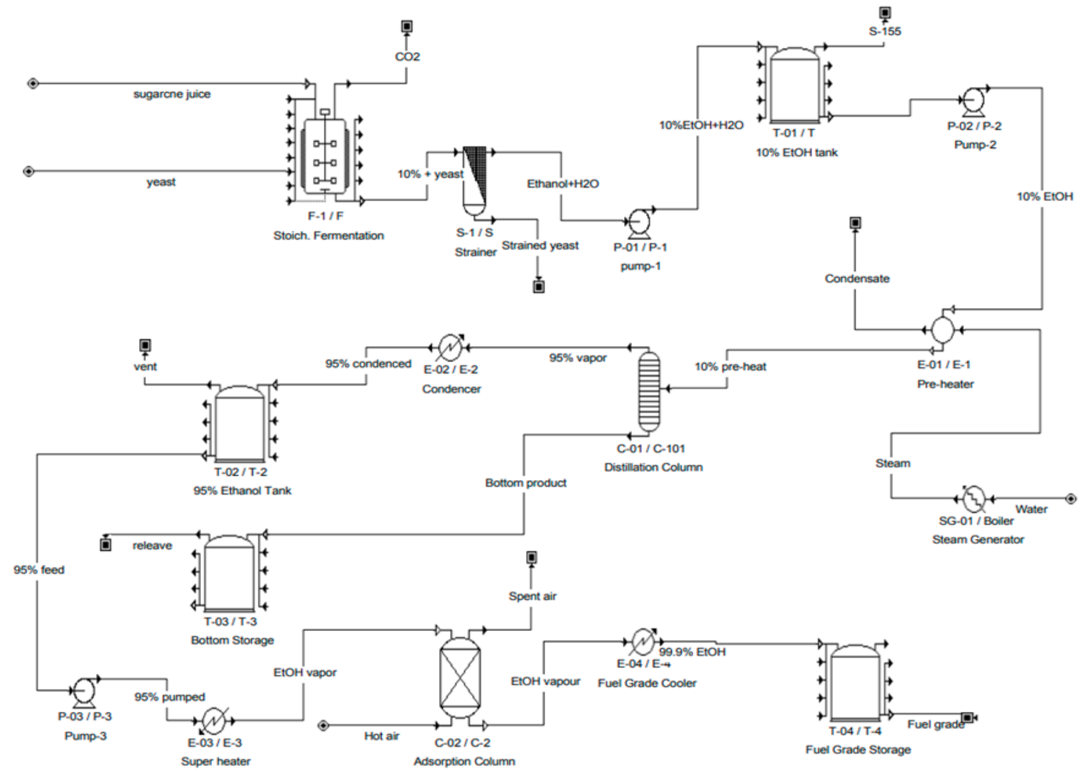

Figure 6. A Process Flow Diagram (PFD) route for sugarcane juice to bioethanol project in Nigeria [88, 108]

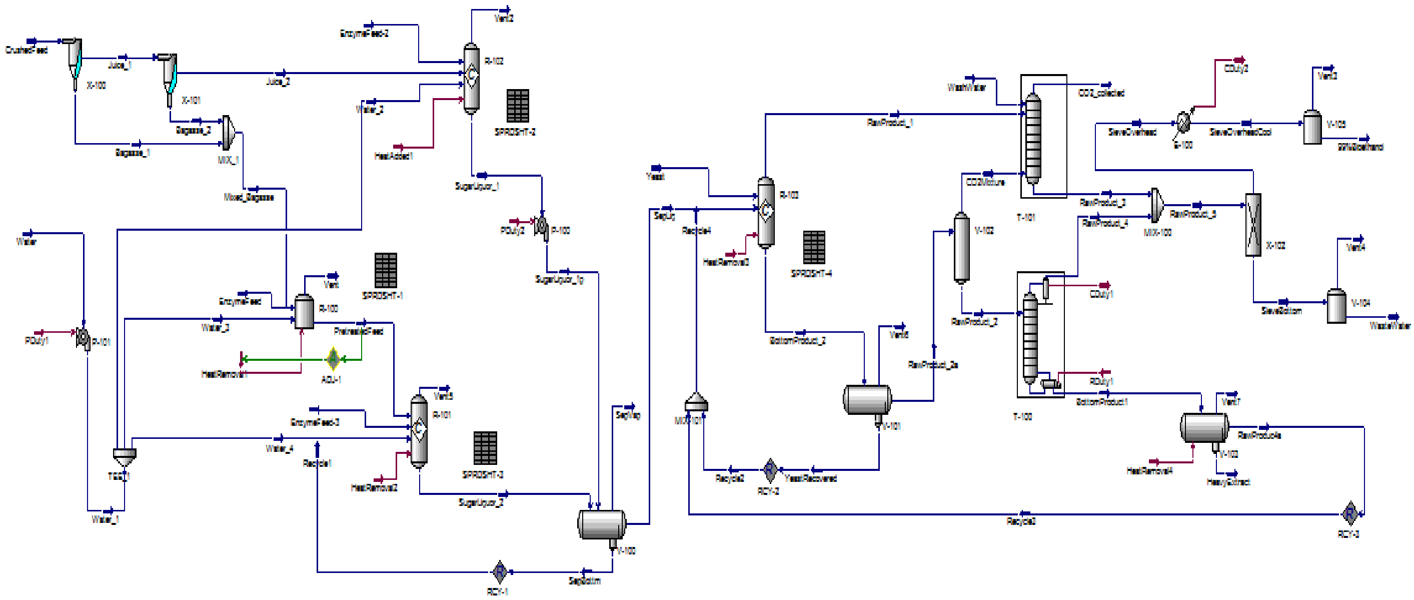

Figure 7. A PFD for the combined transformation of sugarcane juice and bagasse into bioethanol in Nigeria [57]

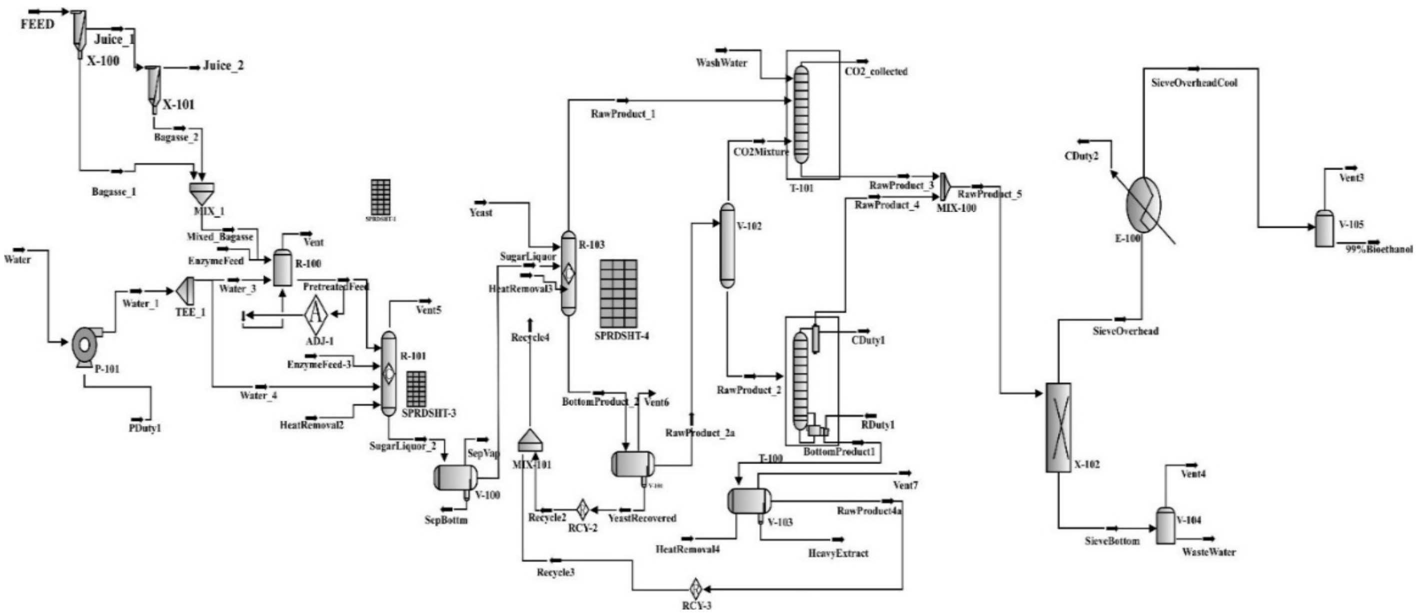

Figure 8. The PFD showing the process route for sorghum bagasse into bioethanol in Nigeria [95]

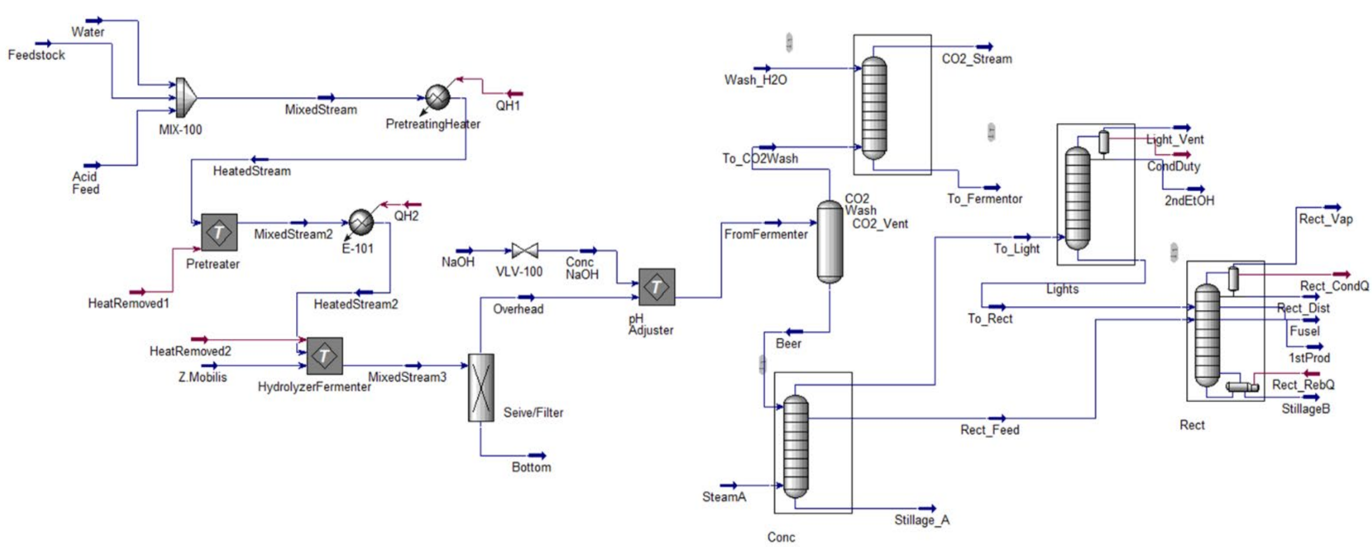

Figure 9. The PFD displaying the process route for transforming rice husk into bioethanol in Nigeria [106, 107]

Unlike the sugar and cellulose-based feedstocks whose economic feasibility studies have been reportedly conducted, literature is yet to give significant attention to the economic feasibility studies of starch-based materials, except for the study of Ogbonma et al. [48] that accounted for the economic feasibility of utilizing cassava, which was only feasible provided the plant would be situated next to the farm. However, the literature survey indicates that the stability of currency exchange rates like the Naira-Dollar exchange in Nigeria has an extended role in promoting the economic feasibility of establishing a bioethanol fuel plant across Nigeria's states and other developing nations. Also, the reports from Abemi et al. [14] and Oyegoke et al. [56] emphasize the need for developing governments to introduce a subsidy for bioethanol production to promote green fuel consumption in developing nations.

9. BIOETHANOL STUDIES TREND TOWARD THE PROMOTION OF BIOREFINERIES IN NIGERIA

The distribution of works done so far on the laboratory investigations [43, 45, 51-55, 61, 63-66, 68, 69, 71, 76, 86, 87, 110], process scale-up studies [14, 57, 58, 88, 95, 106], and the economics feasibility studies [14, 48, 56, 58, 107, 109, 111] towards the commercialization of bioethanol is graphically represented in Figure 5, where the proportion of starch [46-48, 81, 82, 84, 85, 90, 91, 112], cellulose [51, 53, 57, 58, 61, 71, 74, 77, 78, 83, 95, 109] and sugar-based [14, 44, 45, 56, 57] feedstock studied so far and the form of studies and volume of works done so far are presented.

The survey of laboratory studies carried out in the literature indicates that many laboratory research works are giving significant attention to the study of bioethanol production kinetics and optimization, even though the literature survey indicates that greater attention is given to the study of bioethanol production optimization with lesser attention given to the investigation of the reaction kinetics of the production processes, which enable the process scale-up studies to be feasibly investigated with the use of the findings obtained from the laboratory studies.

Table 5. Economic studies report for bioethanol production (CC=Capital cost, OC=Operating cost)

Ref.	Type	Feedstock/Material used (Production capacity in the study)	CC (OC)	ROI (IRR) %	NPV/NPW	Other economic parameters	Key findings made
[58]	Cellulose	Sugar cane bagasse (143 million liters)	n.r. (n.r.)	12.83 (12.10)	NGN 37.48 million	Payback period (PBP) at 10 % of 6.9 years	143 million liters of fuel-quality bioethanol require 402 metric tonnes of crushed sugar cane bagasse.
[95]	Cellulose	Sorghum bagasse (9,408 kg of bioethanol from 50,000 kg sorghum bagasse)	$1.92/L (0.83 $/L)	n.r. (n.r.)	n.r.	n.r.	The project would require capital and operating costs of $1.92 and $0.83, respectively, to produce one liter of fuel-grade bioethanol from sorghum bagasse.
[109]	Cellulose	Sorghum bagasse (59,778,931.90 L of bioethanol)	$0.64 /L (0.89 $/L)	49.99 (n.r.)	- $212 million	n.r.	It was found that it was not economically feasible to replace fuel used in Nigeria due to high exchange rates.
[107]	Cellulose	Rice husk (17.7 million liters (1789.45 kg/h) of bioethanol)	0.27 US$/L (0.51US$/L or 183.6 NGN/L)	9.89 (16.10)	$5 million	5.5 years (PBP) of 25 years	The report's findings recommend subsidizing and tax-exempt biofuel production to encourage investors and promote cleaner fuels in emerging countries.
[57]	Cellulose & sugar	Combined cellulose and sugar feedstock (148 million liters of fuel grade bioethanol)	$51 million ($ 89 million)	n.r. (n.r.)	n.r.	n.r.	375,000 liters of bioethanol can be produced from a metric tonne of crushed sugarcane at an investment and manufacturing cost of $0.34/L and $0.61/L, respectively.
[56]	Cellulose & sugar	Combined cellulose and sugar feedstock (148 million liters of fuel grade bioethanol)	$51 million or 0.34$/L) ($89million or 0.61$/L))	8.40 (11.51)	$ 20.90 million (at 10 % discount)	PBP at 10 % of 9.64 years	A plant producing 148 million liters of fuel-grade bioethanol from 402 metric tonnes per year of crushed sugarcane would be economically feasible in Nigeria.
[48]	Starch	Cassava (0.34 g-ethanol/g-cassava flour)	n.r. ($46,875)	n.r. (n.r.)	n.r.	Cost price calculated as ₦102.5/l (US$0.641/l)	It was recommended that the plant be integrated with the cassava farm is grown to make the process workable.
[14]	Sugar	Cane molasses (86 million liters of bioethanol per annum)	$ 12.86 million ($ 51.70 million)	-124. 22 (14.69)	-$85.45 million	PBP is infinity (∞)	Bioethanol production in Nigeria from molasses is economically viable if the government subsidizes it and the naira-dollar exchange rate declines.

A literature survey (presented in Figure 10) regarding the promotion of bioethanol fuels adoption in Nigeria indicates that greater attention has been given to the studies of the cellulose-based feedstock in the laboratory (46 %) and economic feasibility (8 %) studies, while sugar (4 %) and cellulose (5 %) based feedstock studies (8 %) have dedicated greater attention to the case of process scale-up studies, being vital to the commercialization of the laboratory established fact on bioethanol production in Nigeria. Moreover, the survey further indicates that the bulk of the works have mainly focused greater attention to the laboratory studies (with 81 %) while giving lesser attention to the study of process scale-up (with 8 %) and economic feasibility (with 11 %) studies with a tremendous potential of attracting the attention of government and private investor that would incur their fund on the establishment of biorefineries in Nigeria.

Moreover, it is necessary to pay more attention to the investigation into the laboratory study of the bioethanol production kinetics, the process scale-up studies of the laboratory established fact, and the exploration of the economics relevance before materializing the project and this would bring about significant pre-insights for both the government and private investors.

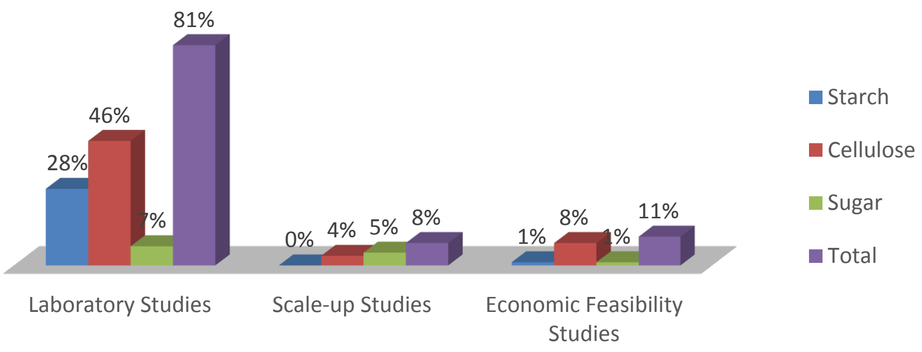

Figure10. Distribution of studies carried out at different stages in Nigeria for bioethanol production

10. CONCLUSIONS

Many research attempts to unveil the technical and economic implications of embracing bioethanol fuels in developing nations like Nigeria were successfully surveyed. The survey, which included the exploration of the laboratory-scale, process scale-up studies, and techno-economic studies carried out so far as part of the vital component of research, can be used to gain the confidence of both private investors and government to explore the financial benefits for potential investors in Nigeria.

From the literature review that has been carried out through careful research, it can be seen that bioethanol yield from sugarcane juice was the highest amongst other sugar-based feedstocks. Banana stem, rice husk, and elephant grass stem produced more bioethanol than other lignocellulosic feedstocks. The starch-based feedstock has cassava as the highest bioethanol yielding feedstock. However, the starch-based feedstock may compete with human food. The high-octane number and complete combustion of bioethanol due to oxygen presence serve as a significant advantage over fossil fuel. This makes it the center of energy research for both developed and developing countries.

However, Nigeria is far behind in the production of bioethanol despite the availability of feedstocks. Feasibility studies, process scale-up, and pilot studies have shown that venturing into bioethanol production as a country would be a good investment. Despite the work done so far, there is still room for improvement and areas to consider. Only a few studies have examined process scale-up, modeling, and economic feasibility studies for many lab-scale technologies. Politically, the snaring revelation hindering the effective sail of biofuel production may not be far from the politicking on the part of business personalities and oil rig moguls whose income and business empires might cripple down if biofuel production and utilization substitute petroleum in the Nigerian economy. It is, therefore, necessary to review bioethanol production policies in Nigeria by the appropriate authorities.

In addition, findings from literature survey have pointed to the need for further studies to focus on the investigation of process scale-up for bioethanol production through the use of starch-based and some other lignocellulosic (yet to be investigated) materials, including the exploration of its economic benefits to the national development of developing nations like Nigeria and other African countries. Moreover, the findings of this survey have also shown the need for the government to subsidize bioethanol production due to the unstable exchange rates. Therefore, adequate funds should support the transition towards green energy by supporting scale-up, feasibility, pilot study, and implementation by both government and private establishments.

11. ACKNOWLEDGEMENT

The authors acknowledge the support of PENCIL research team members and their affiliates.

REFERENCES

1. Abdeshahian, P., Dashti, M.G., Kalil, M.S. and Yusoff, W.M.W., "Production of biofuel using biomass as a sustainable biological resource", ***Biotechnology***, Vol. 9, (2010), 274-282. (https://doi.org/10.3923/biotech.2010.274.282).
2. Virmond, E., Rocha, J.D., Moreira, R.F.P.M. and Jose, H.J., "Valorization of agroindustrial solid residues and residues from biofuel production chains by thermochemical conversion: A review, citing Brazil as a case study", ***Brazilian Journal of Chemical Engineering***, Vol. 30, (2013), 197-229. (https://doi.org/10.1590/S0104-66322013000200001).
3. Ahorsu, R., Medina, F. and Constantí, M., "Significance and challenges of biomass as a suitable feedstock for bioenergy and biochemical

production: A review", ***Energies***, Vol. 11, No. 3366, (2018), 1-19. (https://doi.org/10.3390/en11123366).

4. Banque africaine de développement, "Fossil fuel extraction in Africa: Carbon risks and economic realities", (2021). (https://www.afdb.org/fr/news-and-events/fossil-fuel-extraction-in-africa-carbon-risks-and-economic-realities-18891), (Accessed: 17 March 2021).
5. FOEI, "Dirty energy in Africa", (2016). (https://www.foei.org/wp-content/uploads/2016/11/DIRTY-ENERGY-IN-AFRICA-EN-FINAL.pdf), (Accessed: 17 March 2021).
6. IEA, "IRENA perspectives for the energy transition: Investment needs for a low-carbon energy system", (2021). (https://www.irena.org/-/media/Files/IRENA/Agency/Publication/2017/Mar/Perspectives_for_the_Energy_Transition_2017.pdf) (Accessed: 17 March 2021).
7. "Biomass and energy: From primary resources to final energy products", Encyclopédie de l'énergie, (2021). (https://www.encyclopedie-energie.org/en/biomass-energy-primary-resources-final-energy-products/), (Accessed: 17 March 2021).
8. Perera, F., "Pollution from fossil-fuel combustion is the leading environmental threat to global pediatric health and equity: Solutions exist", ***International Journal of Environmental Research and Public Health***, Vol. 15, No. 16, (2018) 1-17. (https://doi.org/10.3390/ijerph15010016).
9. Bušić, A., Marđetko, N., Kundas, S., Morzak, G., Belskaya, H., Šantek, M.I., Komes, D., Novak, S. and Šantek, B., "Bioethanol production from renewable raw materials and its separation and purification: A review", ***Food Technology & Biotechnology***, Vol. 56, No. 3, (2018), 298-311. (https://doi.org/10.17113/ftb.56.03.18.5546).
10. Tan, J.H., Sigaud, J., Claros Baptista, A. and Ozza, T., "Alcohol-type fuels for mobility PSM project-energy transition", IFP School Publication, Paris, (2015). (https://www.fondation-tuck.fr/upload/docs/application/pdf /2016-05/psmreport15_team_5.pdf).
11. UNCTAD, "Biofuel production technologies: Status, prospects and implications for trade and development", New York and Geneva, (2008). (https://unctad.org/system/files/official-document/ditcted200710_en.pdf).
12. Ohimain, E.I., "Emerging bio-ethanol projects in Nigeria: Their opportunities and challenges", ***Energy Policy***, Vol. 38, No. 11, (2010), 7161-7168. (https://doi.org/10.1016/j.enpol.2010.07.038).
13. Galadima, A., Garba, Z.N., Ibrahim, B.M., Almustapha, M.N., Leke, L. and Adam, I.K., "Biofuels production in Nigeria: The policy and public opinions", ***Journal of Sustainable Development***, Vol. 4, No. 4, (2011), 22. (https://doi.org/10.5539/jsd.v4n4p22).
14. Abemi, A., Oyegoke, T., Dabai, F.N. and Jibril, B.Y., "Technical and economic feasibility of transforming molasses into bioethanol in Nigeria", ***Proceedings of the National Engineering Conference***, ABU, Zaria, (2018), 531-537. (https://www.researchgate.net/publication/337223844_Technical_and_Economic_Feasibility_of_Transforming_Molasses_into_Bioethanol_in_Nigeria).
15. Franziska, M.-L., Marco, K., Jens, S., Riazi, M.R. and David, C., "Biofuels production processes and technologies", Biofuels production and processing technology, CRC Press, (2017), 153-182. (https://www.routledge.com/Biofuels-Production-and-Processing-Technology/Riazi-Chiaramonti/p/book/9781498778930).
16. Zabed, H., Sahu, J.N., Boyce, A.N. and Faruq, G., "Fuel ethanol production from lignocellulosic biomass: An overview on feedstocks and technological approaches", ***Renewable and Sustainable Energy Reviews***, Vol. 66, No. 1, (2016), 751-774. (https://doi.org/10.1016/j.rser.2016.08.038).
17. The Nations, "Nigeria can save N1.2trl from ethanol, other imports", Latest Nigeria News, Nigerian Newspapers, Politics, The Nations Newspaper Publication, (2016). (https://thenationonlineng.net//nigeria-can-save-n1-2trl-from-ethanol-other-imports/).
18. Advanced Biofuels USA, "Nigeria imports 350m litres of ethanol yearly as experts suggest solutions", (2019). (https://advancedbiofuelsusa.info/nigeria-imports-350m-litres-of-ethanol-yearly-as-experts-suggest-solutions/), (Accessed: 15 June 2021).
19. Femi, I., "Nigeria imports 350m litres of ethanol yearly as experts suggest solutions", Nigeria news, Nigeria and world news, The Guardian Newspaper, (2019). (https://guardian.ng/features/nigeria-imports-350m-litres-of-ethanol-yearly-as-experts-suggest-solutions/).
20. Olurounbi, R., "NNPC driving Nigeria's biofuel agenda: Nowhere near 2020 target", (2021). (https://www.theafricareport.com/42590/nigerias-biofuel-success-must-include-more-private-investment/), (Accessed: 15 June 2021).
21. Biofuels International Magazine, "Nigeria invests in new bioethanol plant as it diversifies away from oil", (2021). (https://biofuels-news.com/news/nigeria-invests-in-new-bioethanol-plant-as-it-diversifies-away-from-oil/), (Accessed: 15 June 2021).
22. Biofuel Digest, "Site work begins at planned NNPC ethanol project in Kogi State", (2021). (https://www.biofuelsdigest.com/bdigest/2020/02/17/site-work-begins-at-planned-nnpc-ethanol-project-in-kogi-state/), (Accessed: 15 June 2021).
23. Biofuels Digest, "Ethanol push in Kebbi State could result in $1b in annual revenues", (2021). (https://www.biofuelsdigest.com/bdigest/2020/06/09/ethanol-push-in-kebbi-state-could-result-in-1b-in-annual-revenues/), (Accessed: 15 June 2021).
24. Biofuels Digest, "NNPC to cultivate cassava plantations for biofuels", (2021). (https://www.biofuelsdigest.com/bdigest/2020/07/26/nnpc-to-cultivate-cassava-plantations-for-biofuels/), (Accessed: 15 June 2021).
25. Biofuel Digest, "Nigeria signs MOU with Israeli methanol company for local production", (2021). (https://www.biofuelsdigest.com/bdigest/2020/08/06/nigeria-signs-mou-with-israeli-methanol-company-for-local-production/), (Accessed: 15 June 2021).
26. Biofuel Digest, "Officials break ground at Osun ethanol biorefinery", (2021), (https://www.biofuelsdigest.com/bdigest/2020/09/22/officials-break-ground-at-osun-ethanol-biorefinery/), (Accessed: 15 June 2021).
27. Biofuel Digest, "MOU signed to develop cassava-based biorefinery in Nigeria's Plateau State", (2021). (https://www.biofuelsdigest.com/bdigest/2020/12/28/mou-signed-to-develop-cassava-based-biorefinery-in-nigerias-plateau-state/), (Accessed: 15 June 2021).
28. Lászlok, A., Takács-György, K. and Takács, I., "Examination of first generation biofuel production in some selected biofuel producing countries in europe: A case study", ***Agricultural Economics-Czech***, Vol. 66, No. 10, (2020) 469-476. (https://doi.org/10.17221/237/2020-AGRICECON).
29. Biofuel, "Biofuels-first generation biofuels", (2021). (http://biofuel.org.uk/first-generation-biofuel.html), (Accessed: 18 March 2021).
30. Naik, S.N., Goud, V.V., Rout, P.K. and Dalai, A.K., "Production of first and second generation biofuels: A comprehensive review", ***Renewable and Sustainable Energy Reviews***, Vol. 14, No. 2, (2010), 578-597. (https://doi.org/10.1016/j.rser.2009.10.003).
31. Eckert, C.T., Frigo, E.P., Albrecht, L.P., Albrecht, A.J.P., Christ, D., Santos, W.G., Berkembrock, E. and Egewarth, V.A., "Maize ethanol production in Brazil: Characteristics and perspectives", ***Renewable and Sustainable Energy Reviews***, Vol. 82, (2018), 3907-3912. (https://doi.org/10.1016/j.rser.2017.10.082).
32. Manochio, C., Andrade, B.R., Rodriguez, R.P. and Moraes, B.S., "Ethanol from biomass: A comparative overview", ***Renewable and Sustainable Energy Reviews***, Vol. 80, (2017), 743-755. (https://doi.org/10.1016/j.rser.2017.05.063).
33. van der Hoeven, D., "First generation bioethanol deserves revaluation", Nova-Institute | Bio Based Press, (2021). (https://www.biobasedpress.eu/2017/09/first-generation-bioethanol-deserves-revaluation/), (Accessed: 18 March 2021).
34. Ghaderi, H., Asadi, M. and Shavvalpour, S.A., "Switchgrass-based bioethanol supply chain network design model under auto-regressive moving average demand", ***Journal of Renewable Energy and Environment (JREE)***, Vol. 3, No. 3, (2016), 1-10. (https://doi.org/10.30501/JREE.2016.70087).
35. Goshadrou, A., "Surfactant-aided phosphoric acid pretreatment to enable efficient bioethanol production from glycyrrhiza glabra residue paperinfo", ***Journal of Renewable Energy and Environment (JREE)***, Vol. 6, No. 4, (2019), 10-15. (https://doi.org/10.30501/JREE.2019.101505).
36. Aditiya, H.B., Mahlia, T.M.I., Chong, W.T., Nur, H. and Sebayang, A.H., "Second generation bioethanol production: A critical review", ***Renewable and Sustainable Energy Reviews***, Vol. 66, (2016), 631-653. (https://doi.org/10.1016/j.rser.2016.07.015).
37. Robak, K. and Balcerek, M., "Review of second generation bioethanol production from residual biomass", ***Food Technology and Biotechnology***, Vol. 56, No. 2, (2018), 174-187. (https://doi.org/10.17113/ftb.56.02.18.5428).

38. Saïdane-Bchir, F., el Falleh, A., Ghabbarou, E. and Hamdi, M., "3rd generation bioethanol production from microalgae isolated from slaughterhouse wastewater", ***Waste and Biomass Valorization***, Vol. 7, No. 5, (2016), 1041-1046. (https://doi.org/10.1007/s12649-016-9492-6).

39. Jambo, S.A., Abdulla, R., Mohd Azhar, S.H., Marbawi, H., Gansau, J.A. and Ravindra, P., "A review on third generation bioethanol feedstock", ***Renewable and Sustainable Energy Reviews***, Vol. 65, (2016), 756-769. (https://doi.org/10.1016/j.rser.2016.07.064).

40. Scott, S.A., Davey, M.P., Dennis, J.S., Horst, I., Howe, C.J., Lea-Smith, D.J. and Smith, A.G., "Biodiesel from algae: Challenges and prospects", ***Current Opinion in Biotechnology***, Vol. 21, No. 3, (2010), 277-286. (https://doi.org/10.1016/j.copbio.2010.03.005).

41. Lardon, L., Hélias, A., Sialve, B., Steyer, J.P. and Bernard, O., "Life-cycle assessment of biodiesel production from microalgae", ***Environmental Science and Technology***, Vol. 43, No. 17, (2009), 6475-6481. (https://doi.org/10.1021/es900705j).

42. Nwufo, O.C., Nwaiwu, C.F., Igbokwe, J.O. and Nwafor, O.M.I., "Production and characterisation of bio-ethanol from various Nigerian feedstocks", ***International Journal of Ambient Energy***, Vol. 37, No. 5, (2015), 469-473. (https://doi.org/10.1080/01430750.2014.986290).

43. Nwogwugwu, N.U., Abu, G.O., Akaranta, O. and Chinakwe, E.C., "Application of response surface methodology for optimizing the production of bioethanol from calabash (*crescentia cujete*) substrate using *saccharomyces cerevisiae*", ***Journal of Advances in Microbiology***, Vol. 17, No. 2, (2019), 1-12. (https://doi.org/10.9734/jamb/2019/v17i230139).

44. Gaffa, K.T., "Production of ethyl alcohol from molasses using continous process", ***Nigerian Journal of Biotechnology***, Vol. 8, No. 1, (1997), 35-39. (https://www.ajol.info/index.php/njb/article/view/125908).

45. Suleiman, B., Abdulkareem, S.A., Afolabi, E.A., Musa, U., Mohammed, I.A. and Eyikanmi, T.A., "Optimization of bioethanol production from Nigerian sugarcane juice using factorial design", ***Advances in Energy Research***, Vol. 4, No. 1, (2016), 69-86. (https://doi.org/10.12989/eri.2016.4.1.069).

46. Ogundari, I.O., Momodu, A.S., Famurewa, A.J., Akarakiri, J.B. and Siyanbola, W.O., "Analysis of sustainable cassava biofuel production in Nigeria", ***Energy & Environment***, Vol. 23, No. 4, (2012), 599-618. (https://doi.org/10.1260/0958-305X.23.4.599).

47. Ademiluyi, F.T. and Mepba, H.D., "Yield and properties of ethanol biofuel produced from different whole cassava flours", ***ISRN Biotechnology***, Vol. 2013, No. 916481, (2013), 1-6. (https://doi.org/10.5402/2013/916481).

48. Ogbonna, C.N. and Okoli, E.C., "Economic feasibility of on-farm fuel ethanol production from cassava tubers in rural communities", ***African Journal of Biotechnology***, Vol. 12, No. 37, (2013), 5618-5626, (https://doi.org/10.5897/AJB2013.12855).

49. Ojewumi, M.E., Job, A.I., Samson Taiwo, O., Mopelola Obanla, O., Ayoola, A.A., Ojewumi, E.O. and Oyeniyi, E.A., "Bio-conversion of sweet potato peel waste to bio-ethanol using *saccharomyces cerevisiae*", ***International Journal of Pharmaceutical and Phytopharmacological Research***, Vol. 8, No. 3, (2018), 46-54. (https://eijppr.com/article/bio-conversion-of-sweet-potato-peel-waste-to-bio-ethanol-using-saccharomyces-cerevisiae).

50. Ojewumi, M.E., Emetere, M.E., Amaefule, C.V., Durodola, B.M. and Adeniyi, O.D., "Bioconversion of orange peel waste by *escherichia coli* and *saccharomyces cerevisiae* to ethanol", ***International Journal of Pharmaceutical Sciences and Research***, Vol. 10, No. 3, (2019), 1246-1252. (https://doi.org/10.13040/IJPSR.0975-8232.10(3).1246-52).

51. Oyeleke, S.B., Dauda, B.E.N., Oyewole, O., Okoliegbe, I.N. and Ojebode, T., "Production of bioethanol from cassava and sweet potato peels", ***Advances in Environmental Biology***, Vol. 6, No. 1, (2012), 241-245. (http://www.aensiweb.com/old/aeb/2012/241-245.pdf).

52. Oiwoh, O., Ayodele, B.V., Amenaghawon, N.A. and Okieimen, C.O., "Optimization of bioethanol production from simultaneous saccharification and fermentation of pineapple peels using *saccharomyces cerevisiae",* ***Journal of Applied Sciences and Environmental Management***, Vol. 22, No. 1, (2018), 54-59. (https://doi.org/10.4314/jasem.v22i1.10).

53. Ebabhi, A.M., Adekunle, A.A. and Adeogun, O.O., "Potential of some tuber peels in bioethanol production using *candida tropicalis*", ***Nigerian Journal of Basic and Applied Sciences***, Vol. 26, No. 2, (2019), 17-22. (https://doi.org/10.4314/njbas.v26i2.3).

54. Adegunloye, D. and Udenze, D., "Effect of fermentation on production of bioethanol from peels of cocoyam using *aspergillus niger* and *saccharomyces cerevisiae*", ***Journal of Advances in Microbiology***, Vol. 4, No. 2, (2017), 1-8. (https://doi.org/10.9734/jamb/2017/34032).

55. Christopher, O.O. and Felix, A.A., "Comparative studies on production of bioethanol from rice straw using bacillus subtilis and trichoderma viride as hydrolyzing agents", ***Microbiology Research Journal International***, Vol. 28, No. 3, (2019), 1-12. (https://doi.org/10.9734/mrji/2019/v28i330134).

56. Oyegoke, T. and Dabai, F., "Techno-economic feasibility study of bioethanol production from a combined cellulose and sugar feedstock in Nigeria: 2-Economic analysis", ***Nigerian Journal of Technology***, Vol. 37, No. 4, (2018), 921-926. (https://doi.org/10.4314/njt.v37i4.9).

57. Oyegoke, T. and Dabai, F., "Techno-economic feasibility study of bioethanol production from a combined cellulose and sugar feedstock in Nigeria: 1-Modeling, simulation and cost evaluation", ***Nigerian Journal of Technology***, Vol. 37, No. 4 (2018), 913-920. (https://doi.org/10.4314/njt.v37i4.8).

58. Oyegoke, T., Dabai, F., Abubakar, M.J. and Jibiril, B.Y., "Process modelling and economic analysis for cellulosic bioethanol production in Nigeria", ***Proceedings of the 1st National Conference On Chemical Technology (NCCT 2017)***, (2017), 125-128. (https://www.researchgate.net/publication/337223934_Process_Modelling_and_Economic_Analysis_for_Cellulosic_Bioethanol_Production_in_Nigeria).

59. Zabochnicka-Świątek, M. and Sławik, L., "Bioethanol - production and utilization", ***Archivum Combustionis***, Vol. 30, No. 3, (2010), 237-246. (http://yadda.icm.edu.pl/yadda/element/bwmeta1.element.baztech-article-BWM4-0030-0046).

60. Saddler, J., Ebadian, M. and Mcmillan, J.D., "Advanced biofuels-Potential for cost reduction", IEA Bioenergy Task 41 Report, (2020). (https://www.liquidbiofuels.org.nz/resource/advanced-biofuels-potential-for-cost-reduction).

61. Tsunatu, D.Y., Atiku, K.G., Samuel, T.T., Hamidu, B.I. and Dahutu, D.I., "Production of bioethanol from rice straw using yeast extracts peptone dextrose", ***Nigerian Journal of Technology (NIJOTECH)***, Vol. 36, No. 1, (2017), 296-301. (https://doi.org/10.4314/njt.v36i1.36).

62. Olayemi, S., Ibikunle, A. and Olayemi, J., "Production of ethanol from cassava and yam peels using acid hydrolysis", ***American Academic Scientific Research Journal for Engineering Technology, and Sciences (ASRJETS)***, Vol. 52, No. 1, (2019), 67-78. (https://asrjetsjournal.org/index.php/American_Scientific_Journal/article/view/3195).

63. Obianwa, C., Edak, A.U. and Godwin, I., "Bioethanol production from cassava peels using different microbial inoculants", ***African Journal of Biotechnology***, Vol. 15, No. 30, (2016), 1608-1612. (https://doi.org/10.5897/ajb2016.15391).

64. Akponah, E.A. and Akpomie, O.O., "Analysis of the suitability of yam, potato and cassava root peels for bioethanol production using saccharomyces cerevisae", ***International Research Journal of Microbiology (IRJM)***, Vol. 2, No. 10, (2011), 393-398. (https://www.interesjournals.org/articles/ analysis-of-the-suitability-of-yam-potato-and-cassava-root-peels-for-bioethanol-production-using-saccharomyces-cerevisae.pdf).

65. Monday, O.A., "Statistical investigation on the hydrolysis and fermentation processes of cassava peels in the production of bioethanol", ***International Journal of Statistical Distributions and Applications***, Vol. 3, No. 3, (2017), 47-55. (https://doi.org/10.11648/j.ijsd.20170303.14).

66. Isah, Y., Kabiru, H.D., Danlami, M.A. and Kolapo, S.F., "Comparative analysis of bioethanol produced from cassava peels and sugarcane bagasse by hydrolysis using *saccharomyces cerevisiae*", ***Journal of Chemical Society of Nigeria***, Vol. 44, No. 2, (2019), 233-238. (http://journals.chemsociety.org.ng/index.php/jcsn/article/view/263/0).

67. Oyegoke, T., Obadiah, E., Mohammed, Y.S., Bamigbala, O.A. and Owolabi, O.A., "Utilization of rice husk for the bioethanol production: A waste to wealth innovation study", ***Proceedings of Sustainability Challenges & Transforming Opportunities: "Amidst Covid19"***, Anuradha, S., Jyoti, B., Ravi, K.S. and Subodhika, S.E., Eds., Authorspress Global Network, New Delhi, Vol. 1, (2021), 54-63. (https://doi.org/10.13140/RG.2.2.15491.22561).

68. Ezeonu, C.S., Arowora, K.A., Imo, C. and Onwurah, I.N.E., "Bioethanol production from fungal treated rice husks fermented with bakers *saccharomyces cerevisiae* and yeast isolates from palm wine", ***Journal of Fundamentals of Renewable Energy and Applications***, Vol. 8, No. 4, (2018), 1-5. (https://doi.org/10.4172/2090-4541.1000262).

69. Ahmad, F.U., Bukar, A. and Usman, B., "Production of bioethanol from rice husk using *aspergillus niger* and *trichoderma harzianum*", ***Bayero Journal of Pure and Applied Sciences***, Vol. 10, No. 1, (2018), 280-294. (https://doi.org/10.4314/bajopas.v10i1.56s).

70. Mustafa, H.M., Bashir, A. and Dahiru, S.M., "Production of bioethanol from sulfuric acid pretreated rice husk using co-culture of *saccharomyces cerevisiae* and *aspergillus niger*", ***Science World Journal***, Vol. 14, No. 1, (2019), 107-110. (https://www.ajol.info/index.php/swj/article/view/208454).

71. Madu, J.O. and Agboola, B.O., "Bioethanol production from rice husk using different pretreatments and fermentation conditions", ***3 Biotech***, Vol. 8, No. 1, (2018), 1-6. (https://doi.org/10.1007/s13205-017-1033-x).

72. Vohra, M., Manwar, J., Manmode, R., Padgilwar, S. and Patil, S., "Bioethanol production: Feedstock and current technologies", ***Journal of Environmental Chemical Engineering***, Vol. 2, No. 1, (2014), 573-584. (https://doi.org/10.1016/j.jece.2013.10.013).

73. Mojović, L., Pejin, D., Grujić, O., Markov, S., Pejin, J., Rakin, M., Vukašinović, M., Nikolić, S. and Savić, D., "Progress in the production of bioethanol on starch-based feedstocks", ***Chemical Industry and Chemical Engineering Quarterly***, Vol. 15, No. 4, (2009), 211-226. (https://doi.org/10.2298/CICEQ0904211M).

74. Ingale, S., Joshi, S.J. and Gupte, A., "Production of bioethanol using agricultural waste: Banana pseudo stem", ***Brazilian Journal of Microbiology***, Vol. 45, No. 3, (2014), 885-892. (http://europepmc.org/article/PMC/4204973).

75. Akponah, E.A. and Akpomie, O.O., "Analysis of the suitability of yam, potato and cassava root peels for bioethanol production using saccharomyces cerevisae", ***International Research Journal of Microbiology (IRJM)***, Vol. 2, No. 10, (2011), 393-398. (https://www.interesjournals.org/articles/analysis-of-the-suitability-of-yam-potato-and-cassava-root-peels-for-bioethanol-production-using-saccharomyces-cerevisae.pdf).

76. Aiyejagbara, M., Aderemi, B., Ameh, A., Ishidi, E., Aiyejagbara, E., Ibeneme, U. and Olakunle, M.S., "Production of bioethanol from elephant grass (pennisetum purpureum) stem", ***International Journal of Innovative Mathematics, Statistics & Energy Policies***, Vol. 4, No. 1, (2016), 1-9. (http://seahipaj.org/journals-ci/mar-2019/mar-2016/IJIMSEP/full/ IJIMSEP-M-1-2016.pdf).

77. Nyachaka, C.J., Yawas, D.S. and Pam, G.Y., "Production and performance evaluation of bioethanol fuel from groundnuts shell waste", ***American Journal of Engineering Research (AJER)***, Vol. 2, No. 12, (2013), 303-312. (http://www.ajer.org/papers/v2(12)/ZH212303312.pdf).

78. Juwon, O.E. and Oluwatoyin, O.F., "Production of bioethanol from selected lignocellulosic agrowastes", ***Journal of Advances in Biology & Biotechnology***, Vol. 21, No. 2, (2019), 1-17. (https://doi.org/10.9734/jabb/2019/v21i230089).

79. Charanchi, A., Musa, S.A. and Hussaini, I.M., "Studies on bioethanol production from rice stalk using co-cultures of *aspergillus niger* and *saccharomyces cerevisiae*", ***UMYU Journal of Microbiology Research (UJMR)***, Vol. 3, No. 2, (2018), 88-95. (https://www.umyu.edu.ng/ujmr/images/ujmr_dec18/UJMR%203_2%202018_014.pdf).

80. Stanley, H.O., Erewa, A.O. and Ariole, C.N., "Feasibilitiy study of bioethanol production: A case of spent mushroom and waste paper as potential substrate", ***Biotechnology Journal International***, Vol. 22, No. 3, (2019), 1-8. (https://doi.org/10.9734/bji/2018/v22i330057).

81. Ajibola, F.O., Edema, M.O. and Oyewole, O.B., "Enzymatic production of ethanol from cassava starch using two strains of *saccharomyces cerevisiae*", ***Nigerian Food Journal, Official Journal of Nigerian Institute of Food Science and Techonology***, Vol. 30, No. 2, (2012), 114-121. (https://doi.org/10.1016/S0189-7241(15)30044-8).

82. Betiku, E. and Alade, O.S., "Media evaluation of bioethanol production from cassava starch hydrolysate using *saccharomyces cerevisiae*", ***Energy Sources, Part A: Recovery, Utilization and Environmental Effects***, Vol 36, No. 18, (2014), 1990-1998. (https://doi.org/10.1080/15567036.2011.557690).

83. Braide, W., Kanu, I., Oranusi, U. and Adeleye, S., "Production of bioethanol from agricultural waste", ***Journal of Fundamental and Applied Sciences***, Vol. 8, No. 2, (2016), 372. (https://doi.org/10.4314/jfas.v8i2.14).

84. Umo, A., Egemba, K., Bassey, E. and Etuk, B., "Optimization of the ethanol fermentation of cassava wastewater using response surface method", ***Global Journal of Engineering Research***, Vol. 12, No. 1, (2013), 13-23. (https://doi.org/10.4314/gjer.v12i1.2).

85. Etudaiye, H., Ukpabi, U., Egesi, E. and Ikpeama, A., "Evaluation of flour and starch qualities from three cassava varieties for ethanol production using a novoenzyme and a strain of dried *saccharomyces cerevisiae* (yeast)", ***Annals of Advanced Agricultural Sciences***, Vol. 4, No. 1, (2020), 1-7. (https://doi.org/10.22606/as.2020.41001).

86. Balat, M., "Production of bioethanol from lignocellulosic materials via the biochemical pathway: A review", ***Energy Conversion and Management***, Vol. 52, No. 2, (2011), 858-875. (https://doi.org/10.1016/j.enconman.2010.08.013).

87. Nwuche, C.O., "Preliminary evaluation of sensitivity of *saccharomyces cerevisiae* lc 269108 to thermal and ethanol stresses in fermentation of agro-wastes for bioethanol production", ***Nigerian Journal of Biotechnology***, Vol. 36, No. 1, (2019), 122-129. (https://doi.org/10.4314/njb.v36i1.16).

88. Misau, I.M., Bugaje, I.M., Mohammed, J., Mohammed, I.A. and Diyau'deen, B.H., "Production of bio-ethanol from sugarcane: A pilot scale study in Nigeria", ***International Journal of Engineering Research and Applications (IJERA)***, Vol. 2, No. 4, (2012), 1142-1151. (https://www.academia.edu/3858133/Production_Of_Bio_Ethanol_From_Sugarcane_A_Pilot_Scale_Study_In_Nigeria).

89. Izah, S.C. and Ohimain, E.I., "Bioethanol production from cassava mill effluents supplemented with solid agricultural residues using bakers' yeast (*saccharomyces cerevisiae*)", ***Journal of Environmental Treatment Techniques***, Vol. 3, No. 1, (2015), 47-54. (https://www.cabdirect.org/cabdirect/abstract/20153245899).

90. Ogbonna, C.N. and Okoli, E.C., "Evaluation of the potentials of some cassava varieties in Nigeria for bio-ethanol production", ***Bio-Research***, Vol. 8, No. 2, (2010), 674-678 (https://doi.org/10.4314/br.v8i2.66888).

91. Ndubuisi, I.A., Nweze, J.E., Onoyima, N.J., Yoshinori, M. and Ogbonna, J.C., "Ethanol production from cassava pulp by a newly isolated thermotolerant LC375240", ***Energy and Power Engineering***, Vol. 10, No. 10, (2018), 457-474. (https://doi.org/10.4236/epe.2018.1010029).

92. Nogueira, T., de Sales Cordeiro, D., Abarza Muñoz, R.A., Fornaro, A., Miguel, A.H. and de Fatima Andrade, M., "Bioethanol and biodiesel as vehicular fuels in Brazil—Assessment of atmospheric impacts from the long period of biofuels use", Biofuels-Status and Perspective, InTech, (2015). (https://www.intechopen.com/chapters/49145).

93. ATC, "Fuel additives: Use and benefits", (2013). (https://www.atc-europe.org/public/Doc113%202013-10-01.pdf).

94. National Geography, "Biofuels, from ethanol to biodiesel, facts and information", (2021). (https://www.nationalgeographic.com/environment/article/biofuel), (Accessed: 18 March 2021).

95. Ajayi, O.O., Onifade, K.R., Onadeji, A. and Oyegoke, T., "Techno-economic assessment of transforming sorghum bagasse into bioethanol fuel in Nigeria: 1-Process modeling, simulation, and cost estimation", ***Journal of Engineering Studies and Research***, Vol. 26, No. 3, (2020), 154-164. (https://doi.org/10.29081/jesr.v26i3.219).

96. Nwofe, P.A., "Utilization of solar and biomass energy-apanacea to energy sustainability in a developing economy", ***International Journal of Energy and Environmental Research***, Vol. 2, No. 3, (2014), 10-19. (https://www.eajournals.org/journals/international-journal-of-energy-and-environmental-research-ijeer/vol-2issue3september-2014/utilization-solar-biomass-energy-panacea-energy-sustainability-developing-economy/).

97. Agba, A.M.O., Ushie, M.E., Abam F.I., Michael S.A. and James, O., "Developing the biofuel industry for effective rural transformation in Nigeria", ***European Journal of Scientific Research***, Vol. 40, No. 3, (2010), 441-449. (https://www.researchgate.net/publication/278329081_Developing_the_Biofuel_Industry_for_Effective_Rural_Transformation_in_Nigeria).

98. Adegbite, O., Oni, O. and Adeoye, I., "Competitiveness of pineapple production in Osun State, Nigeria", ***Journal of Economics and Sustainable Development***, Vol. 5, No. 2, (2014), 205-214. (https://core.ac.uk/download/pdf/234646236.pdf).

99. Ndukwe, C., Okwesili, J. and Chidi. I.N., "Urban solid waste management and environmental sustainability in Abakaliki urban, Nigeria", ***European Scientific Journal***, Vol. 12, No. 23, (2016), 160. (https://doi.org/10.19044/esj.2016.v12n23p155).

100. NBS (2017-2019), "Survey of agricultural produces & annual abstract of statistics", NBS Abuja, (2017). (https://www.nigerianstat.gov.ng/).

101. NBS, "National survey on agricultural exportable commodities collaborative survey", National Bureau of Statistics, Central Bank of

Nigeria, Federal Ministry of Agriculture & Rural Development and Federal Ministry of Trade & Investment, (2013). (http://nigeria.countrystat.org/documents/detail/en/c/454826/).

102. Knoema Nigeria, "Total primary energy consumption", World Data Atlas/Nigeria/Energy Report, (2018). (https://knoema.com/atlas/Nigeria/Primary-energy-consumption).

103. Wikipedia, "Process simulation", (2021). (https://en.wikipedia.org/wiki/Process_simulation), (Accessed: 27 March 2021).

104. Adeniyi, A.G. and Ighalo, J.O., "Computer-aided modeling of thermochemical conversion processes for environmental waste management", Handbook of Environmental Materials Management, Springer International Publishing, (2020), 1-16. (https://doi.org/10.1007/978-3-319-58538-3_185-1).

105. Ashok, K.V., Process modelling and simulation in chemical, biochemical and environment, CRC Press, (2015).

106. Oyegoke, T., Sardauna, M.Y., Abubakar, H.A. and Obadiah, E., "Exploration of biomass for the production of bioethanol: A process modelling and simulation study", ***Renewable Energy Research and Application***, Vol. 2, No. 1, (2021), 1-10. (https://doi.org/10.22044/RERA.2020.10287.1042).

107. Oyegoke, T., Obadiah, E., Mohammed, Y.S., Bamigbala, O.A., Owolabi, O.A., Geoffrey, T.T., Oyegoke, A. and Onadeji, A., "Exploration of biomass for the production of bioethanol: A techno-economic feasibility study of using rice (oryza sativa) husk", ***Renewable Energy Research and Application***, Online (2022), Article-in-press, 1-19. (https://doi.org/10.22044/RERA.2020 .10288.1043).

108. Misau, M.I., Muhammad, B.I., Ali, M.I. and Jibril, M., "Design and construction of a bioethanol pilot plant in Nigeria", ***Journal of Applied Phytotechnology in Environmental Sanitation***, Vol. 3, No. 1, (2014), 11-16. (https://www.researchgate.net/publication/294086101_DESIGN_AND_CONSTRUCTION_OF_A_BIO-ETHANOL_PILOT_PLANT_IN_NIGERIA).

109. Oyegoke, T., Ajayi, O.O. and Kolawole, R.O., "Techno-economic assessment of transforming sorghum bagasse into bioethanol fuel in Nigeria: 2-Economic analysis", ***Proceedings of the 2nd AfroBiotech Conference***, Black Lives Matter in Science, Engineering and Medicine; AIChE, (2020). (https://www.researchgate.net/publication/345750944_Techno-economic_Assessment_Of_Transforming_Sorghum_Bagasse_Into_Bioethanol_Fuel_In_Nigeria_2_-Economic_Analysis).

110. Evuensiri O.O., Victor, I., Obiora, N., Akachukwu, B.E. and Ekpe, M.N.O., "Bioethanol production from corn stover using *saccharomyces cerevisiae*", ***International Journal of Scientific & Engineering Research***, Vol. 7, No. 8, (2016), 290-293. (https://www.ijser.org/onlineResearchPaperViewer.aspx?Bioethanol-production-from-corn-stover-using-Saccharomyces-cerevisiae.pdf).

111. Oyegoke, T., Obadiah, E., Mohammad, S.Y., Bamigbala, O.A., Owolabi, O.A., Oyegoke, A., Onadeji, A. and Mantu, A.I., "Exploration of biomass for the production of bioethanol: Economic feasibility and optimization studies of transforming maize cob into bioethanol as a substitute for fossil fuels", ***Proceedings of 29th European Biomass Conference and Exhibition***, Maselle, France, (2021), 1270-1275. (https://doi.org/10.5071/29THEUBCE2021-4BV.9.13).

112. Akpomie, O.O., "Bio-ethanol production from cassava effluent using zymomonas mobilis and *saccharomyces cerevisiae* isolated from rafia palm (elaesis guineesi) SAP", ***Pelagia Research Library, European Journal of Experimental Biology***, Vol. 3, No. 4, (2013), 247-253. (https://www.imedpub.com/abstract/bioethanol-production-from-cassava-effluent-using-zymomonas-mobilis-and-saccharomyces-cerevisiae-isolated-from-rafia-palm-elaesis-guineesi-sap-14787.html).

Journal of Renewable Energy and Environment

Journal Homepage: www.jree.ir

Materials and Energy Research Center

MERC

Research Article

The Effect of Roof Integrated Photovoltaic (RIPV) on Building Indoor Air in African Tropical Climate

Aloys Martial Ekoe A. Akata*

Department of Physics, Faculty of Science, University of Douala, P. O. Box: 2701, Douala, Cameroon.

PAPER INFO

Paper history:
Received: 28 November 2020
Revised in revised form: 21 February 2021
Scientific Accepted: 12 March 2021
Published: 21 November 2021

Keywords:
Building Integrated Photovoltaic (BIPV),
Thermal Comfort,
Heat Transfer,
Indoor Air Temperature,
Photovoltaic,
Solar Roof

ABSTRACT

Photovoltaic energy has the potential to become one of the major energy sources used in the households in the tropical region of Africa, where the solar radiation intensity is abundant and almost constant over the year. Solar photovoltaic systems present many advantages when they are integrated in the building structure envelope and have a significant influence on the indoor air temperature of dwelling buildings due to the thermal resistance modification. In this paper, a simplified model of the photovoltaic system integrated on the roof of a residential building according to the building construction customs and materials has been designed and modeled. The heat transfer is studied in several situations: with and without a Building Integrated Photovoltaic (BIPV) system and for a building with and without false ceiling. The BIPV system installed over an effective area of 35 m^2 increases the building indoor air temperature of approximately 5 °C which is corrected by the heat insulation optimization of the false ceiling made up with building local materials. The final indoor air temperature obtained is in good agreement with the ASHRAE standards and can, therefore, be applied to tropical regions.

https://doi.org/10.30501/jree.2021.259138.1166

1. INTRODUCTION

Tropical countries are situated between latitude +15 °C and -15 °C and are extended to the warm and humid zones of Central Africa, Central America, southern Asia, and northern South America; temperatures range between 24 and 33 °C and the humidity may be frequently between 60 and 100 %. The tropical climate is expanded on to three different continents: Oceania, Asia, and Africa. Hence, the energy consumption of a building in a tropical climate of each of these continents is not automatically identical, but is closely related to the geographical location of the country. In Australia, air conditioning (space heating and/or cooling) is the main source of energy consumption (35 %) followed by residential appliances (24 %), water heating (23 %), and lighting (7 %) [1]. As Australia is located in the tropical region of Oceania where in the south regions of Australia, the winter is mild and the summer hot and the temperatures oscillate between 10 and 21 °C. Hence, the comfort resumes to increase the indoor air temperature. An opposite perception of the thermal comfort exits in Malaysia and other East Asia countries, where the comfort resumes to lower the indoor air temperature. Concerning the country of Cameroon, to meet the needs of an increasing energy demand remains a mission accomplished to a lesser extent; despite setting up new energy sources such as power gas stations and steam-generating stations, the cover of the national territory in electric power still remains low enough, about less than 50 % and 10 % in urban and rural areas, respectively. This is due to the great distance between the production and consumption sites, hence inducing a significant energy loss during its transport representing almost 30 % of the electric power produced [2]. From the analysis made on tropical countries, a focus can be made on the two following problems: 1) Reducing the energy consumption of the residential building used for space cooling; 2) Reducing the dependence of traditional (non-renewable) energy sources. A common solution to these two problems can be found: the use of renewable energy.

1.1. Photovoltaic systems

Renewable energies refer to energy sources that are renewed quickly enough to be considered as inexhaustible on the human scale. There are many types of renewable energies: solar energy, wind energy, biomass energy, hydraulic energy, etc. As their use has a negligible impact on our environment, the conception of a sustainable development passes through an increasing implementation of renewable energy sources. Among the renewable energy sources, solar energy has the capacity to become one of the major energy sources in tropical climates. Solar energy should therefore constitute the real source of electrical production and thermal energy in all sectors, particularly the residential sector because of its on-site production. Indeed, Chen et al. [3] claimed that from incident

*Corresponding Author's Email: ekoealoys@yahoo.fr (A.M. Ekoe A. Akata)
URL: https://www.jree.ir/article_140549.html

Please cite this article as: Ekoe A. Akata, A.M., "The effect of roof integrated photovoltaic (RIPV) on building indoor air in African tropical climate", ***Journal of Renewable Energy and Environment (JREE)***, Vol. 9, No. 1, (2022), 53-62. (https://doi.org/10.30501/jree.2021.259138.1166).

solar radiation, measured in the city of Brazl, in the period of 2007 to 2012, they obtained an average power generation of 11.0 kWh/day and efficiency of the modules in the order of 12.6 %.

In the past, it was common to lay PV panels on the roof of the already designed building; this concept is called Building Applied Photovoltaic (BAPV) [4]. This solution was not very adequate as it was necessary to spend both for the roof and PV panels; in addition to that, the increasing temperature of the PV panels leads to a reduction in their efficiency [5]. All that contributed to the elaboration of the BIPV concept, i.e., the solar photovoltaic system was integrated in the structure of the building envelope. PV panels, therefore, replace a part of the materials used in the construction of the building roof [6]. It is also possible to integrate photovoltaic to the walls. This concept enables to make savings on building materials and space integration. To maintain the PV panels' temperature to a value enabling their optimal functioning, the idea of the hybrid PV/T solar collector was put forward. Chow et al. [7] proposed an aluminum-alloy flat-box type PVT collector using water as the coolant fluid and the fin efficiency approached unity, leading to the thermal efficiency of 57.4 %. Ekoe et al. [8] proposed as solution the setting-up of fins on the back sheet of the photovoltaic module of the Building Integrated Semitransparent PhotoVoltaic Thermal system (BISPVT) system; the heat extracted from the air circulating in the rectangular duct at the back sheet of the PV module can be used to warm the building indoor air temperature. An annual production of 76.66 kWh of thermal energy at an overall thermal efficiency rate of 56.07 % is obtained with a system area of 36 m^2. They thus arrived to the same conclusions as Maturi et al. [9] who got the same results experimentally. The so-extracted energy can be used in electric power production and also, the thermal energy can be used to warm the building indoor air temperature and to produce hot domestic water. The so-used sensor is called a PhotoVoltaic Thermal (PV/T) sensor. This concept developed by the authors of [10-12] has shown its effectiveness. Even though energy production through PV systems is important, the indoor air quality of the building is another aspect that should be considered carefully.

1.2. The effect of PV on thermal comfort of a building

The results obtained from various researches show that proper ventilation and the absence of airtight devices, installed to reduce energy consumption, favor the indoor/outdoor air exchange and thus contribute to the enhancement of Indoor Air Quality. Several studies have been carried out to quantify the impact of a solar photovoltaic system on the building indoor air temperature and humidity (Iath). Benradouane et al. [13] designed and adapted a thermo-solar house on the site of Tlemcen, Algeria which allows a significant storage of the heat coming from solar rays in order to do cancel the use of auxiliary energy sources. They found that South, East, and West orientations facilitated obtaining good results. Obeng et al. [14] conducted a study in the rural households of Ghana as they depended mainly on kerosene lanterns for lighting after sunset. They compared households with and without solar PV in off-grid rural Ghana and came to two major conclusions: firstly, the proportion of household members being affected by indoor smoke from kerosene lanterns could be reduced by 50 % thanks to the use of solar PV lighting. Secondly, solar PV lighting can probably reduce the proportion of household members who get blackened nostrils from soot associated with kerosene lanterns by approximately a third. These conclusions reflect the reality as during their operation, PV panels produce no air pollution, hazardous waste, or noise.

In order to analyze the comfort aspect (thermal and lighting aspects) of PV modules and PV systems for vertical integration, Lopez et al. [15] presented a work dealing with the specific design of the test facility and the methodology employed for BIPV reproducing the internal conditions of a real building. The temperatures they obtained during the conducted experiments never went above the interval 23 °C and 27 °C as specified by the "European Adaptive Standard", EN 15251:2007-08, but were sometimes below the minimum specified value. Green buildings not only provide an improved worker productivity and work quality as a result of a more comfortable office environment, but also an improved public health resulting from reduced indoor air pollution. Wen I-Jyh et al. [16] conducted a study where they designed a ventilated BIPV with a double roof structure in order to introduce indoor ventilation and also provide itself with environmental control. From the results obtained, they concluded that both ventilated BIPV designs proposed in this study can provide appropriate indoor thermal environments.

Two other research works deserve to be mentioned. The first one is the study done by Dominguez et al. [17] who quantified the indirect benefits of a photovoltaic roof for the insulation of the cement roof of the Powell Structural systems Laboratory (PoSL) at the University of San Diego, California. The heat flux modeling of theirs has shown a significant reduction in daytime roof heat flux under the PV array, while at night, the conditions reversed. They have thus obtained a 5.9 $kWhm^{-2}$ (or 38 %) reduction in annual cooling load. The second one comes from Ekoe et al. [18] who studied the influence of the integration of solar systems in the envelope structure of the building on the indoor air temperatures and humidity of a building under the tropical climatic conditions of Yaoundé, Cameroon. They have found that BIPV increases the building's indoor air temperature by 4°C, when compared to a building of the same size without PV integrated. They have also shown that a judicious choice of the building materials and the orientation of the building allow minimizing that temperature difference. Among these two options, the choice of the building materials is the solution accessible to everyone.

1.3. False ceiling in tropical regions

Various techniques can be used to improve the thermal comfort of a building, namely the HVAC system, energy production, and the elements of the building's envelope. The appropriate use of such techniques depends on the typology of the building, the construction habits, and climatic conditions of the area. The studies on the rational use of energy in buildings located in tropical regions have been focused on the reduction of energy consumption in buildings through the optimum utilization of the thermal insulation of the envelope. In the case of Cameroon, the main source of energy consumption is air conditioning followed by lighting. Therefore, the thermal comfort resumes to the lowering of the indoor air temperature. This can be efficiently achieved by increasing the thermal inertia of the building through the use of a false ceiling.

In the Cameroonian context, the false ceiling is a solid and horizontal surface that closes up a living room parallel to the floor. It is made up of local materials, especially wood. The false ceiling is used for decoration of the building and the hiding of electric cables. It can also be used for the installation of ceiling fans; people are used to employ ceiling light in order to obtain a better lighting than when the lamps are fixed on the wall. The space between the false ceiling and the roof is referred to as the dead space. The air contained in the dead space greatly influences the indoor comfort. Indeed, a great part of the heat gained by the building is done through the elements of the roof. Normally, almost all the heat is transferred to the building, resulting in indoor thermal discomfort. Hence, the use of the false ceiling increases the thermal inertial of the building, reduces the thermal heat transferred in the leaving space, and produces more comfortable conditions for the occupants of the building. As wood is among the local building materials, its use as false ceiling is the ideal solution to obtain comfortable indoor air conditions.

The authors [19] established a transient 1-D model to study the role of such a ceiling in the reduction of the ambient indoor air temperature. The use of false ceiling only without reflector sheet reduced the heat gain introduced to space for a whole day by 66.8 %, while the use of a false ceiling with reflector sheet increased the reduction percentage of heat gained from the concrete roof to be 81.6 % during the same period. However, the building that they have studied did not have PV panels, the roof was made up of concrete and the temperature of the building was controlled.

Basically, the roof of the building can be described as the upper part of the envelope which protects the building against the climatic elements that could be harmful to the inhabitants of the building. The climatic elements include sun light, rain, birds excrement, etc. The materials used in the roof construction vary from one geographical area to another. In the tropical sub-Saharan African climate and specifically in urban zones, the roofs are mainly made up of Aluminum due to its reflecting properties. The Aluminum sheets are fixed with wooden slats to prevent them from getting carried away by wind. This construction style is reproduced in almost all the buildings in urban areas. Concerning buildings with many floors, such roof is used to cover the last floor of the building. However, due to the conducting properties of Aluminum, a great part of the heat absorbed by the roof is transferred to the floor of the building. To reduce the quantity of heat transferred to the floor of the building, the simple roof, i.e., the roof made only of steel, can be completed by the addition of the false ceiling in order to provide pleasant indoor conditions to the occupants of the building. In this paper, the simple roof refers to a roof made up of only Aluminum, while the term roof indicates the unit made up of the Aluminum, the dead space, and the false ceiling.

Our study comes after all those studies and focuses on two important aspects: the presence or not of false ceiling and PV panels on the roof of the building, and their influence on the indoor air temperature and humidity. Modeling of the roof heat flow through the different elements of the envelope of the building has been done for a tropical climate of Cameroon in order to characterize the comfort conditions inside the building according to those aspects.

2. PROBLEM IDENTIFICATION

In Cameroon, the energy used for building lighting represents almost 20 % of the energy consumption in the residential sector and almost 25 % in offices and commercial buildings. The electric power produced by the BIPV system could be used for the lighting of the building, the corridor, and the outside light; however, this paper does not focus on the electric power which can be produced by the BIPV system. The building under consideration is situated in Yaoundé at 4.051N, 9.768E, and a site altitude of 103 m. The size of the building is 15 m × 11 m with an average height of 6.5 m. The roof is south oriented. The building is insulated by a layer of sand, cement, and paint. The Photovoltaic system is integrated at the roof top covering an effective area of 450 m^2. The BIPV system is made of polycrystalline PV modules. The BIPV system, area of 35 m^2, and made up of 20 PV modules and peak power of 4 kWh is oriented in opposite direction with the wind in order to optimize the natural convection. Moreover, the space left between the false ceiling and the roof (dead space) also takes part in the temperature lowering of the ambient air of the building. Thus, the height of the false ceiling can be chosen as 0.75 m with a thickness of 4 mm, depending on the other dimensions of the building.

3. MODELLING OF ROOF PV

As envisaged in the summary and the introduction, several cases will be studied, as shown in Figure 1:

1. The building does not have a false ceiling nor PV panels (A);
2. The building has a false ceiling, but lacks PV panels (B);
3. The building has a false ceiling and a Semitransparent Photovoltaic system is integrated as the roof top (C).

The following assumptions have been made in order to write the energy balance equations:

a. A one-dimensional heat conduction is considered in the present study;
b. The system under consideration is in quasi-steady state;
c. The incident solar radiation is uniform on both sides of the roof;
d. The building is considered as one piece without internal heat source;
e. Air properties are constant with time and temperature.

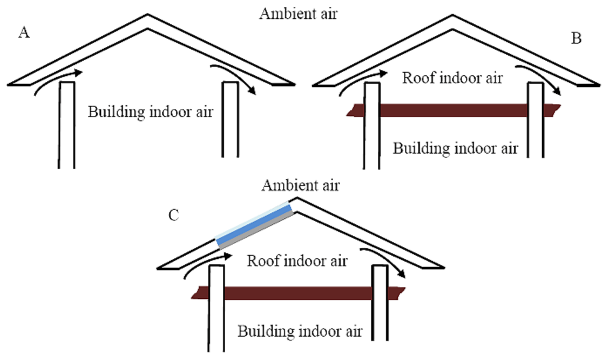

Figure 1. Pictorial view of the different cases studied, A) without BIPV system and false ceiling; B) false ceiling, without BIPV system; C) with BIPV system and ceiling false ceiling

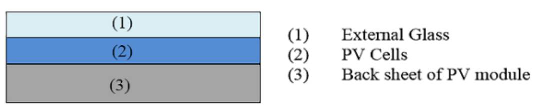

Figure 2. Pictorial view of studied BIPV module

3.1. Simple roof

Figure 1A shows a pictorial view of the building in the absence of the false ceiling and the BIPV system. Following Figure 1A, the energy balance for each component of the thermal system is:

Roof

On the outer surface of the roof, the equation expressing the energy balance is:

$$\left(T_s-T_r\right)/R_r=A_r\alpha_r I(t)+h_0A_r\left(T_a-T_s\right) \tag{1}$$

By replacing each term by its expression, we have obtained the expression of temperature on the outer surface of the roof:

$$T_s=\left\{T_r+R_r\left[A_r\alpha_r I\left(t\right)+h_0A_r\right]\right\}/\left[1+h_0A_rR_r\right] \tag{2}$$

On the inner surface of the roof, the equation expressing the energy balance is:

$$\left(T_s-T_r\right)/R_r=h_{i,roof}A_r\left(T_r-T_{in}\right) \tag{3}$$

By replacing each term by its expression, we have obtained the expression of temperature on the inner surface of the roof:

$$T_r=\left[T_s+T_{in}h_{i,roof}A_rR_r\right]/\left[1+h_{i,roof}A_rR_r\right] \tag{4}$$

The expression of the heat flux getting in the building through the roof is given by:

$$\varphi_1=\left(T_a-T_{in}\right)/\left[\left(1/h_0\right)+\left(e_{al}/k_{al}\right)+\left(1/h_{i,roof}\right)\right] \tag{5}$$

Ambient air of the building

The energy balance equation for the ambient air in the building is given by:

$$\dot{m}_r C_{air}\frac{dT_{in}}{dt}=\left(T_a-T_{in}\right)\begin{bmatrix}K_{11}+AU_0\\ -0.33N_0\dot{V}+K_{12}\end{bmatrix}+h_{i,roof}A_r(T_r-T_{in}) \tag{6}$$

Upon solving Eq. (6) and applying the initial condition $T_{in}\left(t=0\right)=T_{in,\ initial}$, the building air temperature is obtained as follows:

$$T_{in}=\left(F_{in1}/G_{in1}\right)+\left[T_{in_{initial}}-\left(F_{in1}/G_{in1}\right)\right]\exp\left(-G_{in1}t\right) \tag{7}$$

3.2. Roof with false ceiling

Figure 1B shows a pictorial view of the building having a false ceiling in the absence of a BIPV system. The major difference between Case 3.1 and Case 3.2 is the reduction of heat transferred to the leaving space due to the presence of the false ceiling to the building. Following Figure 1B, the energy balance for each component of the thermal system is as follows:

Roof

i. On the outer surface of the roof, by applying the first principle of thermodynamics, the equation of the energy balance is the same as that in Case 3.1.

ii. On the inner surface of the roof, by applying the first principle of thermodynamics and replacing each term by its expression, we have obtained the expression of temperature on the inner surface of the roof:

$$T_r=\left(T_s+T_{av}h_{i,av}A_rR_r\right)/\left(1+h_{i,av}A_rR_r\right) \tag{8}$$

False ceiling air temperature

The energy balance equation for the ambient air in the false ceiling is given by:

$$\dot{m}_r C_{air}\frac{dT_{av}}{dt}=\left(T_a-T_{av}\right)K_{21}-\left(T_{av}-T_{in}\right)K_{22}+h_{i,av}A_r(T_r-T_{av}) \tag{9}$$

By integrating Eq. (9) and applying the initial condition $T_{av}\left(t=0\right)=T_{av_{initial}}$, the false ceiling air temperature is obtained as follows:

$$T_{av}=\left(F_{av1}/G_{av1}\right)+\left[T_{av_{initial}}-\left(F_{av1}/G_{av1}\right)\right]\exp\left(-G_{av1}t\right) \tag{10}$$

The expression of the heat flux getting in the building through the roof is given by:

$$\varphi_2=US\left(\Delta T\right)=\left(T_a-T_{in}\right)\bigg/\left\{\begin{matrix}\left(1/h_0\right)+\left(e_{al}/k_{al}\right)+\left(1/h_{i,av}\right)\\ +\left(e_{cpl}/k_{cpl}\right)+\left(1/h_{i,in}\right)\end{matrix}\right\} \tag{11}$$

Ambient air of the building

The energy balance equation for the air in the building is given by:

$$\begin{aligned}\dot{m}_r c_{air}\frac{dT_{in}}{dt} &= q_{wall}+q_{floor}+q_{openings}\\ &-q_{air,replenishement}+q_{false\_ceiling}\end{aligned} \tag{12}$$

By replacing each term by its expression and applying the initial condition $T_{in}\left(t=0\right)=T_{in_{initial}}$, the building ambient air temperature is obtained as follows:

$$T_{in}=\left(F_{in2}/G_{in2}\right)+\left[T_{in_{initial}}-\left(F_{in2}/G_{in2}\right)\right]\exp\left(-G_{in2}t\right) \tag{13}$$

3.3. PV roof with false ceiling

Figure 1C shows a pictorial view of the building having a false ceiling and a BIPV system, while Figure 2 shows a pictorial view of the PV collector. The major difference between Case 3.3 and case 3.2 is the roof heat flux which will differ, due to the addition of the PV modules to the roof of the building. Following Figure 1C, the energy balance for each component of the thermal system is as follows:

PV module

At the glass cover of the photovoltaic module, by applying the first principle of thermodynamics, the equation of the energy balance is:

$$-\tau_g I(t)+\alpha_g I(t)+\left(k_g/e_g\right)\left[A_r\left(T_c-T_g\right)-h_0A_r\left(T_g-T_a\right)\right]=0 \tag{14}$$

By replacing each term by its expression, we have obtained the expression of temperature at the Glass cover of the photovoltaic module:

$$T_g = \left[\begin{matrix} I(t)(\alpha_g - \tau_g) \\ +(k_g/e_g)T_c + h_0 T_a \end{matrix} \right] \Big/ \left[(e_g/k_g) + (1/h_0) \right]^{-1} \tag{15}$$

At the Solar cell of the photovoltaic module, by applying the first principle of thermodynamics, the equation of the energy balance is as follows:

$$\begin{aligned} &\tau_g\alpha_c\beta_c I(t) + \tau_g\alpha_T(1-\beta_c)I(t) - \tau_g\alpha_c\beta_c\eta_c I(t) - (k_{bs}/e_{bs})(T_c - T_{bs}) \\ &- \left[(e_g/k_g) + (1/h_0) \right]^{-1} (T_c - T_a) = 0 \end{aligned} \tag{16}$$

By replacing each term by its expression, we have obtained the expression of temperature at the Solar cell of the photovoltaic module:

$$T_c = \frac{\left[\left(\frac{e_g}{k_g} + \frac{1}{h_0} \right)^{-1} T_a + \left(\frac{e_{bs}}{k_{bs}} \right)^{-1} T_{bs} + (\tau\alpha)_{eff}\, I(t) \right]}{\left[\left(\frac{e_g}{k_g} + \frac{1}{h_0} \right)^{-1} + \left(\frac{e_{bs}}{k_{bs}} \right)^{-1} \right]} \tag{17}$$

At the Back sheet of the PV module, by applying the first principle of thermodynamics, the equation of the energy balance is:

$$h_{cbs}(T_c - T_{bs}) + h_{ibsav}(T_{av} - T_{bs}) = 0 \tag{18}$$

By replacing each term by its expression, we have obtained the expression of temperature at the Back sheet of the PV module:

$$T_{bs} = (h_{cbs}T_c + h_{ibsav}T_{av}) / (h_{cbs} + h_{ibsav}) \tag{19}$$

False ceiling air temperature

The energy balance equation for the air in the air gap is given by:

$$\begin{aligned} m_r c_{air} \frac{dT_{av}}{dt} &= q_{wall,roof} + q_{c\text{-}i} - q_{air,interior} \\ &- q_{air,replenishement} \end{aligned} \tag{20}$$

By proceeding similarly as in Case 4.2, the building air temperature is obtained as:

$$T_{av} = (F_{av3}/G_{av3}) + \left[T_{av_{initial}} - (F_{av3}/G_{av3}) \right] \exp(-G_{av3}t) \tag{21}$$

To compute the expression of the heat flux getting in the building through the roof, Figure 3 illustrates the thermal resistance of the insulation. Following Figure 3, the roof heat flux is obtained by :

$$\begin{aligned} \varphi_3 &= US(\Delta T) = (T_a - T_{in}) / R_{total} \\ R_{total} &= R_{conv_{ext}} + \left\{ 1 / \left[(1/R_{roof}) + (1/R_{BIPV}) \right] \right\} \\ &+ R_{conv_{av}} + R_{cpl} + R_{conv_{in}} \end{aligned} \tag{22}$$

Ambient air of the building

The energy balance equation for the air in the building is given by:

$$\begin{aligned} \dot{m}_r c_{air} \frac{dT_{in}}{dt} &= q_{wall} + q_{floor} + q_{openings} \\ &- q_{air,replenishement} + q_{false\_ceiling} \end{aligned} \tag{23}$$

By replacing each term by its expression and applying the initial condition $T_{in}(t=0) = T_{in_{initial}}$, the building ambient air temperature is obtained as follows:

$$T_{in} = (F_{in2}/G_{in2}) + \left[T_{in_{initial}} - (F_{in2}/G_{in2}) \right] \exp(-G_{in2}t) \tag{24}$$

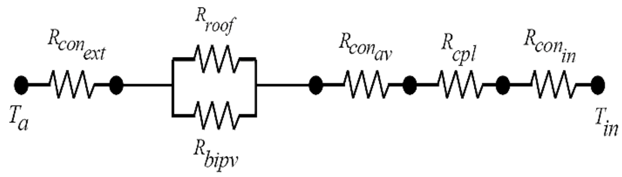

Figure 3. Thermal resistance

4. OPERATING PARAMETERS

In order to obtain the dynamic behavior of the three thermal systems and determine the ambient air temperature of the building, we used hourly global and diffuse solar radiation data over the town of Yaoundé, Cameroon for the year 2016 obtained from the Energy and Environmental Technologies Laboratory of the Department of Physics at the University of Yaoundé I. In addition, the hourly ambient temperature variation from the climatic data issued by the Atmospheric Physics Laboratory was used.

The total solar radiation over inclined roof is obtained using Eq. (25) [20]:

$$I(t) = \left[I_g(t) - I_d(t) \right] R_b + \frac{1}{2}(1+\cos\theta)I_d(t) + \frac{1}{2}(1-\cos\theta)\rho_{alb}I_g(t) \tag{1}$$

1. The equation of the energy balance on the outer surface of the roof is used to obtain the outer roof temperature. The latter is introduced in the equation of the energy balance on the inner surface of the roof in order to have the expression of the inner roof temperature as a function of the temperature of the ambient air of the building.
2. The so-obtained expression is introduced in the equation (differential) of the energy balance of the room to have an analytical expression of the indoor air temperature of the building.
3. A system of equation is therefore obtained and solved numerically with MATLAB R2016b software.
4. The same procedure is repeated for the two other thermal systems, as shown below.
5. The whole procedure is illustrated in Figure 4, including the computation of the roof heat flux.

Design specification and operating parameters of the building are presented in Table 1. These have been used as input parameters for energy analysis.

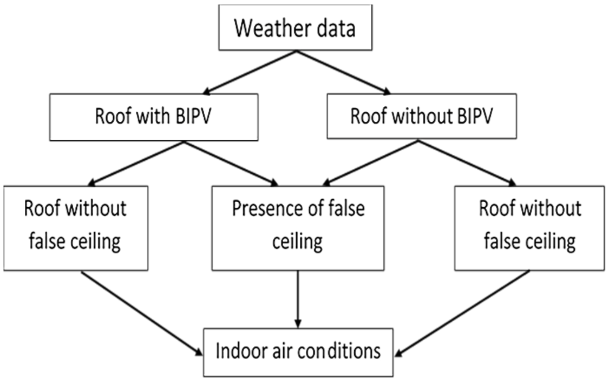

Figure 4. Flow chart of the modeling of the thermal system

Table 1. Design parameters of a building and semitransparent PV module

Parameters	Values
b	6.3 m
d	4.5 m
PV roof area	28.35 m^2
C_f	0.38
C_{air}	1005 J kg^{-1} K^{-1}
α_C	0.9
α_T	0.5
β_C	0.83
τ_g	0.9
η_C	0.12

5. RESULTS AND DISCUSSION

Figure 5 illustrates the variations of average solar radiation and ambient temperature of Yaoundé for the year 2018.

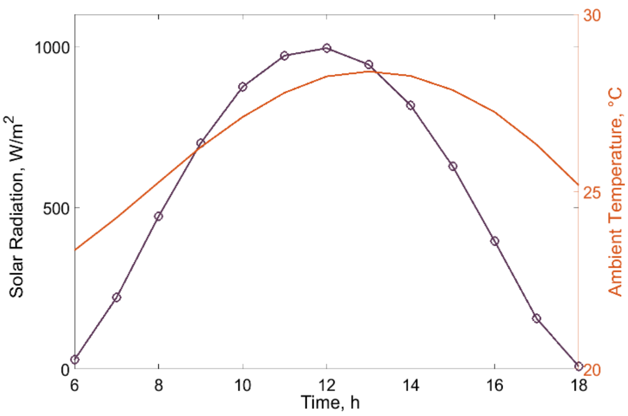

Figure 5. Average solar radiation and ambient temperature

The peak irradiation on the horizontal surface is 994.13 W/m^2 and the peak solar radiation obtained with a tilt angle of 20° South is 992.62 W/m^2. The solar radiation is maximal when the tilt angle is close from the latitude of the location under investigation. However, taking into account the building habits in the tropical climate of Cameroon, a tilt angle of 4° is rarely used for the installation of the roof. This is to avoid the labor cost and work required for cleaning the roof and the photovoltaic system of the horizontal roof. Hence, the solar radiation obtained with a tilt angle of 20° South is used in the rest of this work.

Figure 6 shows the average hourly variations of the average indoor temperature in the case of the roof only. The maximum average indoor air temperature is 30 °C around 12.00 A.M., which is 2 °C higher than the maximum average ambient temperature. This fact can be explained by the weak thermal resistance in the case of a simple roof; the roof is made only of steel; this favors a great heat absorption of heat which will be transferred to the living space.

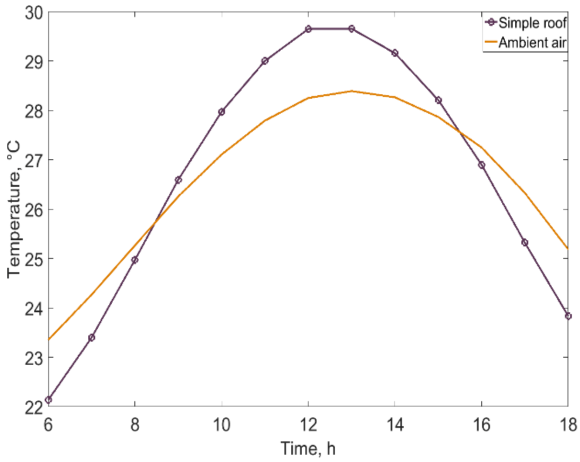

Figure 6. Average indoor air temperature of the building with a simple roof

The introduction of the false ceiling leads to a significant reduction in the room air temperature illustrated in Figure 7; the average maximum value of the indoor air temperature declines to 27.13 °C. The new indoor air temperature is almost 3 °C less than the case of simple roof. This significant temperature reduction is due to the addition of the false ceiling to the roof of the building, as this addition will increase the thermal resistance of the roof.

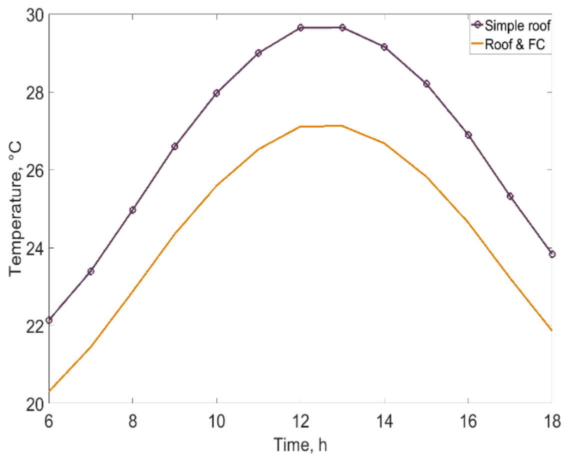

Figure 7. Average indoor air temperature of the building with Simple roof and false ceiling (FC)

The integration of the BIPV system on the roof top of the building, even though beneficial to the building because of the production of electric and thermal power, has the inconvenience of increasing the indoor air temperature of the building, as shown in Figure 8. The average air temperature of 33 °C is obtained. The difference in temperature caused by the introduction of the BIPV in the envelope of the building can be estimated to about 5 °C. Such a temperature may cause uncomfortable conditions for the occupants of the building.

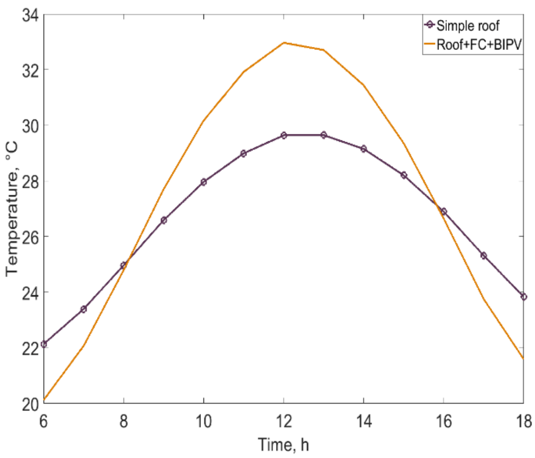

Figure 8. Average indoor air temperature of the building with roof, false ceiling, and the BIPV system

To overcome this inconvenience, a wooden layer can be placed just at the back sheet of the PV module, or the thickness of the false ceiling can be increased. The issue of placing a wooden layer just at the back sheet of the PV module is shown in Figure 9 (a). The average indoor air temperature rise due to the BIPV integration on the roof of the building has been completely reduced when the thickness of the wooden layer is equal to half that of the false ceiling and to an optimal value of 27.1 °C when the thickness of the wooden layer is equal to twice that of the false ceiling, as shown in Figure 9 (b). These results show that a great part of the heat gained by a building is distributed through the envelope of the building and especially the roof, hence succeeding in the reduction of heat transfer through the roof leads to the significant reduction of the heat exchanges between a building and its surroundings, and the consequence is a comfortable temperature of the indoor air of the building.

The results shown in Figure 9 enable us to assert that an increase in the thickness of the wooden layer just at the back sheet of the PV module leads to a greater reduction in the average indoor air temperature of the building. This assertion can be explained by the thermal inertia of building materials which plays a significant role in thermal comfort of the buildings. It is the case of materials as the wood which has weak thermal inertia and is adapted to the climatic zones where one wants to improve the thermal comfort of the interior section of the room. The increase of the wooden layer will certainly cause an increase in the weight of the framework, the latter being expected to firmly support the insulation. Hence, it is essential to correctly dimensionalize the wooden layer, taking into account the rest of the roof and the other elements of the building; this dimensioning will permit to obtain an acceptable weight of the whole framework. The use of an insulation layer placed under the roof can therefore be considered as an interesting solution to lower the indoor air temperature, thereby increasing the thermal comfort of the room in tropical climates. The insulating material is not necessarily the same and the choice of the material may vary from one location to another, but the final aim remains the same. The authors [21] recommend using 50 mm of fibreglass and foil aluminium to respectively reduce the ceiling temperature by about 3 °C and 2 °C in the tropical climate of Malaysia. However, in Cameroon, the use of wood as an insulating material is very common, hence favoring its use in the BIPV system.

The maximum average indoor air temperature of the room obtained with the addition of the wooden layer under the back sheet of the PV module is 27.1 °C, depending on the thickness of the wooden layer. The ideal interval of temperature is 23 to 26 °C in summer, and 20 to 23.5°C in winter, as recommended by the ASHRAE standards. The temperatures obtained from the modelling done in this work are slightly higher than those recommended by the ASHRAE, but these temperatures can be considered as comfortable in a tropical climate of Cameroon, where the subjects accommodate easily to such a temperature as they live in a hot climatic area, and they have adapted their bodies to temperatures greater than 27 °C without the use of an air-condition system, even though 27 °C is considered as hot by the international standards; hence, the important results obtained from our modelling can be applied to the case of Cameroon for the production of electric power using solar radiation.

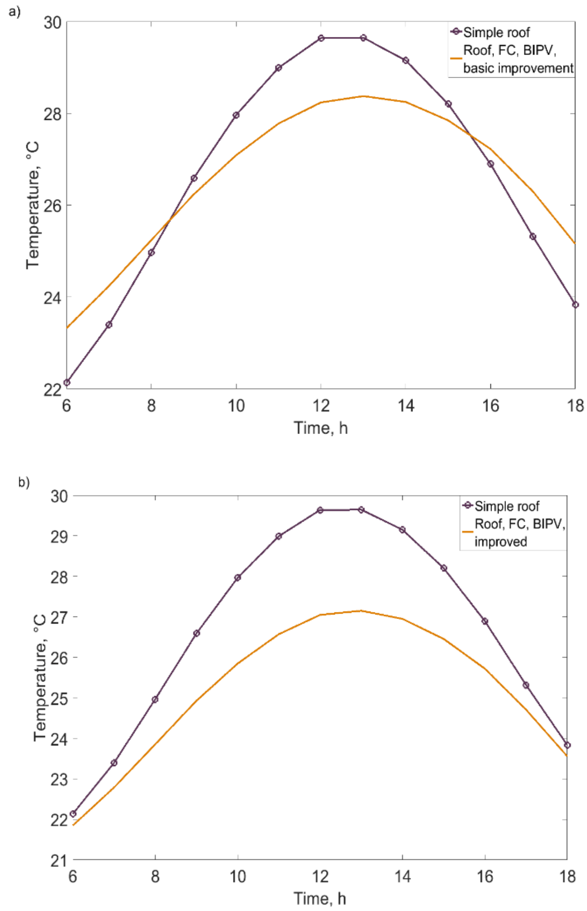

Figure 9. Average indoor temperature of the building with simple roof, false ceiling and the BIPV system when a) the thickness of the wooden layer is equal to half that of the false ceiling; b) the thickness of the wooden layer is equal to double that of the false ceiling

Figure 10 (a) shows that the indoor air temperature could be affected by an increase in the size of the BIPV surface replacing the roof of the building, while Figure 10 (b) focuses on the influence on indoor air temperature with an increase in the speed of the wind in the air in the space between roof and false ceiling in which case the space is not closed. As it can be expected, the temperature will rise if the number of PV panels increases. A quasi-regular increase is observed. The limit will be reached when the whole roof is replaced by PV panels. However, as the present study is done in the tropical climate, such a rise is not too much useful, as the produced heat cannot be used for the heating of the indoor space. Hence, a compromise should be found between the number of PV panels to be installed and the maximum value of the indoor temperature which must not be exceeded. In Figure 10 (b), the speed of the air between roof and false ceiling has, been doubled, resulting in a significant reduction in the maximum temperature of indoor temperature. The maximum indoor temperature reached in the present case is 25.63 °C, a value almost 2 °C less than the one obtained in the previous case. Such result is logic, as an increase in the speed of the air between the roof and the false ceiling will create a fast removal of the heat stocked on the back sheet of PV panels, hence preventing heat from entering in the indoor air space. Therefore, increasing in the speed of the air between the roof and the false ceiling can greatly contribute to the reduction of the indoor air temperature caused by an increase in the size of the BIPV system, thereby improving the thermal comfort of the occupants of the building.

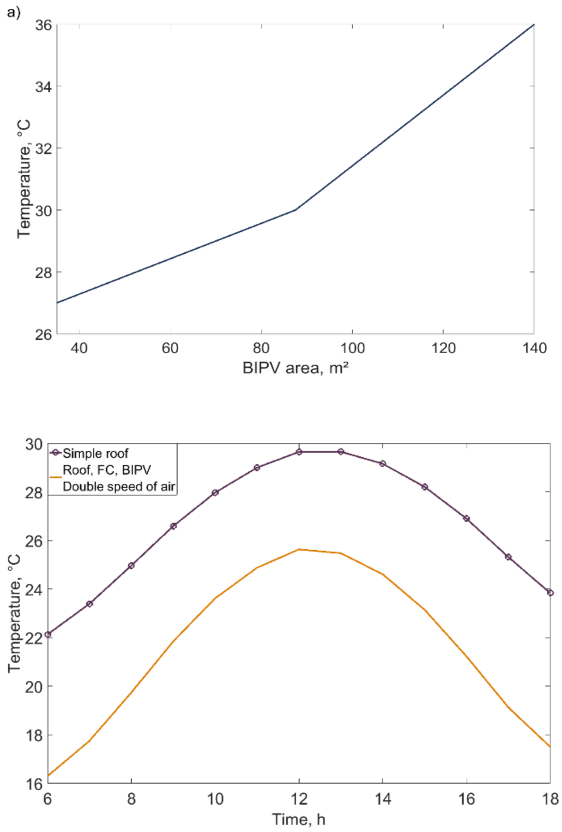

Figure 10. Average indoor temperature of the building with roof, false ceiling and the BIPV system when (a) the size of the BIPV system is increased; (b) the speed of the air in the dead space is doubled

Figure 11 illustrates the roof heat flux of the building for the different cases studied in the modelling. It can be observed that the highest values of heat flux are obtained when the BIPV system is added to the roof and the false ceiling, followed the case of the simple roof. The use of the wooden layer just under the PV modules greatly reduces the roof heat flux, hence showing the positive effects on the indoor comfort conditions of the wooden layer placed just under the PV panels. Another observation that can be made from Figure 11 is that the roof heat flux is maximal during the period comprised between 10 a.m. and 4 P.M.; this observation can be explained by the fact that the highest values of temperatures are obtained during the noon and the afternoon, and the accumulated effect of the irradiation absorbed since the morning will have the overall effect of lowering the thermal resistance of the envelope elements. The results obtained clearly show that the maximum heat transfer in a residential building is done through the roof of the building. The roof heat flux in case of the simple roof is maximum at noon, as it reaches 250 W/m^2, a value almost 8 times greater than the heat flux density through the walls (29 W/m^2 in Yaoundé, 38 W/m^2 in Garoua from the authors of [22]). This value declines to 155.77 W/m^2, thanks to the use of the false ceiling. Introducing PV panels to the roof increases the roof heat flux, with a maximum value of 300 W/m^2, but an appropriate use of the false ceiling brings back the heat flux to a value of 169 W/m^2 and to 132 W/m^2 with the increase of the wooden layer placed just under the PV module. Therefore, reducing indoor temperature can lead to a reduction in the roof heat flux, hence the improvement of the thermal comfort of the occupants of the building. These results are in accordance with previous studies [23] and show all the benefits of an appropriate use of local building materials to increase the indoor comfort of buildings.

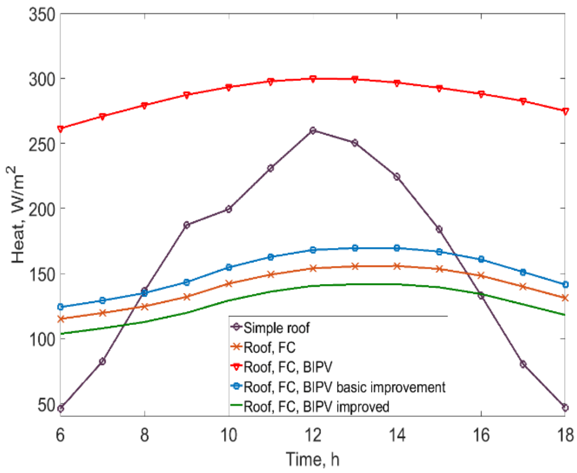

Figure 11. Heat transfer through the roof to the leaving space in the five (05) cases studied

The heat transfer model for the indoor air temperature of the building is simplistic, as the results of this modelling were obtained by considering the entire building as a unique piece without internal heat source. The different temperatures of each room of the building have not been studied, whereas such a study could have improved the degree of precision of the modelling. Taking into account the heat generated by the occupants and the devices of the building would certainly lead to an increase in the temperature of the indoor air of the building. In addition, the heat loss due to ventilation (mechanical or natural) of the building is not sufficiently taken into account in the model. Another factor to consider is that the heat transfer through radiation should be more considered in the elaboration of the modelling, as radiation occupies an important place in the heat exchanges between the building and its environment, especially those taking place through the roof of the building. Also, means must be implemented to reduce the temperature of the PV cells, e.g., adding fins at the back of the PV module, or increasing the natural ventilation around the PV module. This ventilation may be done by creating small adjustable openings around building envelope just under the ceiling or making an open roof-ceiling system.

6. CONCLUSIONS

We presented three distinct but related concepts: first, the irradiation on a tilted surface; second, the lowering of the indoor temperature variation; last, the reduction of the roof heat transfer. The thermal analysis of each of the three systems, the first one consisting of a building without a false ceiling and a BIPV system, the second one consisting of a building with a false ceiling in the absence of a BIPV system, and the third one consisting of a building with a false ceiling and a BIPV system on which a wooden layer is later added just under the back sheet of the PV module was conducted. This study allowed us to demonstrate that:

1. Taking into account the building customs of Cameroon, a tilt angle of 20°S, can be adopted as the tilt angle of the solar roof of our modeling.
2. The building with a roof only had a high room air temperature, approximately 30 °C. The roof heat flux in case of the roof only reaches a maximum of 250 W/m^2, but the use of a false ceiling lowers the density flux to 169 W/m^2.
3. The introduction of the false ceiling lowers the indoor temperature by about 2.5 °C.
4. The association between the false ceiling and a BIPV system makes the room air temperature rise to approximately 32.5 °C.
5. The addition of a wooden layer just under the back sheet of the PV module brings back the room air temperature to 27.71 °C, when the thickness of the wooden layer is equal to twice that of the false ceiling.
6. The increased area of the BIPV system yields an increase in the indoor air temperature; the latter increase can be reduced by increasing the speed of air located in the dead space.
7. The addition of the PV brings back the roof heat flux to the rise, about 300 W/m^2, but this value can be greatly reduced by the appropriate use of the false ceiling and the natural ventilation (134 W/m^2).
8. The reduction of the indoor temperature and the roof heat flux increase the thermal comfort of the occupants of the building.
9. As the wood is considered to be among the building local materials, we recommend its use for the optimization of thermal insulation between the roof system and the floor supporting that roof.

The practice of optimizing the building envelope through the thermal insulation of this envelope should be required either in the construction of new buildings or the renovations of already existing buildings in Cameroon. The use of a well-planned false ceiling makes the solar roof more attractive in a tropical region of Africa.

7. ACKNOWLEDGEMENT

The research was carried out and supported by the corresponding author's grant.

NOMENCLATURE

A	Area (m^2)
b	Height of the BISPVT system (m)
C	Specific heat (J/kg K)
C_f	The conversion factor of the thermal power plant
d	Width of the BISPVT system (m)
dx	Elemental length (m)
dt	Elemental time (s)
e	Thickness (m)
h	Heat transfer coefficient (W/m^{2}K)
k	Thermal conductivity (W/mK)
L	Length (m)
$\dot{m}$	Mass flow rate (kg/s)
R	Thermal resistance (K/W)
T	Temperature (K)
t	Time (s)
I(t)	Incident solar radiation (W/m^2)
U	Overall heat transfer coefficient (W/m^{2}K)
$(UA)_t$	Overall heat transfer coefficient from room to ambient air (W/K)
V	Volume (m^2), Velocity (m/s)
Greek letters	
α	Absorptivity
β	Packing factor, Volume expansion Coefficient
θ	Inclination of roof (rad)
τ	Transmissivity
η	Efficiency
$(\alpha\tau)_{eff}$	Product of effective absorptivity and transmittivity
ρ_{alb}	Albedo
ϑ	Viscosity
φ	Heat flux (W/m^2)
Subscripts	
a	Ambient
al	Aluminum
av	Air in the gap
bs	Back sheet of PV
c	PV cell
door	Door
Fc	False ceiling
g	Glass cover of PV
i	Inner surface
in	Indoor air of the building
n	Number
o	Outer surface
r	Roof
s	Roof exterior surface
T	Tedlar

APPENDIX

$$G_{in1} = \frac{1}{\dot{m}_r c_{air}} \begin{bmatrix} K_{11}+K_{12}+AU_0 \\ -0.33N_0\dot{V}+h_{i,roof}A_r \end{bmatrix}$$

$$F_{in1} = \frac{1}{\dot{m}_r c_{air}} \left\{ T_a \begin{bmatrix} K_{11}+K_{12} \\ +AU_0-0.33N_0\dot{V} \end{bmatrix} + T_r h_{i,roof} A_r \right\}$$

$$G_{in1} = \frac{1}{\dot{m}_r c_{air}} \begin{bmatrix} K_{11}+K_{12}+AU_0 \\ -0.33N_0\dot{V}+h_{i,roof}A_r \end{bmatrix}$$

$$F_{in1} = \frac{1}{\dot{m}_r c_{air}} \left\{ T_a \begin{bmatrix} K_{11}+K_{12} \\ +AU_0-0.33N_0\dot{V} \end{bmatrix} + T_r h_{i,roof} A_r \right\}$$

$$G_{av1} = \frac{1}{\dot{m}_r c_{air}} \begin{bmatrix} K_{21}-0.33N_0\dot{V} \\ +K_{22}+h_{i,av}A_r \end{bmatrix}$$

$$F_{av1} = \frac{1}{\dot{m}_r c_{air}} \left\{ \begin{matrix} T_a \left[K_{21}-0.33N_0\dot{V} \right] \\ +K_{22}T_{in}+h_{i,av}A_r T_r \end{matrix} \right\}$$

$$G_{in2}=\frac{1}{\dot{m}_r c_{air}}\begin{bmatrix}K_{22}+K_{23}+K_{24}\\+AU_0-0.33N_0\dot{V}\end{bmatrix}$$

$$F_{in2}=\frac{1}{\dot{m}_{fc}c_{air}}\left\{\begin{matrix}T_a\begin{bmatrix}K_{23}+K_{24}\\-0.33N_0\dot{V}+AU_0\end{bmatrix}\\+K_{22}T_{av}\end{matrix}\right\}$$

$$G_{av3}=\frac{1}{\dot{m}_{fc}c_{air}}\begin{bmatrix}K_{31}-0.33N_0\dot{V}\\+K_{32}+h_{ibsav}A_r\end{bmatrix}$$

$$F_{av3}=\frac{1}{\dot{m}_{fc}c_{air}}\left\{\begin{matrix}T_a\left[K_{31}-0.33N_0\dot{V}\right]T_{in}K_{32}\\+h_{ibsav}A_rT_{bs}\end{matrix}\right\}$$

$$K_{21}=K_{31}=\left(\begin{matrix}\frac{1}{h_0A_{wall}}+\frac{e_{wall}}{k_{wall}A_{wall}}\\+\frac{1}{h_{i,wall\_fc}A_{wall}}\end{matrix}\right)^{-1}$$

$$K_{22}=K_{32}=\left(\begin{matrix}\frac{1}{h_{i,av}A_{fc}}+\frac{e_{plywood}}{k_{plywood}A_{fc}}\\+\frac{1}{h_{i,in}A_{fc}}\end{matrix}\right)^{-1}$$

$$K_{11}=\left(\frac{1}{h_0A_{wall}}+\frac{e_{wall}}{k_{wall}A_{wall}}+\frac{1}{h_{i,wall}A_{wall}}\right)^{-1}$$

$$K_{12}=\left(\begin{matrix}\frac{1}{h_0}\left[\frac{1}{A_{door}}+\frac{1}{A_{wd}}\right]+\frac{e_{door}}{k_{door}A_{door}}\\+\frac{e_{wd}}{k_{wd}A_{wd}}+\frac{1}{h_{i,door}A_{door}}+\frac{1}{h_{i,wd}A_{wd}}\end{matrix}\right)^{-1}$$

REFERENCES

1. Ang, B.W. and Xu, X., "Energy efficiency indicator", Encyclopedia of quality of life and well-being research, Michalos, A.C. Ed., Vol. 7, Springer, Dordrecht, (2014), 1894-1897. (https://doi.org/10.1007/978-94-007-0753-5_875).
2. Stouter, P., Earthbag building in the humid tropics : Simple structures, (2011). (http://www.earthbagbuilding.com/pdf/earthbagbuilding2.pdf), (Accessed: 05 September 2020).
3. Chen, H.-J., Shu, C.-M., Chiang, C.-M. and Lee, S.-K., "The indoor thermal research of the HCRI-BIPV smart window", ***Energy Procedia***, Vol. 12, (2011), 593-600. (https://doi.org/10.1016/j.egypro.2011.10.080).
4. Akwa, J.V., Konrad, O., Kaufmann, G.V. and Machado, C.A., "Evaluation of the photovoltaic generation potential and real-time analysis of the photovoltaic panel operation on a building facade in southern Brazil", ***Energy and Buildings***, Vol. 69, (2014), 462-433. (https://doi.org/10.1016/j.enbuild.2013.11.007).
5. James, T., Goodrich, A., Woodhouse, M., Margolis, R. and Ong, S., "Building-integrated photovoltaics (BIPV) in the residential sector: An analysis of installed rooftop system prices", ***National Renewable Energy Laboratory***, Technical Report, NREL/TP-6A20-53103, (2011). (https://www.nrel.gov/docs/fy12osti/53103.pdf).
6. Kalogirou, S.A. and Tripanagnostopoulos, Y., "Hybrid PV/T solar systems for domestic hot water and electricity production", ***Energy Conversion and Management***, Vol. 47, (2006), 3368-3382. (https://doi.org/10.1016/j.enconman.2006.01.012).
7. Chow, T.T., He, W. and Ji, J., "Hybrid photovoltaic-thermosyphon water heating system for residential application", ***Solar Energy***, Vol. 80, (2006), 298-306. (https://doi.org/10.1016/j.solener.2005.02.003).
8. Ekoe A Akata, A.M., Njomo, D. and Agrawal, B., "Thermal energy optimization of building integrated semi-transparent photovoltaic thermal systems", ***International Journal of Renewable Energy Development (IJRED)***, Vol. 4, No. 2, (2015), 113-123. (https://doi.org/10.14710/ijred.4.2.113-123).
9. Maturi, L., Lollini, R., Moser, D. and Sparber, W., "Experimental investigation of a low cost passive strategy to improve the performance of building integrated photovoltaic systems", ***Solar Energy***, Vol. 111, (2015), 288-296. (https://doi.org/10.1016/j.solener.2014.11.001).
10. Chow, T.T., He, W., Ji, J. and Chan, A.L.S., "Performance evaluation of photovoltaic thermosyphon system for subtropical climate application", ***Solar Energy***, Vol. 81, (2007), 123-130. (https://doi.org/10.1016/j.solener.2006.05.005).
11. Pierrick, H., Christophe, M., Leon, G. and Patrick, D., "Dynamic numerical model of a high efficiency PV-T collector integrated into a domestic hot water system", ***Solar Energy***, Vol. 111, (2015), 68-81. (https://doi.org/10.1016/j.solener.2014.10.031).
12. Rawat, P., Debbarma, M., Mehrotra, S., Sudhakar, K., Centre, E. and Pradesh, M., "Design, development and experimental investigation of solar photovoltaic/thermal (PV/T) water collector system", ***International Journal of Science, Environment and Technology***, Vol. 3, No. 3, (2014), 1173-1183. (https://www.researchgate.net/publication/263448257_DESIGN_DEVELOPMENT_AND_EXPERIMENTAL_INVESTIGATION_OF_SOLAR_PHOTOVOLTAICTHERMAL_PVT_WATER_COLLECTOR_SYSTEM).
13. Benradouane, N., "Performances thermiques d'une maison solaire", ***Rev. Energ. Ren.***, Vol. 9, (2006), 43-52. (https://www.cder.dz/download/Art9-1_6.pdf).
14. Obeng, G.Y., Akuffo, F.O., Braimah, I., Evers, H.-D. and Mensah, E., "Impact of solar photovoltaic lighting on indoor air smoke in off-grid rural Ghana", ***Energy for Sustainable Development***, Vol. 12, (2008), 55-61. (https://doi.org/10.1016/S0973-0826(08)60419-6).
15. López, C.S.P., Tenconi, L., Castro, F. L., Brambillasca, S., Gonzalez, F.J.N., and Martín, E.C., "Controlled environment test laboratory for comfort performance studies on façade-integrated BIPV", ***Proceedings of the 27th European Photovoltaic Solar Energy Conference and Exhibition***, (2012), 4335-4339. (https://doi.org/10.4229/27thEUPVSEC2012-5BV.1.57).
16. Wen, I.J., Chang, P.C., Chiang, C.M. and Lai, C.M., "Performance assessment of ventilated BIPV roofs collocating with outdoor and indoor openings", ***Journal of Applied Sciences***, Vol. 8, (2008), 3572-3582. (https://doi.org/10.3923/jas.2008.3572.3582).
17. Dominguez, A., Kleissl, J. and Luvall, J.C., "Effects of solar photovoltaic panels on roof heat transfer", ***Solar Energy***, Vol. 85, (2011), 2244-2255. (https://doi.org/10.1016/j.solener.2011.06.010).
18. Ekoe a Akata, A.M., Njomo, D., and Mempouo, B., "The effect of building integrated photovoltaic system (BIPVs) on indoor air temperatures and humidity (Iath) in the tropical region of Cameroon", ***Future Cities and Environment***, Vol. 1, (2015), 1-10. (https://doi.org/10.1186/s40984-015-0002-y).
19. Ali, H.A.R., Ibrahim, S.T., Morsy, M.G. and Abdel-Rahman, A.K., "The effect of using false ceiling on roof cooling load", ***Journal of Engineering Sciences***, Vol. 42, No. 3, (2014), 666-682. (https://doi.org/10.21608/JESAUN.2014.115021).
20. Duffie, J.A. and Beckman, W.A., Solar engineering of thermal processes, Fourth Edition, Wiley, (2013). (https://doi.org/10.1002/9781118671603).
21. Harimi, M., Harimi, D., Kurian, V.J. and Nurmin, B., "Evaluation of the thermal performance of metal roofing under tropical climatic conditions", ***Proceedings of The 2005 World Sustainable Building Conference***, Tokyo, (2005). 709-716. (https://www.irbnet.de/daten/iconda/CIB3434.pdf).
22. Kameni Nematchoua, M., Ricciardi, P., Reiter, S. and Yvon, A., "A comparative study on optimum insulation thickness of walls and energy savings in equatorial and tropical climate", ***International Journal of Sustainable Built Environment***, Vol. 6, (2017), 170-182. (https://doi.org/10.1016/j.ijsbe.2017.02.001).
23. Ekoe A Akata, A.M., Njomo, D. and Agrawal, B., "Assessment of Building Integrated Photovoltaic (BIPV) for sustainable energy performance in tropical regions of Cameroon", ***Renewable and Sustainable Energy Reviews***, Vol. 80, (2017), 1138-1152. (https://doi.org/10.1016/j.rser.2017.05.155).

Journal of Renewable
Energy and Environment

Journal Homepage: www.jree.ir

Materials and Energy Research Center
MERC

Research Article

Surface Modification of Copper Current Collector to Improve the Mechanical and Electrochemical Properties of Graphite Anode in Lithium-Ion Battery

Mohsen Babaiee*, Mohammad Zarei-Jelyani*, Shaghayegh Baktashian, Rahim Eqra

Department of Energy Storage, Institute of Mechanics, Shiraz, Iran.

PAPER INFO

Paper history:
Received: 20 June 2021
Revised in revised form: 17 August 2021
Scientific Accepted: 30 August 2021
Published: 05 December 2021

Keywords:
Li-Ion Battery,
Current Collector,
Surface Modification,
Cu Foil,
Graphite

ABSTRACT

A mechanical technique was applied to the copper current collector of lithium-ion battery anode to improve interface adhesion between Cu foil and anode film. The mechanical and electrochemical performances of graphite anodes coated on Bare Cu Foil (BCF) and Modified Cu Foil (MCF) were evaluated. The BCF and MCF anodes exhibited adhesion strengths of 1.552 and 1.617 MPa, respectively. The electrochemical studies of BCF and MCF anodes showed that the initial discharge capacity of graphite anode coated on the MCF (323.6 mAh g^{-1}) was about 8 % higher than the BCF anode (299.9 mAh g^{-1}). The BCF anode capacity reached 227.9 mAh g^{-1} after 100 charge/discharge cycles at 0.5C rate, while this value was 247.7 mAh g^{-1} for MCF anode. The results of electrochemical impedance spectra demonstrated that the diffusion coefficient of lithium-ion for MCF anode was about 56 % higher than that for BCF anode. On the other hand, the surface modification of the copper current collector reduced the charge transfer resistance of anode from 28.5 Ω to 23.2 Ω.

https://doi.org/10.30501/jree.2021.290435.1219

1. INTRODUCTION

Given that the essential requirement of an eco-friendly energy including regulations on CO_2 emission and fossil fuel reduction is increasing, many studies are being carried out worldwide to develop high-performance energy storage systems [1, 2]. Recently, storage of electrical energy remains critically dependent on Lithium-Ion Batteries (LIBs). Therefore, advanced LIBs are required to address the increasing demand for energy sources with high capacities, which present high energy density, high power density, and better cycle stability than existing LIBs [3-7]. At present, the development of new materials for cathode, anode, membrane, and electrolyte are the most attractive approaches to improving the performance of LIBs [8-10]. Numerous researches have attempted to evaluate new electrode materials [11-13] and high-performance membranes and electrolytes [14, 15]. Some studies have also considered degradation mechanisms such as structural volume changes of active electrode material during lithiation and delithiation processes [16, 17].

However, the factors that affect LIB performance are limited to electrode materials, membranes, and electrolytes. As a critical component in LIBs, the current collector enhances battery performance significantly [18, 19]. The current collector not only acts as a bed for loading active materials, but also is responsible for collecting the electrical current produced by the electrode active materials and conducting it to the output. Unlike other battery components, current collectors, especially copper foils, have received insignificant attention, while they have a crucial impact on lithium-ion battery performance. In a conventional anode electrode of LIB, the surface of the copper foil is coated with graphite slurry. Bond strength, contact impedance of graphite/copper foil interface, and chemical and electrochemical stability are the significant factors impacting cycling stability and capacity of a lithium-ion battery [20, 21].

Mechanical damage to current collector foils in LIBs can lead to external electronic failure followed by battery failure [22]. Furthermore, it has been shown that the organic electrolyte of LIBs gradually etches the copper current collector [23], leading to the degradation of battery performance during long charge/discharge processes. In addition, in the case of traditional copper foils, the smooth surface of copper foil may cause poor contact with the graphite. This can cause high impedance in the contact interface as well as high risk of chemical corrosion in case of electrolyte exposure [24, 25].

Kang et al. synthesized a thin uniform and Compact Oxide Layer (COL) on an Al current collector for LIB cathode through the oxidation process using KMnO4 as an oxidant. They found that the COL on an Al current collector could

*Corresponding Author's Email: babaiee.mohsen@gmail.com (M. Babaiee); m.zarei@isrc.ac.ir (M. Zarei-Jelyani)
URL: https://www.jree.ir/article_141272.html

Please cite this article as: Babaiee, M., Zarei-Jelyani, M., Baktashian, Sh. and Eqra, R., "Surface modification of copper current collector to improve the mechanical and electrochemical properties of graphite anode in lithium-ion battery", ***Journal of Renewable Energy and Environment (JREE)***, Vol. 9, No. 1, (2022), 63-69. (https://doi.org/10.30501/jree.2021.290435.1219).

effectively protect it from corrosion and exhibit good adhesion properties and electrochemical performance for extensive cycle life [26].

Jeon et al. used two types of Cu foil, conventional flat Cu foil and rough Cu foil, to fabricate silicon (Si) electrodes for flexible and high-energy-density LIBs. When Cu foils with a roughness of 3 mm were used for the Si electrode, they delivered much better cycle performance, especially under lower binder content and in the mechanically stressed condition [27].

Jiang et al. synthesized a thin graphene film on the surface of Cu current collector by a large-scale Low-Pressure Chemical Vapor Deposition (LPCVD) process. Their modified Cu foil was used as a current collector to support spinel $Li_4Ti_5O_{12}$ anode directly. They represented that graphene coating Cu foil could effectively improve the overall Li storage performance of $Li_4Ti_5O_{12}$ anode [28].

Zhang et al. applied ultrafast laser ablation for the surface modification of Cu foil for preparation of artificial graphite anode films for LIBs. Improved adhesive force and electrochemical performance were confirmed in anode films on laser structured Cu foils [29].

In the present study, a mechanical abrasion method has been employed for the copper current collector (Figure 1) to increase its specific surface area and enhance mechanical performance. This surface treatment will increase the contact strength between the graphite active material and the current collector. Furthermore, the interface impedance is reduced and the corrosion resistance against the electrolyte increases using this surface modification method. Therefore, the surface treatment of copper foil improves the insertion/de-insertion process of lithium ions in/from the structure of graphite anode. This practical, simple and effective method can be applied to lithium-ion batteries with a long cycle life.

Figure 1. Schematic of current collector treatment and anode electrode preparation process

2. EXPERIMENTAL

2.1. Meterials

The active material for anode slurries was Mesocarbon Microbeads (MCMB, Gelon) with 16.5-19 µm mean diameter (d50), 1.28 g cm^{-3} tap density, and a specific surface area of less than 1.5 m^2 g^{-1}. The conductivity agent of Carbon black (CB, Super P Li, Gelon) with a density of 160 kg m^{-3} was used. A blend of carboxymethyl cellulose (CMC) and styrene-butadiene rubber (SBR) was utilized as the binder. The current collector of the electrode was Copper foil with a thickness of 9 µm.

2.2. Mechanical modification of current collector surface

The copper current collector was abraded using sandpaper (mesh 1000) to increase the roughness of the surface and the contact strength between the active material and the current collector. After mechanical treatment, the surface of copper foil was cleaned with acetone to prepare the current collector for coating of anode slurry. Figure 2 represents microscopic images of the surface of the copper foil before and after the abrasion process at 60 and 200x magnifications.

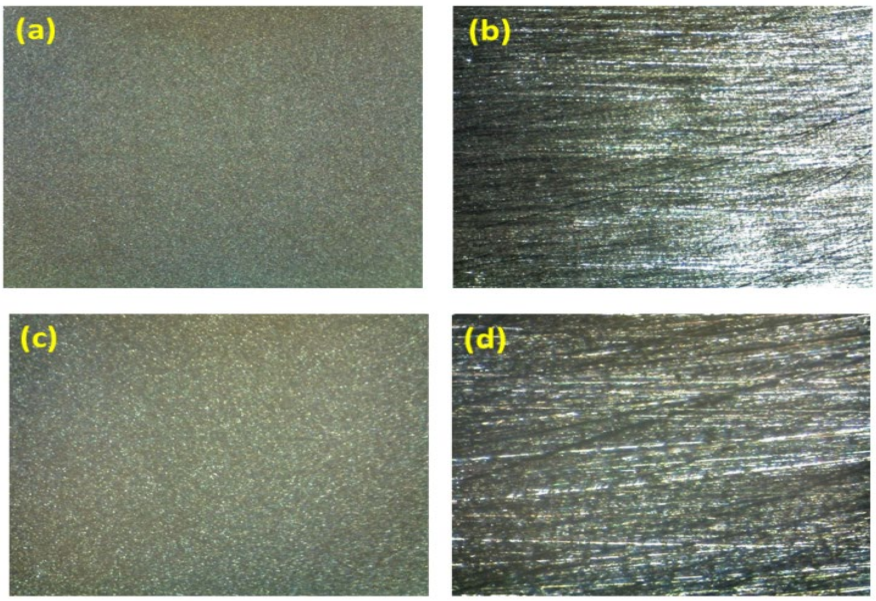

Figure 2. Microscopic images of the surface of the copper foil before abrasion process at: (a) 60x and (c) 200x magnifications and after abrasion process at (b) 60x and (d) 200x magnifications

2.3. Electrodes preparation

The composition of anode slurry coated on different current collectors is shown in Table 1. Active material (MCMB) and conductive agent (CB) were heated in a vacuum oven for 2 hours at 120 ºC to prepare the anode electrodes. A planetary mill was used for 30 minutes at a rate of 200 rpm in order to grind and mix the active and conductive materials. According to Table 1, the required amounts of CMC and SBR were mixed with distilled water and, then, were stirred for 24 h at ambient temperature. Afterward, the active material of the anode and conductivity agent were added to the binder solution. A vacuum-mixer was applied for degasing and further mixing of the blend at a rate of 200 rpm for 1.5 h. The homogenous prepared slurry was coated on bare Cu foil (BCF) and modified Cu foil (MCF) using a doctor-blade method. Then, the electrodes were dried overnight at 60 ºC and pressed using a roll press. This was to warrant good contact between the current collector and electrode mass, as well as between the electrode components. Figure 3 shows the SEM images of the anode electrodes with 1000 and 5000x magnifications.

Table 1. Composition of anode electrode components

Component	Composition (wt %)
Active material (MCMB)	94.5
Conductive agent (CB)	1
CMC	2.25
SBR	2.25

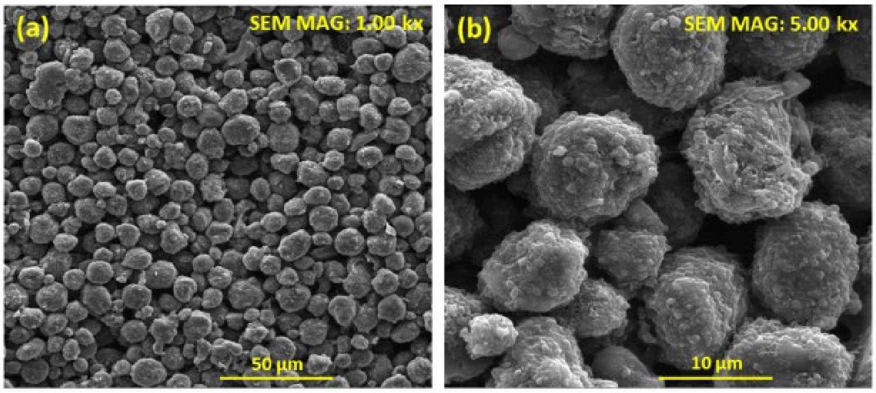

Figure 3. The SEM images of the anode electrodes with (a) 1000x and (b) 5000x magnifications

2.4. Cell assembly

The electrode sheets were punched to prepare the disks of the electrode with a diameter of 14 mm. Prior to assembly of a coin cell, the disks of the electrode were dried under vacuum at 60 ºC for 2 hours. The assembly of CR2032 coin-type half-cells was conducted in a glove box with oxygen and moisture levels lower than 0.5 ppm. The separator was a porous polymer film with a thickness of 25 µm. A solution of 1 M $LiPF_6$ in a mix of EC/DEC (1:1) (MTI Corporation) was utilized as an electrolyte. A foil of Li-metal with 0.6 mm thickness and 16 mm diameter (Gelon LIB Group) was employed as reference and counter electrodes. Finally, the sealing of cells was performed by an electric coin cell crimping machine (MTI Corporation). After assembly, the cells spent 3 hours in a resting state to ensure perfect electrolyte penetration through the pores of electrode and membrane.

2.5. Chraracterization

Quantification of the adhesion strength of anode coatings on the copper foil was conducted using a universal testing machine (Gotech). As shown in Figure 4, double-sided adhesive tape was used to fix an electrode disk between two parallel plates. A pre-compression load equal to 20 kg.f was applied to achieve a reproducible adhesive bond between compression grips and electrode. The disjunction speed of the grips was set at 5 mm/min. The value of the measured tensile stress was considered as adhesion strength.

Coin half-cells were charged and discharged by a battery tester (Neware technology ltd.) to evaluate the electrochemical performance at 0.5C rate in the range of 0.01-2.0 V. All electrochemical experiments were conducted at ambient temperature.

Electrochemical Impedance Spectroscopy (EIS) tests were performed under a frequency window of 10 mHz-100 kHz (open-circuit voltage was selected as the applied bias voltage). An equivalent electronic circuit was applied to simulate the experimental Nyquist plots using the NOVA software.

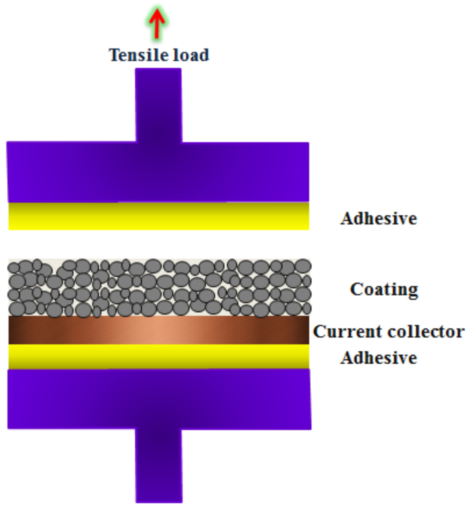

Figure 4. Mechanism of adhesion strength test

3. RESULTS AND DISCUSSION

Figure 5 shows the adhesion strength of MCMB anodes coated on Bare Cu Foil (BCF) and Modified Cu Foil (MCF). The BCF and MCF anodes exhibit adhesion strengths of 1.552 and 1.617 MPa, respectively. Therefore, the anode electrode coated on the modified current collector has better adhesion properties, which can improve the mass loading of the electrode and increase the energy density of the LIB.

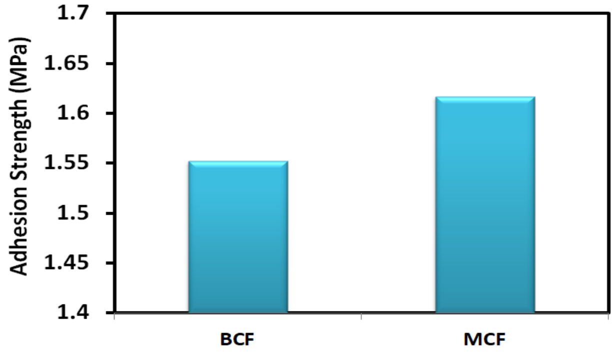

Figure 5. Adhesion strength of MCMB anodes coated on BCF and modified Cu foil (MCF)

Figure 6 represents the cycling performance of BCF and MCF anodes during 100 charge/discharge cycles at a rate of 0.5C. The initial discharge capacities of BCF and MCF anodes are 299.9 and 323.6 mAh g^{-1}, respectively. The modification of the surface of the current collector increases the initial discharge capacity of the MCMB anode by 7.9 %. In addition, the MCF anode capacity reaches 247.7 mAh g^{-1} after 100 cycles, while the BCF anode capacity is equal to 227.9 mAh g^{-1} in the 100th cycle. This means that after 100 cycles, the discharge capacity of the modified anode is 8.7 % higher than that of the BCF anode. On the other hand, the BCF anode has only passed 46 cycles to reach the capacity of 247.7 mAh g^{-1} (equal to the final capacity of the MCF anode after 100 cycles). This indicates that the cycle life of the modified anode is 2.2 times longer than that of the BCF anode to reach the capacity of 247.7 mAh g^{-1}. Figure 7 shows the discharge voltage profiles for BCF and MCF anodes at 1st, 20th, 40th, 60th, 80th, and 100th cycles. The electrochemical parameters of the voltage profiles are presented in Table 2.

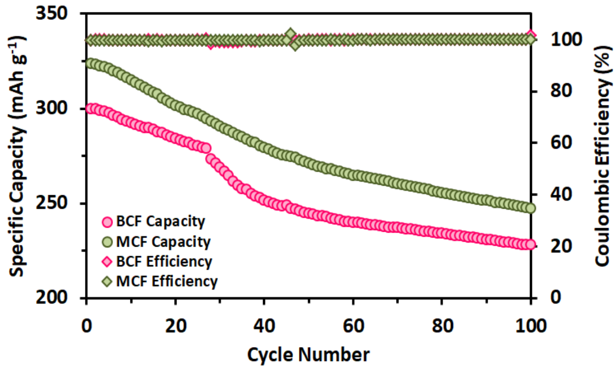

Figure 6. Cycling performance of BCF and MCF anodes during 100 charge/discharge cycles at 0.5C

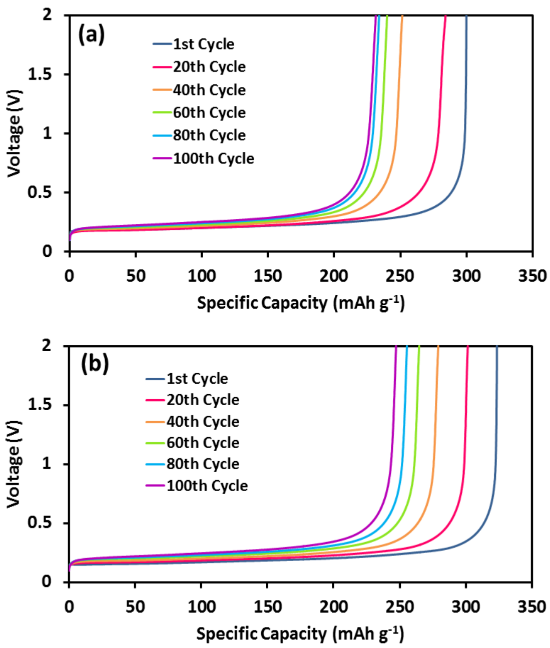

Figure 7. Discharge voltage profiles for BCF and MCF anodes at 1st, 20th, 40th, 60th, 80th, and 100th cycles

Table 2. The electrochemical parameters of the voltage profiles

Anode	Discharge capacity (mAh g^{-1})					
	1st cycle	20th cycle	40th cycle	60th cycle	80th cycle	100th cycle
BCF	299.9	284.2	251.2	240.1	234.0	227.9
MCF	323.6	301.6	279.2	264.2	255.5	247.7

Figure 8 demonstrates the differential capacity curves for anode half-cells of BCF (Figure 8a) and MCF (Figure 8b) in the discharge process of 20th, 40th, 60th, 80th, and 100th cycles. In these figures, two peaks are observed as the anode discharges from low voltage to high voltage, related to the delithiation process [30]. As shown in Figure 8a and b, the delithiation peaks are shifted to higher voltage during cycling, indicating that the resistance of anode half-cells increases as cycle number increases [31]. Figure 8c and d compares the differential capacity profiles of BCF and MCF anodes in the discharge process of 20th and 100th cycles, respectively. According to Figure 8c, it can be said that the average discharge voltage of the MCF anode is lower than that of BCF anode since the peak related to de-insrtion of lithium ions for the MCF anode occurs at lower voltages than that for BCF. Therefore, if the MCF and BCF anodes are employed in a full cell of LIB, the battery prepared by the MCF anode will have a higher discharge voltage. On the other hand, the higher peak intensity for the MCF anode points to the higher capacity of the MCF anode than that of the BCF anode.

Figure 9a displays the half-cells Nyquist plots of BCF and MCF anodes after 100 charge/discharge cycles. Each impedance spectrum shows two semicircles, simulated using an equivalent circuit (Figure 9a). The R_s shows the resistance of bulk electrolyte and high-frequency semicircle is considered the SEI film resistance (R_{SEI}). The observed semicircle at a medium frequency indicates the charge-transfer resistance (R_{ct}) of the lithiation process between the electrolyte and the electrode. CPE_{SEI} and CPE_{ct} elements are constant phase elements associated with R_{SEI} and R_{ct}, respectively. The low-frequency slope is attributed to Warburg impedance that represents the diffusion process of Li^+ ion in the electrode-electrolyte interface [32].

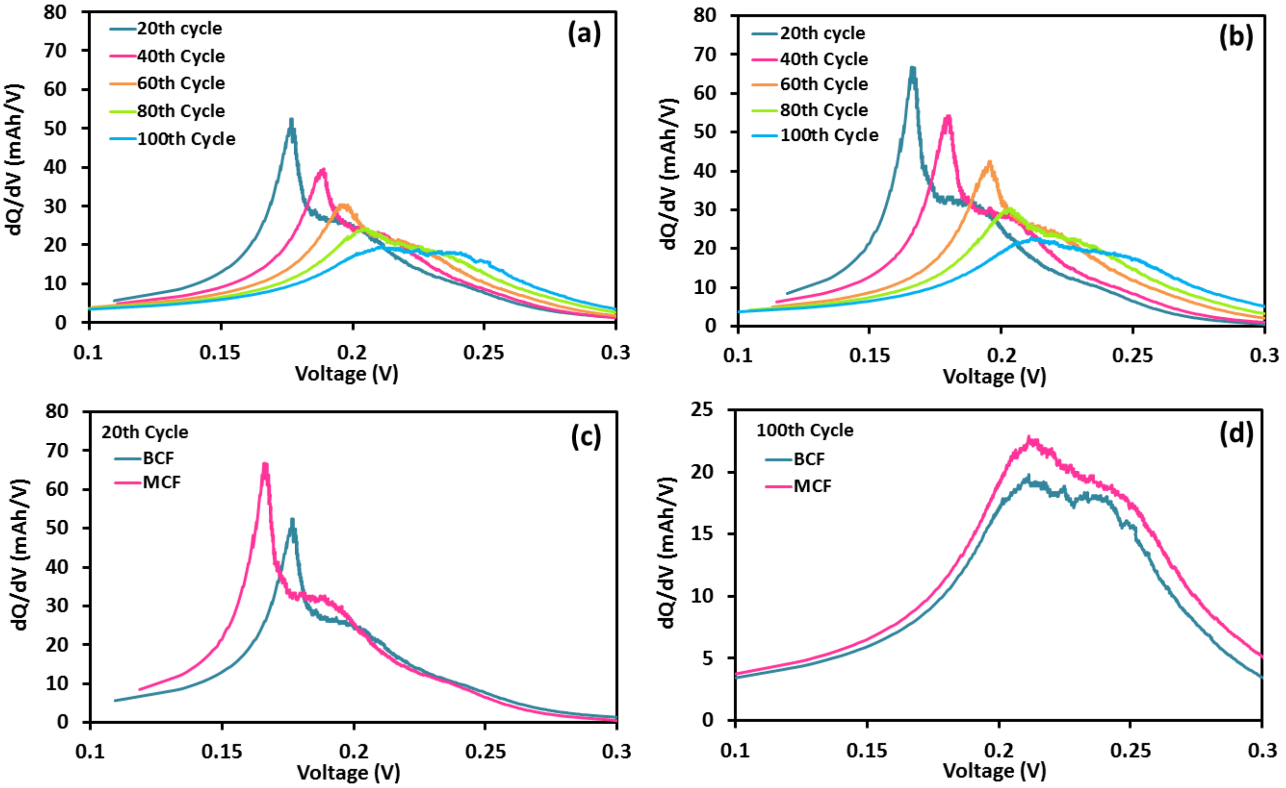

Figure 8. The differential capacity curves for anode half-cells of: (a) BCF, (b) MCF in the discharge processes of 20th, 40th, 60th, 80th, and 100th cycles; comparison of the differential capacity profiles of BCF and MCF anodes in the discharge process of (c) 20th cycle and (d) 100th cycle

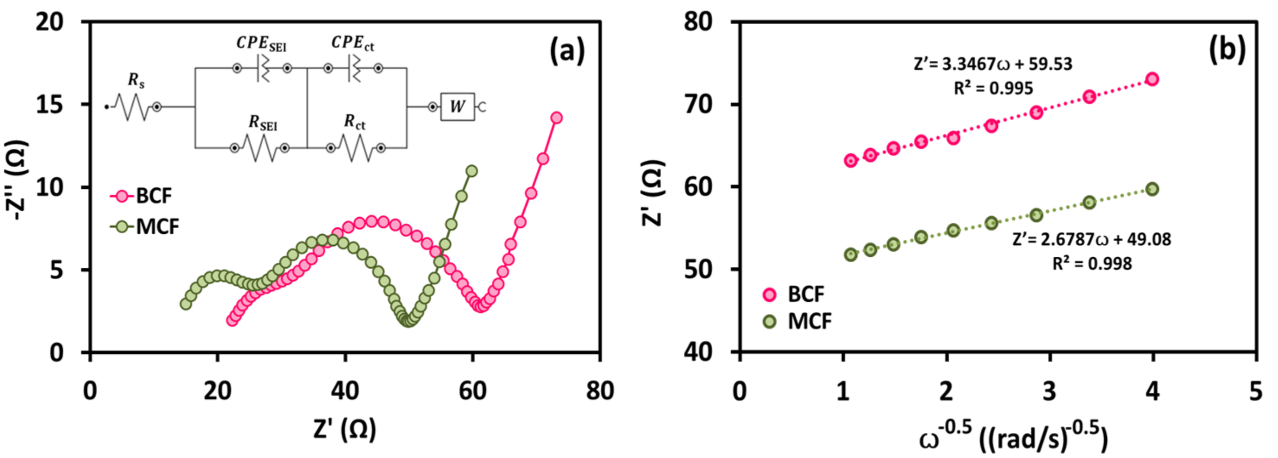

Figure 9. (a) The half-cells Nyquist plots of BCF and MCF anodes after 100 charge/discharge cycles at 0.5C; (b) diagram of the real part resistance with the inverse square root of the angular speed for the anodes of BCF and MCF (in the low-frequency region)

Table 3 presents the simulation results obtained from impedance spectrum of BCF and MCF anodes. The values of R_s are 20.1 Ω and 12.4 Ω for BCF and MCF electrodes, respectively. This indicates that the surface modification process of Cu foil has reduced the R_s by about 40 %. In addition, the MCF anode has lower charge-transfer resistance (23.2 Ω) than the BCF anode (28.5 Ω) after 100 cycles at a rate of 0.5C.

Figure 9b shows a diagram of the real part resistance with the inverse square root of the angular speed for the anodes of BCF and MCF (in the low-frequency region). In order to determine the Warburg factor (σ) and lithium diffusion coefficient (D_{Li^+}), Equations (1) and (2) were applied, respectively [33].

$$Z' = R_s + R_{SEI} + R_{ct} + \sigma\omega^{-0.5} \quad (1)$$

$$D_{Li^+} = \frac{R^2T^2}{2A^2n^2F^4C^2\sigma^2} \quad (2)$$

where the parameters are defined as follows:

Z′: real part resistance
ω: angular frequency
R: gas constant
T: absolute temperature
A: electrode surface area
F: Faraday constant
C: Li–ion molar concentration in an active material

According to Equation (1), the slope of the line obtained in Figure 9b represents the Warburg factor (σ), which is equal to 3.347 and 2.679 for the BCF and MCF anodes, respectively. Since all parameters of Equation (2) are the same for BCF and

MCF anodes except σ, the ratio of lithium diffusion coefficients is calculated using Equation (3).

$$\frac{D_{Li^+,MCF}}{D_{Li^+,BCF}} = (\frac{\sigma_{BCF}}{\sigma_{MCF}})^2 \quad (3)$$

The surface modification of the current collector has increased the lithium-ion diffusion coefficient by about 56 % according to Equation (3). The higher lithium diffusion coefficient for the MCF anode can be attributed to this electrode tortuosity. The tortuosity can augment the conductivity of the electrolyte and the effective diffusion coefficient. The short distances of diffusion can be made across the electrode as the tortuosity decreases. It can yield an increase in the lithium diffusion coefficient.

Table 3. Simulation results obtained from impedance spectrum of BCF and MCF anodes

Sample	R_s (Ω)	R_{SEI} (Ω)	CPE_{SEI}		R_{ct} (Ω)	CPE_{ct}		W (mMho)
			Y_o (μMho)	N		Y_o (μMho)	N	
BCF	20.1	11.5	139	0.579	28.5	984	0.614	219
MCF	12.4	13.7	20.8	0.693	23.2	742	0.656	267

4. CONCLUSIONS

In the present study, a mechanical method was applied to surface modification of copper current collector to be used in the preparation of lithium-ion battery anodes. The general conclusions are as follows:

(1) Improvement of the mechanical properties of the modified anode was confirmed using the adhesion strength test.
(2) The electrochemical studies of BCF and MCF anodes showed that the initial discharge capacity of graphite anode coated on the MCF (323.6 mAh g^{-1}) was about 8 % higher than the BCF anode (299.9 mAh g^{-1}).
(3) The BCF anode capacity reached 227.9 mAh g^{-1} after 100 charge/discharge cycles at 0.5C rate, while this value was 247.7 mAh g^{-1} for MCF anode.

The results of electrochemical impedance spectra demonstrated that the diffusion coefficient of lithium ion for MCF anode was about 56 % higher than that for BCF anode. On the other hand, the surface modification of the copper current collector reduced the charge transfer resistance of anode from 28.5 Ω to 23.2 Ω.

5. ACKNOWLEDGEMENT

The authors would like to thank the Energy Storage Department of Institute of Mechanics for financial support.

REFERENCES

1. Moghim, M.H., Eqra, R., Babaiee, M., Zarei-Jelyani, M. and Loghavi, M. M., "Role of reduced graphene oxide as nano-electrocatalyst in carbon felt electrode of vanadium redox flow battery", ***Journal of Electroanalytical Chemistry***, Vol. 789, (2017), 67-75. (https://doi.org/10.1016/j.jelechem.2017.02.031).

2. Zarei-Jelyani, M., Rashid-Nadimi, S. and Asghari, S., "Treated carbon felt as electrode material in vanadium redox flow batteries: A study of the use of carbon nanotubes as electrocatalyst", ***Journal os Solid State Electrochemistry***, Vol. 21, (2017), 69-79. (https://doi.org/10.1007/s10008-016-3336-y).

3. Loghavi, M.M., Eqra, R. and Mohammadi-Manesh, H., "Preparation and characteristics of graphene/Y_2O_3/$LiNi_{0.8}Co_{0.15}Al_{0.05}O_2$ composite for the cathode of lithium-ion battery", ***Journal of Electroanalytical Chemistry***, Vol. 862, (2020), 113971. (https://doi.org/10.1016/j.jelechem.2020.113971).

4. Gholami, M., Zarei-jelyani, M., Babaiee, M., Baktashian, Sh. and Eqra, R., "Physical vapor deposition of TiO_2 nanoparticles on artificial graphite: An excellent anode for high rate and long cycle life lithium-ion batteries", ***Ionics***, Vol. 26, (2020), 4391-4399. (https://doi.org/10.1007/s11581-020-03579-5).

5. Zarei-Jelyani, M., Baktashian, Sh., Babaiee, M. and Eqra, R., "Improved mechanical and electrochemical properties of artificial graphite anode using water-based binders in lithium-ion batteries", ***Journal of Renewable Energy and Environment (JREE)***, Vol. 5, (2018), 34-39. (http://dx.doi.org/10.30501/jree.2018.93555).

6. Zarei-Jelyani, M., Sarshar, M., Babaiee, M. and Tashakor, N., "Development of lifetime prediction model of lithium-ion battery based on minimizing prediction errors of cycling and operational time degradation using genetic algorithm", ***Journal of Renewable Energy and Environment (JREE)***, Vol. 5, (2018), 60-63. (http://dx.doi.org/10.30501/jree.2018.93531).

7. Sarshar, M., Zarei-Jelyani, M. and Babaiee, M., "Application of semi empirical and multiphysics models in simulating lithium ion battery operation", ***Proceedings of the 10th International Chemical Engineering Congress and Exhibition***, Isfahan, Iran, (2018). (https://www.researchgate.net/publication/325010205_Application_of_semi_empirical_and_Multiphysics_models_in_simulating_lithium_ion_battery_operation), (Accessed: 29 November 2021).

8. Chen, J., Xu, Y., Cao, M., Zhu, C., Liu, X., Li, Y. and Zhong, S., "A stable 2D nano-columnar sandwich layered phthalocyanine negative electrode for lithium-ion batteries", ***Journal of Power Sources***, Vol. 426, (2019), 169-177. (https://doi.org/10.1016/j.jpowsour.2019.04.027).

9. Yan, K., Lee, H.W., Gao, T., Zheng, G., Yao, H., Wang, H. and Cui, Y., "Ultrathin two-dimensional atomic crystals as stable interfacial layer for improvement of lithium metal anode", ***Nano Letters***, Vol. 14, (2014), 6016-6022. (https://doi.org/10.1021/nl503125u).

10. Zhang, J., Liu, Z., Kong, Q., Zhang, C., Pang, S., Yue, L. and Cui, G., "Renewable and superior thermal-resistant cellulose-based composite nonwoven as lithium-ion battery separator", ***ACS Applied Materials & Interfaces***, Vol. 5, (2013), 128-134. (https://doi.org/10.1021/am302290n).

11. Chen, J., Zhang, Q., Zeng, M., Ding, N., Li, Z., Zhong, S. and Yang, G., "Carboxyl-conjugated phthalocyanines used as novel electrode materials with high specific capacity for lithium-ion batteries", ***Journal of Solid State Electrochemistry***, Vol. 20, (2016), 1285-1294. (https://doi.org/10.1007/s10008-016-3126-6).

12. Zhang, L., Liu, Z., Cui, G. and Chen, L., "Biomass-derived materials for electrochemical energy storages", ***Progress in Polymer Science***, Vol. 43, (2015), 136-164. (https://doi.org/10.1016/j.progpolymsci.2014.09.003).

13. Zhu, C., Chen, J., Liu, S., Cheng, B., Xu, Y., Zhang, P. and Zhong, S., "Improved electrochemical performance of bagasse and starch-modified $LiNi_{0.5}Mn_{0.3}Co_{0.2}O_2$ materials for lithium-ion batteries", ***Journal of Materials Science***, Vol. 53, (2018), 5242-5254. (https://doi.org/10.1007/s10853-017-1926-4).

14. Li, Y., Chen, X., Dolocan, A., Cui, Z., Xin, S., Xue, L. and Goodenough, J.B., "Garnet electrolyte with an ultralow interfacial resistance for Li-metal batteries", ***Journal of the American Chemical Society***, Vol. 140, (2018), 6448-6455. (https://doi.org/10.1021/jacs.8b03106).

15. Huang, B., Xu, B., Li, Y., Zhou, W., You, Y., Zhong, S. and Goodenough, J.B., "Li-ion conduction and stability of perovskite $Li_{3/8}Sr_{7/16}Hf_{1/4}Ta_{3/4}O_3$", ***ACS Applied Materials & Interfaces***, Vol. 8, (2016), 14552-14557. (https://doi.org/10.1021/acsami.6b03070).

16. Ji, J., Liu, J., Lai, L., Zhao, X., Zhen, Y., Lin, J. and Ruoff, R.S., "In situ activation of nitrogen-doped graphene anchored on graphite foam for a

high-capacity anode", ***ACS Nano***, Vol. 9, (2015), 8609-8616. (https://doi.org/10.1021/acsnano.5b03888).

17. Li, J., Zhang, Q., Xiao, X., Cheng, Y.T., Liang, C. and Dudney, N.J., "Unravelling the impact of reaction paths on mechanical degradation of intercalation cathodes for lithium-ion batteries", ***Journal of the American Chemical Society***, Vol. 137, (2015), 13732-13735. (https://doi.org/10.1021/jacs.5b06178).
18. Zuo, T.T., Wu, X.W., Yang, C.P., Yin, Y.X., Ye, H., Li, N.W. and Guo, Y.G., "Graphitized carbon fibers as multifunctional 3D current collectors for high areal capacity Li anodes", ***Advanced Materials***, Vol. 29, (2017), 1700389. (https://doi.org/10.1002/adma.201700389).
19. Shin, D.Y., Park, D.H. and Ahn, H.J., "Interface modification of an Al current collector for ultrafast lithium-ion batteries", ***Applied Surface Science***, Vol. 475, (2019), 519-523. (https://doi.org/10.1016/j.apsusc.2019.01.016).
20. Lu, L.L., Ge, J., Yang, J.N., Chen, S.M., Yao, H.B., Zhou, F. and Yu, S.H., "Free-standing copper nanowire network current collector for improving lithium anode performance", ***Nano Letters***, Vol. 16, (2016), 4431-4437. (https://doi.org/10.1021/acs.nanolett.6b01581).
21. Park, H., Um, J.H., Choi, H., Yoon, W.S., Sung, Y.E. and Choe, H., "Hierarchical micro-lamella-structured 3D porous copper current collector coated with tin for advanced lithium-ion batteries", ***Applied Surface Science***, Vol. 399, (2017), 132-138. (https://doi.org/10.1016/j.apsusc.2016.12.043).
22. Zhang, P., Ma, Z., Wang, Y., Zou, Y., Sun, L. and Lu, C., "Lithiation-induced interfacial failure of electrode-collector: A first-principles study", ***Materials Chemistry and Physics***, Vol. 222, (2019), 193-199. (https://doi.org/10.1016/j.matchemphys.2018.10.018).
23. Shu, J., Shui, M., Huang, F., Xu, D., Ren, Y., Hou, L. and Xu, J., "Comparative study on surface behaviors of copper current collector in electrolyte for lithium-ion batteries", ***Electrochimica Acta***, Vol. 56, (2011), 3006-3014. (https://doi.org/10.1016/j.electacta.2011.01.004).
24. Nara, H., Mukoyama, D., Shimizu, R., Momma, T. and Osaka, T., "Systematic analysis of interfacial resistance between the cathode layer and the current collector in lithium-ion batteries by electrochemical impedance spectroscopy", ***Journal of Power Sources***, Vol. 409, (2019), 139-147. (https://doi.org/10.1016/j.jpowsour.2018.09.014).
25. Wu, J., Zhu, Z., Zhang, H., Fu, H., Li, H., Wang, A. and Hu, Z., "Improved electrochemical performance of the silicon/graphite-tin composite anode material by modifying the surface morphology of the Cu current collector", ***Electrochimica Acta***, Vol. 146, (2014), 322-327. (https://doi.org/10.1016/j.electacta.2014.09.075).
26. Kang, S., Xie, H., Zhai, W., Ma, Z.F., Wang, R. and Zhang, W., "Enhancing performance of a lithium ion battery by optimizing the surface properties of the current collector", ***International Journal of Electrochemical Science***, Vol. 10, (2015), 2324-2335. (http://www.electrochemsci.org/papers/vol10/100302324.pdf), (Accessed: 29 November 2021).
27. Jeon, H., Cho, I., Jo, H., Kim, K., Ryou, M.H. and Lee, Y.M., "Highly rough copper current collector: improving adhesion property between a silicon electrode and current collector for flexible lithium-ion batteries", ***RSC Advances***, Vol. 7, (2017), 35681-35686. (https://doi.org/10.1039/C7RA04598K).
28. Jiang, J., Nie, P., Ding, B., Wu, W., Chang, Z., Wu, Y. and Zhang, X., "Effect of graphene modified Cu current collector on the performance of $Li_4Ti_5O_{12}$ anode for lithium-ion batteries", ***ACS Applied Materials & Interfaces***, Vol. 8, (2016), 30926-30932. (https://doi.org/10.1021/acsami.6b10038).
29. Zhang, N., Zheng, Y., Trifonova, A. and Pfleging, W., "Laser structured Cu foil for high-performance lithium-ion battery anodes", ***Journal of Applied Electrochemistry***, Vol. 47, (2017), 829-837. (https://doi.org/10.1007/s10800-017-1086-x).
30. Yoon, T., Chapman, N., Nguyen, C.C. and Lucht, B.L., "Electrochemical reactivity of polyimide and feasibility as a conductive binder for silicon negative electrodes", ***Journal of Materials Science***, Vol. 52, (2017), 3613-3621. (https://doi.org/10.1007/s10853-016-0442-2).
31. Mao, C., Wood, M., David, L., An, S.J., Sheng, Y., Du, Z., Meyer III, H.M., Ruther, R.E. and Wood III, D.L., "Selecting the best graphite for long-life, high-energy Li-ion batteries", ***Journal of The Electrochemical Society***, Vol. 165, No. 9, (2018), A1837-A1845. (https://iopscience.iop.org/article/10.1149/2.1111809jes/pdf), (Accessed: 29 November 2021).
32. Steinhauer, M., Risse, S., Wagner, N. and Friedrich, K.A., "Investigation of the solid electrolyte interphase formation at graphite anodes in lithium-ion batteries with electrochemical impedance spectroscopy", ***Electrochimica Acta***, Vol. 228, (2017), 652-658. (https://doi.org/10.1016/j.electacta.2017.01.128).
33. Zarei-Jelyani, M., Babaiee, M., Baktashian, Sh. and Eqra, R., "Unraveling the role of binder concentration on the electrochemical behavior of mesocarbon microbead anode in lithium–ion batteries: Understanding the formation of the solid electrolyte interphase", ***Journal of Solid State Electrochemistry***, Vol. 23, (2019), 2771-2783. (https://doi.org/10.1007/s10008-019-04381-8).

JREE: Vol. 9, No. 1, (Winter 2022) 70-77

Journal of Renewable Energy and Environment

Journal Homepage: www.jree.ir

Materials and Energy Research Center
MERC

Research Article

A New Interleaved ZVT High Step-Up Converter with Low Count Elements for Photovoltaic Applications

Babak Tohidi, Majid Delshad *, Hadi Saghafi

Department of Electrical Engineering, Isfahan (Khorasgan) Branch, Islamic Azad University, P. O. Box: 81551-39998, Isfahan, Isfahan, Iran.

PAPER INFO

Paper history:
Received: 27 April 2021
Revised in revised form: 06 August 2021
Scientific Accepted: 22 August 2021
Published: 11 December 2021

Keywords:
High Step-Up,
Zero Voltage Transition,
Interleaved,
Current Ripple Cancelation

ABSTRACT

A new interleaved high step-up converter with Zero Voltage Transition (ZVT) is proposed for operation in this paper. The main advantages of the proposed converter are low input current ripple and low voltage stress on the power switches, high efficiency, low total component count, and eliminating reverse recovery problem of power diodes. Due to the soft switching operation of the switches and diodes in the converter, the efficiency has been enhanced. Also, the switches do not have capacitive turn on loss due to ZVT operation. The proposed converter uses only one power switch to provide ZVT conditions for all switches and the clamp capacitor transfers its energy to the lifting capacitor, which causes increase in voltage gain of the converter. Because of the interleaved structure, the converter has a low input ripple current and this advantage makes it very suitable for solar applications. The proposed converter is analysed and a 580W prototype is made to verify theoretical analyses.

https://doi.org/10.30501/jree.2021.279818.1198

1. INTRODUCTION

With the scarcity of fossil fuels and their replacement by green energy sources such as photovoltaic systems, fuel cells, and wind power, not only do greenhouse gas emissions decrease but also the increase in flexibility and reliability in power generation is ensured [1-3]. To maintain DC bus voltage (380-400 V), renewable and distributed generation of the microgrid is essential among the fundamental factors in sustaining high DC bus voltage. In photovoltaic systems, output voltage is low and variable and in order to provide DC line requirements, high step-up DC-DC converters are used widely in the power conversion stage. Besides, to harness greater power, reliability, and efficiency, Photovoltaic arrays are installed with modular DC-DC structures [4-6].

The conventional boost converters have a small number of elements, simple modeling, and design, but have many disadvantages such as high voltage peak on the switch and diode, narrow duty cycle, and reverse recovery problem of the diode. There are several voltage-boosting techniques such as switched capacitors, voltage multiplier, switched inductors or voltage lifting, magnetic coupling, and multistage structures [7-9].

Non-isolated converters often have an uncomplicated structure with lower weight and cost than isolated ones. These converters are not suitable for extracting high power levels. One of the main advantages of these converters is their electrical connections between the input and output and greater efficacy compared to the isolated ones [10-15].

The multiphase interleaved techniques manage to increase power density and reduce input current ripple. Several types of interleaved high step-up converters have been presented recently, which use an auxiliary circuit to recycle leakage inductances energy and provide zero-voltage conditions for the main switches [16-21].

A high step-up interleaved DC-DC converter with ZVT performance was introduced in [18]. An auxiliary circuit including auxiliary switches and clamp capacitors was used to reduce switching losses and control spike voltage of all switches. A transformer with three windings is employed to boost the voltage and reduce the voltage stress of all switches. Leakage inductance controls the current of output diodes and improves the problem of reverse recovery of these diodes. However, the gain of the converter is low. In addition, the voltage of output diode is twice that of output voltage, which is a considerable amount given the operation of this converter at high voltages. The use of two additional switches also may control circuit complexity.

The converter introduced in [19] also uses a combination of coupled inductors with three windings and voltage boosters to provide a high voltage gain converter. This converter, thanks to the use of three coupled inductors and voltage boosters, provides a suitable voltage gain while reducing the voltage stress of its semiconductor elements. If the winding ratio is uniform, its voltage gain will be four times a boost converter. Under such conditions, the voltage across the main switches and clamp diodes is a quarter of the output voltage, and other

*Corresponding Author's Email: delshad@khuisf.ac.ir (M. Delshad)
URL: https://www.jree.ir/article_141495.html

Please cite this article as: Tohidi, B., Delshad, M. and Saghafi, H., "A new interleaved ZVT high step-up converter with low count elements for photovoltaic applications", ***Journal of Renewable Energy and Environment (JREE)***, Vol. 9, No. 1, (2022), 70-77. (https://doi.org/10.30501/jree.2021.279818.1198).

diodes withstand stress equal to Vo/2. However, such a coil structure, called WCCI, is a bit complicated, while the number of elements used in the circuit is relatively large.

Another technique to eliminate switching losses is using the lossless snubber for the switch and the snubber does not impose significant losses on the converter, but the switch drain-source current and voltage stresses increase meaningfully [22-24].

The converters in [25, 26] are interleaved high step-up ones in which an active clamp technique is used to conduct ZV condition. In the main form of the technique, there are two additional switches, duty cycle losses, and high circulating current in the auxiliary circuits.

The converter in [27] is a high step-up converter with switching in zero voltage which applies a new auxiliary circuit with the coupled inductor. The number of elements is relatively large. On the other hand, the coupled inductor in the auxiliary circuit makes the complexity of the converter's operation. Moreover, the driver's circuit should be isolated since the lack of common ground with the source of power MOSFETs. In [21], a high step-up converter with two auxiliary switches was proposed. The major disadvantage of the mentioned circuit is the existence of the auxiliary switch with the floating switch's source. In [21], a high step-up converter using a mini boost converter to recover leakage energy of coupled inductor and transfer it to the load was introduced. The main problem of this converter is the hard switching operation of converter which causes switching losses and limits the switching frequency of the converter. In [28], a new auxiliary circuit for the interleaved converter was introduced. The circuit can be extended to more phases and its energy was transferred to the output in an effective way. However, the critical problems we are facing in this converter are the number of the auxiliary circuit elements as well as use of a coupled inductor in the auxiliary circuit which makes the circuit's operation more complicated.

In [15] and [29], high step-up converters were introduced in which the coupled inductors accompanied with lift voltage capacitors were used to increase voltage gain. The energy in the leakage inductance was absorbed in clamp capacitor. However, in these converters, the soft switching conditions were highly depended on the load. In the light load conditions, the soft switching disappeared and the efficiency was reduced.

In the proposed converter, an active switch was reduced compared to similar ZVT converters, which reduced the conduction losses and the complexity of the circuit operation. Since all switches in the proposed converter operate under ZV condition, unlike ZCS converters, they do not have capacitive turn-on losses.

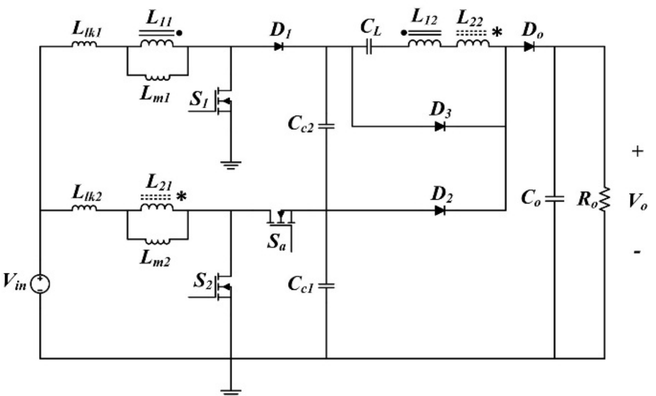

Figure 1. The proposed interleaved high step-up converter

2. THE PROPOSED CONVERTER

2.1. The converter description

The proposed interleaved step-up DC-DC converter with ZVT operation is shown in Figure 1. As shown in the figure, the converter has two main power switches S_1 and S_2 and just an auxiliary switch S_a. Also, capacitors C_{c1} and C_{c2} are used to clamp voltage, the capacitor C_L is employed to lift the voltage gain, and C_o is used to get voltage ripple. To increase the gain, the inductors L_{11}, L_{12}, L_{21}, L_{22} have been coupled, which are modeled by magnetizing inductances L_{m1} and L_{m2} and leakage inductances L_{k1} and L_{k2}, respectively. The converter also includes four diodes D_1, D_2, D_3, and D_o.

2.2. The operation of the proposed high step-up converter

The operation of the proposed converter can be divided into eight operating intervals in a switching cycle. The proposed converter equivalent circuits of the intervals are shown in Figure (2) and the performance of each mode will be examined separately below. The following hypotheses are considered for the simplicity of the proposed converter analysis.

i. The magnetizing inductors are large enough and their current is considered constant in a steady state.
ii. The output and clamp capacitors are designed large enough, and capacitor voltages are assumed to be fixed in a switching cycle.
iii. All semiconductor elements including diodes and switches are modeled ideal.

The main switches are on and the diodes are off before the first mode. The load current is also supplied by the output capacitor and the magnetizing inductances of the converter are charged linearly.

Mode 1 ($t_0<t<t_1$)

This mode starts when S_2 is turned off, and the body diodes of S_a and diode D_o conduct, while the diodes D_1, D_2, and D_3 are off. Therefore, S_a is able to turn on under ZV condition. Also, the leakage inductance energy of L_{lk2} is transmitted through the body diode of S_a to capacitor C_{c1}, and the voltage of switch S_2 is clamped by C_{c1}. On the other hand, when the D_o conducts, the energy of L_{m2} transmits to the output through the secondary side of coupled inductor (L_{22}). The output diode due to the existence of the leakage inductance (L_{lk2}) turns on under ZCS and the currents of L_{m1} and L_{lk1} increase linearly. This mode ends when the L_{lk2} current reaches the secondary winding current (I_{sec}) level.

Mode 2 ($t_1<t<t_2$)

In this state, the current transfers from the anti-parallel diode of S_a to the S_a. In this situation, the current of S_1 continues increasing and the output diode is on. Moreover, only the diode D_o and switches S_1 and S_a conduct and the output is still supplied through capacitors C_{c1}, C_{c2}, and C_L. L_{lk2} current is decreasing with a slight slope and L_{m1} and L_{lk1} currents increase. This state ends when the S_a turns off under ZV condition.

Mode 3 ($t_2<t<t_3$)

When the S_a switch is off, the switch S_2 anti-parallel diode conducts. Therefore, the switch in this interval can be pulsed under ZV conditions. The leakage current of L_{LK2} increases rapidly, which leads to a decrease in the secondary current. As the leakage current of L_{lk2} reaches the current of L_{m2}, the secondary current goes zero and the D_o diode is switched off under ZCS conditions. The decreasing rate of the output diode current is controlled by the leakage inductor L_{lk2}, which leads to the improvement of the reverse recovery problem of this diode. Then, after Do turns off and D_3 turns on, L_{m2} is charged via S_2. This interval ends when S_1 is opens.

Mode 4 (t_3<t<t_4)

In this state, switch S_1 turns off and diode D_1 starts conducting, while diodes D_2 and D_o are off. The energy of L_{LK1} is transmitted through diodes D_1 to capacitors C_{c2} and C_{c1}, and the S_1 switch voltage is clamped by both capacitors C_{c2} and C_{c1}.

Mode 5 (t_4<t<t_5)

This situation begins with diode D_2 turning on as ZCS. When D_4 turns on, the energy stored in capacitor C_{c1} is transferred to the C_L series capacitor. With the secondary current and increase in the voltage of C_L, the voltage across diode D_3 decreases. The energy L_{lk1} is also transferred to the C_{c2} clamp capacitor. Also, the energy of C_{c1} is transferred to the C_L through D_2. The D_o diode is off and the output load energy is supplied through the C_o capacitor, and the inductors L_{m2} and L_{lk2} are receiving energy from the input source. This situation ends when D_1 turns off.

Mode 6 (t_5<t<t_6)

When zero L_{lk1} inductor current reaches zero, diode D_1 turns off as ZCS, thus solving the reverse recovery problem of this diode. In this situation, the L_{m1} current passes through the secondary windings, and the C_L capacitor is charged linearly by L_{m1}. Capacitor C_{c1} also continues to transfer its energy through diode D_2 to capacitor C_L and the current D_2 is reduced. The D_o diode is still off and the output load is supplied by the output capacitor.

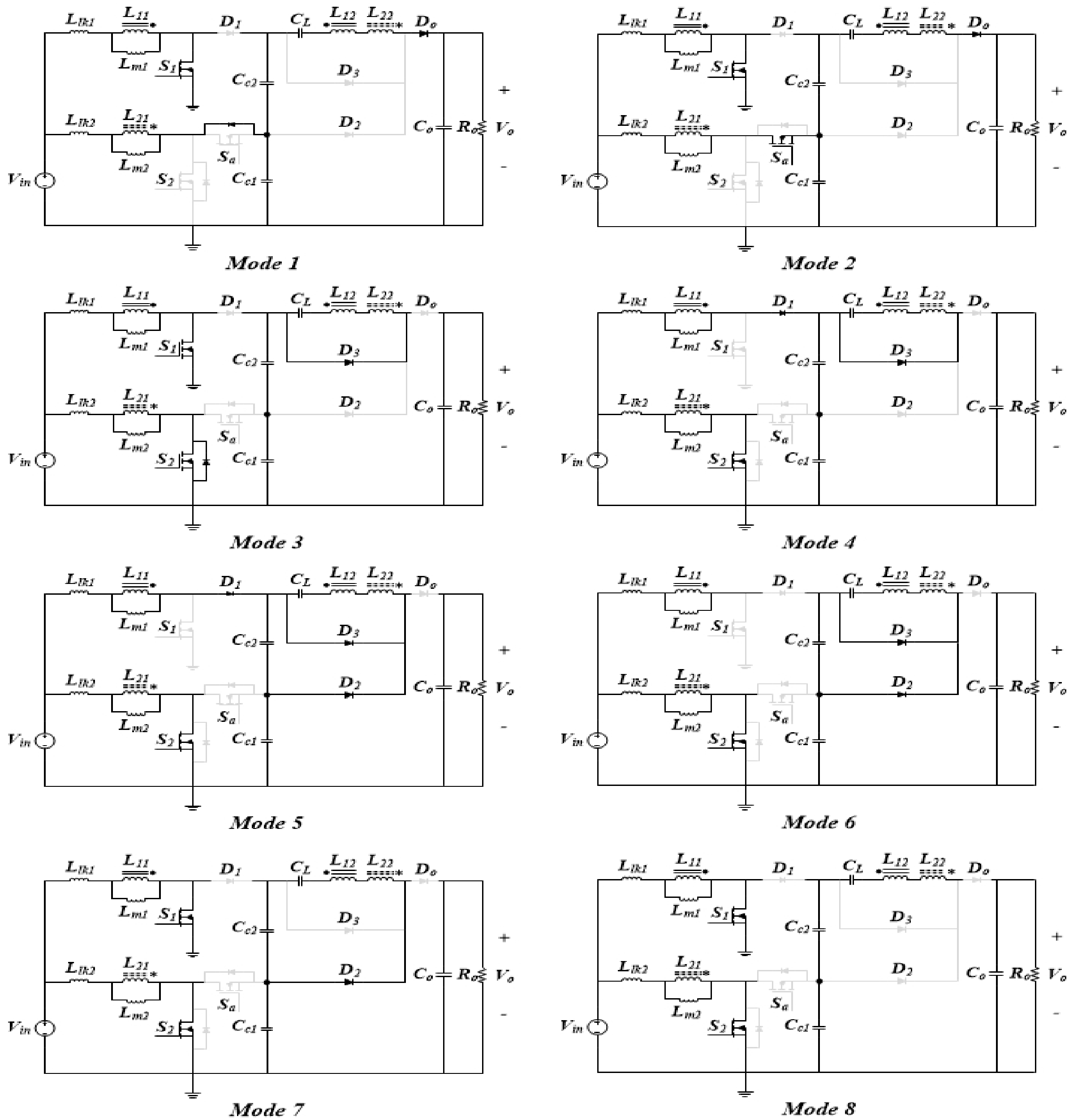

Figure 2. The proposed converter equivalent circuit in the separated eight operation modes

3. PROPOSED CONVERTER DESIGHN CONSIDERATION

3.1. Voltage gain

The voltages of capacitors C_{C1} and C_{C2} are obtained by the volt-second balance relationship of L_{m1} and L_{m2}, respectively.

$$V_{in}DT = (V_{Cc1} - V_{in})(1 - D)T \tag{1}$$

$$V_{Cc1} = \frac{V_{in}}{1-D} \tag{2}$$

$$V_{in}DT = (V_{Cc2} - V_{in})(1 - D)T \tag{3}$$

$$V_{Cc2} = \frac{V_{in}}{1-D} \tag{4}$$

when S_1 is off and D_3 is on, the V_{CL} is obtained by writing KVL in the loop containing the secondary windings and diode D_3.

$$KN(V_{Cc2} - V_{in}) + KNV_{in} - V_{CL} = 0 \tag{5}$$

By inserting the capacitor voltage C_{c2} from Equation (4) in the above equation, the capacitor voltage C_L is obtained as follows:

$$V_{CL} = KN\frac{V_{in}}{1-D} \tag{6}$$

when switch S_1 is off and diode D_1 is on, by writing the KVL relation in the outer loop, the converter voltage gain can be calculated:

$$\frac{V_o}{V_{in}} = \frac{2+2KN+(K-1)D}{1-D} \tag{7}$$

If the coupling factor is considered one, the voltage gain equals to (2+2N)/(1-D) in the ideal state. Figure 3 shows the proposed converter voltage gain versus different duty ratios.

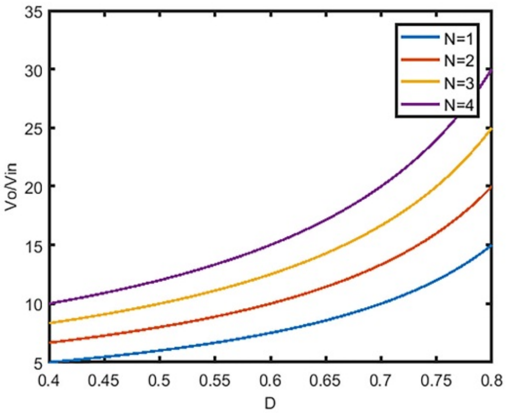

Figure 3. The proposed converter gain versus different duty cycles and turn ratios

3.2. Voltage stress of the semiconductor elements

The voltage of switches S_1 and S_2 is clamped at the voltage level of capacitors C_{c1} and C_{c2}. Therefore, S_1 and S_2 voltage stresses are obtained as follows. The voltage of D_1 is at the level of the total voltage of the clamped capacitors C_{c1} and C_{c2}.

$$V_{S1} = V_{S2} = \frac{V_{in}}{1-D} = \frac{V_o}{2+2KN+(K-1)D} \tag{8}$$

$$V_{D1} = V_{Cc1} + V_{Cc2} = \frac{2V_o}{2+2KN+(K-1)D} \tag{9}$$

when switch S_2 is off, the voltage of D_3 is calculated by writing the following KVL relation.

$$V_{in} - K(V_{C1} - V_{in}) - V_{C1} - V_{D3} + V_o = 0 \tag{10}$$

By placing the voltage relation of capacitor C_{c2} in the above relation and using the voltage gain relation, the voltage of D_3 is obtained as follows:

$$V_{D3} = \frac{2KN}{2+2KN+(K-1)D}V_o \tag{11}$$

The voltage stresses of diodes D_2 and D_0 are obtained according to the following equation.

$$V_{D2} = V_{Do} = V_o - \frac{V_{in}}{1-D} = \frac{1+2KN+(K-1)D}{2+2KN+(K-1)D}V_o \tag{12}$$

Figure 4 shows the normalized voltage stress of semiconductor elements in terms of output voltage per turn ratios of the windings. As can be seen, upon decreasing the voltage stress of the converter switches with increasing turn ratio (N), the voltage of D_3, D_2, and D_o increases subsequently, which can limit N. However, the stress of the proposed converter diodes is always lower than the output voltage.

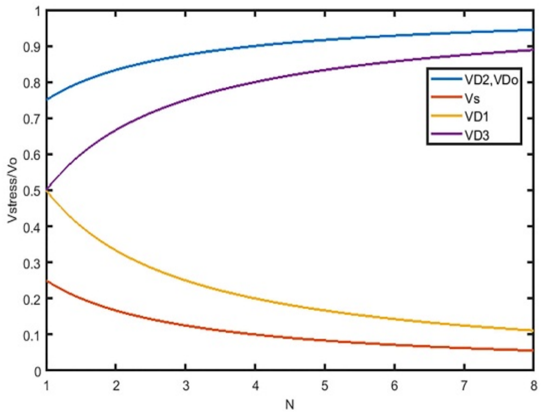

Figure 4. The normalized voltage stress of semiconductor elements in terms of output voltage per turns ratio of the windings

3.3. Design of inductors

To design the inductors, first, the relationship of the magnetizing inductances current is calculated in terms of output current. Then, according to the output power and the amount of inductor current ripple, the values of inductors are obtained. Since the role of capacitor C_{c1} is the voltage clamp of switch S_2 and energy absorption of L_{lk2} and it has a small current, in the calculations, the charge and discharge currents of capacitor C_{c1} as well as diode current D_2 are omitted. Also, the magnetizing inductors are large enough to assume that their current is constant. In addition, the capacitors are designed to be sufficiently large and their voltage can be assumed constant in a steady state. The circumference of the coils of the coupled inductors is considered equal to 2 and the inductors are designed in an ideal state where the coupling coefficient is equal to 1, K =1. When S_1 is turned off, a factor of I_{Lm1}, like AI_{Lm1}, is induced to the secondary. As a result, capacitor C_{c2} is charged with current (1-A) I_{Lm1}. The C_L capacitor is also charged with AI_{Lm1} current, while the S_1 is off. The following equations can be written according to converter operation in turned-on switches.

$$(1-A)I_{Lm1}(1-D)T = \frac{I_{Lm2}}{2}(1-D)T \quad (13)$$

$$I_{Lm2} = 2(1-A)I_{Lm1} \quad (14)$$

The current-second balance of capacitor C_{c2} can be written as follows:

$$AI_{Lm1}(1-D)T = \frac{I_{Lm2}}{2}(1-D)T \quad (15)$$

The current-second balance of the C_L capacitor can be written as follows:

$$I_{Lm1} = I_{Lm2} \quad (16)$$

The input current is equal to the sum of the currents of L_{m1} and L_{m2}, and the following relations are accepted for magnetizing currents.

$$I_{in} = I_{Lm1} + I_{Lm2} \quad (17)$$

$$I_{in} = 2I_{Lm1} \quad (18)$$

$$I_{Lm1} = I_{Lm2} = \frac{2}{1-D}I_{out} \quad (19)$$

During DT, the inductors L_{m1} and L_{m2} are charged linearly by the input voltage source, V_{in}. Therefore, according to the above relation and considering the current ripple of the inductors, the values of inductors L_{m1} and L_{m2} can be calculated according to the following relation:

$$L_{m1} = L_{m2} = \frac{V_{in}D}{\Delta I_{Lm}f} \quad (20)$$

3.4. Design of capacitors

The capacitors are designed according to current-second balance. Thus, based on the discharge current of capacitors C_1 and C_3 and considering the same discharge energy for these two capacitors, the value of these capacitors can be obtained:

$$\frac{I_{Lm2}}{2}(1-D)T = C\Delta V_C \quad (21)$$

$$C_{c2} = C_L = \frac{I_{out}}{f\Delta V_C} \quad (22)$$

During (1-D) T, the output capacitor C_o is discharged by the I_{out} current in the output. Therefore, the value of C_o can be designed as follows:

$$I_{out}(1-D)T = C_0\Delta V_{C0} \quad (23)$$

$$C_0 = \frac{I_{out}(1-D)}{f\Delta V_{Co}} \quad (24)$$

The L_{lk2} energy is absorbed by C_{c1}, which should cause a small voltage ripple in this capacitor.

$$C_{c1} = \frac{L_{lk2}I_{Lm2}^2}{2\Delta V_{Cc1}} \quad (25)$$

4. THE EXPERIMENTAL RESULTS

The prototype of the converter is designed and implemented according to Table 1. The photograph of the implemented converter is shown in Figure 5. The measured voltage and current of switches S_1 and S_2 are shown in Figures 6a and 6b, respectively. In Figure 6a, the current starts to increase with slope and, therefore, zero current switching is established; in addition, the switch voltage has been clamped well. In Figure 6b, the switch current is negative at the turn-on instant, and as a result, its body diode conducts and provides ZV condition. Due to zero voltage switching, the capacitive turn-on losses can be neglected. Figure 6c illustrates the measured drain-source voltage and current of S_a. This switch turns on under ZV condition and all the advantages of S_2 have been established for the auxiliary switch.

Figure 6d shows the current of D_o, and according to this figure, diode turns off under ZC condition. Thus, reverse recovery problem is solved. The practical currents of D_1 and D_2 are given in Figures 6e and 6f, respectively, which indicate that the mentioned diodes do not have a reverse recovery problem.

The proposed converter efficiency has been measured at different loads, as shown in Figure 7. As can be seen from the diagram, the efficiency of the converter is 94 % at full load, which also decreases efficiency with decreasing load, and this is due to constant circuit losses in the clamp circuit. The proposed converter has higher efficiency of 5 % than the hard-switched counterpart. In the hard-switched counterpart, due to the parasitic inductance of coupled inductors, a clamp circuit is required to protect the switches, imposing high losses on the converter.

Table 1. The specification of the proposed interleaved high gain converter

Parameter	Description	Value/Part no.
V_{in}	Input voltage	48 V
V_{out}	Output voltage	480 V
P_{out}	Output power	580 W
f_{sw}	Switching frequency	50 kHz
C_L	Charge-pump capacitor	22 µF
C_{c1},C_{c2}	Clamp capacitor	22 µF
C_o	Output capacitor	47 µF
S_1,S_2	Main switches	IRF740
Sc	Auxiliary switch	IRF740
D_1, D_2,D_3,D_o	Clamp diodes	MUR860

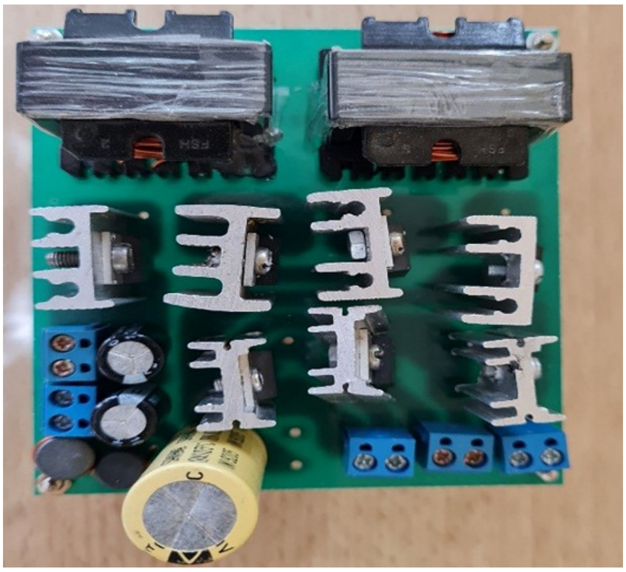

Figure 5. The photograph of the implemented converter

Figure 6. Practical results of the semiconductor elements, a) Measured voltage and current waveforms of S_1 (50 V/div, 10 A/div, 2.5 µs/div), b) Measured voltage and current waveforms of S_2 (50 V/div, 10 A/div, 2.5 µs/div), c) Measured voltage and current waveforms of S_a (50 V/div, 5 A/div, 2.5 µs/div), d) Measured current waveform of D_o (5 A/div, 2.5 µs/div), e) Measured current waveform of D_1 (10 A/div, 2.5 µs/div), f) Measured current waveform of D_2 (2 A/div, 2.5 µs/div)

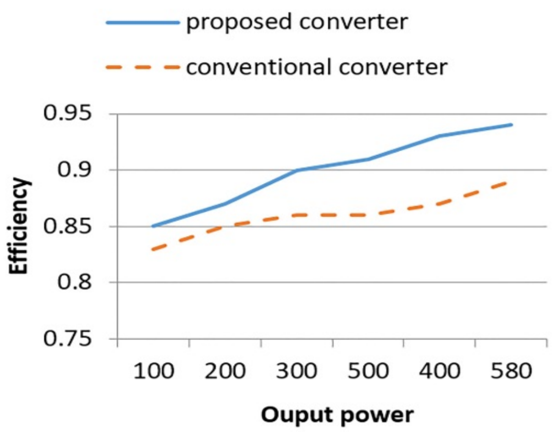

Figure 7. The proposed converter efficiency in comparison with hard-switched counterpart versus different loads

4.2. The comparison between the proposed high step-up converter and the other ones

In this section, the proposed converter is compared with a number of recent high step-up interleaved converters. As can be seen from Table 2, only the converter [26] has fewer elements than the proposed converter. However, the proposed converter has a double voltage gain and the main switch voltage stress is half that of [26].

In terms of voltage gain, converters [14, 28] are in better gain than the proposed converter; however, the converter [14] has four switches that make the operation of the converter more complex and the converter [28] has 24 elements, which increase the conduction loss of the converter and reduce the power density compared to the suggested converter.

Converters [15, 17, 29] operate under ZCS condition and as a result, there are capacitive turn-on losses in these converters. Since the voltage across the switches is high, these losses have a significant role in the total converter losses. Converters [22, 30-31] are hard switching converters. Therefore, in addition to conductive losses, there are switching losses that reduce converter efficiency. Converter [30] has only one switch, which has limited the power of the converter. Likewise, the hard switching of the power switches has reduced the switching frequency and increased the volume of the converter. According to Table 2, it can be concluded that the proposed converter has a small number of elements and high voltage gain compared to the recent converters, which is highly effective in reducing conduction losses and volume of the converter.

Table 2. The Comparison between the proposed converter and the converters in [14, 15, 17, 21, 25-31]

Parameters / References	Voltage gain	Voltage stress	Switching frequency (kHz)	No. of switches	Total component count	Switching condition
[14]	$\frac{4n}{1-D}$	$\frac{V_{Out}}{4n}$	50	4	17	ZVS
[15]	$\frac{2(1+n)}{1-D}$	$\frac{V_{Out}}{2(1+n)}$	100	2	16	ZCS
[17]	$\frac{2(1+n)}{1-D}$	$\frac{V_{Out}}{2(1+n)}$	100	2	15	ZCS
[21]	$\frac{1+nD}{1-D}$	$\frac{V_{Out}}{1+n}+\frac{n(1-D)}{1+nD}$	25	3	15	Hard
[25]	$\frac{2(1+n)}{1-D}$	$\frac{V_{Out}}{2(1+n)}$	100	2	17	ZVS
[26]	$\frac{(1+n)}{1-D}$	$\frac{V_{Out}}{(1+n)}$	50	4	12	ZVS
[27]	$\frac{2(1+n)}{1-D}$	$\frac{V_{Out}}{2(1+n)}$	100	3	16	ZVS
[28]	$\frac{1+3n}{1-D}$	$\frac{V_{Out}}{1+3n}$	100	3	24	ZVS
[29]	$\frac{2(1+n)}{1-D}$	$\frac{V_{Out}}{2(1+n)}$	118	2	18	ZCS
[30]	$\frac{(4+n(2-D)-D)}{1-D}$	$\frac{V_{Out}}{(4+n(2-D)-D)}$	40	1	18	Hard
[31]	$\frac{(2+n)}{1-D}$	$\frac{V_{Out}}{(2+n)}$	100	2	14	Hard
Proposed converter	$\frac{2(1+n)}{1-D}$	$\frac{V_{Out}}{2(1+n)}$	100	3	13	ZVS-ZCS

5. CONCLUSIONS

In the proposed converter, the combined coupled-inductor structure and the switched capacitor were used to increase the gain. The interleaved technique was employed to reduce total current ripple in the input, which helped achieve the maximum power point of solar cells. To increase the switching frequency and decrease the switching losses, an auxiliary circuit with a minimum number of elements was proposed. The auxiliary switch was also soft switched, so the auxiliary circuit did not impose substantial losses on the converter. On the other hand, the energy of clamp capacitors were transferred to C_L capacitor and then, passed to the output. Therefore, the energy of auxiliary circuit and leakage inductances were not wasted and the clamp capacitors were also effective in increasing the voltage gain. The auxiliary switch was gated in complementary with the S_2 and did not require a separate control algorithm which simplified the implementation of the control circuit. It is recommended that for the future work, the possibility of integrating the auxiliary circuit with the voltage multiplier circuit should be considered to reduce the number of the converter elements and, consequently, decrease the volume and cost of the converter.

6. ACKNOWLEDGEMENT

The authors are thankful to the Power Electronics Research Laboratory (PERL) at the Islamic Azad University of Isfahan for providing Hi-tech equipment and support this work technically.

NOMENCLATURE

ZVT	Zero voltage transition
ZVS	Zero voltage switching
ZCS	Zero current switching
K	Coupling factor
D	Duty cycle
WCCI	Winding cross coupled inductor
KVL	Kirchoff's voltage law
MOSFET	Metal oxide semiconductor field effect transisitor

REFERENCES

1. Li, W. and He, X., "Review of nonisolated high-step-up DC/DC converters in photovoltaic grid-connected applications", ***IEEE Transactions on Industrial Electronics***, Vol. 58, No. 4, (2011), 1239-1250. (https://doi.org/10.1109/TIE.2010.2049715).

2. Fallahzadeh, S., Abjadi, N., Kargar, A. and Blaabjerg, F., "Applying sliding-mode control to a double-stage single-phase grid-connected PV system", ***Journal of Renewable Energy and Environment (JREE)***, Vol. 8, No. 1, (2011), 1-12. (https://doi.org/10.30501/jree.2020.233358.1114).

3. Hassani, M.Y., Maalandish, M. and Hosseini, S.H., "A new single-input multioutput interleaved high step-up DC–DC converter for sustainable energy applications", ***IEEE Transactions on Power Electronics***, Vol. 36, No. 2, (2021), 1544-1552. (https://doi.org/10.1109/TPEL.2020.3011218).

4. Nouri, T., Shaneh, M. and Ghorbani, A., "Interleaved high step-up ZVS DC–DC converter with coupled inductor and built-in transformer for renewable energy systems applications", ***IET Power Electronics***, Vol. 13, No. 16, (2020), 3537-3548. (https://doi.org/10.1049/iet-pel.2020.0162).

5. Li, W., Lv, X., Deng, Y., Liu, J. and He, X., "A review of non-isolated high step-up DC/DC converters in renewable energy applications", ***Proceedings of Twenty-Fourth Annual IEEE Applied Power Electronics Conference and Exposition***, Washington, DC, USA, (2009), 364-369. (https://doi.org/10.1109/APEC.2009.4802683).

6. Esmaeli, A., "An intelligent PV panel structure to extract the maximum power in mismatch irradiance", ***Journal of Renewable Energy and Environment (JREE)***, Vol. 2, No. 1, (2015), 25-31. (https://doi.org/10.30501/jree.2015.70061).

7. Forouzesh, M., Siwakoti, Y.P., Gorji, S.A., Blaabjerg, F. and Lehman, B., "Step-up DC–DC converters: A comprehensive review of voltage-boosting techniques, topologies, and applications", ***IEEE Transactions on Power Electronics***, Vol. 32, No. 12, (2017), 9143-9178. (https://doi.org/10.1109/TPEL.2017.2652318).

8. Tofoli, F.L., Pereira, D.D.C. and Paula, W.J., "Survey on non-isolated high-voltage step-up DC–DC topologies based on the boost converter", ***IET Power Electronics***, Vol. 8, No. 10, (2015), 2044-2057. (https://doi.org/10.1049/iet-pel.2014.0605).

9. Kim, P., Lee, S., Park, J. and Choi, S., "High step-up interleaved boost converters using voltage multiplier cells", ***Proceedins of 8th International Conference on Power Electronics - ECCE Asia,*** Jeju, South Korea, (2011), 2844-2851. (https://doi.org/10.1109/ICPE.2011.5944782).

10. Schirone, L. and Macellari, M., "Design of high-efficiency non-insulated step-up converters", ***IET Power Electronics***, Vol. 8, No. 5, (2015), 743-749. (https://doi.org/10.1049/iet-pel.2014.0554).

11. Loera-Palomo, R. and Morales-Saldaña, J.A., "Family of quadratic step-up DC–DC converters based on non-cascading structures", ***IET Power Electronics***, Vol. 8, No. 5, (2015), 793-801. (https://doi.org/10.1049/iet-pel.2013.0879).

12. Zheng, Y., Xie, W. and Smedley, K.M., "Interleaved high step-up converter with coupled inductors", ***IEEE Transactions on Power Electronics***, Vol. 34, No. 7, (2019), 6478-6488. (https://doi.org/10.1109/TPEL.2018.2874189).

13. Yu, W., Hutchens C., Lai, J.S., Zhang, J., Lisi, G., Jabbari, A.D, Smith, D. and Hegardy, T., "High efficiency converter with charge pump and coupled inductor for wide input photovoltaic AC module applications", ***Proceedings of IEEE Energy Conversion Congress and Exposition***, San Jose, CA, USA, (2009), 3895-3900. (https://doi.org/10.1109/ECCE.2009.5316154)

14. Zhu, X., Zhang, B. and Jin, K., "Hybrid nonisolated active quasi-switched DC-DC converter for high step-up voltage conversion applications", ***IEEE Access***, Vol. 8, (2020), 222584-222598. (https://doi.org/10.1109/ACCESS.2020.3043816).

15. Seo, S.-W., Ryu, J.-H., Kim, Y. and Choi, H.H., "Non-isolated high step-up DC/DC converter with coupled inductor and switched capacitor", ***IEEE Access***, Vol. 8, (2020), 217108-217122, (https://doi.org/10.1109/ACCESS.2020.304173).

16. Li, W., Fan, L., Zhao, Y., He, X., Xu, D. and Wu, B., "High-step-up and high-efficiency fuel-cell power-generation system with active-clamp flyback–forward converter", ***IEEE Transactions on Industrial Electronics***, Vol. 59, No. 1, (2012), 599-610. (https://doi.org/10.1109/TIE.2011.2130499).

17. Forouzesh, M., Shen, Y., Yari, K., Siwakoti, Y.P. and Blaabjerg, F., "High-efficiency high step-up DC–DC converter with dual coupled inductors for grid-connected photovoltaic systems", ***IEEE Transactions on Power Electronics***, Vol. 33, No. 7, (2018), 5967-5982. (https://doi.org/10.1109/TPEL.2017.2746750).

18. Li, W.; Li, W. and He, X., "Zero-voltage transition interleaved high step-up converter with built-in transformer", ***IET Power Electronics***, Vol. 4, No. 5, (2011), 523-531. (https://doi.org/10.1049/iet-pel.2010.0133).

19. Nouri, T., Hosseini, S.H., Babaei, E. and Ebrahimi, J., "Interleaved high step-up DC–DC converter based on three-winding high-frequency coupled inductor and voltage multiplier cell", ***IET Power Electronics***, Vol. 8, No. 2, (2015), 175-189. (https://doi.org/10.1049/iet-pel.2014.0165).

20. Li, W., Xiang, X., Li, C., Li, W. and He, X., "Interleaved high step-up ZVT converter with built-in transformer voltage doubler cell for distributed PV generation system", ***IEEE Transactions on Power Electronics***, Vol. 28, No. 1, (2013), 300-313. (https://doi.org/10.1109/TPEL.2012.2199771).

21. Dwari, S. and Parsa, L., "An efficient high-step-up interleaved DC–DC converter with a common active clamp", ***IEEE Transactions on Power Electronics***, Vol. 26, No. 1, (2011), 66-78. (https://doi.org/10.1109/TPEL.2010.2051816).

22. Delshad, M., Madiseh, N.A., Amini, M.R., and Yazdani, M.R., "Implementation of soft-switching bidirectional flyback converter without auxiliary switch", ***IET Power Electronics***, Vol. 6, No. 9, (2013), 1884-1891. (https://doi.org/10.1049/iet-pel.2012.0472).

23. Shamsi, T., Delshad, M. and Adib, E., "A new simple-structure passive lossless snubber for DC-DC boost converters", ***IEEE Transactions on Industrial Electronics***, Vol. 68, No. 3, (2021), 2207-2214. (https://doi.org/10.1109/TIE.2020.2973906).

24. Gerami, E., Delshad, M., Amini, M.R. and Yazdani, M.R., "A new family of non-isolated PWM DC-DC converter with soft switching", ***IET Power Electronics***, Vol. 12, No. 2, (2019), 237-244. (https://doi.org/10.1049/iet-pel.2018.5351).

25. Li, W., Xiang, X., Li, C., Li, W. and He, X., "Interleaved high step-up ZVT converter with built-in transformer voltage doubler cell for distributed PV generation system", ***IEEE Transactions on Power Electronics***, Vol. 28, No. 1, (2013), 300-313. (https://doi.org/10.1109/TPEL.2012.2199771).

26. Li, W. and He, X., "ZVT interleaved boost converters for high-efficiency, high step-up DC-DC conversion", ***IET Electric Power Applications***, Vol. 1, No. 2, (2007), 284-290. (https://digital-library.theiet.org/content/journals/10.1049/iet-epa_20060239).

27. Akhlaghi, B., Molavi, N., Fekri, M. and Farzanehfard, H., "High step-up interleaved ZVT converter with low voltage stress and automatic current sharing", ***IEEE Transactions on Industrial Electronics***, Vol. 65, No. 1, (2018), 291-299. (https://doi.org/10.1109/TIE.2017.2723861).

28. Packnezhad, M., Farzanehfard, H. and Adib, E., "Integrated soft switching cell and clamp circuit for interleaved high-step-up converters," ***IET Power Electronics***, Vol. 12, No. 3, (2019), 430-437. (https://doi.org/10.1049/iet-pel.2018.5446).

29. Alghaythi, M.L., O'Connell, R.M., Islam, N.E., Khan, M.M.S. and Guerrero J.M., "A high step-up interleaved DC-DC converter with voltage multiplier and coupled inductors for renewable energy systems", ***IEEE Access***, Vol. 8, (2020), 123165-123174. (https://doi.org/10.1109/ACCESS.2020.3007137).

30. Andrade, A.M.S., Schuch, S.L. and da Silva Martins, M. L., "Analysis and design of high-efficiency hybrid high step-up DC–DC converter for distributed PV generation systems", ***IEEE Transactions on Industrial Electronics***, Vol. 66, No. 5, (2019), 3860-3868. (https://doi.org/10.1109/TIE.2018.2840496).

31. Zheng, Y., Brown, B., Xie, W. and Li, S., "High step-up DC–DC converter with zero voltage switching and low input current ripple", ***IEEE Transactions on Power Electronics***, Vol. 35, No. 9, (2020), 9416-9429.(https://doi.org/10.1109/TPEL.2020.2968613).

Journal of Renewable Energy and Environment

Journal Homepage: www.jree.ir

Materials and Energy Research Center

MERC

Research Article

Performance Evaluation and Optimization of a Solar-Assisted Multi-Belt Conveyor Dryer Based on Response Surface Methodology

Hemad Zareiforoush*, Adel Bakhshipour, Iraj Bagheri

Department of Biosystems Engineering, Faculty of Agriculture, University of Guilan, P. O. Box: 41635-1314, Rasht, Guilan, Iran.

PAPER INFO

Paper history:
Received: 08 June 2021
Revised in revised form: 25 August 2021
Scientific Accepted: 25 September 2021
Published: 29 December 2021

Keywords:
Drying,
Specific Energy,
Energy Efficiency,
Solar-Assisted Dryer,
Solar Water Heater

ABSTRACT

Drying process is an important post-harvest stage of food crops production which accounts for about 20 % of the world's energy consumption in the industrial sector. One of the effective ways to reduce the share of fossil fuel consumption in the food drying process is to develop new drying systems based on the use of renewable energy sources. In this research, a novel solar-assisted multi-belt conveyor dryer was developed and its performance was analysed. The required thermal energy for drying process was supplied by the combination of solar-gas water heaters and four solar-powered infrared (IR) lamps. The experimental factors included the speed and temperature of the drying air and the power of IR lamps. The performance characteristics were drying time, Overall Specific Energy (OSE), Non-Solar Specific Energy (NSE), Overall Energy Efficiency (OEE), and Solar-Assisted Energy Efficiency (SEE). The optimization process of the drying system was carried out using Response Surface Methodology (RSM) by defining two general modes for the energy sources of the drying system, namely overall mode and solar-assisted mode. Based on the results, the lowest OSE (17.30 MJ/kg water evaporated) was obtained when the speed and temperature of the drying air were equal to 7 m/s and 40 °C, respectively, without using IR power. The lowest NSE (2.71 MJ/kg water evaporated) was achieved by applying the treatment of 7 m/s * 40 °C * 300 W. The maximum OEE was equal to 13.92 % whilst the maximum SEE was obtained as 88.71 %. Both of the mentioned maximum values were obtained at the speed and temperature combination of 7 m/s and 40 °C and their difference was applying 300 W IR power to gain maximum SEE and no IR utilization for the maximum OEE. According to RSM analysis, the optimum working conditions for the drying system included the treatment of 7 m/s * 39.96 ºC * 300 W. Under this condition, the drying time, NSE, and SEE values were equal to 180.95 min, 1.062 MJ/kg water evaporated, and 84.63 %, respectively.

https://doi.org/10.30501/jree.2021.285697.1203

1. INTRODUCTION

Global developments in the field of environmental protection and the depletion of fossil fuel sources are accelerating the trend towards the use of renewable energy and are attracting much more attention in the world. Reduction of fossil energy sources along with population and economic growth and increasing air and environment pollution make it necessary to use renewable energy sources according to their economic justification.

Since the moisture content of fresh food and agricultural crops is often high, drying operations are required to remove the excess water to preserve the quality and durability of the products during their storage. Drying process is an important post-harvest stage of food crops production with a considerable energy consumption. About twenty percent of the world's energy consumption in the industrial sector is related to the drying process [1, 2]. Depending on the type and quality of food that should be dehydrated, several methods have been developed over time to dry the products [3]. During the drying process, significant amounts of thermal energy are consumed and in most cases, the type of energy used in the drying process is fossil fuel [4].

One of the most potential applications of dryers is to dehydrate medicinal herbs. This is because of the several benefits of medicinal herbs for human health and that most of these plants are not available in fresh form throughout the year. Consequently, they must be dried to be available at any time of the year. Since the qualitative characteristics of medicinal plants such as microbial activity constituents can be significantly affected by the drying treatment and environmental conditions, they must often be dried immediately after harvesting from the farm [5]. It has been proved that traditional methods like open sun drying have many disadvantages and negative effects on the quality of products because of uncontrolled heat transfer and low drying rate. On the other hand, biomass-based and infrared drying methods are accompanied with high cost, high levels of fossil fuel consumption, and environmental pollution [6]. It has been

*Corresponding Author's Email: hemad.zareiforoush@guilan.ac.ir (H. Zareiforoush)
URL: https://www.jree.ir/article_142561.html

Please cite this article as: Zareiforoush, H., Bakhshipour, A. and Bagheri, I., "Performance evaluation and optimization of a solar-assisted multi-belt conveyor dryer based on response surface methodology", ***Journal of Renewable Energy and Environment (JREE)***, Vol. 9, No. 1, (2022), 78-92. (https://doi.org/10.30501/jree.2021.285697.1203).

reported that the quality and medicinal value of stevia leaves can be remarkably degraded by open sun drying. Considering the aforementioned challenges, solar drying can be a good idea to substitute or integrate with the traditional and conventional dryers in drying process of medicinal plants.

Solar drying has been proved to be a useful method to preserve the original quality of the product [6]. In recent years, several studies have been done by researches to use the solar dryers for different agricultural and food products such as mint [7], red pepper [8], turmeric (Curcuma longa) [9], rough rice [10], potato [11], and thyme [12]. Lamnatou et al. [13] applied a solar system for apples, carrots, and apricots drying. They found a suitable method for attaining a level of temperature for the warm outlet air using a special collector. Akbulut and Durmuş [14] studied the energy and exergy indices as affected by air flow rate and drying duration. Mehran et al. [4] used a solar dryer in the fluidized-bed mode during the drying process of rough rice grains. They studied the kinetics of drying process, solar energy utilization factor, and drying efficiency. Manrique et al. [15] developed a hybrid solar dryer for coffee beans using the combinative energy of coffee husk pellets combustion and a photovoltaic system and compared the results with those of the conventional method. The uniformity of the products during the drying process has been also investigated using non-destructive methods such as image processing and computational fluid dynamics [16].

An important field of study regarding solar dryers which has been attended by researches is to find the governing mathematical models of the drying operation and to optimize the dryer performance. The most important issues studied in the literature included applying and fitting mathematical models to anticipate and describe the drying behaviour of food products during their dehydration process [12], to evaluate the performance indicators of the developed drying systems such as solar efficiency and solar fraction [17], and to define the optimal working conditions for the proposed solar drying systems [18]. Sami et al. [19] applied several mathematical models to energy and exergy analyses in an indirect solar cabinet dryer. Afriyiye et al. [20] demonstrated that their suggested simulation code could predict temperatures with an error of less than 1.5 %. Akpinar [21] fitted the drying curves of mint leaves to several mathematical models. They reported that "Wang and Singh" model was the superior model to describe the thin-layer drying behavior of mint leaves during forced convection solar drying and natural sun drying. Subbian et al. [18] used Response Surface Methodology to determine the appropriate working conditions of a solar tunnel dryer for drying mango slices with acceptable desirability. The combination of Response Surface Methodology and multi-layered finite element model has also been applied to find the optimal working conditions during simulated solar drying of rough rice grains [22].

A good idea to use solar energy sources in the drying process of food products is to use solar water heaters. One of the advantages of solar water heaters is their ability to save thermal energy so that when there is no sufficient access to solar radiation, it is possible to supply the thermal energy in the form of hot water stored in the solar water heater reservoir. Moreover, by using solar water heaters, it is possible to store thermal energy in the form of a closed cycle for a long time. Several researchers have attempted to benefit from the mentioned advantages of solar water heaters in different application areas. Jahangiri et al. [23] studied the possibility of applying solar water heaters to supply domestic hot water and space heating demands in ten regions of Canada. They found that applying such equipment would lead to an annual reduction of about 984 m^3 in natural gas consumption and 2080 kg in Greenhouse Gas emissions. In another research, Pahlavan et al. [24] indicated that as a result of using solar water heaters in 37 stations in Algeria, considerable amounts of thermal energy of about 100 MWh and 150 MWh could be produced for sanitary hot water and space heating, respectively. The software-based economic analysis demonstrates a significant improvement in the capital return and fossil fuel reduction indices by applying solar water heaters to supply warm water for buildings [25]. The capability of solar water heaters of different types to supply the domestic hot water has been also investigated and proven in Turkey [26] and Zambia [27].

Review of the literature shows that no experimental study has been conducted so far on the performance analysis and optimization of a hybrid solar-assisted multi-belt conveyor dryer including the combination of solar-powered IR lamps and solar water heater in the drying process of stevia leaves. Therefore, in this research, a hybrid solar dryer consisting of a multi conveyor belt drying chamber whose required thermal energy could be supplied with a thermosiphon type solar water heater and four IR lamps was applied for stevia leaves drying. The system is capable of altering the source of thermal energy automatically between the solar and gas water heater based on the drying conditions and information of drying air humidity/temperature sensors. The performance characteristics of the drying system were experimentally evaluated and the optimal working conditions of the dryer were also determined using Response Surface Methodology (RSM).

2. EXPERIMENTAL

2.1. Sample preparation

Fresh stevia leaf samples were provided from Agricultural Biotechnology Research Institute of Iran-North Branch (ABRII), Rasht, Iran. Stevia is known as a natural sweetener with remarkably high sweetness as compared with sugar [28]. The initial moisture content of the leaves was measured based on oven drying method and using the following equation [29]:

$$MC_{d.b.} = \frac{M_i - M_f}{M_f} \times 100 \qquad (1)$$

where M_i and M_f are the mass of fresh and dried sample (g), respectively, and $MC_{d.b.}$ is the dry basis moisture content of the product.

2.2. Hybrid solar dryer

A hybrid solar dryer consisting of a multi-conveyor belt drying chamber whose required thermal energy could be supplied with the combination of a thermosiphon type solar water heater, a gas water heater, and four infrared lamps was applied for product drying. The IR lamps were supplied by a photovoltaic system consisting of three 250 W solar panels. More details on the working procedure of the combined gas-solar water heater were reported by [4]. The schematic of the developed drying system is shown in Figure 1. Using a centrifugal blower, the air was passed through a heat exchanger into a cube-shape drying chamber with the dimensions of 150 × 150 × 80 cm^3. The drying chamber consisted of four belt conveyors which were placed at 20 cm vertical distance with respect to each other. The conveyor belts were of Teflon open mesh type which allowed a continuous and uniform airflow through the samples. Each conveyor moved in the opposite direction to its adjacent conveyor. The conveyors were driven by a 750 W electromotor whose speed was controlled using a variable frequency drive (LS Model IC5, South Korea). The conveyors were run at a constant and low linear speed. They were connected to each other by belt and pulley mechanism. The drying chamber was equipped with four 250 W IR lamps so that one IR lamp was placed above each belt conveyor. The IR lamps were connected together through a series-type electrical circuit. A variable resistor rotary potentiometer was employed to adjust the input power of IR lamps to desired powers. The power consumption of IR circuit was monitored by a digital Power Meter (Lutron DW-6163, Taiwan). Five digital temperature/relative humidity sensors (AM2301/DHT21, China) were used inside the drying chamber in order to control the inlet air. One of the sensors was placed at the drying chamber inlet port and the other four ones were situated above each conveyor belt. The sensors data were collected and sent to the computer using a microcontroller board. The rotational speed of the centrifugal blower could be adjusted using a variable frequency drive, which was the same type of the one used for driving the conveyor belts electromotor. Afterwards, the inlet air speed could be measured by a digital flowmeter (Lutron YK-80, Taiwan). The overall and internal view of the developed dryer is presented in Figure 2.

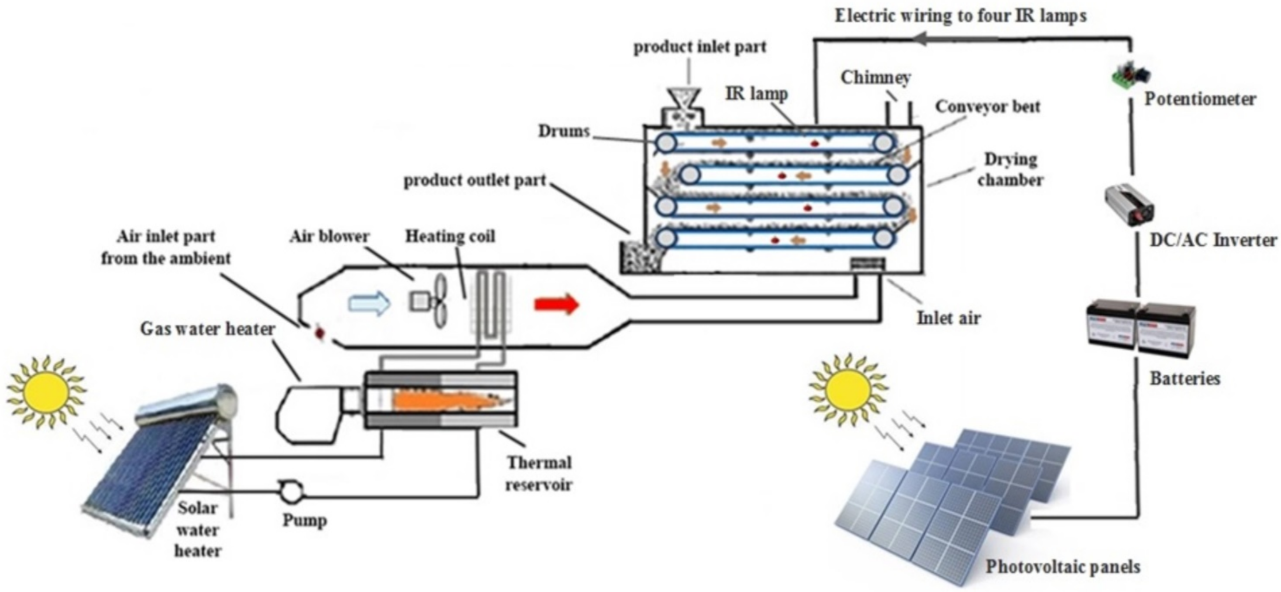

Figure 1. Schematic of the developed solar-assisted dryer working procedure

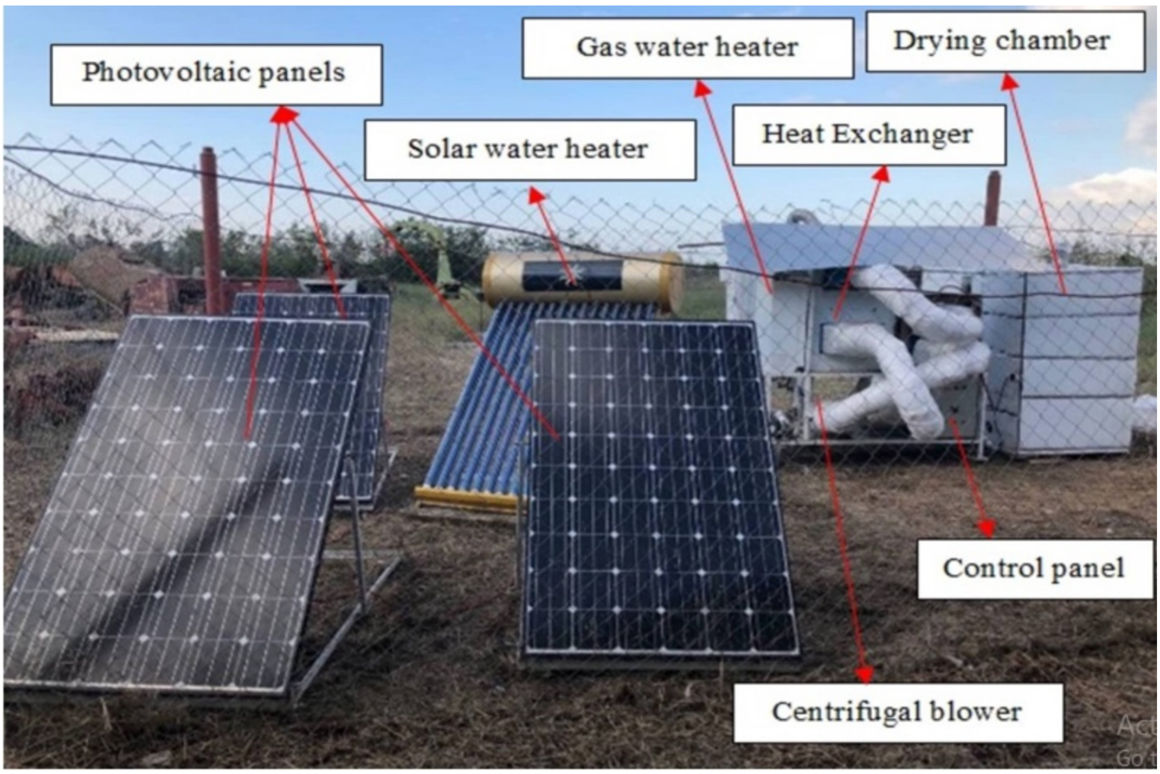

(a)

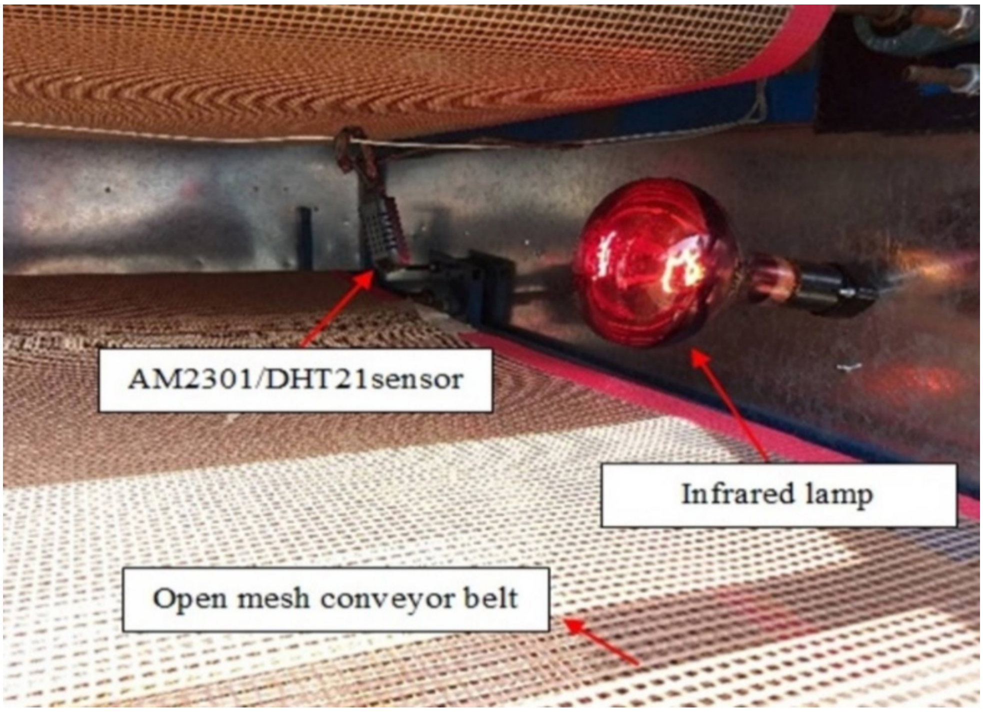

(b)

Figure 2. Experimental setup of the developed drying system: a) Overall view; b) Internal view of drying chamber

2.3. Performance evaluation

The experiments were carried out during July 2019 to September 2019 at the University of Guilan, Rasht, Iran. At each experiment, 300 g of stevia leaves were poured on the highest conveyor in the drying chamber. With the rotation of conveyors, stevia leaves were transferred from the highest conveyor to reach the end part of the lowest conveyor. The goal of the drying process was to dehydrate stevia leaves from a moisture content of about 3.47 (% d.b.) to less than 0.10 (% d.b.). Three factors including drying temperature (30, 40, and 50 °C), inlet air speed (7, 8, and 9 m/s), and infrared power (0, 150, and 300 W) were defined to evaluate the performance of the drying system. The performance indicators included energy consumption, energy efficiency, and drying time. The mentioned indices are defined in the following.

2.3.1. OSE

OSE refers to the total energy used to dehydrate leaves during the drying process. It was calculated as follows [30]:

$$\mathrm{OSE} = \frac{E_t}{m_{ew}} \quad (2)$$

where E_t is the overall energy consumed by the dryer (MJ) and mew is the mass of removed water (kg). The E_t value was calculated based on the following formula:

$$E_t = E_{gwh} + E_{swh} + E_{irc} + E_{cb} \quad (3)$$

where E_{gwh} is energy consumption of the gas water heater, E_{swh} is the thermal energy gain of the solar water heater, E_{irc} is energy consumption of infrared lamps, E_{cb} is energy consumption of centrifugal blower, all in terms of MJ, and mew is the mass of removed water (kg).

2.3.1.1. E_{gwh}

E_{gwh} was measured using the following equation [30]:

$$E_{gwh} = V_g \times E_{eq} \quad (4)$$

where V_g is the volume of natural gas consumed by the water heater (m^3) and E_{eq} is the equivalent energy of natural gas (MJ/m^3), which is equal to 8600 kcal or 35.96 MJ/m^3 in Iran [31].

2.3.1.2. E_{swh}

In order to calculate E_{swh}, the following formula was used [32]:

$$E_{swh} = m_w \times c_p \times (T_{fw} - T_{iw}) \quad (5)$$

where m_w is the mass of stored water in the solar heater tank (kg), c_p is water specific heat (J/kgºC), and T_{fw} and T_{iw} are the final and initial temperatures of water (ºC), respectively.

2.3.1.3. E_{cb}

The value of E_{cb} was obtained using the following formula [33]:

$$E_{cb} = \Delta P_t \times Q_a \times t \quad (6)$$

where ΔP is pressure loss (kPa), Q_a volumetric airflow of the blower (m^3/s), and t drying time (s).

2.3.1.4. E_{irc}

The value of consumed energy by IR lamps (E_{irc}) was determined as follows:

$$E_{irc} = P_{ir} \times t \quad (7)$$

where P_{ir} is the power consumed by IR circuit including four IR lamps (W) and t is drying time (s).

In order to calculate mew value in Eq. (2), the following equation was used [34]:

$$m_{ew} = \frac{m_0 \times (MC_0 - MC_f)}{(100 - MC_f)} \quad (8)$$

where m_0 is the mass of fresh leaves (kg) and MC_0 and MC_f are initial and final moisture contents of the leaves, respectively.

2.3.2. NSE

Considering the fact that a part of the required thermal energy was supplied by renewable energy sources, a special energy index was defined to indicate how much fossil fuel as a non-renewable energy source was used for moisture removal in the developed drying system. The difference between OSE and NSE points to the effectiveness of the solar energy usage. Hence, the NSE of the drying system is defined as follows:

$$NSE = \frac{E_{ns}}{m_{ew}} \quad (9)$$

where E_{ns} is the non-solar type of energy (MJ) and was defined via the following equation:

$$E_{ns} = E_{gwh} + E_{cb} \quad (10)$$

2.3.3. OEE

OEE was calculated using the equation below [33]:

$$OEE = \frac{E_e}{E_t} \quad (11)$$

where E_e is moisture evaporation energy for (MJ) and can be obtained as follows [33]:

$$E_e = h_{fg}.m_{ew} \quad (12)$$

In order to calculate the latent heat of vaporization with respect to absolute temperature (T_{abs}), the following equations were applied [33]:

$$h_{fg} = 2.503 \times 10^6 - 2.386 \times 10^3 (T_{abs} - 273.16) \quad (13)$$
$$273.16 \leq T_{abs}(k) \leq 338.72$$

$$h_{fg} = (7.33 \times 10^{12} - 1.60 \times 10^7 T_{abs}{}^2)^{0.5} \quad (14)$$
$$338.72 \leq T_{abs}(k) \leq 533.16$$

2.3.4. SEE

In the calculation of SEE, the solar energy consumption was neglected from the overall input energy of the drying system. In fact, this index was defined to show how much renewable energy sources would be effective in promoting the efficiency of the drying system. The SEE was calculated via the following equation:

$$SEE = \frac{E_e}{E_{ns}} \quad (15)$$

2.4. Modeling and optimization

RSM is known as an applicable method to find the optimal condition of factors interaction. It can also help estimate the optimal process conditions with the least number of experiments [35]. In this research, the Box-Behnken method was used for statistical analyses and to obtain the optimum working conditions for the solar dryer [36]. The related analyses were performed using Design Expert Software (version 11.0.3). Three code levels (-1, 0, +1) were considered for each independent variable (Table 1). The flowchart of RSM applied to the solar drying process is shown in Figure 3.

The optimization process of the drying system was performed considering two working modes. In the first mode (named as overall mode), the energy consumption of both solar and non-solar energy sources was considered in the evaluations. In this mode, three performance characteristics namely drying time, OSE, and OEE were defined as goals in the optimization process. In the second mode (called as solar-assisted mode), only the non-solar energy sources (gas water heater and centrifugal blower) were considered in the system optimization. In this condition, the performance indicators consisted of NSE, SEE, and drying time. The second mode was defined to illustrate the effect of applying renewable energy sources in the drying system.

Table 1. The code levels of independent variables

Independent variable	Coded values		
	-1	**0**	**1**
A: Drying air velocity (m/s)	7	8	9
B: Drying air temperature (°C)	30	40	50
C: IR circuit power (W)	0	150	300

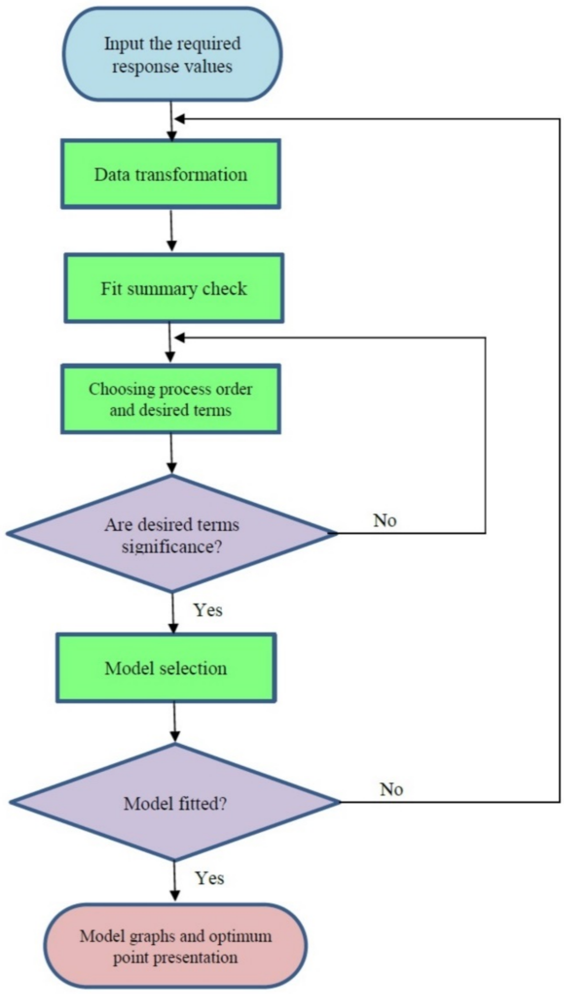

Figure 3. The flowchart of RSM applied to the solar drying process

3. RESULTS AND DISCUSSION

3.1. Overall mode optimization

3.1.1. Statistical analysis

Based on the RSM analysis, 17 working conditions were defined for evaluating the drying system. The results of the experimental tests and the related data predicted by Box-Behnken method are presented in Table 2. Analyses of data indicated that Quadratic model was successfully able to fit the three responses (drying time, OSE, and OEE) versus the independent variables.

Analysis of variance for the three responses together with the coefficient estimates is given in Table 3. The positive sign of the estimated regression coefficients obtained from the model points to the growing influence of the working factors on the responses, while the negative sign coefficients show a decreasing influence on the responses [37]. The magnitude of the coefficients indicates that the related working factor has a greater influence on the responses. The results revealed that the individual factors significantly affected the performance characteristics of the drying system.

3.1.2. Overall drying time

The interaction of "IR power * air temperature" on drying time was statistically significant (p-value < 0.0001). In Figure 4, it can be observed that drying time decreased with the increase of air temperature. Other researchers also reported similar results in this regard [38]. Increasing IR power from 0 to 300 W shortened the drying time. Nevertheless, the slope of the related curve was lower than that of the inlet air temperature. According to Table 2, the lowest value of drying time was 104 minutes which was obtained by applying the combination of 8 m/s * 50 °C * 300 W. The longest time of drying (567 minutes) was obtained upon choosing the values of 8 m/s, 30 °C, and 0 W for the working factors. There are similar researches in the literature that prove the effect of applying radiative IR lamps on the reduction of the drying process time [11].

Table 2. The design points suggested by Box-Behnken method for the experiments and their related experimental and predicted data in overall mode optimization

Run	Independent variables			Real responses (Experiment)			Predicted responses (Model)		
	IR power (W)	Air temperature (ºC)	Air velocity (m/s)	Drying time (min)	Specific energy consumption (MJ/kg water)	Energy efficiency (%)	Drying time (min)	Specific energy consumption (MJ/kg water)	Energy efficiency (%)
1	150	50	9	139	23.67	10.07	137.49	23.92	9.90
2	300	50	8	104	20.74	11.50	116.12	20.85	11.35
3	150	40	8	248	30.15	7.98	249.6	30.18	7.98
4	150	30	9	394	34.85	6.98	395.75	34.15	7.12
5	0	30	8	567	20.78	11.70	554.88	20.67	11.85
6	300	40	7	191	32.21	7.47	180.63	31.38	7.76
7	0	50	8	221	17.60	13.55	212.12	16.53	14.01
8	0	40	7	355	17.30	13.92	365.63	17.66	13.61
9	150	40	8	251	30.27	7.95	249.6	30.18	7.98
10	150	50	7	176	18.70	12.75	174.25	19.41	12.60
11	300	40	9	159	32.95	7.31	148.37	32.58	7.62
12	300	30	8	279	38.29	6.35	287.88	39.35	5.87
13	150	40	8	247	29.84	8.07	249.6	30.18	7.98
14	0	40	9	316	22.48	10.71	326.37	23.30	10.42
15	150	30	7	429	32.06	7.58	430.51	31.82	7.75
16	150	40	8	250	30.25	7.96	249.60	30.18	7.98
17	150	40	8	252	30.39	7.92	249.60	30.18	7.98

Table 3. Analysis of variance of Quadratic model for drying time, overall energy consumption, solar fraction and energy efficiency in overall mode optimization

Source	df	Drying time (min)			Overall specific energy (MJ/kg water)			Overall energy efficiency (%)		
		Sum of squares	F-value❈	Coefficient estimate	Sum of squares	F-value	Coefficient estimate	Sum of squares	F-value	Coefficient estimate
Model	9	2.140E+05	180.81**	249.60	682.98	102.00**	30.18	96.39	77.94**	7.98
A	1	65884.50	501.05**	-90.75	264.84	355.98**	5.75	37.19	270.63**	-2.16
B	1	1.324E+05	1006.56**	-128.63	256.28	344.46**	-5.66	29.06	211.45**	1.91
C	1	2556.13	19.44**	-17.88	23.38	31.43**	1.71	5.54	40.33**	-0.8324
AB	1	7310.25	55.59**	42.75	51.65	69.42**	-3.59	2.73	19.84**	0.8257
AC	1	12.25	0.0932ns	1.75	4.96	6.66*	-1.11	2.32	16.87**	0.7612
BC	1	1.0000	0.0076ns	-0.5000	1.18	1.59ns	0.5435	1.07	7.77*	-0.5166
A^2	1	203.38	1.55 ns	6.95	50.35	67.68**	-3.46	11.49	83.60**	1.65
B^2	1	5517.64	41.96**	36.20	23.70	31.86**	-2.37	5.51	40.11**	1.14
C^2	1	7.12	0.0541ns	-1.30	0.9994	1.34ns	-0.4872	0.2092	1.52ns	0.2229
Residual	7	920.45			5.21			0.9619		

❈: A-IR power; B-Air temperature; C-Air velocity; ** significant in 1 % probability level; * significant in 5 % probability level; ns: not statistically significant

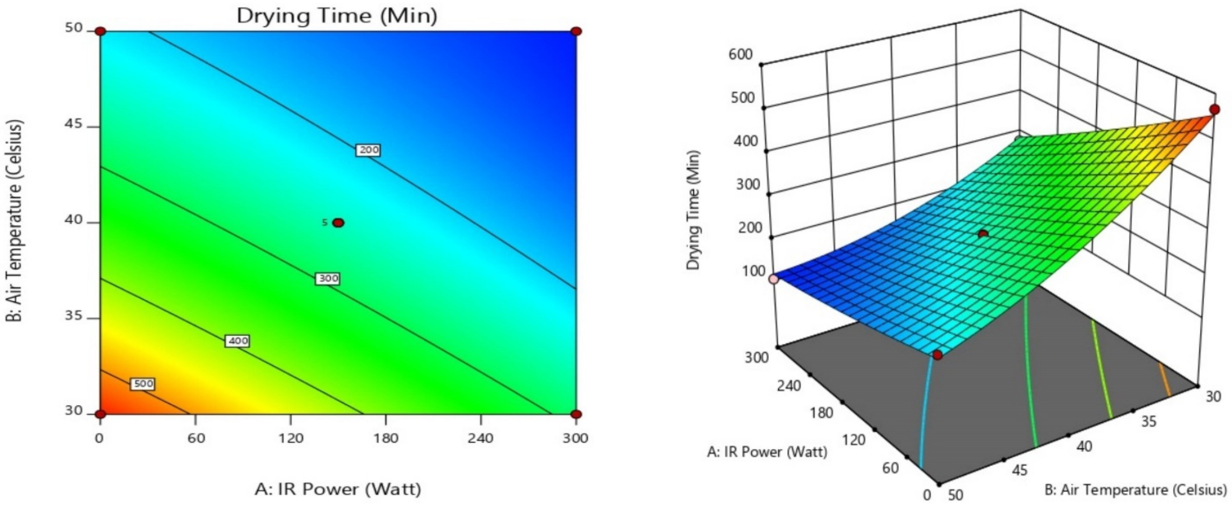

(a) (b)

Figure 4. The interaction effect of IR Power * air temperature on drying time in: a) Contour and b) 3D surface diagrammatic view

3.1.3. OSE

OSE was significantly affected by the interactions of “IR power * air temperature” and “IR power * air speed” at 1 % and 5 % probability levels, respectively. In Figure 5, upon increasing air temperature, a kind of parabolic change with a decreasing approach is made to the amount of OSE. Increasing the IR power similarly causes a parabolically increasing trend in the value of specific energy. The OSE increased with increase in air speed. The result was related to the higher electricity consumption of the centrifugal blower for supplying higher air speeds. The lowest value of OSE (17.30 MJ/kg water evaporated) was obtained by applying the combination of 7 m/s * 40 °C * 0 W, for the inlet air speed, air temperature, and IR power, respectively. The highest OSE (38.29 MJ/kg water evaporated) corresponded to the combination of 8 m/s * 30 °C * 300 W. It has been reported that the energy consumption of a multi-conveyor belt dryer supplied with natural gas ranged from 467.99 to 4607.94 kJ [39].

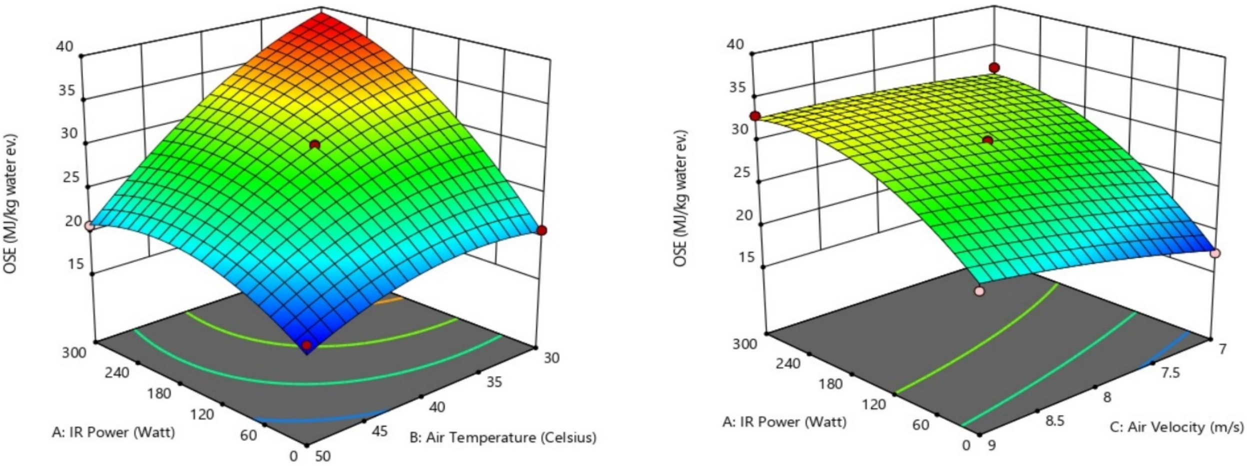

(a) (b)

Figure 5. Interaction effects of: a) IR Power * Inlet air temperature and b) IR Power * Inlet air speed OSE

3.1.4. OEE

OEE is a good indicator to show the overall energy input used for removing extra water from the products in drying systems [30]. The variations of OEE with respect to the interaction of "IR power * air temperature" and "IR power * air speed" are depicted in Figure 6. The aforementioned interaction effects were significant at a 1 % probability level (p-value < 0.0001). It was observed that with increasing IR power from 0 to 300 W, the value of OEE decreased. This indicates that at higher levels of IR power, a greater amount of energy is wasted in the system. It should be noted that this conclusion was derived by supposing the required thermal energy of the dying system to be supplied by only non-solar sources. In other words, if the overall convection and radiant thermal energy of the drying system were provided only by non-solar sources, the OEE decreased by increasing IR power. Increasing the drying air temperature caused the OEE to increase. Meanwhile, OEE decreased by increasing air speed. A similar trend has been reported by other researchers [33]. The highest OEE was 13.92 %, which was obtained by applying the working levels of 7 m/s, 40 °C, and 0 W, whilst the lowest OEE (6.35 %) belonged to the levels of 8 m/s, 30 °C, and 300 W. Sami et al. [19] reported that by applying the air temperature of 69 ºC, the highest values of collector output exergy and energy in their studied indirect solar cabinet dryer were 2.5 kW and 1.12 kW, respectively.

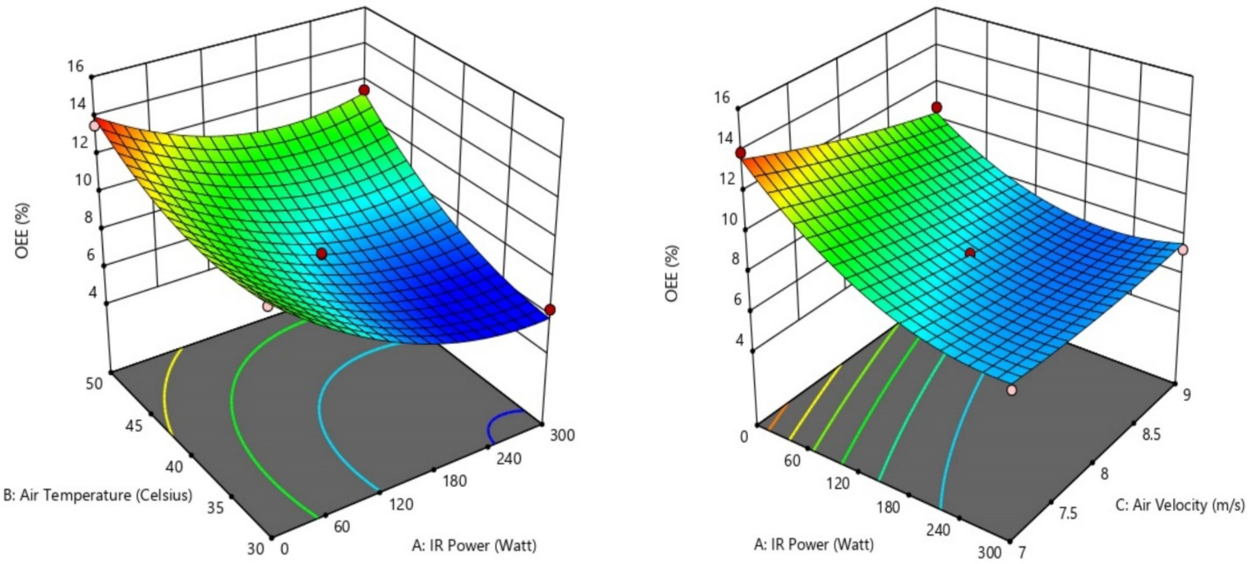

(a) (b)

Figure 6. Interaction effects of: a) Inlet air temperature × IR Power and b) IR Power × Inlet air speed on OEE

3.1.5. Optimum conditions

The working condition of the developed drying system was optimized using the desirability function method in Design Expert software. The goal of the optimization process in the overall mode was to minimize drying time and OSE and to maximize the OEE. Accordingly, 43 points were suggested by the software with desirability values of higher than 0.90. The top ten solutions for the optimization process are presented in Table 4. The first optimum point for the drying system included the IR power of 80.64 W, air temperature of 50 ºC, and air speed of 7 m/s. In such a condition, the values of drying time, OSE, and OEE were 198.74 min, 17.15 MJ/kg water evaporated, and 13.92 %, respectively. As shown in Table 4, in most of the points suggested by RSM, the values of IR power, inlet air speed, and air temperature were close to 80 W, 7 m/s, and 50 ºC, respectively. This finding implies that when the drying system is supplied by non-renewable energy sources, the lower levels of IR power and inlet air speed are desired because of the high energy consumption of the IR circuit and centrifugal blower.

The graphical view of the optimum point with respect to the interaction of "IR power * air temperature" is shown in Figure 7. The optimum points are presented inside a small box in each chart. The values of the responses were normalized so that they varied between 0 as minimum value (blue color) to 1 as maximum value (red color). It can be observed that the optimum point was obtained at lower levels of drying time (blue region), lower levels of OSE (blue region), and higher levels of OEE (red region) with a high level of desirability (red region). Lin et al. [40] evaluated the optimum conditions for dehydration of potato slices in an IR-assisted freeze dryer at an air temperature of 37 °C, slice thickness of 8 mm, and distance of 50 mm from the IR radiation. They reported that the drying process could be successfully optimized through the development of the second-order polynomial model.

Table 4. The top ten suggested optimal working conditions of the drying system in the overall optimization mode

No.	IR power (W)	Drying air temperature (ºC)	Drying air velocity (m/s)	Drying time (min)	Overall specific energy consumption (MJ/kg water evaporated)	Overall energy efficiency (%)	Desirability	
1	80.640	50.000	7.000	198.741	17.155	13.919	0.927	**Selected**
2	77.080	50.000	7.040	199.406	17.151	13.919	0.926	
3	79.374	49.948	7.004	199.551	17.163	13.919	0.926	
4	77.413	49.992	7.000	200.011	17.022	13.995	0.925	
5	75.802	49.995	7.000	200.601	16.948	14.036	0.925	
6	73.505	50.000	7.000	201.428	16.839	14.095	0.924	
7	77.120	49.807	7.000	201.547	17.178	13.923	0.924	
8	72.365	49.997	7.000	201.886	16.790	14.123	0.924	
9	60.118	50.000	7.239	202.455	17.109	13.920	0.923	
10	80.640	49.705	7.000	202.968	17.198	13.919	0.923	

Jafari et al. [41] used RSM for optimizing the drying process of eggplant slices by IR power. The suggested optimum conditions in their research were determined as air speed of 1.14 m/s, IR power of 1500 W, and slice thickness of 4.9 mm. Jha and Tripathy [22] reported that the optimized working conditions during simulated solar drying of rough rice grains included power of 700 W, drying air speed of 3.5 m/s, and grain moisture content of 12 %, which resulted in optimal temperature, milling yield, and drying time of 46 °C, 71.48 %, and 90 min, respectively, and a desirability factor of 0.92.

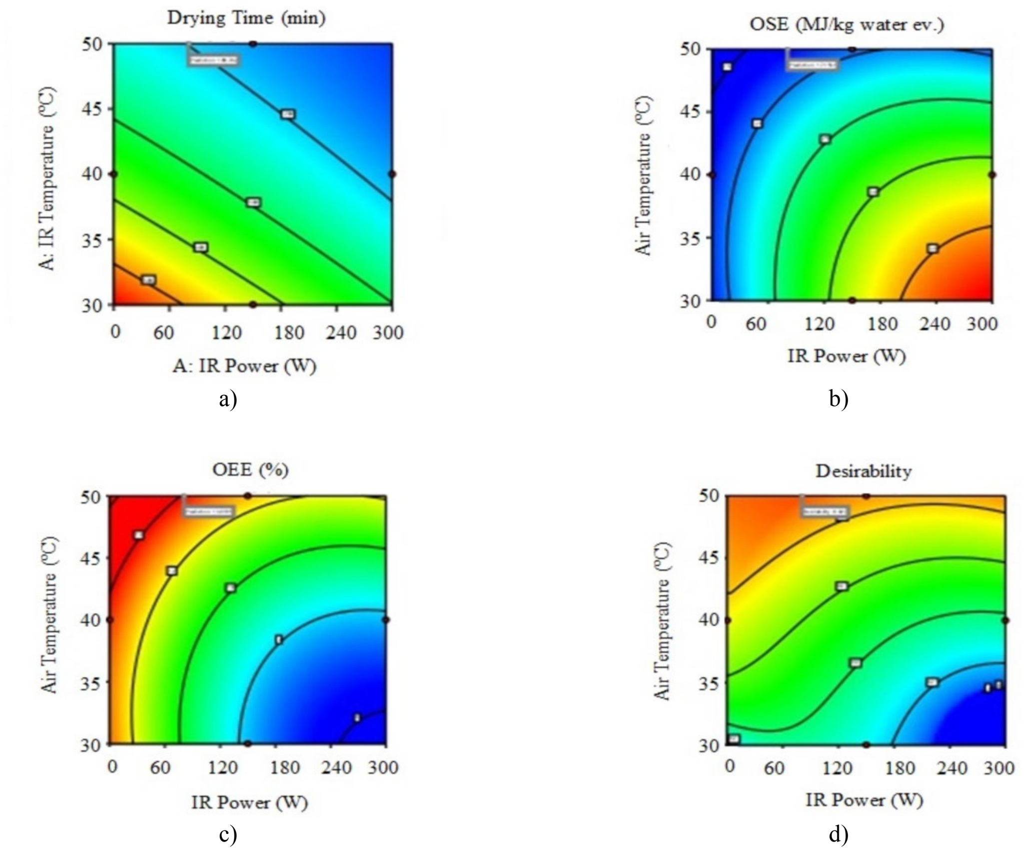

Figure 7. Suggested optimum point in the overall mode based on the combination of working factors for the values of: a) Drying time, b) OSE, c) OEE, and d) Desirability of the optimum point

3.2. Solar-assisted mode optimization

3.2.1. Statistical analysis

In the solar-assisted mode of optimization, the input independent variables for the drying system included IR power, inlet air speed, and air temperature. In this mode, the energy consumption of only non-solar energy sources of the drying system (i.e., gas water heater and centrifugal blower) was considered in the system optimization. The performance indicators of the drying system (responses of the RSM model) consisted of drying time, NSE, and SEE. The 17 working conditions determined by RSM analysis to conduct the experiments and to find the performance indicators of the drying system, together with the corresponding predicted values, are given in Table 5. It can be observed that there is an acceptable accordance between the values of the predicted responses and the experimental data.

The results revealed that the quadratic model based on Box-Behnken method was the superior model to describe the three responses based on the performance factors of the dryer. Table 6 presents the variance analysis of the three responses namely drying time, NSE, and SEE with respect to the three evaluated factors. The coefficient estimates based on the quadratic model are also given. In the solar-assisted optimization mode, all of the three performance indicators of the drying system were significantly influenced by the individual effects of the working factors (Table 6). Among the interaction effects on drying time, only the interaction of "IR power * air temperature" was statistically significant (p-value < 0.0001). The comparison between the predicted data and the actual data in the case of drying time, NSE, and SEE is shown in Figure 8. It can be observed that the values of the model were better fitted to the actual values in the case of drying time than the two other responses. This may be due to the parabolic variation trend of NSE and SEE with respect to independent variables.

Table 5. The design points suggested by Box-Behnken method for the experiments and their related experimental and predicted data in solar-assisted mode optimization

Run	Independent variables			Real responses (Experiment)			Predicted responses (Model)		
	IR Power (W)	Air temperature (ºC)	Air velocity (m/s)	Drying time (min)	NSE (MJ/kg water)	SEE (%)	Drying time (min)	NSE (MJ/kg water)	SEE (%)
1	300	50	8	104	10.84	21.97	116.13	11.61	26.68
2	150	50	7	176	10.20	23.35	174.26	11.09	23.43
3	150	30	9	394	6.13	39.63	395.74	5.25	40.17
4	150	40	8	248	3.44	69.98	249.6	3.47	69.94
5	150	40	8	251	3.56	67.69	249.6	3.47	69.94
6	0	30	8	567	7.70	31.56	554.87	6.93	27.48

7	150	50	9	139	16.99	14.03	137.5	16.15	14.72
8	300	40	7	191	2.71	88.71	180.63	1.08	84.88
9	150	40	8	252	3.67	65.55	249.6	3.47	69.94
10	0	40	9	316	5.08	47.41	326.37	6.72	51.86
11	150	40	8	247	3.13	76.90	249.6	3.47	69.94
12	150	40	8	250	3.54	68.06	249.6	3.47	69.94
13	0	50	8	221	17.60	13.54	212.13	16.78	9.32
14	150	30	7	429	5.00	48.61	430.5	5.83	48.54
15	300	40	9	159	2.91	82.80	148.37	2.98	78.34
16	0	40	7	355	4.20	57.33	365.63	4.14	62.40
17	300	30	8	279	4.48	54.25	287.87	5.30	59.08

Table 6. Analysis of variance of Quadratic model for in solar-assisted mode optimization

Source	df	Drying time (min)			Non-solar specific energy (MJ/kg water)			Solar-assisted energy efficiency (%)		
		Sum of squares	F-value❁	Coefficient estimate	Sum of squares	F-value	Coefficient estimate	Sum of squares	F-value	Coefficient estimate
Model	9	2.140E+05	180.81**	+249.60	343.38	24.25**	+3.47	8962.07	29.58**	+69.64
A	1	65884.50	501.05**	-90.75	23.22	14.76**	-1.70	1197.63	35.57**	+12.24
B	1	1.324E+05	1006.56**	-128.63	130.56	82.99**	+4.04	1278.83	37.99**	-12.64
C	1	2556.13	19.44**	-17.88	10.10	6.42*	+1.12	145.65	4.33ns	-4.27
AB	1	7310.25	55.59**	+42.75	3.12	1.98ns	-0.8825	50.78	1.51ns	-3.56
AC	1	12.25	0.0932ns	+1.75	0.1173	0.0746ns	-0.1713	4.02	0.1195ns	+1.00
BC	1	1.0000	0.0076ns	-0.5000	7.97	5.07*	+1.41	0.0294	0.0009ns	-0.0858
A²	1	203.38	1.55 ns	+6.95	0.7281	0.4628ns	+0.4158	2.85	0.0847ns	-0.8228
B²	1	5517.64	41.96**	+36.20	165.76	105.36**	+6.27	6235.07	185.21**	-38.48
C²	1	7.12	0.0541ns	-1.30	0.1061	0.0675ns	-0.1588	0.2658	0.0079ns	+0.2512
Residual	7	920.45			11.01			235.66		+69.64

❁: A-IR power; B-Air temperature; C-Air velocity; ** significant in 1 % probability level; * significant in 5 % probability level; ns: not statistically significant

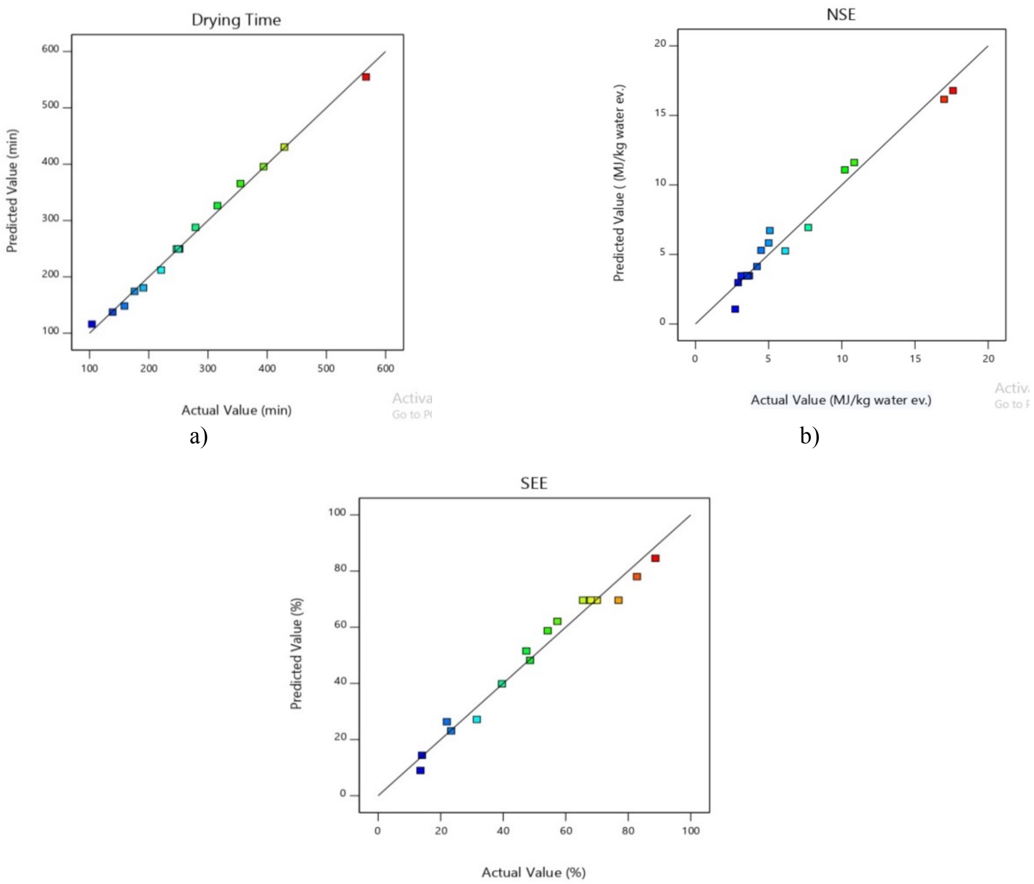

a) b)

(c)

Figure 8. The comparison of the predicted data and the actual data in the case of: a) drying time, b) NSE, and c) SEE

3.2.2. NSE

Variance analysis indicated that the interactions of "IR power × air temperature" and "air temperature × air speed" were significant. The highest NSE was equal to 17.60 MJ/kg water evaporated, which was obtained at an air speed of 8 m/s, air temperature of 50 °C, and IR power of 0 W. The lowest value of NSE (2.71 MJ/kg water evaporated) belonged to the air speed of 7 m/s, air temperature of 40 °C, and IR power of 300 W. The 3D graphical view of the mentioned interaction effect is shown in Figure 9. It can be seen that increasing the drying air temperature resulted in a parabolic increasing trend in the value of NSE. However, with increasing the air speed, the amount of NSE remained at an almost constant level. Increasing the value of NSE at the highest level of drying air temperature was due to the fact that at 50 ºC drying temperature, the thermal energy provided by the solar water heater was not sufficient to complete the drying process. Therefore, at this level of drying temperature, the gas water heater was turned on for a longer time and consequently, the energy consumption increased. Mehran et al. [4] reported that the values of specific energy and solar fraction in their developed solar rough rice dryer ranged from 8 to 22 kWh/kg water and 0.18 to 0.54, respectively. Benhamza et al. [16] indicated that applying an optimized chimney for drying chamber of an indirect solar dryer could decrease the required drying temperature by 7 degrees. In another research, Moghimi et al. [42] developed the performance of a household solar dryer for fruit and vegetables and analysed the dryer using Computational Fluid Dynamics (CFD). Their simulation analyses showed that the drying capacity could be upgraded by more than 50 % by adding a new type tray. According to these findings, one of the future works related to the current study may be the optimization of drying chamber based on analytical methods such as CFD simulations and finite volume method.

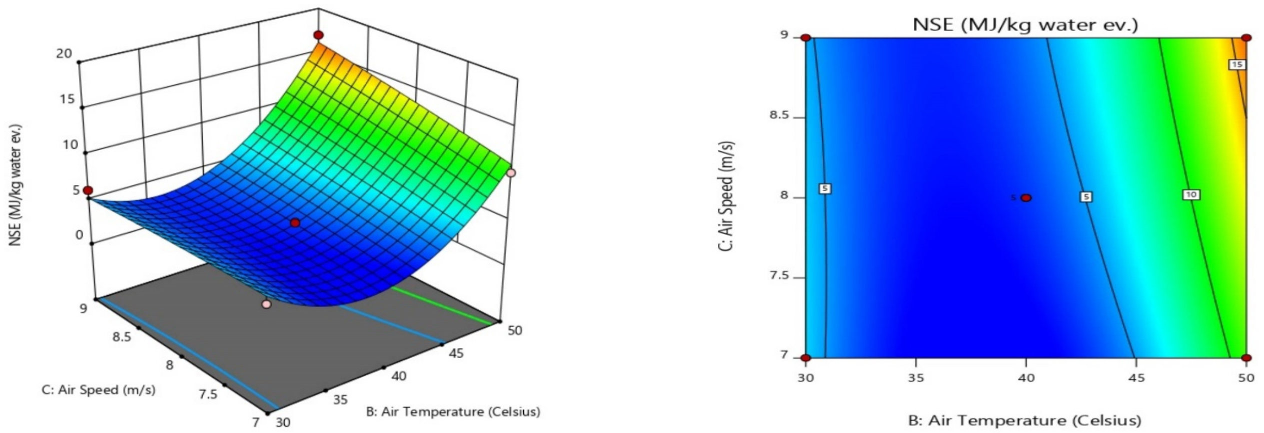

(a) (b)

Figure 9. Variations of NSE considering the interaction effect of Inlet air speed * Inlet air temperature in: a) Contour and b) 3d surface view

3.2.3. SEE

The variations of SEE considering the interaction effects of "air temperature * IR power" and "IR power * air speed" are shown in Figure 10. As can be seen, among the three input variables, IR power and inlet air speed caused a linear variation in the SEE. Compared with the inlet drying temperature of 35 ºC, the SEE increased at a temperature of 45 ºC. By applying 45 ºC temperature, the centrifugal blower worked for a shorter span of time and lower loss in the input energy to the system occurred. The drop in the SEE at the highest temperature level occurred because the gas water heater worked for more time. Subbian et al. [18] reported a decrease in thermal efficiency of their developed solar dryer with increasing drying air temperature.

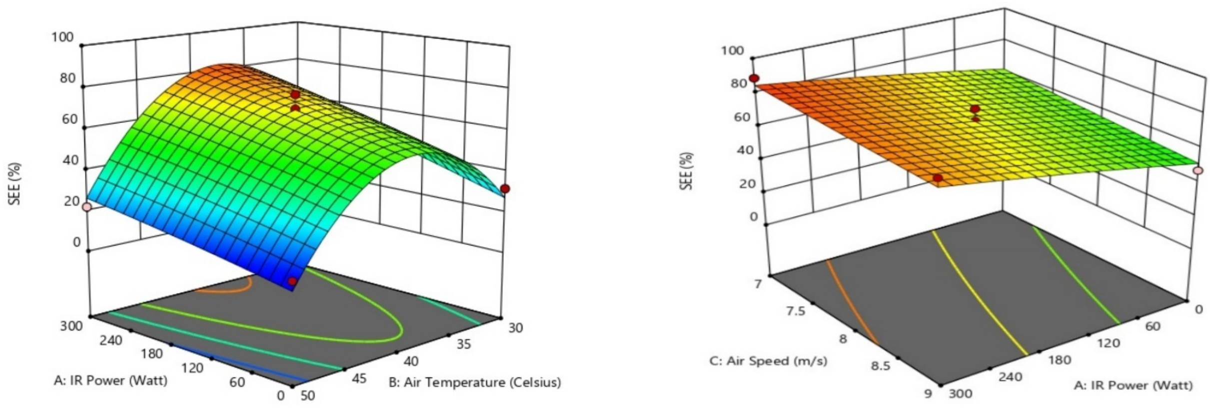

(a) (b)

Figure 10. Interaction effect of a) IR Power * Inlet air temperature and b) Inlet air speed * IR Power on the SEE

The results also revealed that the value of SEE increased with increasing the IR power. In the first optimization mode, it was observed that two different results would be obtained when the drying system gain the IR power in the form of non-solar or solar powered forms. The higher the non-solar powered IR heating, the lower the SEE, while the higher the solar powered IR heating, the higher the SEE. The highest SEE (88.71 %) was obtained at the levels combination of 7 m/s * 40 °C * 300 W, while the lowest SEE (6.35 %) was attributed to the condition of 8 m/s * 50 °C * 0 W. Manrique et al. [15] reported that approximately 10 % of total electrical energy requirement in their developed dryer could be provided by solar energy. Zoukit et al. [43] reported that the maximum values of energy efficiency in their proposed hybrid solar dryer ranged from 37 to 42 % in different evaluated conditions. Akpinar [21] reported that the energy utilization ratio in their developed drying system ranged from 7.826 % to 46.285 %.

3.2.4. Optimum conditions in solar-assisted mode

The goals of the optimization process in the second working mode were: to minimize the drying time, to minimize the NSE, and to maximize the SEE. In this mode, 68 points were found with desirability values of higher than 0.918. Table 7 presents the top ten solutions for the optimization process. The superior optimum point was obtained in the condition of 300 W * 39.96 ºC * 7 m/s. At this point, the values of drying time, NSE, and SEE were obtained as 180.95 min, 1.062 MJ/kg water, and 84.63 %, respectively. According to Table 7, it can be found that most of suggested working conditions by the optimization process in the solar-assisted mode were close to the point of 300 W * 40 ºC * 7 m/s. In terms of the effectiveness of IR lamps in the drying system, this finding was in contrast with the results of the first optimization mode. In the second optimization mode, which represents the real working conditions of the drying system, it was suggested that the highest level of IR power should be applied in order to achieve a higher drying efficiency. It can also be found that by applying solar-powered IR lamps in the drying system can result in a 10 ºC reduction in the inlet drying temperature, achieving a considerably decreased energy consumption and improved energy efficiency, as compared with the overall optimization mode. The situation of the suggested optimum point versus the evaluated working factors is shown in Figure 11. The applied optimization method was appropriately able to maintain the three responses at their desired levels. In the case of drying time and NSE, the related charts mostly tended to blue color (representing the normalized minimum values), while for the SEE and desirability indices, the optimization plots tended to red colors (maximum regions). It can also be observed that the optimization plot of the NSE was more filled with blue color than the OSE chart (Figure 5b). This shows that by using solar energy in the drying process, wider combinations of the working factors could be applied to achieve lower fossil energy consumption. According to the findings of this research, it is concluded that the application of the developed drying system can result in a remarkable reduction in the need for fossil fuel sources and consequently, a considerable decrease in the amount of greenhouse gases emission into the atmosphere. In recent years, several researchers have investigated the application of solar energy to drying systems of agricultural crops as well as optimization of the drying systems. Suzihaque and Driscoll [44] developed a solar dryer for coffee beans with the ability of heat recovery and optimized the dryer dimensions based on heat and mass transfer models. They concluded that the optimum values of the dryer height and length and coffee bed thickness were equal to 0.4030 m, 0.7920 m, and 0.0278 m, respectively. Sethi and Dhiman [45] developed a hybrid greenhouse dryer for fenugreek drying by combination of solar-biomass energy. Optimization process demonstrates that to have a drying air temperature of 32.3-62.4 ºC, the heating requirements of the dryer may range from 0.348 to 12.18 kW.

Table 7. The top ten suggested optimal working conditions of the drying system in the solar-assisted optimization mode

No.	IR power (W)	Drying air temperature (ºC)	Drying air velocity (m/s)	Drying time (min)	NSE (MJ/kg water evaporated)	Solar-assisted energy efficiency (%)	Desirability	
1	300.000	39.961	7.000	180.955	1.062	84.626	0.924	**Selected**
2	300.000	39.846	7.002	181.924	1.046	84.797	0.924	
3	299.998	39.983	7.008	180.661	1.076	84.561	0.924	
4	300.000	39.869	7.015	181.548	1.066	84.713	0.924	
5	300.000	39.732	7.000	182.938	1.027	84.969	0.924	
6	300.000	39.917	7.031	180.921	1.093	84.581	0.924	
7	300.000	39.902	7.040	180.924	1.103	84.569	0.924	
8	299.718	40.073	7.000	180.148	1.084	84.426	0.924	
9	299.998	39.927	7.051	180.565	1.120	84.491	0.924	
10	299.999	39.491	7.000	185.069	0.996	85.286	0.923	

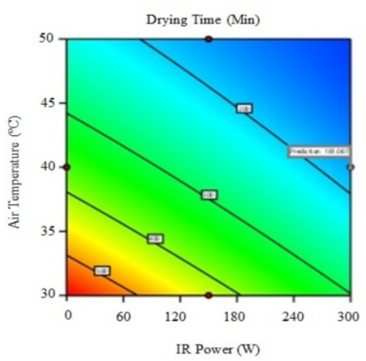

a)

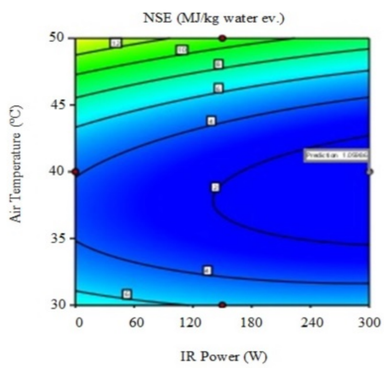

b)

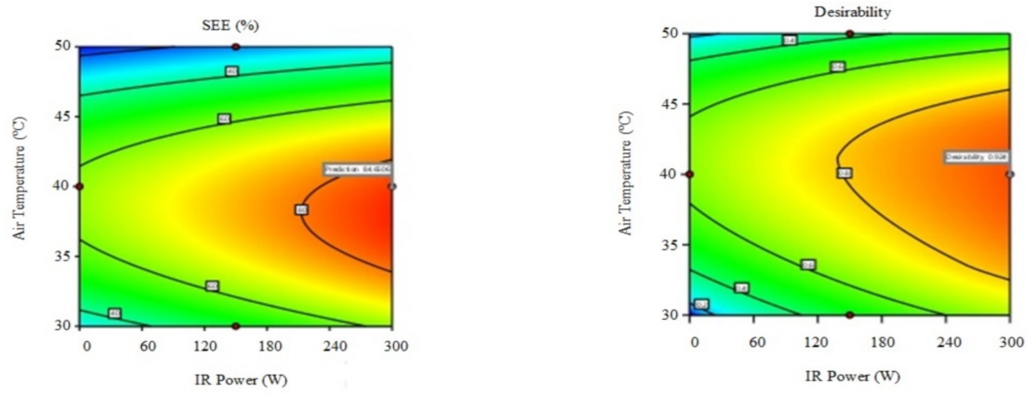

c) d)

Figure 11. Suggested optimum point in the solar-assisted mode based on the combination of working factors for the values of: a) Drying time, b) NSE, c) SEE, and d) Desirability of the optimum point

4. CONCLUSIONS

In this study, the energy efficiency and performance characteristics of a solar-assisted multi-belt conveyor dryer were evaluated experimentally. The RSM-based optimization process was performed considering two general working modes for the drying system. In the first mode (named as the overall mode), the energy consumption of both solar and non-solar energy sources was considered in the analyses. In the second mode (called as solar-assisted mode), only the non-solar energy sources (gas water heater and centrifugal blower) were considered in the system optimization. According to the results obtained, the following conclusions were derived:

• The increase in the inlet temperature resulted in a kind of parabolic change with a decreasing trend in the value of OSE. Increasing the IR power similarly caused a parabolic change in the specific energy. However, the trend of variations in this case increased.

• It was observed that upon increasing IR power, the OEE decreased. This indicates that at the higher levels of non-solar IR power, a more amount of energy was wasted in the system. The value of OEE increased upon increasing the inlet temperature.

• Depending on whether the dryer gains the IR power in the form of non-solar or solar powered forms, two different results can be obtained. The higher the non-solar powered IR heating, the lower the energy efficiency, while the higher the solar powered IR heating, the higher the energy efficiency.

• The overall comparison between the values of OEE and SEE indicated that the variation of OEE versus the inlet temperature was increasing and approximately linear, while the SEE had a parabolic increasing trend with respect to the increased temperature.

• The value of OEE in the drying system ranged from 5.87 to 14.01 %, whilst the SEE during the experiments was obtained in the range of 9.32-84.88 %. The considerable difference between the values of OEE and SEE is a good indicator to illustrate the effect of renewable energy sources in the second optimization mode. In other words, in the second optimization mode, the lower amounts of fuel-based energy sources were used for moisture removal from the product. This finding can lead to a significant improvement in the process cost, energy consumption, and efficiency in the long term.

• The majority of the suggested working conditions by the optimization process in the solar-assisted mode corresponded to the treatment of 300 W * 40 ºC * 7 m/s. This finding was in contrast with the results of the first optimization mode in terms of the effectiveness of IR lamps in the drying system. In the second optimization mode, which represents the real working conditions of the drying system, it was suggested that in order to have a higher drying efficiency, the highest level of IR power should be applied.

• Comparison of the optimum points suggested that by using RSM in the two defined optimization modes, it was found that applying solar-powered IR lamps in the drying system could result in a 10 ºC reduction in the inlet drying temperature while achieving considerably decreased energy consumption and improved energy efficiency, as compared with the overall optimization mode.

• According to the findings of this research, it is concluded that the application of the developed drying system can result in a remarkable reduction in the need for fossil fuel sources that can consequently cause a decrease in the amount of greenhouse gases emission into the atmosphere. The developed drying system may also be converted into a very low or even zero fossil energy consuming dryer if the centrifugal blower is powered by solar-based electrical energy.

• One of the working limitations of the proposed drying system was the unpredictability of the prevailing weather conditions in the region of study so that the thermal energy generation capacity of the solar system might be affected by occasional cloudiness. However, thanks to the capability of the proposed system to store the thermal energy in the water heater reservoir and solar panel batteries, it was made possible to supply a considerable part of the required heat in such conditions.

• Since previous studies have demonstrated that the application of an optimized chimney for drying chamber of solar dryers could decrease the required drying temperature and thermal energy, the future works may be focused on the optimization of the system drying chamber based on analytical methods such as computational fluid dynamics. Moreover, the development of an automated control system for the dryer to instantaneously monitor and adjust the major working parameters of the drying process can be one of the other future areas of interest.

5. ACKNOWLEDGEMENT

The authors would like to thank the University of Guilan for financially support of this research under grant number of 128234.

NOMENCLATURE

ΔP	Total pressure drop (kPa)
c_p	Specific heat of water (J/kg ºC)
E_{cb}	Energy consumption of the centrifugal blower (MJ)
E_e	Energy required for moisture evaporation (MJ)
E_{eq}	Energy equivalent of natural gas (MJ/m^3)
E_{gwh}	Energy consumption of the gas water heater (MJ)
E_{irc}	Energy consumption of IR circuit (MJ)
E_{ns}	Non-solar type of energy consumed by the drying system (MJ)
E_{swh}	Energy consumption of solar water heater (MJ)
E_t	Overall energy consumed by the drying system (MJ)
h_{fg}	Latent heat of vaporization (MJ/kg)
i	Number of variables
IR	Infrared
m_0	Initial mass of the product (kg)
MC_0	Initial moisture content of the product (%)
$MC_{d.b.}$	Product moisture based on the dry mass (% d.b.)
MC_f	Final moisture content of the product (%)
m_{ew}	Mass of water evaporated during the drying process (kg)
M_f	Final mass of dried sample (g)
M_i	Initial mass of sample (g)
m_w	Mass of water in the tank (kg)
NSE	Non-solar specific energy (MJ)
OSE	Overall specific energy (MJ)
OEE	Overall energy efficiency (MJ)
P_{ir}	Power consumed by IR circuit (W)
Q_a	Volumetric airflow of blower (m^3/s)
RSM	Response Surface Methodology
SEE	Solar-assisted energy efficiency (MJ)
t	Drying time (s)
T_{fw}	Final temperature of water (ºC)
T_{iw}	Initial temperature of water (ºC)
V_g	Volume of consumed natural gas by the water heater (m^3)
X_i	Coded (independent) variable
X_j	Dependent variable
Y_i	Estimated response
β_{ij}	Constant of variables interaction
β_j	Variables constant
β_{jj}	Constant of second-order parameter
β_o	Model constant
ε	Random error

REFERENCES

1. Lingayat, A.B., Chandramohan, V., Raju, V. and Meda, V., "A review on indirect type solar dryers for agricultural crops–Dryer setup, its performance, energy storage and important highlights", ***Applied Energy***, Vol. 258, (2020), 114005. (https://doi.org/10.1016/j.apenergy.2019.114005).
2. El Hage, H., Herez, A., Ramadan, M., Bazzi, H. and Khaled, M., "An investigation on solar drying: A review with economic and environmental assessment", ***Energy***, Vol. 157, (2018), 815-829. (https://doi.org/10.1016/j.energy.2018.05.197).
3. Sagar, V. and Kumar, P.S., ″Recent advances in drying and dehydration of fruits and vegetables: A review", ***Journal of Food Science and Technology***, Vol. 47 No. 1, (2010), 15-26. (https://dx.doi.org/10.1007%2Fs13197-010-0010-8).
4. Mehran, S., Nikian, M., Ghazi, M., Zareiforoush, H. and Bagheri, I., ″Experimental investigation and energy analysis of a solar-assisted fluidized-bed dryer including solar water heater and solar-powered infrared lamp for paddy grains drying", ***Solar Energy***, Vol. 190, (2019), 167-184. (https://doi.org/10.1016/j.solener.2019.08.002).
5. Jin, W., Mujumdar, A.S., Zhang, M. and Shi, W., "Novel drying techniques for spices and herbs: A review", ***Food Engineering Reviews***, Vol. 10, No. 1, (2018), 34-45. (https://doi.org/10.1007/s12393-017-9165-7).
6. Lakshmi, D., Muthukumar, P., Layek, A. and Nayak, P.K., "Performance analyses of mixed mode forced convection solar dryer for drying of stevia leaves", ***Solar Energy***, Vol. 188, (2019), 507-518. (https://doi.org/10.1016/j.solener.2019.06.009).
7. Eltawil, M.A., Azam, M.M. and Alghannam, A.O., "Energy analysis of hybrid solar tunnel dryer with PV system and solar collector for drying mint (MenthaViridis)", ***Journal of Cleaner Production***, Vol. 181, (2018), 352-364. (https://doi.org/10.1016/j.jclepro.2018.01.229).
8. Hamdi, I., ELkhadraoui, A., Kooli, S., Farhat, A. and Guizani, A., "Drying of red pepper slices in a solar greenhouse dryer and under open sun: Experimental and mathematical investigations", ***Innovative Food Science & Emerging Technologies***, (2019). (https://doi.org/10.1016/j.ifset.2019.01.001).
9. Karthikeyan, A. and Murugavelh, S., "Thin layer drying kinetics and exergy analysis of turmeric (Curcuma longa) in a mixed mode forced convection solar tunnel dryer", ***Renewable Energy***, Vol. 128, (2018), 305-312. (https://doi.org/10.1016/j.renene.2018.05.061).
10. Yahya, M., Fudholi, A. and Sopian, K., "Energy and exergy analyses of solar-assisted fluidized bed drying integrated with biomass furnace", ***Renewable Energy***, Vol. 105, (2017), 22-29. (https://doi.org/10.1016/j.renene.2016.12.049).
11. Ziaforoughi, A. and Esfahani, J.A., "A salient reduction of energy consumption and drying time in a novel PV-solar collector-assisted intermittent infrared dryer", ***Solar Energy***, Vol. 136, (2016), 428-436. (https://doi.org/10.1016/j.solener.2016.07.025).
12. El-Sebaii, A. and Shalaby, S., "Experimental investigation of an indirect-mode forced convection solar dryer for drying thymus and mint", ***Energy Conversion and Management***, Vol. 74, (2013), 109-116. (https://doi.org/10.1016/j.enconman.2013.05.006).
13. Lamnatou, C., Papanicolaou, E., Belessiotis, V. and Kyriakis, N., "Experimental investigation and thermodynamic performance analysis of a solar dryer using an evacuated-tube air collector", ***Applied Energy***, Vol. 94, (2012), 232-243. (https://doi.org/10.1016/j.apenergy.2012.01.025).
14. Akbulut, A. and Durmuş, A., "Energy and exergy analyses of thin layer drying of mulberry in a forced solar dryer", ***Energy***, Vol. 35, No. 4, (2010), 1754-1763. (https://doi.org/10.1016/j.energy.2009.12.028).
15. Manrique, R., Vásquez, D., Chejne, F. and Pinzón, A., "Energy analysis of a proposed hybrid solar–biomass coffee bean drying system", ***Energy***, (2020), 117720. (https://doi.org/10.1016/j.energy.2020.117720).
16. Benhamza, A., Boubekri, A., Atia, A., Hadibi, T. and Arıcı, M., "Drying uniformity analysis of an indirect solar dryer based on computational fluid dynamics and image processing", ***Sustainable Energy Technologies and Assessments***, Vol. 47, (2021), 101466. (https://doi.org/10.1016/j.seta.2021.101466).
17. Atalay, H., Coban, M.T. and Kıncay, O., "Modeling of the drying process of apple slices: Application with a solar dryer and the thermal energy storage system", ***Energy***, Vol. 134, (2017), 382-391. (https://doi.org/10.1016/j.energy.2017.06.030).
18. Subbian, V., Kumar, S.S., Chaithanya, K., Arul, S.J., Kaliyaperumal, G. and Adam, K.M., "Optimization of solar tunnel dryer for mango slice using response surface methodology", ***Materials Today: Proceedings***, Vol. 46, (2021). (https://doi.org/10.1016/j.matpr.2021.02.382).
19. Sami, S., Etesami, N. and Rahimi, A., ″Energy and exergy analysis of an indirect solar cabinet dryer based on mathematical modeling results", ***Energy***, Vol. 36, No. 5, (2011), 2847-2855. (https://doi.org/10.1016/j.energy.2011.02.027).
20. Afriyie, J.K., Rajakaruna, H., Nazha, M.A. and Forson, F., "Mathematical modelling and validation of the drying process in a chimney-dependent solar crop dryer", ***Energy Conversion and Management***, Vol. 67, (2013), 103-116. (https://doi.org/10.1016/j.enconman.2012.11.007).
21. Akpinar, E.K., "Drying of mint leaves in a solar dryer and under open sun: Modelling, performance analyses", ***Energy Conversion and Management***, Vol. 51, No. 12, (2010), 2407-2418. (https://doi.org/10.1016/j.enconman.2010.05.005).
22. Jha, A. and Tripathy, P., "Optimization of process parameters and numerical modeling of heat and mass transfer during simulated solar drying of paddy", ***Computers and Electronics in Agriculture***, Vol. 187, (2021), 106215. (https://doi.org/10.1016/j.compag.2021.106215).

23. Jahangiri, M., Alidadi Shamsabadi, A. and Saghaei, H., "Comprehensive evaluation of using solar water heater on a household scale in Canada", ***Journal of Renewable Energy and Environment (JREE)***, Vol. 5, No. 1, (2018), 35-42. (https://dx.doi.org/10.30501/jree.2018.88491).

24. Pahlavan, S., Jahangiri, M., Alidadi Shamsabadi, A. and Khechekhouche, A., "Feasibility study of solar water heaters in Algeria, A review", ***Journal of Solar Energy Research***, Vol. 3, No. 2, (2018), 135-146. (https://jser.ut.ac.ir/article_67424.html).

25. Zaniani, J.R., Dehkordi, R.H., Bibak, A., Bayat, P. and Jahangiri, M., "Examining the possibility of using solar energy to provide warm water using RETScreen4 software (Case study: Nasr primary school of pirbalut)", ***Current World Environment***, Vol. 10, (2015), 835. (http://dx.doi.org/10.12944/CWE.10.Special-Issue1.101).

26. Siampour, L., Vahdatpour, S., Jahangiri, M., Mostafaeipour, A., Goli, A., Alidadi Shamsabadi, A. and Atabani, A., "Techno-enviro assessment and ranking of Turkey for use of home-scale solar water heaters", ***Sustainable Energy Technologies and Assessments***, Vol. 43, (2021), 100948. (https://doi.org/10.1016/j.seta.2020.100948).

27. Jahangiri, M., Akinlabi, E.T. and Sichilalu, S.M., "Assessment and modeling of household-scale solar water heater application in Zambia: Technical, environmental, and energy analysis", ***International Journal of Photoenergy***, (2021). (https://doi.org/10.1155/2021/6630338).

28. Periche, A., Castelló, M.L., Heredia, A. and Escriche, I., "Influence of drying method on steviol glycosides and antioxidants in Stevia rebaudiana leaves", ***Food Chemistry***, Vol. 172, (2015), 1-6. (https://doi.org/10.1016/j.foodchem.2014.09.029).

29. ASABE, "Moisture measurement—Unground grain and seeds", American Society of Agricultural and Biological Engineers, (2019).

30. Firouzi, S., Alizadeh, M.R. and Haghtalab, D., "Energy consumption and rice milling quality upon drying paddy with a newly-designed horizontal rotary dryer", ***Energy***, Vol. 119, (2017), 629-636. (https://doi.org/10.1016/j.energy.2016.11.026).

31. Sharifi, H., Babapour, Sh. and Sherkati, Sh., "Evaluation of problems caused by thermal degradation of consumed gas in Iran's thermal power stations", Tehran, Iran, (2004).

32. Ceylan, I., "Energy and exergy analyses of a temperature controlled solar water heater", ***Energy and Buildings***, Vol. 47, (2012), 630-635. (https://doi.org/10.1016/j.enbuild.2011.12.040).

33. Tohidi, M., Sadeghi, M. and Torki-Harchegani, M., "Energy and quality aspects for fixed deep bed drying of paddy", ***Renewable and Sustainable Energy Reviews***, Vol. 70, (2017), 519-528. (https://doi.org/10.1016/j.rser.2016.11.196).

34. Anum, R., Ghafoor, A. and Munir, A., "Study of the drying behavior and performance evaluation of gas fired hybrid solar dryer", ***Journal of Food Process Engineering***, Vol. 40, No. 2, (2017), 12351. (https://doi.org/10.1111/jfpe.12351).

35. Myers, R.H., Montgomery, D.C. and Anderson-Cook, C.M., Response surface methodology: Process and product optimization using designed experiments, John Wiley & Sons, (2016). (https://www.wiley.com/en-us/Response+Surface+Methodology%3A+Process+and+Product+Optimization+Using+Designed+Experiments%2C+4th+Edition-p-9781118916018).

36. Yang, Z.-H., Huang, J., Zeng, G.-M., Ruan, M., Zhou, C.-S., Li, L. and Rong, Z.G., "Optimization of flocculation conditions for kaolin suspension using the composite flocculant of MBFGA1 and PAC by response surface methodology", ***Bioresource Technology***, Vol. 100, No. 18, (2009), 4233-4239. (https://doi.org/10.1016/j.biortech.2008.12.033).

37. Chen, X., Du, W. and Liu, D., "Response surface optimization of biocatalytic biodiesel production with acid oil", ***Biochemical Engineering Journal,*** Vol. 40, No. 3, (2008), 423-429. (https://doi.org/10.1016/j.bej.2008.01.012).

38. Singh, G.D., Sharma, R., Bawa, A. and Saxena, D., "Drying and rehydration characteristics of water chestnut (Trapa natans) as a function of drying air temperature", ***Journal of Food Engineering***, Vol. 87, No. 2, (2008), 213-221. (https://doi.org/10.1016/j.jfoodeng.2007.11.027).

39. Soodmand-Moghaddam, S., Sharifi, M. and Zareiforoush, H., "Investigation of fuel consumption and essential oil content in drying process of lemon verbena leaves using a continuous flow dryer equipped with a solar pre-heating system", ***Journal of Cleaner Production***, Vol. 233, (2019), 1133-1145. (https://doi.org/10.1016/j.jclepro.2019.06.083).

40. Lin, Y.P., Lee, T.Y., Tsen, J.H. and King, V.A.E., "Dehydration of yam slices using FIR-assisted freeze drying", ***Journal of Food Engineering***, Vol. 79, No. 4, (2007), 1295-1301. (https://doi.org/10.1016/j.jfoodeng.2006.04.018).

41. Jafari, F., Movagharnejad, K. and Sadeghi, E., "Infrared drying effects on the quality of eggplant slices and process optimization using response surface methodology", ***Food Chemistry***, (2020), 127423. (https://doi.org/10.1016/j.foodchem.2020.127423).

42. Moghimi, P., Rahimzadeh, H. and Ahmadpour, A., "Experimental and numerical optimal design of a household solar fruit and vegetable dryer", ***Solar Energy***, Vol. 214, (2021), 575-587. (https://doi.org/10.1016/j.solener.2020.12.023).

43. Zoukit, A., El Ferouali, H., Salhi, I., Doubabi, S. and Abdenouri, N., "Simulation, design and experimental performance evaluation of an innovative hybrid solar-gas dryer", ***Energy***, Vol. 189, (2019), 116279. (https://doi.org/10.1016/j.energy.2019.116279).

44. Suzihaque, M. and Driscoll, R., "Effects of solar radiation, buoyancy of air flow and optimization study of coffee drying in a heat recovery dryer", ***Procedia Engineering***, Vol. 148, (2016), 812-822. (https://doi.org/10.1016/j.proeng.2016.06.617).

45. Sethi, V. and Dhiman, M., "Design, space optimization and modelling of solar-cum-biomass hybrid greenhouse crop dryer using flue gas heat transfer pipe network", ***Solar Energy***, Vol. 206, (2020), 120-135. (https://doi.org/10.1016/j.solener.2020.06.006).

JREE: Vol. 9, No. 1, (Winter 2022) 93-105

Journal of Renewable Energy and Environment

Journal Homepage: www.jree.ir

Materials and Energy Research Center

MERC

Research Article

Chlorella vulgaris Cultivation Using Triangular External Loop Airlift Photobioreactor: Hydrodynamic and Mass Transfer Studies

Shiva Shadpour [a], Ali Pirouzi [a*], Mohsen Nosrati [b], Hoda Hamze [c]

[a] *Department of Chemical Engineering, University of Science and Technology of Mazandaran, P. O. Box: 48518-78195, Behshahr, Mazandaran, Iran.*
[b] *Biotechnology Group, Faculty of Chemical Engineering, Tarbiat Modares University, P. O. Box: 14115-143, Tehran, Tehran, Iran.*
[c] *Chemistry and Chemical Engineering Research Center of Iran (CCERCI), P. O. Box: 14335-186, Tehran, Tehran, Iran.*

PAPER INFO

Paper history:
Received: 13 June 2021
Revised in revised form: 04 August 2021
Scientific Accepted: 10 August 2021
Published: 08 January 2022

Keywords:
Airlift Photobioreactor,
Chlorella vulgaris,
Hydrodynamics,
Mass Transfer,
Mixing Time

ABSTRACT

Long mixing time, high power consumption, and small mass transfer coefficients are common problems in the photobioreactor design for microalgae culture which have a great effect on system efficiency and performance, CO_2 stabilization, and biomass production. In this study, a special design of the triangular external loop airlift photobioreactor was studied. The bioreactor's geometry was such that the angle between hypotenuse and the horizontal side (α) could vary. This configuration created an effective gas-liquid countercurrent flow in the downcomer section. In the present research, hydrodynamic and mass transfer of the reactor were investigated on the microalgae productivity under different design and operating parameters. The optimum conditions for the enhancement of *Chlorella vulgaris* productivity were explored by analyzing the mixing time (t_m), volumetric power consumption (P/V), mass transfer coefficients (k_La), bubble diameter (d), and gas holdup (ε) as responses. The results showed that the hypotenuse angle of $\alpha = 59^o$ and the superficial gas velocities of the $V_{gs1} = 0.0050$ m.s^{-1} for the downcomer and $V_{gs2} = 0.008$ m.s^{-1} for the riser of the reactor were the best conditions to achieve the highest biomass productivity. The responses' values obtained in the optimum condition were as follows: k_La_R= 19.67 (h^{-1}), k_La_D = 23.79 (h^{-1}), k_La_S = 23.76 (h^{-1}), $\theta_m = t_m/t_c$= 0.41, and $P/V = 62.83\ W/m^3$, which had a smaller deviation than the actual values. The highest concentration of *Chlorella vulgaris* ($X_{max} = 1.4$ g.l^{-1}) achieved in this work was obtained in a shorter span of time (11th day of cultivation) based on the growth curve in optimized conditions.

https://doi.org/10.30501/jree.2021.290449.1216

1. INTRODUCTION

A photobioreactor (PBR) is specialized equipment designed to cultivate photosynthesis microorganisms such as microalgae species and operates under optimal light, mixing time, and mass transfer [1]. This equipment provides the ability to produce pure microalgae from CO_2 (free of any contamination) [2]. Airlift photobioreactor and bubble columns are systems in which the mixing of the fluids is performed by the gas bubbles created by the sparger placed at the base of the column [3]. An external-loop airlift PBR is one kind of the bubble-column that provides more favorable culture conditions by making a proper mixing process through the liquid phase circulating [4]. In these photobioreactors, lower turbulence is observed than the bubble column because of the adjustment of the vortexes by the bubble formation [5]. Also, due to the mixing improvement at the external-loop airlift PBR, a more homogenous environment for microalgae culture is provided [6, 7].

Nonetheless, the economic feasibility of microalgae production in these devices is significantly affected by cultivation technology and process designing [8]. It has been proven that the microorganism growth rate is dependent on the mixing process. However, the mobility of the culture medium (either mechanically or by aeration) along severe tensions can influence the growth rate negatively, which consequently made the biomass separation difficult [9]. In addition, it is expected that the superficial gas velocities could be effective in the mixing, CO_2 adsorption, and availability of the light and nutrient in the culture system. The previous research carried out by Powtongsook et al. (2006) [10] has shown the influence of varying superficial gas velocities on the growth of *H. pluvialis* cells in an airlift PBR. They have reported that the main reason for growth decline is the increased shear stress due to high sparging rates [10]. Also, other research studies have proven morphological damages to the microorganisms due to the hydrodynamic tensions [11].

Besides, it is now well established that the microalgae growth is controlled by the mass transfer of CO_2 from gas to liquid phase [12]. CO_2 diffusion from the gas phase to the mass bulk is related to the overall mass transfer coefficient

*Corresponding Author's Email: a.pirouzi@mazust.ac.ir (A. Pirouzi)
URL: https://www.jree.ir/article_143018.html

Please cite this article as: Shadpour, Sh., Pirouzi, A., Nosrati, M. and Hamze, H., "*Chlorella vulgaris* cultivation using triangular external loop airlift photobioreactor: Hydrodynamic and mass transfer studies", ***Journal of Renewable Energy and Environment (JREE)***, Vol. 9, No. 1, (2022), 93-105. (https://doi.org/10.30501/jree.2021.290449.1216).

(k_La), which itself is influenced by the bubble size, mixing rate, and the superficial gas velocity through the media [13]. Several works have been conducted to formulate the mass transfer and seek the best condition in gas-liquid systems [13-15]. It is very significant to consider that good mixing should be achieved with the least power usage. According to the investigations, mixing time decreases with increasing aeration rates. Also, the volume of the photobioreactor and its geometry influence the mixing time [16]. Moreover, the mixing time in the airlift PBRs increases significantly with the addition of the riser height.

Additionally, the gas holdup as an essential factor in photobioreactor design and its scale-up are associated with the superficial gas velocity, fluid circulation rate, the nozzle type, and the gas bubble sparger [17-19]. With the increment of gas feeding, the gas holdup of the bioreactor is reduced. For example, based on previous studies, more gas holdup implies a longer mixing time and higher mass transfer coefficients in the bioreactors [19]. It is not an absolute principle and can be changed by the photobioreactors' geometry and arrangement and, consequently, by the gas flow regime [19, 20].

Therefore, process optimization and improvement of biomass productivity require studying hydrodynamics and mass transfer of culture mediums. According to the reports, despite the high energy demand of photobioreactors, the biomass produced is very low. An innovative design of a photobioreactor can result in high microalgae growth rates and lower production costs [21]. Due to their many advantages, the airlift photobioreactors, including their high compatibility with three-phase media, lack of stirring equipment, and proper mixing, compared to the stirred tank and the type of bubble column, provide a suitable environment for biotechnology processes [22]. In these bioreactors, a regular stream is generated through the system using aeration principles to prevent shear stresses. Through the feeding of carbon dioxide-rich air, the mixing process and CO_2 supply in such systems are provided [23]. The mixing intensity, hydrodynamic, and mass transfer properties are critical design parameters of the bioreactors [20, 23].

In this study, the specific case of a triangular external loop airlift photobioreactor has been studied to cultivate *Chlorella vulgaris*. In earlier photobioreactors, the downcomer have demonstrated poor mass transfer and gas hold-up, which limits the residence time of air bubbles in this section of photobioreactors. In the present study, the creation of a countercurrent flow and high vortices in the downcomer increased the performance of the mixing and mass transfer process. This work aimed to investigate the influences of the geometry and operational parameters on the system performance. We evaluated how superficial gas velocities can influence the hydrodynamic and mass transfer behavior. This research set out to understand the effect of another critical factor better, the angle between the hypotenuse (downcomer) and the bioreactor's horizontal side (α). Response Surface Methodology (RSM) combined with the Central Composite Design (CCD) was applied to data analysis.

2. EXPERIMENTAL

2.1. Photobioreactor

Plexiglass-made triangular external loop photobioreactor with a working volume of 63 l was utilized for the research. A schematic diagram of the experimental setup is presented in Figure 1. The PBR includes two main sections: the upstream tube (riser) and the external loop, connected to the reactor from the top at an angle of 45° acting as the downcomer. The bioreactor's geometry is such that the angle between hypotenuse and the horizontal side (α) can vary. In this system, the gas was sparged from two locations: the lowest point of the hypotenuse and the riser. So, the gas and liquid were contacted co-current and countercurrent at the riser and downcomer, respectively. The mixing rate created in this way depends on the bioreactor's shape and geometry and superficial gas velocities. The superficial gas velocities of the downcomer and riser were denoted by V_{gs1} and V_{gs2}, respectively. All tests were performed at 25 °C and controlled using a computer Temperature Loop Controller (TLC), and a heat exchanger. The pH was adjusted by sodium hydroxide (1 M) and hydrochloric acid (1 M) solutions through two metering pumps controlled by the computer.

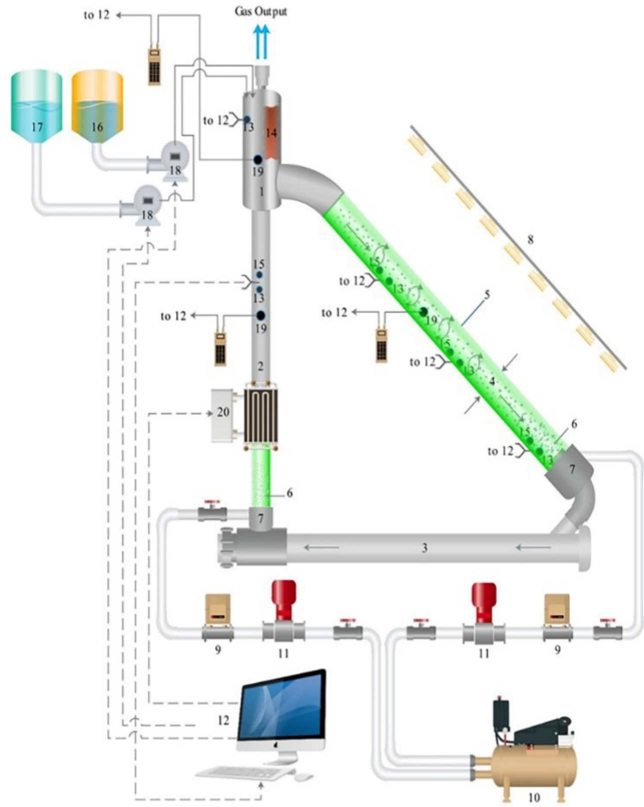

Figure 1. Schematic of an external airlift loop PBR. 1: Separator; 2: Riser; 3: Horizontal side; 4: Diameter of hypotenuse; 5: Downcomer; 6: Bubble; 7: Bubble sparger; 8: Light source; 9: Digital gas flow meter; 10: Compressor; 11: Gas sterilizer, filter; 12: PC; 13: Thermometer; 14: Heater; 15: pH probe; 16: NaOH solution; 17: HCl solution; 18: Dozing pump; 19: DO sensor; 20: Heat exchanger

3. METHOD

3.1. *Chlorella vulgaris* cultivation

The strain *Chlorella vulgaris* (ISC23) was provided from microalgae bank at Shahid Beheshti University, Tehran, Iran. The culture medium (N8) used in this study contained the following components: $Na_2HPO_4.2H_2O$ (0.260 g/l)), $MgSO_4.7H_2O$ (0.050 g/l), KH_2PO_4 (0.232 g/l), $CaCl_2.6H_2O$ (0.010 g/l), KNO_3 (1.000 g/l), Fe-EDTA (0.010 g/l), and trace elements solution of 1 ml. The trace elements mixture was made by the following constituents: $Al_2(SO_4)_3$ (3.580 g/l), $MnCl_2.4H_2O$ (12.980 g/l), $ZnSO_4.7H_2O$ (1.830 g/l), and

$CuSO_4.5H_2O$ (3.200 g/l). The pH of the medium was adjusted in the range of 6.8-7.0. The tap water was used for all experimental runs, and the required CO_2 was supplied through aeration.

3.2. Measurements

Liquid mixing is one of the essential factors that should be considered in the design and operational conditions. Good mixing in the bioreactor leads to minimizing the nutrient's transmission period into biomass during the culture. Here, mixing time (t_m) is characterized by the time needed to obtain 95 % complete mixing through the system [16]. This time is calculated by the acid trace technique [24]. Circulation time (t_c) and superficial fluid velocity were estimated by this method. The time needed for the flow to thoroughly loop around the reactor is specified by the circulation time and determined by the time period between the two pH consecutive peaks. The overall liquid velocity was calculated by dividing the tracer's travelled length by the circulation time [25]. The proportion of the airflow rate (Q) and each section's cross-sectional area was calculated as the superficial gas velocity (V_{gs}) of the section [26].

The overall gas holdup (ε) as a function of volume expansion to the initial volume (un-aerated volume) was measured using a volume expansion technique [27]. The volume expansion of a region of the reactor is defined as a differential hydrostatic pressure of two heads of that region. A U-tube inverted differential manometer measured the pressure difference.

The liquid phase's volumetric mass transfer coefficient (k_La) was estimated by the dynamic gassing out measurements [19]. In this method, Dissolved Oxygen (DO) was withdrawn from the liquid phase by injecting N_2 gas. Since the O_2 removal was completed, the air was introduced and the increase in dissolved O_2 concentration was recorded with time by a DO electrode. The following expression determined mass balance for oxygen:

$$\frac{dC}{dt} = k_La(C^* - C) \tag{1}$$

where C and C^* denote the dissolved O_2 concentration and the saturated one, and t points to the time.

The power per unit volume (P/V) referred to the volumetric power consumption as described by the following equation [16, 28]:

$$\frac{P}{V} = \frac{\rho_L \times g \times (A_D V_{gs1} + A_R V_{gs2})}{A_D + A_R} \tag{2}$$

where A_R and A_d are the cross-sectional areas of the riser and downcomer sections, respectively, ρ_L is the liquid density, and g is the gravitational acceleration.

3.3. Experimental design

The studies are focused on three parts of the downcomer (the hypotenuse), riser (the vertical side), and gas-liquid separator of this system. The effects of three main independent factors including superficial gas velocities inside the riser (V_{gs2}), the downcomer (V_{gs1}), and the angle (α) are investigated on the hydrodynamic and mass transfer performance. In order to optimize the mentioned factors, the RSM with combined CCD has been used. The upper and lower limits of the variables were obtained by performing preliminary tests. The parameters range and level are presented in Table 1. If gas feeding rates are higher than the limits, it leads to liquid overflow from the upper tube of the separator. Also, given the geometry of the PBR, there is no possibility of changing the angle out of the mentioned range. Based on these three main variables and their limitations, twenty experiments were designed and carried out. The quantities of mass transfer coefficients (k_La), gas holdup (ε), mixing time (t_m), fluid circulation time (t_c), bubble diameter (d), and volumetric power (P/V) have been measured as responses. The results were analyzed by the Design-Expert software version 7 (Stat-Ease Inc., Silicon Valley, CA, USA) based on the second-order model as follows:

$$Y = \beta_0 + \sum_{i=1}^{3} \beta_i x_i + \sum_{i=1}^{3} \beta_{ii} x_i^2 + \sum_{i=1}^{2} \sum_{j=i+1}^{3} \beta_{ij} x_i x_j \tag{3}$$

where Y is the response factor, x_i and x_j are the independent variables, and β_0, β_i, β_{ii}, and β_{ij} are the regression coefficients.

Due to a large number of the designed experiments and time-consuming processes of microalgae culture, hydrodynamic and mass transfer studies were performed without microorganisms. Then, to confirm the results, microalgae culture was done under optimum experimental conditions and results were compared with the control experiments.

Table 1. Range and levels of the parameters studied

Variables	Symbols	Real values of coded levels				
		-α	-1	0	+1	+α
Superficial gas velocity (m s^{-1})	V_{gs1}	0.0005	0.0014	0.0037	0.0060	0.0069
Superficial gas velocity (m s^{-1})	V_{gs2}	0.0040	0.0069	0.0139	0.0209	0.0238
Hypotenuse angle (°)	α	10	25	45	65	80

4. RESULTS AND DISCUSSION

According to CCD, twenty experiments were carried out with three factors, each at five levels. The complete experimental design, along with measured responses, is summarized in Table 2. To correlate the factors to the responses, regression models based on Eq. (3) were assessed and the derived equations with their R^2 values (Coefficients of Determination) are presented in Table 3. These equations indicate the influence of the operating variables on each response. The significance of each parameter, which was evaluated by the probability value (p-value), is listed in Table 4. More detailed discussions are given in the following paragraphs.

Table 2. Hydrodynamic and mass transfer responses to the change of three main factors (α, V_{gs1}, and V_{gs2}) according to RSM-designed experiments

No.	Factors			Mass transfer coefficients			Gas holdup			Bubble diameter		Dimensionless time	Power consumption
	α	V_{gs1}	V_{gs2}	k_La_R	k_La_D	k_La_S	ε_R	ε_D	ε_S	d_R	d_D	θ_m	P/V
	(°)	(m.s^{-1})		(h^{-1})			(-)			(mm)		(-)	(W.m^{-3})
1	45	0.0069	0.0139	20.0	22.0	26.0	0.1654	0.1567	0.1983	4.85	---	0.13	79.34
2	25	0.0014	0.0209	14.5	15.0	14.0	0.1642	0.1485	0.1742	---	6.92	0.77	47.07
3	45	0.0005	0.0139	9.0	13.0	18.0	0.0823	0.0885	0.1014	4.65	6.73	1.27	25.46
4	65	0.0060	0.0069	19.5	24.0	27.0	0.1147	0.1054	0.1369	3.40	6.69	1.06	57.91
5	45	0.0037	0.0139	14.0	15.0	22.0	0.1300	0.1270	0.1578	4.20	5.60	0.85	52.40
6	25	0.0060	0.0069	14.5	14.0	18.5	0.1776	0.1545	0.1799	4.19	7.47	2.08	61.40
7	45	0.0037	0.0139	14.7	14.9	20.5	0.1265	0.1232	0.1559	4.18	5.50	0.84	52.40
8	45	0.0037	0.0238	26.0	17.0	22.0	0.1649	0.1541	0.1976	4.19	6.17	0.29	67.62
9	10	0.0037	0.0139	---	15.9	18.0	---	0.3169	0.3040	3.88	---	---	55.95
10	45	0.0037	0.0139	14.0	16.0	22.0	0.1295	0.1274	0.1583	4.19	5.60	0.85	52.40
11	45	0.0037	0.0139	14.9	15.1	21	0.1295	0.1273	0.1578	4.19	5.6	0.86	52.40
12	25	0.0014	0.0069	12.0	14.0	12.5	0.1152	0.1068	0.1174	4.19	6.43	0.47	28.28
13	65	0.0060	0.0209	23.0	19.3	24.0	0.1420	0.1348	0.1862	4.23	6.62	1.70	75.62
14	80	0.0037	0.0139	21.5	22.0	21.5	0.1235	0.1146	0.1503	4.60	5.79	1.36	50.72
15	65	0.0014	0.0069	13.0	12.3	25.0	0.0691	0.0667	0.0885	5.17	5.81	2.01	26.68
16	45	0.0037	0.0139	15	15.3	21.5	0.1353	0.1333	0.1625	4.21	5.70	0.86	52.40
17	25	0.0060	0.0209	17.5	21.5	20.5	0.2158	0.1890	0.2336	4.19	6.99	2.12	80.18
18	45	0.0037	0.0139	13.5	15	21.5	0.1202	0.1200	0.1501	4.19	5.5	0.86	52.40
19	45	0.0037	0.0040	18.0	14.0	19.0	0.0990	0.0895	0.1022	4.19	5.01	0.75	37.17
20	65	0.0014	0.0209	20.5	8.8	26.0	0.1256	0.1192	0.1510	4.22	5.27	1.87	37.39

Table 3. Final equations of the response surfaces in terms of the actual factors

Response	Predictive equations	R^2
k_La_R	$= +12.81091 + 0.12923 \times \alpha + 1.25040 \times V_{gs1} - 6.40459 \times V_{gs2} + 1.12573 \times V_{gs2}^2$	0.9670
k_La_D	$= +3.0907 + 0.12916 \times \alpha - 0.53343 \times V_{gs1} + 3.29846 \times V_{gs2} + 0.048753 \times \alpha \times V_{gs1} - 0.067437 \times \alpha \times V_{gs2}$	0.9401
k_La_S	$= +4.06975 + 0.29483 \times \alpha + 2.73178 \times V_{gs1} - 0.038852 \times \alpha \times V_{gs1}$	0.8682
ε_R	$= +0.10697 - (3.54646E-3) \times \alpha + 0.025321. V_{gs1} + 0.020399 \times V_{gs2} - (1.61625E-4) \times \alpha \times V_{gs1} - (1.73701E-3) \times V_{gs1} \times V_{gs2} + (3.16465E-5) \times \alpha^2 + (3.16465E-5) \times \alpha^2$	0.9863
ε_D	$= +0.24250 - 7.45953 \times \alpha + (9.74253E-3) \times V_{gs1} + 0.013135 \times V_{gs2} + (6.21996E-5) \times \alpha^2$	0.8859
ε_S	$= +0.19649 - (5.99506E-3) \times \alpha + 0.013958 \times V_{gs1} + (5.09299E-5) \times \alpha^2$	0.8864
t_m	$= -610.96505 + 20.49450 \times \alpha + 190.06425 \times V_{gs1} + 140.40684 \times V_{gs2} - 6.09612 \times \alpha \times V_{gs1} - 2.54045 \times \alpha \times V_{gs2} -29.77444 \times V_{gs1} \times V_{gs2} - 0.12445 \times \alpha^2$	0.9771
t_C	$= -111.79037 + 4.62685 \times \alpha + 1.68643 \times V_{gs1} + 68.15776 \times V_{gs2} - 0.052903 \times \alpha^2 - 10.46168 \times V_{gs2}^2$	0.9740
P/V	$= +1.34021 - 0.067732 \times \alpha + 8.83612 \times V_{gs1} + 6.50685 \times V_{gs2} - 0.11701 \times \alpha \times V_{gs1} - (8.62890E-3) \times \alpha \times V_{gs2} +(7.50069E-4) \times \alpha^2$	0.9601

k_La_R, k_La_D, and k_La_S: mass transfer coefficient in the riser, downcomer, and separator, respectively. ε_R, ε_D, and ε_S: gas holdup of the riser, downcomer, and separator, respectively. t_m: mixing time. t_C: Circulation time. P/V: Volumetric power consumption

Table 4. ANOVA table for studied responses

Responses	k_La_R	k_La_D	k_La_S	ε_R	ε_D	ε_S	t_m	t_c	P/V
	P values								
Model	<0.0001	0.0005	<0.0001	<0.0001	<0.0001	<0.0001	<0.0001	<0.0001	<0.0001
A	<0.0001	0.0236	<0.0001	<0.0001	<0.0001	<0.0001	<0.0001	0.1433	<0.0001
B	<0.0001	0.0001	0.0029	<0.0001	0.0124	<0.0001	<0.0001	0.0445	<0.0001
C	<0.0001	0.5390	---	<0.0001	0.0100	<0.0001	<0.0001	0.0002	<0.0001
AB	---	0.0303	0.0425	0.0027	---	---	<0.0001	---	<0.0001
AC	---	0.0225	---	---	---	---	<0.0001	---	<0.0001
BC	---	---	---	0.0135	---	---	<0.0001	---	---
A^2	---	---	---	<0.0001	0.0007	0.0004	<0.0001	<0.0001	<0.0001
B^2	---	---	---	---	---	---	<0.0001	---	---
C^2	<0.0001	---	---	---	---	---	<0.0001	<0.0001	---
ABC	---	---	---	---	---	---	<0.0001	---	---
A^2B	---	---	---	---	---	---	<0.0001	---	---
A^2C	---	---	---	---	---	---	<0.0001	---	---
AB^2	---	---	---	---	---	---	<0.0001	---	---
A: superficial gas velocity at the downcomer (V_{gs1}), B: superficial gas velocity at the riser (V_{gs2}), C: hypotenuse angle (α)									

Figure 2 shows θ_m changes versus operating factors. Dimensionless time index, $\theta_m = t_m/t_c$, is the mixing time (t_m) on circulation time (t_c). It is used to eliminate photobioreactor geometry's effects on mixing time and provides suitable criteria to evaluate the mixing process type [29]. If the index is less than one, ($\theta_m < 1$), the radial mixing process is superior to the axial mixing caused by fluid circulation through the reactor. Indeed, the smaller θ_m is, the better the desirable mixing. It can be shown that the desirable fluid mixing was located in the range between 45° and 65° of the hypotenuse angle (intersection of the graphs below the line of θ_m=1), where the lowest value of θ_m was 0.41. At the angles out of this range, the axial mixing due to the fluid circulation was mainly superior to the radial mixing. In other words, when the ratio of the mixing time to the circulation time was 0.41, the best condition of the mixing process was achieved in the photobioreactor.

The response analysis of the mixing time (t_m), the time required to achieve 95 % of the complete mixing [24], indicated that the response (t_m) was significantly influenced by the superficial gas velocities (V_{gs1} and V_{gs2}) and by the angle (α). In the downcomer section, two countercurrent and opposite forces interacted; the upward was due to the gas velocity of V_{gs1} and the downward caused by the liquid weight and gas velocity of V_{gs2}. According to Figures 2a and 2b, at minor angles (10° and 25°), the effect of V_{gs1} increased as a result of photobioreactor height reduction and the reduced liquid weight force. The liquid flow and ascending gas bubbles were coordinated at high V_{gs1} and low V_{gs2} in some cases. This phenomenon caused a sharp increase in the mixing time (Figures 2a and 2b) and system inefficiency. It was observed that the downward forces became stronger gradually with increasing the angle, unlike the opposite (upward) force. Therefore, in the angle range of 45°, optimal mixing was achieved at high V_{gs1} and V_{gs2} values (Figure 2c). The counter forces became equal in the range of 45o to 65o, because the suitable mixing (low t_m) could be obtained both at low V_{gs1} and high V_{gs2} and at high V_{gs1} and low V_{gs2}.

At larger angles, the downward force predominated the opposite one due to the system height increment (Figures 2d and 2e). Therefore, such a system operated as conventional airlift photobioreactors, in which the primary mixing process occurred in the riser section. In this condition, the fluid circulation would be superior to the radial mixing process. Hence, liquid circulation times (t_c) were shorter.

Considering that the fluid circulation rate is adjusted by the gas feeding from the base of the vertical side (V_{gs2}), it could be found that the fluid circulation at low V_{gs1} controlled the process of mixing and stirring. When the liquid mixing time (t_m) was much longer than the circulation time (t_c), significant mixing could be done in the riser section. By increasing V_{gs1} up to 0.0050 m.s^{-1}, in addition to reducing the dependency of t_m on V_{gs2}, V_{gs1} strength was equalized to the total force of V_{gs2} and liquid weight in the hypotenuse. As mentioned earlier, this force caused fluid circulation through the system. In this case, changes in V_{gs2} would not affect mixing time. With a further increase in V_{gs1}, the countercurrent fluid flows in the downcomer section promoted good mixing. Indeed, within the range of V_{gs1} higher than 0.0050 m.s^{-1}, the mixing process was controlled by powerful countercurrent flows created in the downcomer section and the resulted mixing came over the fluid circulation. It was observed that the effect of V_{gs2} on t_m increased again upon exceeding V_{gs1}= 0.0050 m.s^{-1} (Figures 2a-2e). The critical point here is that at the angles of 10° and 25°, the values of t_m were much more extensive than those of t_c (Figures 2a and 2b). Accordingly, significant mixing occurred in the riser and there was not enough time for complete mixing because of the low height of the riser at these angles (especially at 10°). It resulted in an excessive increment of mixing time relative to the circulation time of the fluid.

It should be noted that at three angles of 10°, 25°, and 45°, the relationship between t_m and V_{gs2} at $V_{gs1} < 0.005$ m.s^{-1} was direct and inverse at $V_{gs1} > 0.005$ m.s^{-1}. In other words, at low V_{gs1}, the mixing time increased with increasing V_{gs2} and at high V_{gs1}, increasing V_{gs2} reduced mixing time (improving the mixing process). This relationship was reversed at two angles of 65° and 80°.

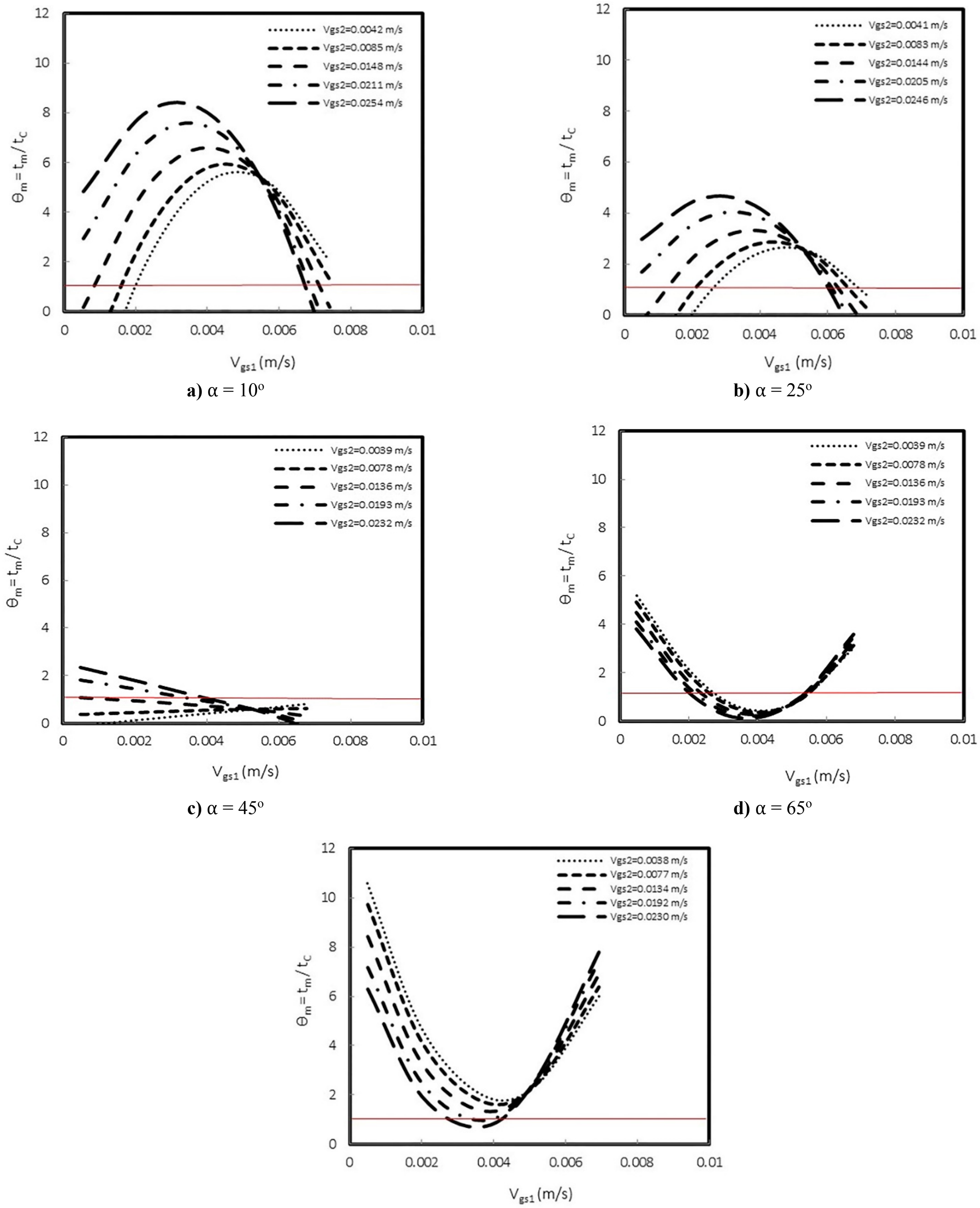

a) α = 10°

b) α = 25°

c) α = 45°

d) α = 65°

e) α = 80°

Figure 2. Variations of θ_m versus superficial gas velocities (V_{gs1} and V_{gs2}) at different angles

Figure 3 displays the variations of the volumetric mass transfer coefficient (k_La_D) and gas holdup (ε_D) of the downcomer for the superficial gas velocities at different angles. Variation of k_La_D as a function of V_{gs1} was minimal at the angle 10°, despite the positive slope of gas holdup (ε_D). The reason for this phenomenon could be the increase in upcoming bubbles diameter and even in some cases, the conversion of gas flow regime from bubbly to slug flow in the downcomer section due to the V_{gs1} increment.

As shown in Figures 3d and 3e, as the angle increased, the k_La_D changes were incremental at constant V_{gs2}. According to the regression equation for k_La_D exhibited in Table 3, the angle (α) had a positive effect on k_La_D, linearly, and the interaction with other factors was less significant. Although it was expected that the slope of the k_La_D - V_{gs1} curve decreased or remained at least constant with a slight decrease in gas holdup (ε_D), the increasing slope was observed in this region, unexpectedly. It could be due to the bubbles' diameter decreasing and enhancing the surface area in the downcomer part.

The effects of V_{gs2} on k_La_D had a different trend. Figure 3 shows that increasing the angle from 10° to 80° resulted in reducing the effect of V_{gs2} on k_La_D to an unknown angle (δ) (45° < δ < 65°) where this effect reached zero; and k_La_D just changed under the influence of V_{gs1}. At the angles lower than δ, an increase in V_{gs2} caused the enhancement of the k_La_D, but it was reversed at higher angles. In other words, high mass transfer coefficients could be obtained at lower V_{gs2}. The effect of fluid weight at the angles higher than δ was more considerable among the downward forces in the hypotenuse because of the height increase. Therefore, it is necessary to reduce the power created by the V_{gs2} to keep the balance. If V_{gs2} was raised in this range, t_c decreased while t_m increased. This decline in the mixing rate was the main reason for mass transfer reduction in this bioreactor section. It is worth noting that the highest values of k_La_D at high angles were obtained at high V_{gs1}s and low V_{gs2}s.

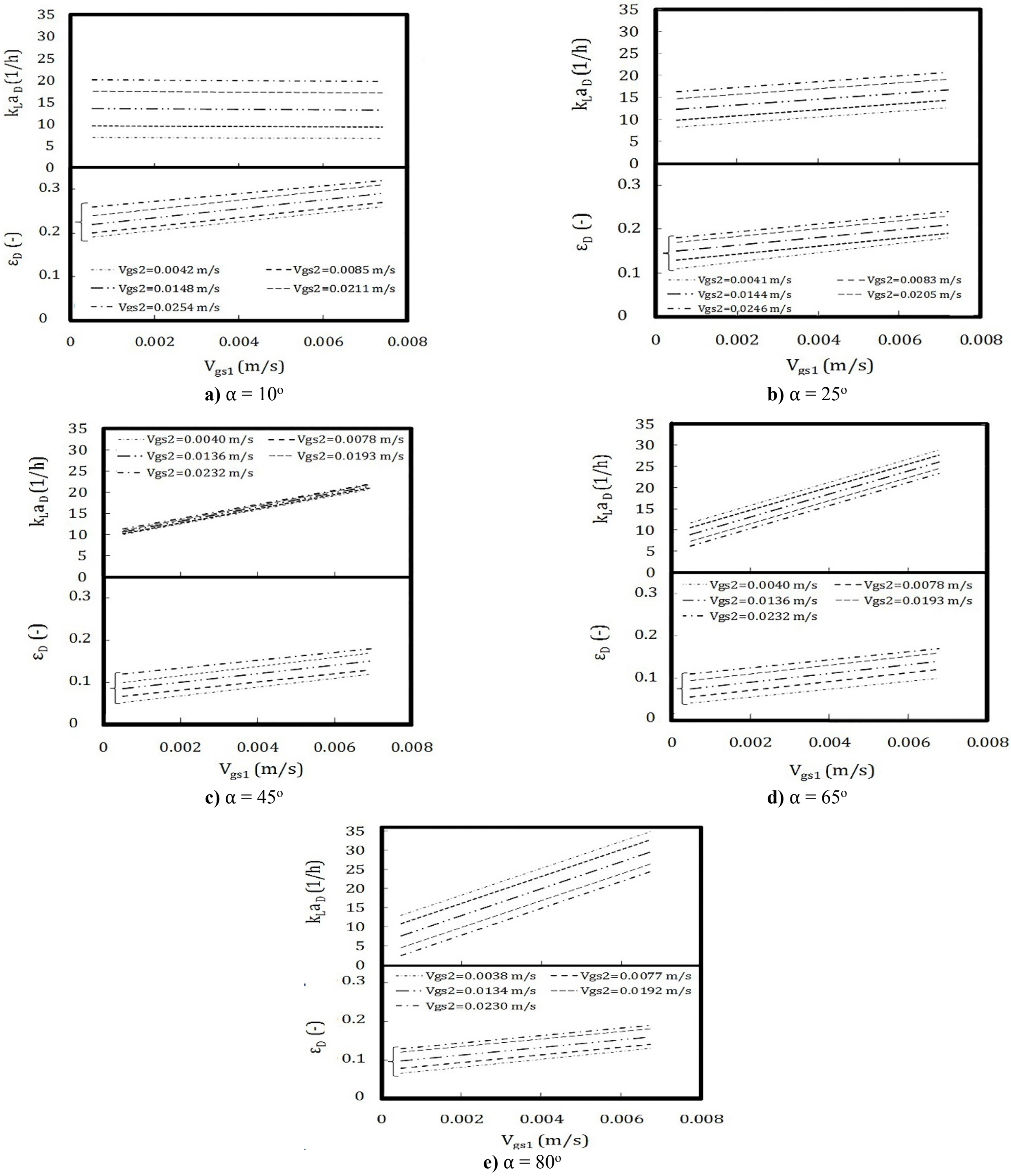

Figure 3. Changes of k_La_D and ε_D versus superficial gas velocities (V_{gs1} and V_{gs2}) at different angles (α)

Figure 4 presents the variations of the volumetric mass transfer coefficient ($k_L a_R$) and gas holdup (ε_R) of the riser versus three independent factors (V_{gs1}, V_{gs2} and α). As demonstrated, $k_L a_R$ had the linear and almost the same relationship (positive effect) with α and V_{gs1} (based on the regression model for $k_L a_R$ exhibited in Table 3). Nevertheless, the changes in $k_L a_R$ versus V_{gs2} had a different trend (negative in linear and positive in square). Figure 4 confirms that increasing the angle from 10^o to an angle (δ) ($45^o < \delta < 65^o$) reduced the gas holdup in the riser (ε_R). Above this angle, ε_R was almost constant.

Regarding Figures 4a-4e, it was clear that the high amounts of $k_L a_R$ could be obtained at the angles above 45^o, high V_{gs1}s, and very low or high V_{gs2}s.

Comparison of Figures 3a-3e and 4a-4e shows that the amount of gas holdup in both regions of the riser and downcomer (ε_R and ε_D) was approximately the same and the gas holdup in the riser was just a little more. At the conventional airlift bioreactors, fluid circulation caused by a difference in fluid density has been reported [30]. This difference is caused by relatively uniform distribution of the bubbles in the liquid and is dependent on the gas holdup gradient [31]. Therefore, gas holdup's equivalence leads to the disability of vertical airlift system in fluid circulation, undesirably. However, the geometry of the new bioreactor caused a regular circulation through the system with the minimum difference of gas holdup between the two sections.

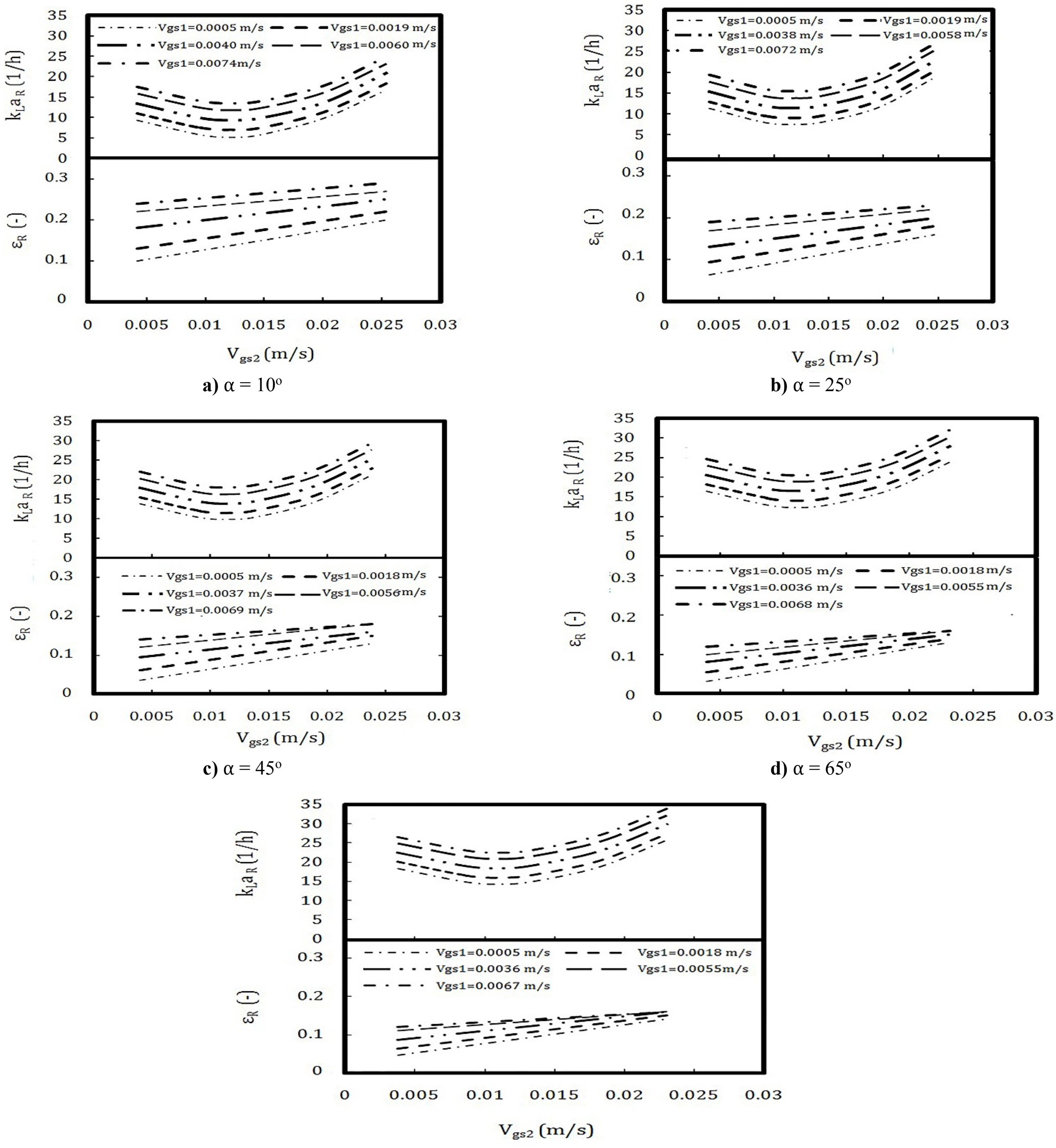

a) α = 10°

b) α = 25°

c) α = 45°

d) α = 65°

e) α = 80°

Figure 4. Changes of $k_L a_R$ and ε_R versus superficial gas velocities (V_{gs1} and V_{gs2}) at different angles (α)

The effect of the three main operating factors on the separator's volumetric mass transfer coefficient (k_La_S) is demonstrated in Figure 5. As shown, k_La_S was strongly affected by two parameters of V_{gs1} and α (see the positive and relatively high coefficients of these two factors in the linear mode of regression model for k_La_S exhibited in Table 3). The influence of V_{gs2} on k_La_S was lower as the k_La difference in the highest and lowest V_{gs2} was just 1.6 h^{-1}. The slope of $k_La_S - V_{gs1}$ curves in the range from 10° to an angle marked as δ (≈ 60°) was always positive (Figures 5a, 5b, and 5c), but at 65° was almost zero (Figure 5d). On the other hand, increasing or decreasing V_{gs1} did not affect the separator's mass transfer amount with the hypotenuse angle of 65°. With a further increase in the angle, the slope became negative (Figure 5e). It means that increasing V_{gs1} would reduce k_La_S. The critical matter in these figures was that the point of V_{gs1}= 0.006 m.s^{-1}, which was the only velocity where the k_La_S value was always constant ($k_La_S \approx 25$ h^{-1}) at all angles. As a result, the maximum values of the k_La_S were observed at high V_{gs1}s and at the angles greater than 45°.

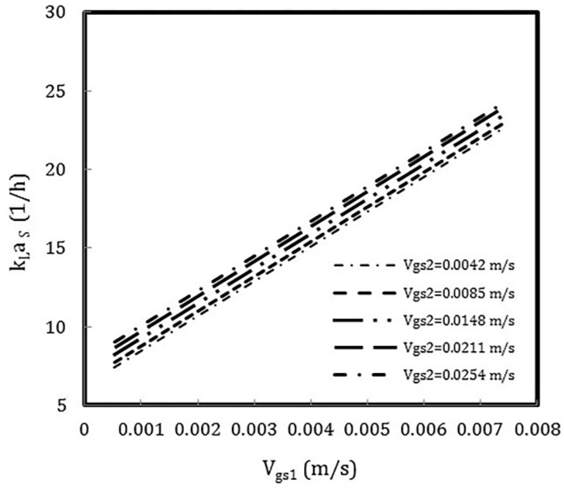

a) α = 10°

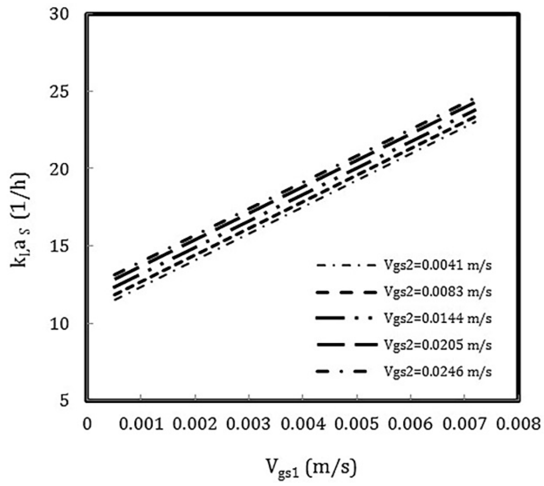

b) α = 25°

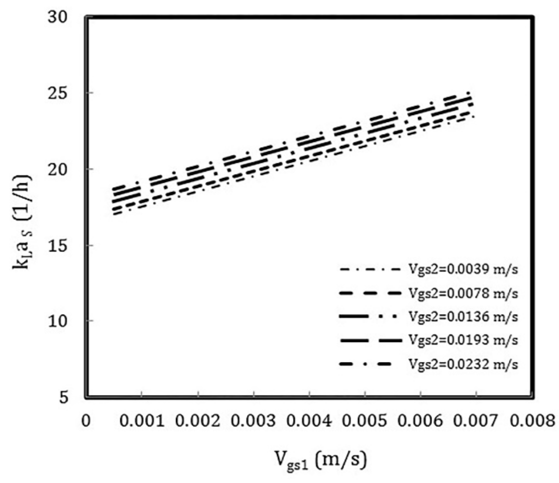

c) α = 45°

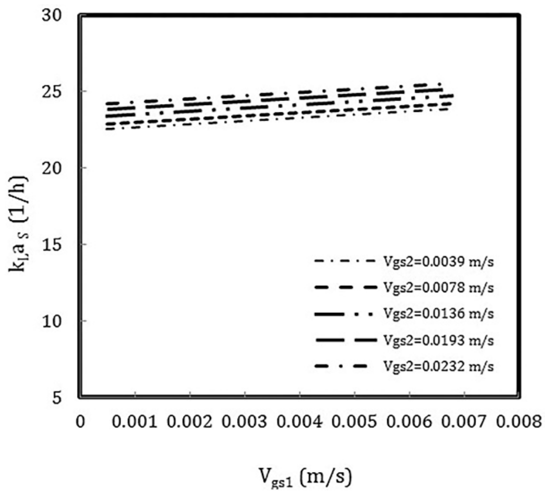

d) α = 65°

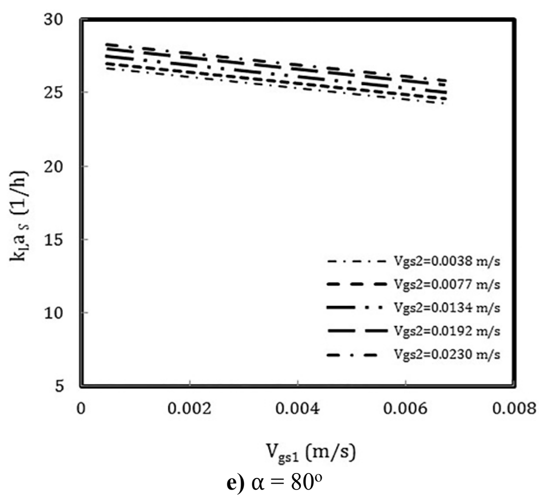

e) α = 80°

Figure 5. Changes of k_La_S versus superficial gas velocities (V_{gs1} and V_{gs2}) at different angles (α)

Figure 6 illustrates the influence of each of three operating variables on a significant characteristic of the system, power consumption per volume (P/V) of the photobioreactor (W/m^3). Accordingly, power consumption variation of the system versus angle was not considerable, and increasing the angle led to an insignificant reduction in it. However, this characteristic was strongly influenced by superficial gas velocities, V_{gs2} and especially V_{gs1}. A linear power consumption increment could be observed upon increase in the velocities. An increase in V_{gs1} raised power consumption and led to a significant increase in k_La_D and k_La_R [see Figures 3 and 4]. As previously mentioned, increasing V_{gs2} could have a positive influence on the volumetric mass transfer coefficient in the riser (k_La_R) and, in addition to power consumption increment, mainly decreased k_La_D. Despite the insignificant effect of the hypotenuse angle (α) on power consumption, the mass transfer coefficients in both riser and downcomer represented high sensitivity. Therefore, by optimizing the photobioreactor's operating conditions, the maximum mass transfer and mixing rates could be achieved along with the minimum power consumption in the system.

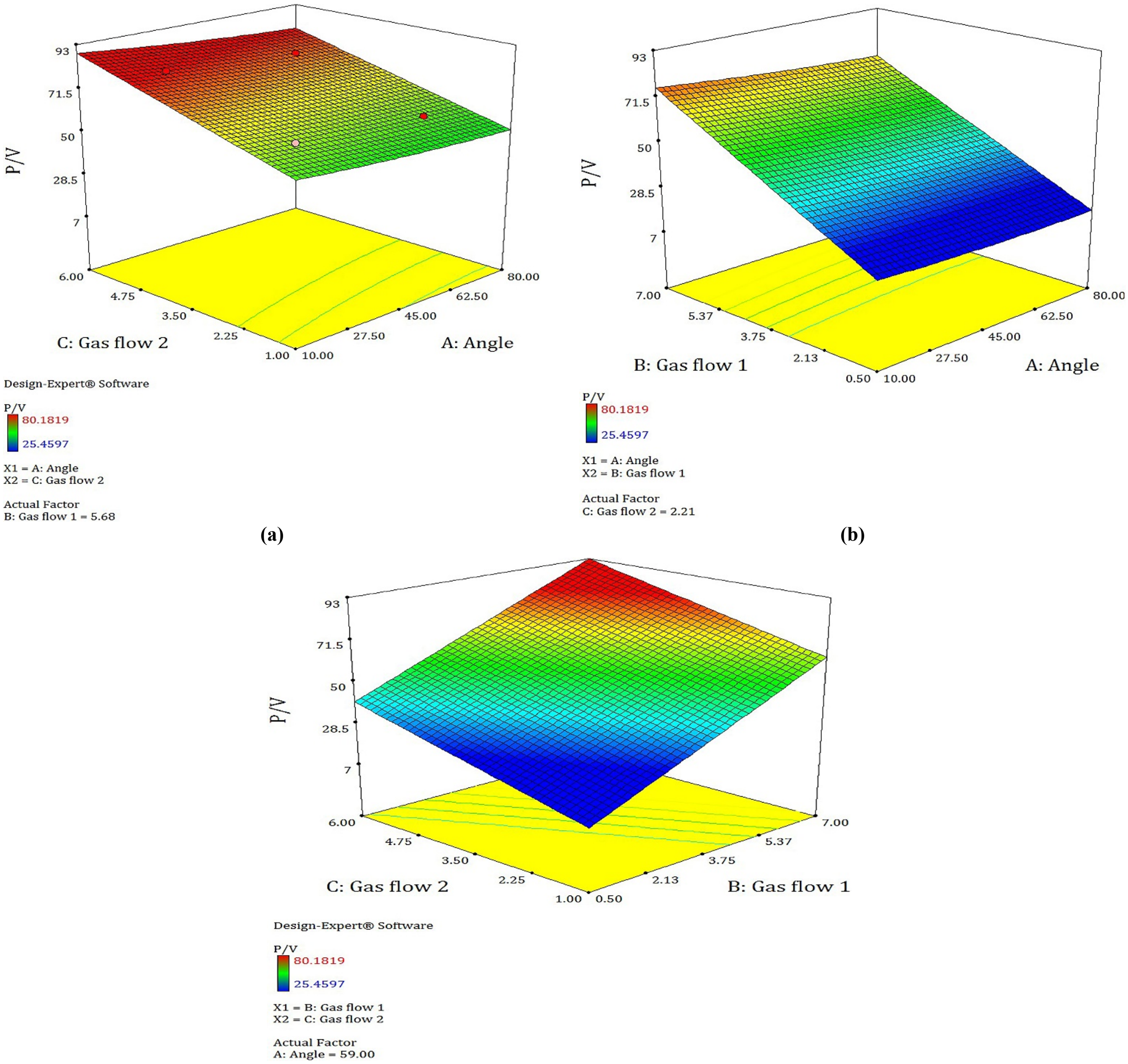

(c)

Figure 6. Power consumption of the photobioreactor at (a) different gas flows 2 (V_{gs2}) and the angle (α); (b) different gas flows 1 (V_{gs1}) and the angle (α); (c) different gas flows 1 (V_{gs1}) and gas flow 2 (V_{gs2})

As mentioned before, the designed experiments' desirable goal was to reach the maximum mass transfer in the shortest mixing time and minimum power consumption, simultaneously. Regarding the analysis, the downcomer's counter forces were identical at the superficial gas velocity of V_{gs1} = 0.0050 m.s^{-1}, where θ_m did not change by V_{gs2} variations. Besides, the $\theta_m - V_{gs1}$ curve at different V_{gs2}s was mainly located in the range of the dimensionless time less than one ($\theta_m < 1$) at an angle of $\delta \approx 60^o$. It means that the mixing time was lower than the circulation time, and the optimum mixing process could be observed in the shortest amount of time.

Also, maximum effective mass transfer was located at large values of V_{gs1} and small amounts of V_{gs2} and the angles higher than 45°. On the other hand, the upper limit of the optimum angle could not exceed 65° to achieve the minimum value of θ_m. It should reduce the superficial gas velocities as much as possible to minimize power consumption. Since the excessive reduction of V_{gs1} had a little adverse effect on the volumetric mass transfer coefficient in the separator ($k_L a_S$), power consumption saving could be achieved by reducing V_{gs2}. As a result, the geometry of the studied photobioreactor had better mass transfer than other configurations. This was caused by better mixing (decreased mixing time) as a result of countercurrent flow in the downcomer when power consumption slightly increased [32].

According to the analysis, each independent variable's influences and limitations to attain the desired goal, the optimum conditions, and the actual and predicted responses are listed in Table 5. The optimal conditions provided by the software were determined as follows: V_{gs1} = 0.0050 m.s^{-1}, V_{gs2} = 0.0080 m.s^{-1}, and α = 59 ~ 60°. The empirical experiments were conducted in optimal conditions to confirm the RSM predictions, and the responses were also measured practically. According to Table 5, there is acceptable consistency between predicted values and experimental results.

4.1. Confirmation of the optimal conditions with microalgae culture

The microorganism's culture at the optimum angle (60°) was performed to confirm the findings and was compared with two angles of 10° and 80° as control conditions. For this purpose, the microalgae growth rate was obtained by dry biomass weight measurements [33]. The same conditions were assigned for the culture medium, considering the operating parameters like temperature, pH, inoculation time, and concentration. As shown in Figure 7, there was a significant difference in the growth rate of *Chlorella vulgaris* at the angle of 60° compared to 10° and 80°. It was confirmed that the optimal mixing rate was a very effective agent in the cultivating process. Increasing the mixing rate improved the accessibility of the nutrients and CO_2. Also, by removing the downcomer's dark zone, the tube center developed the appropriate culture media for microorganisms. Additionally, the growth curves confirmed the optimum conditions and indicated the high impact of the hydrodynamic tensions on the culture. Furthermore, it was found that the maximum concentration of biomass (X_{max}=1.4 g.l^{-1}) was achieved faster (11th day of cultivation) than similar studies [34]. The obtained conditions were compared with some similar studies, as shown in Table 6. These results have drawn much more attention to the significance of the airlift photobioreactors' geometry and design to produce microalgae efficiently.

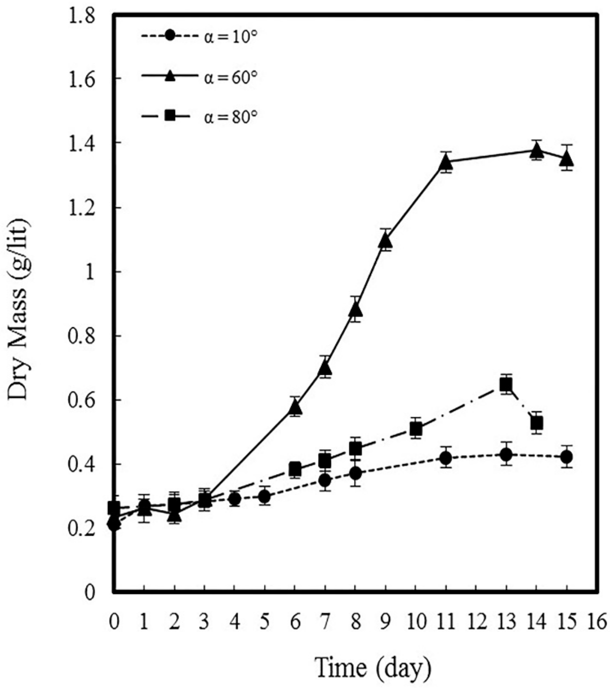

Figure 7. Growth curve of *Chlorella vulgaris* at angles of 10°, 60°, and 80° obtained by dry mass measurement

Table 6. Comparison of growth factors of *Chlorella vulgaris* in photobioreactors of different studies

Reference	Growth factors				Comments
	μ_{max} (day^{-1})	X_{max} (g.L^{-1})	P_{max} (g.L^{-1}.day^{-1})	t_d (day)	
This work	0.214	1.379	0.100	3.200	Carbon source: air, system type: external loop airlift photobioreactor.
[34]	0.130	1.220	0.100		Carbon source: CO_2
[35]	0.205	0.590	---		Carbon source: air, system type: CSTR, operating volume: 10 L.
[36]	---	---	0.100		Carbon source: CO_2
[37]	---	---	0.200		Carbon source: CO_2, system type: 250 ml flask
[38]	---	---	0.010		Carbon source: CO_2, system type: mixed tank, operating volume: 2 L
[39]	---	---	0.020-0.040		Carbon source: CO_2
[40]	---	---	0.030-0.040		Carbon source: CO_2
μ_{max}: maximum specific growth rate, X_{max}: maximum biomass concentration, P_{max}: maximum biomass productivity, t_d: doubling time					

5. CONCLUSIONS

The optimization process of a triangular external loop airlift PBR was performed by the RSM to maximize the volumetric mass transfer coefficients (k_La) and minimize the power consumption per volume (P/V) as well as the mixing time (t_m) as responses. The effects of the three main factors, superficial gas velocities (V_{gs1} and V_{gs2}), and the hypotenuse angle (α) on the system performance were investigated. The optimal values were obtained as follows α = 59º, V_{gs1} = 0.0050 m.s^{-1}, and V_{gs2} = 0.008 m.s^{-1}. It was also found that the V_{gs1} and α were the most effective factors in hydrodynamic and mass transfer behavior of the system. The sensitivity of all responses to V_{gs1} was high and of almost equal importance. However, despite the great influence of α on the mixing and mass transfer, it had less impact on power consumption. Moreover, V_{gs2} variations possessed a considerable effect on the riser's mass transfer coefficient and power consumption and made fewer mixing time changes. Predictive, second-order mathematical models were presented to correlate the individual parameters to the responses with high R^2 ranging from 0.88 to 0.96. Also, mathematical models were confirmed by comparison of the actual and predicted response values.

The dimensionless time (θ_m) was 0.41 under optimum conditions. θ_m less than one ($\theta_m < 1$) was the cause for improving the mixing process due to the fluid's radial distribution rather than its axial circulation. Finally, growth curves of the *Chlorella vulgaris* verified the optimum condition, practically and demonstrated higher biomass concentration and shorter culture duration than those in other studies.

6. ACKNOWLEDGEMENT

The authors would like to gratefully acknowledge the Biotechnology Group, Faculty of Chemical Engineering, Tarbiat Modares University for their support.

REFERENCES

1. Tagliaferro, G.V., Izário Filho, H.J., Chandel, A.K., da Silva, S.S., Silva, M.B. and dos Santos, J.C., "Continuous cultivation of *Chlorella minutissima 26a* in a tube-cylinder internal-loop airlift photobioreactor to support 3G biorefineries", ***Renewable Energy***, Vol. 130, (2019), 439-445. (https://doi.org/10.1016/j.renene.2018.06.041).
2. Carvalho, A.P., Meireles, L.A. and Malcata, F.X., "Microalgal reactors: A review of enclosed system designs and performances", ***Biotechnology Progress***, Vol. 22, No. 6, (2006), 1490-1506. (https://doi.org/10.1021/bp060065r).
3. Essadki, A., Bennajah, M., Gourich, B., Vial, C., Azzi, M. and Delmas, H., "Electrocoagulation/electroflotation in an external-loop airlift reactor—Application to the decolorization of textile dye wastewater: A case study", ***Chemical Engineering and Processing: Process Intensification***, Vol. 47, No. 8, (2008), 1211-1223. (https://doi.org/10.1016/j.cep.2007.03.013).
4. Choi, K.H., "Hydrodynamic and mass transfer characteristics of external-loop airlift reactors without an extension tube above the downcomer", ***Korean Journal of Chemical Engineering***, Vol. 18, No. 2, (2001), 240-246. (https://doi.org/10.1007/BF02698466).
5. Nikakhtari, H. and Hill, G.A., "Continuous bioremediation of phenol-polluted air in an external loop airlift bioreactor with a packed bed", ***Journal of Chemical Technology & Biotechnology: International Research in Process, Environmental & Clean Technology***, Vol. 81, No. 6, (2006), 1029-1038. (https://doi.org/10.1002/jctb.1520).
6. Bahadar, A. and Khan, M.B., "Progress in energy from microalgae: A review", ***Renewable and Sustainable Energy Reviews***, Vol. 27, (2013), 128-148. (https://doi.org/10.1016/j.rser.2013.06.029).
7. Barbosa, M.J., Janssen, M., Ham, N., Tramper, J. and Wijffels, R.H., "Microalgae cultivation in air-lift reactors: Modeling biomass yield and growth rate as a function of mixing frequency", ***Biotechnology and Bioengineering***, Vol. 82, No. 2, (2003), 170-179. (https://doi.org/10.1002/bit.10563).
8. Zeng, X., Danquah, M.K., Chen, X.D. and Lu, Y., "Microalgae bioengineering: From CO_2 fixation to biofuel production", ***Renewable and Sustainable Energy Reviews***, Vol. 15, No. 6, (2011), 3252-3260. (https://doi.org/10.1016/j.rser.2011.04.014).
9. Scarsella, M., Torzillo, G., Cicci, A., Belotti, G., De Filippis, P. and Bravi, M., "Mechanical stress tolerance of two microalgae", ***Process Biochemistry***, Vol. 47, No. 11, (2012), 1603-1611. (https://doi.org/10.1016/j.procbio.2011.07.002).
10. Powtongsook, S., Kaewpintong, K., Shotipruk, A. and Pavasant, P., "Effect of superficial gas velocity on growth of the green microalga haematococcus pluvialis in airlift photobioreactor", Studies in surface science and catalysis, Elsevier, (2006),.481-484. (https://doi.org/10.1016/S0167-2991(06)81638-1).
11. Hoseinkhani, N., Jalili, H., Ansari, S. and Amrane, A., "Impact of bubble size on docosahexaenoic acid production by *Crypthecodinium cohnii* in bubble column bioreactor", ***Biomass Conversion and Biorefinery***, Vol. 11, (2019), 1137-1144. (https://doi.org/10.1007/s13399-019-00510-5).
12. Ugwu, C., Aoyagi, H. and Uchiyama, H., "Photobioreactors for mass cultivation of algae", ***Bioresource Technology***, Vol. 99, No. 10, (2008), 4021-4028. (https://doi.org/10.1016/j.biortech.2007.01.046).
13. Barahoei, M., Hatamipour, M.S. and Afsharzadeh, S., "CO_2 capturing by *Chlorella vulgaris* in a bubble column photo-bioreactor; Effect of bubble size on CO_2 removal and growth rate", ***Journal of CO_2 Utilization***, Vol. 37, (2020), 9-19. (https://doi.org/10.1016/j.jcou.2019.11.023).
14. Geng, S., Li, Z., Liu, H., Yang, C., Gao, F., He, T. and Huang, Q., "Hydrodynamics and mass transfer in a slurry external airlift loop reactor integrating mixing and separation", ***Chemical Engineering Science***, Vol. 211, (2020), 115294. (https://doi.org/10.1016/j.ces.2019.115294).
15. Zhang, L., Wu, M., Han, Y., Liu, M. and Niu, J., "Structural parameter optimization for novel internal-loop iron–carbon micro-electrolysis reactors using computational fluid dynamics", ***Chinese Journal of Chemical Engineering***, Vol. 27, No. 4, (2019), 737-744. (https://doi.org/10.1016/j.cjche.2018.08.001).
16. Reyna-Velarde, R., Cristiani-Urbina, E., Hernández-Melchor, D.J., Thalasso, F. and Cañizares-Villanueva, R.O., "Hydrodynamic and mass transfer characterization of a flat-panel airlift photobioreactor with high light path", ***Chemical Engineering and Processing: Process Intensification***, Vol. 49, No. 1, (2010), 97-103. (https://doi.org/10.1016/j.cep.2009.11.014).
17. Fadavi, A. and Chisti, Y., "Gas holdup and mixing characteristics of a novel forced circulation loop reactor", ***Chemical Engineering Journal***, Vol. 131, No. 1-3, (2007), 105-111. (https://doi.org/10.1016/j.cej.2006.12.037).
18. Yazdian, F., Hajiabbas, M.P., Shojaosadati, S.A., Nosrati, M., Vasheghani-Farahani, E. and Mehrnia, M., "Study of hydrodynamics, mass transfer, energy consumption, and biomass production from natural gas in a forced-liquid vertical tubular loop bioreactor", ***Biochemical Engineering Journal***, Vol. 49, No. 2, (2010), 192-200. (https://doi.org/10.1016/j.bej.2009.12.013).
19. Yazdian, F., Shojaosadati, S.A., Nosrati, M., Mehrnia, M. and Vasheghani-Farahani, E., "Study of geometry and operational conditions on mixing time, gas hold up, mass transfer, flow regime and biomass production from natural gas in a horizontal tubular loop bioreactor", ***Chemical Engineering Science***, Vol. 64, No. 3, (2009), 540-547. (https://doi.org/10.1016/j.ces.2008.09.031).
20. Gao, X., Kong, B. and Vigil, R.D., "Multiphysics simulation of algal growth in an airlift photobioreactor: Effects of fluid mixing and shear stress", ***Bioresource Technology***, Vol. 251, (2018), 75-83. (https://doi.org/10.1016/j.biortech.2017.12.014).
21. Chiu, S.Y., Tsai, M.T., Kao, C.Y., Ong, S.C. and Lin, C.S., "The air-lift photobioreactors with flow patterning for high-density cultures of microalgae and carbon dioxide removal", ***Engineering in Life Sciences***, Vol. 9, No. 3, (2009), 254-260. (https://doi.org/10.1002/elsc.200800113).
22. Lakaniemi, A.M., Intihar, V.M., Tuovinen, O.H. and Puhakka, J.A., "Growth of *Chlorella vulgaris* and associated bacteria in

photobioreactors", ***Microbial Biotechnology***, Vol. 5, No. 1, (2012), 69-78. (https://doi.org/10.1111/j.1751-7915.2011.00298.x).

23. Posten, C., "Design principles of photo-bioreactors for cultivation of microalgae", ***Engineering in Life Sciences***, Vol. 9, No. 3, (2009), 165-177. (https://doi.org/10.1002/elsc.200900003).
24. Mendoza, J., Granados, M., De Godos, I., Acién, F., Molina, E., Banks, C. and Heaven, S., "Fluid-dynamic characterization of real-scale raceway reactors for microalgae production", ***Biomass and Bioenergy***, Vol. 54, (2013), 267-275. (https://doi.org/10.1016/j.biombioe.2013.03.017).
25. Verlaan, P., Van Eijs, A., Tramper, J., Van't Riet, K. and Luyben, K.C.A., "Estimation of axial dispersion in individual sections of an airlift-loop reactor", ***Chemical Engineering Science***, Vol. 44, No. 5, (1989), 1139-1146. (https://doi.org/10.1016/0009-2509(89)87013-7).
26. Shadpoor, S., Pirouzi, A., Hamze, H. and Mazaheri, D., "Determination of bodenstein number and axial dispersion of a triangular external loop airlift reactor", ***Chemical Engineering Research and Design***, Vol. 165, (2021), 61-68. (https://doi.org/10.1016/j.cherd.2020.10.018).
27. Guo, X., Yao, L. and Huang, Q., "Aeration and mass transfer optimization in a rectangular airlift loop photobioreactor for the production of microalgae", ***Bioresource tTechnology***, Vol. 190, (2015), 189-195. (https://doi.org/10.1016/j.biortech.2015.04.077).
28. Kochem, L.H., Da Fré, N.C., Redaelli, C., Rech, R. and Marcílio, N.R., "Characterization of a novel flat-panel airlift photobioreactor with an internal heat exchanger", ***Chemical Engineering & Technology***, Vol. 37, No. 1, (2014), 59-64. (https://doi.org/10.1002/ceat.201300420).
29. Mirón, A.S., García, M.-C.C., Camacho, F.G., Grima, E.M. and Chisti, Y., "Mixing in bubble column and airlift reactors", ***Chemical Engineering Research and Design***, Vol. 82, No. 10, (2004), 1367-1374. (https://doi.org/10.1205/cerd.82.10.1367.46742).
30. Vunjak-Novakovic, G., Kim, Y., Wu, X., Berzin, I. and Merchuk, J.C., "Air-lift bioreactors for algal growth on flue gas: Mathematical modeling and pilot-plant studies", ***Industrial & Engineering Chemistry Research***, Vol. 44, No. 16, (2005), 6154-6163. (https://doi.org/10.1021/ie049099z).
31. Reilly, I., Scott, D., Debruijn, T. and MacIntyre, D., "The role of gas phase momentum in determining gas holdup and hydrodynamic flow regimes in bubble column operations", ***The Canadian Journal of Chemical Engineering***, Vol. 72, No. 1, (1994), 3-12. (https://doi.org/10.1002/cjce.5450720102).
32. Pirouzi, A., Nosrati, M., Shojaosadati, S.A. and Shakhesi, S., "Improvement of mixing time, mass transfer, and power consumption in an external loop airlift photobioreactor for microalgae cultures", ***Biochemical Engineering Journal***, Vol. 87, (2014), 25-32. (https://doi.org/10.1016/j.bej.2014.03.012).
33. Roselet, F., Vandamme, D., Roselet, M., Muylaert, K. and Abreu, P.C., "Screening of commercial natural and synthetic cationic polymers for flocculation of freshwater and marine microalgae and effects of molecular weight and charge density", ***Algal Research***, Vol. 10, (2015), 183-188. (https://doi.org/10.1016/j.algal.2015.05.008).
34. Abreu, A.P., Fernandes, B., Vicente, A.A., Teixeira, J. and Dragone, G., "Mixotrophic cultivation of *Chlorella vulgaris* using industrial dairy waste as organic carbon source", ***Bioresource Technology***, Vol. 118, (2012), 61-66. (https://doi.org/10.1016/j.biortech.2012.05.055).
35. Sacasa Castellanos, C., "Batch and continuous studies of *Chlorella vulgaris* in photo-bioreactors", Electronic Thesis and Dissertation Repository, (2013), 1113. (https://ir.lib.uwo.ca/etd/1113).
36. Yoo, C., Jun, S.-Y., Lee, J.-Y., Ahn, C.-Y. and Oh, H.-M., "Selection of microalgae for lipid production under high levels carbon dioxide", ***Bioresource Technology***, Vol. 101, No. 1, (2010), S71-S74. (https://doi.org/10.1016/j.biortech.2009.03.030).
37. Rodolfi, L., Chini Zittelli, G., Bassi, N., Padovani, G., Biondi, N., Bonini, G. and Tredici, M.R., "Microalgae for oil: Strain selection, induction of lipid synthesis and outdoor mass cultivation in a low-cost photobioreactor", ***Biotechnology and Bioengineering***, Vol. 102, No. 1, (2009), 100-112. (https://doi.org/10.1002/bit.22033).
38. Liang, Y., Sarkany, N. and Cui, Y., "Biomass and lipid productivities of *Chlorella vulgaris* under autotrophic, heterotrophic and mixotrophic growth conditions", ***Biotechnology Letters***, Vol. 31, No. 7, (2009), 1043-1049. (https://doi.org/10.1007/s10529-009-9975-7).
39. Scragg, A., Illman, A., Carden, A. and Shales, S., "Growth of microalgae with increased calorific values in a tubular bioreactor", ***Biomass and Bioenergy***, Vol. 23, No. 1, (2002), 67-73. (https://doi.org/10.1016/S0961-9534(02)00028-4).
40. Illman, A., Scragg, A. and Shales, S., "Increase in Chlorella strains calorific values when grown in low nitrogen medium", ***Enzyme and Microbial Technology***, Vol. 27, No. 8, (2000), 631-635. (https://doi.org/10.1016/S0141-0229(00)00266-0).

JREE: Vol. 9, No. 1, (Winter 2022) 106-111

Journal of Renewable Energy and Environment

Journal Homepage: www.jree.ir

Materials and Energy Research Center

MERC

Research Article

Performance Enhancement of Deep Violet InGaN Double Quantum Wells Laser Diodes with Quaternary Superlattice Barriers Structure

Ghasem Alahyarizadeh [a], Maryam Amirhoseiny [b], Majid Khorsandi [c*]

[a] *Faculty of Engineering, Shahid Beheshti University, P. O. Box: 1983969411, Tehran, Tehran, Iran.*
[b] *Buin Zahra Higher Education Center of Engineering and Technology, Imam Khomeini International University, P. O. Box: 3451745346, Qazvin, Qazvin, Iran.*
[c] *Radiation Application Department, Shahid Beheshti University, P. O. Box: 1983969411, Tehran, Tehran, Iran.*

PAPER INFO

Paper history:
Received: 07 September 2021
Revised in revised form: 31 October 2021
Scientific Accepted: 14 November 2021
Published: 11 January 2022

Keywords:
InGaN Quantum Well Laser,
Superlattice Barriers,
Electrical and Optical Properties,
Numerical Simulation

ABSTRACT

The performance characteristics of InGaN Double-Quantum-Well (DQW) Laser Diodes (LDs) with different barrier structures were studied numerically by Integrated System Engineering Technical Computer-Aided Design (ISE TCAD) software. Three different kinds of structures of barriers including quaternary AlInGaN and AlInGaN/AlGaN superlattice barriers were used and compared with conventional GaN in InGaN-based laser diodes. Replacing the traditional GaN barriers with quaternary AlInGaN increased holes and electrons flowing in the active region and thus, the radiative recombination enhanced the output power. However, it did not reduce the threshold current due to hole and electron overflowing. To investigate the ways of greatly reducing the threshold current, the structure consisting of AlInGaN/AlGaN superlattice barriers was proposed. The simulation showed that electrical and optical characteristics such as output power, Differential Quantum Efficiency (DQE), and slop efficiency were significantly enhanced for LDs containing superlattice barriers compared to the basic structure. This is while the threshold current was considerably reduced. The enhancement was mainly attributed to the improvement of hole injection and also the blocking hole and electron overflowing caused by the reduction of polarization charges at the interface between the barriers, the well, and the Electron Blocking Layer (EBL).

https://doi.org/10.30501/jree.2021.300112.1246

1. INTRODUCTION

III-Nitride materials present unique physical properties such as wide, direct, and tunable bandgap energy, high electron mobility, saturation velocity, coverage of the electromagnetic spectrum, high thermal stability, and high absorption coefficient which made them the best candidate materials for optoelectronics applications including LD, LED, and solar cells. III-Nitride family laser diodes have recently made significant progress in a wide range of applications such as full-color displays, lighting systems, optical storage, chemical sensors, printing, and medical applications [1-3]. GaN-based semiconductor lasers are now commercialized. However, researchers are trying to reach laser diodes with shorter emission wavelengths and excellent performance for the next generation of laser sources. They provide a safer condition for various applications including high-density optical disc systems [4, 5]. Nevertheless, LDs structures enjoy various fundamental properties that necessitate further evaluation.

The active region, including quantum wells and barriers, is the region where the laser action takes place. Although quantum wells are the main source of laser action, the quantum wells coupling is prevented by quantum barriers. Thus, quantum barriers are considered to be essential structural layers that affect the electrical, optical, and performance characteristics of GaN-based optoelectronic devices. Indium composition, doping concentration, and thickness of quantum barriers are the variable parameters that optimize their effects on output performance characteristics [6, 7]. Quantum barriers have significant effects on different recombinations in the active region including radiative and non-radiative recombinations. Among the various effective parameters for enhancing the performance of LDs, poor hole injection efficiency along with electron leakage is a critical factor. Several scientists have attempted to solve this problem by changing the laser structures [8, 9]. Hansen et al. proposed a thin AlGaN cap between the active region and p-type layers to avoid electron overflow [10]. The electron overflow is considerably reduced by utilizing this thin AlGaN layer which is known as an Electron Blocking Layer (EBL) [11-14]. Prior studies indicate that substituting the conventional GaN quantum barriers with the InGaN quantum barriers could effectively reduce polarization effects between the well and barrier and, then, decrease the electron current overflow [13]. Park et al. and Khan et al. demonstrated that optical properties

*Corresponding Author's Email: m_khorsandi@sbu.ac.ir (M. Khorsandi)
URL: https://www.jree.ir/article_143144.html

Please cite this article as: Alahyarizadeh, Gh., Amirhoseiny, M. and Khorsandi, M., "Performance enhancement of deep violet InGaN double quantum wells laser diodes with quaternary superlattice barriers structure", ***Journal of Renewable Energy and Environment (JREE)***, Vol. 9, No. 1, (2022), 106-111. (https://doi.org/10.30501/jree.2021.300112.1246).

of InGaN MQWs could be enhanced with quaternary AlInGaN barriers [15, 16]. The use of quaternary AlInGaN provides an environment to control the lattice constant and bandgap. There are several EBL designs that are used to reduce electron overflow. They include AlInGaN quaternary EBL [17, 18], Strain-free GaN-InAlN SLS EBL [13], W-shaped EBL [19], step and linearly graded EBL [20], tapered and graded AlGaN EBL [21], quaternary AlInGaN/GaN SLS EBL [22], and quaternary AlInGaN multi quantum-barrier EBL [23]. In this regard, built-in polarization is also significantly reduced. Moreover, further designs have been proposed in the literature that use SLS cladding and waveguide layer instead of conventional cladding and waveguide layers [24, 25]. The proposed designs have improved OCF and consequently the output power. Furthermore, some approaches have been also proposed to enhance electron and hole wave functions overlapping in the active region including quantum wells and barriers. However, the performance improvement for InGaN- based LDs is still under process.

In this paper, we numerically compare the electrical and optical characteristics of InGaN MQW LDs with three different barriers structures. To enhance the emission intensity of the laser and reduce the threshold current, we have proposed the quaternary SLS structure on barriers. The performance of the GaN-based LDs can be investigated by analyzing the power characteristics, DQE, conduction, and valence energies in the vertical direction, electron and hole carrier densities, radiative recombination, and LD's optical emission intensity.

2. MATERIALS AND METHODS

The structural parameters such as thickness, material compositions, and doping type of basic LD structure, which is considered as a reference in this study, are given in Table 1. Except for the barriers, all the other layers in three desired LDs consist of the same layers compared to the basic structure. Barriers of LDs structure are replaced by a quaternary AlInGaN layer (structure B) and an AlInGaN/AlGaN superlattice (structure C), respectively. A diagram illustration of the LD structures is depicted in Figure 1.

Table 1. The structural parameters including thickness, material compositions, and doping type of basic LD structure

Component	Thickness (μm)	materials	Doping type
Base layer	0.4	GaN	n
Compliance layer	0.1	$In_{0.05}Ga_{0.95}N$	n
Cladding layer	0.42	$Al_{0.07}Ga_{0.93}N$	n
Waveguiding layer	0.1	GaN	n
Quantum wells (2)	0.0025	$In_{0.082}Ga_{0.918}N$	-
Quantum barriers (3)	0.0085	GaN	-
EBL	0.015	$Al_{0.22}Ga_{0.78}N$	p
Waveguiding layer	0.1	GaN	p
Cladding layer	0.42	$Al_{0.07}Ga_{0.93}N$	p
P-contact layer	0.1	GaN	p

The laser simulation process was performed by ISE-TCAD software. The simulation parameters are the same as those used in our previous studies [12, 26]. All the ternary and quaternary parameters were interpolated by binary alloys listed in Table 2.

Table 2. Room temperature properties of binary III-N materials [27]

Parameter	GaN	AlN	InN
Bandgap energy E_g (eV)	3.47	6.28	0.8
Electron affinity (eV)	4.1	1.9	5.8
Lattice constant a_0 (°A)	3.189	3.112	3.545
Refractive index near E_g	2.506	2.035	2.9
Electron effective mass	0.22 m_e	0.4 m_e	0.11m_e
Heavy hole effective mass	1.595 m_e	2.68 m_e	1.449 m_e
Light hole effective mass	0.261 m_e	0.261 m_e	0.157 m_e
spontaneous polarization Psp	-0.034	-0.090	-0.042
Elastic stiffness constant C_{13}(GPa)	106	108	92
Elastic stiffness constant C_{33}(GPa)	398	373	224
Relative dielectric constant	8.9	8.5	9.5

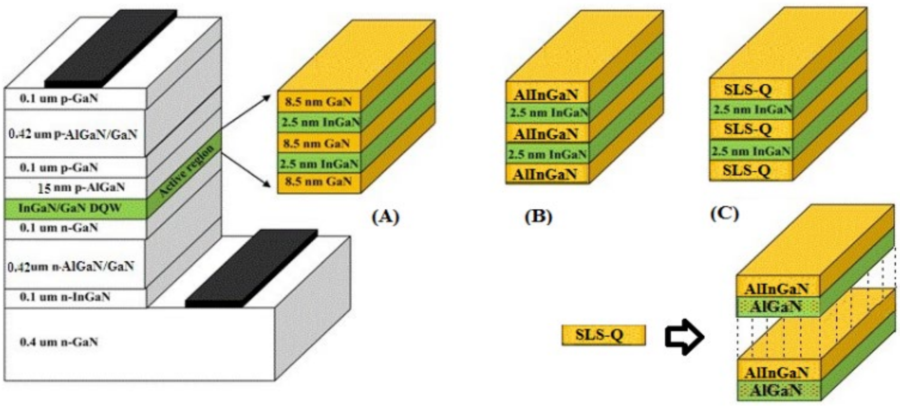

Figure 1. Illustration of InGaN MQW LDs including u-GaN (basic LD), AlGaN/GaN superlattice, and quaternary AlInGaN barri

3. RESULTS AND DISCUSSION

The threshold current, output power, slope efficiency, and Differential Quantum Efficiency (DQE) of the three different structures of deep violet $In_{0.082}Ga_{0.918}N$/GaN DQW LDs are shown in Table 3. Using quaternary AlInGaN barriers presents higher values for the output power, slope efficiency, and DQE, compared with the basic $In_{0.082}Ga_{0.918}N$/GaN DQW LD. Although quaternary barriers considerably enhanced the performance characteristics of LD, they would not decrease the threshold current remarkably. By replacing the barriers structure with AlInGaN/AlGaN quaternary SLS, LDs performance characteristics are still under significant progress compared to the basic structure, but the threshold current is considerably degraded. It can be introduced by comparing the conduction and the valence band energies of the proposed structure.

Figure 2 shows the conduction and valence band energies and the quasi-Fermi levels of the three different structures of deep violet $In_{0.082}Ga_{0.918}N$/GaN DQW LDs. As shown in Figure 2, the barrier structures are strongly affected by conduction, valance band, and the Fermi levels. The differences between conduction band energies and their quasi-Fermi levels can express the possibility of electrons leaking to the EBL layer to flow in the p-type layer. Finding a structure that can increase this difference would help to decrease the electron leakage and reduce the threshold current. On the other hand, the differences between valance band energies and their quasi-Fermi levels can define injection of holes to the active region and promote radiative recombination which would enhance the output power. The best structure should have both factors to improve the output power, slope efficiency, and DQE, whereas the threshold current is reduced.

The barrier's energy band is seriously affected by the built-in electric field induced by the compressive strain. The results show that in quaternary barriers, the electrons will confront a highly effective potential of 569 meV than the basic structure. At the same time, the holes encounter a much lower effective potential of about 123 meV. The higher effective potential between the conduction band and Fermi level decreases the threshold current in p-GaN and SLS barrier structures, as discussed in Table 1.

Table 3. The parameters of InGaN DQW laser with quaternary and SLS quaternary barriers structures

Parameter	Threshold current	Output power	Slop efficiency	DQE %	Wavelength
main:	16.59	33.49	1.627	51.29	390.667
MainQB:	15.01	40.59	1.882	59.17	389.640
All SLSQB:	12.88	39.05	1.860	58.40	389.294

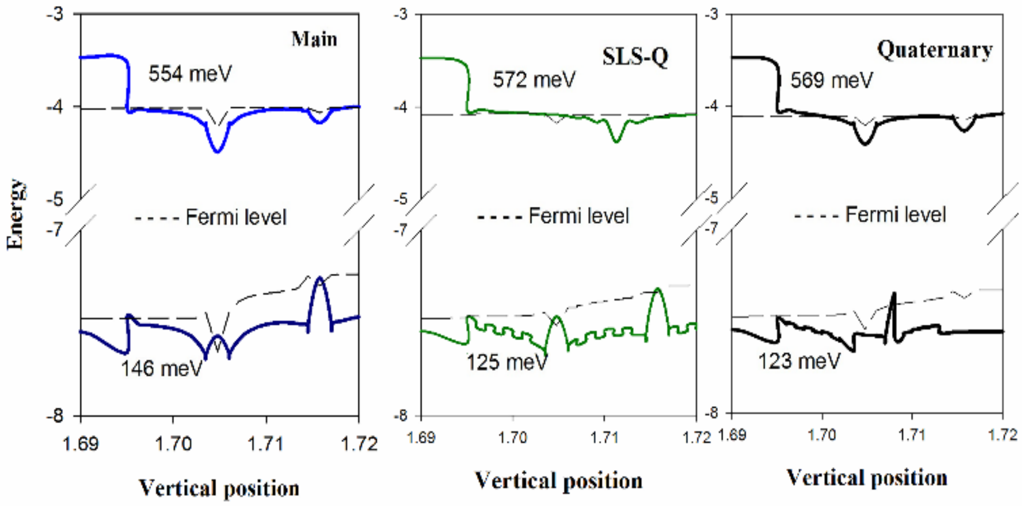

Figure 2. Energy band diagrams of InGaN DQW lasers with quaternary and SLS-Q barriers structures

A strong built-in polarization field due to the spontaneous polarization and a piezoelectric polarization field in the III-nitride structures are other parameters that affect the device's performance. A piezoelectric polarization field can be generated due to the lattice mismatch between different layers in the LD structure, especially between AlGaN and (In)GaN layers. This field can be reduced by using the AlInGaN layer or thin AlGaN, the GaN layer in the SLS structure (Figure 3). The built-in polarization field can pull down the GaN energy band and pull up the AlGaN ones, respectively. Therefore, the energy bands of AlGaN/GaN SLS barriers are bent. Thereupon, the height of the effective potential barrier for electrons increases and, then, the electron leakage is reduced. However, following the decreased effective potential, injection of the holes into the active region increases and consequently, the overall holes concentration also increases [**Error! Bookmark not defined.**]. The same trend can be seen in the carrier current densities in Figure 4.

It can be seen that the quaternary structure has the highest hole's current density in the active region among the other LDs. It is due to the improvement of the hole injection efficiency caused by the lowest effective potential height. Electron carrier density is another carrier that contributes to radiative recombination. As mentioned before, electron and hole leakages have an essential role in the reduction of the threshold current. The SLS barrier structure provides the lowest electron and hole leakage among the three recommended structures.

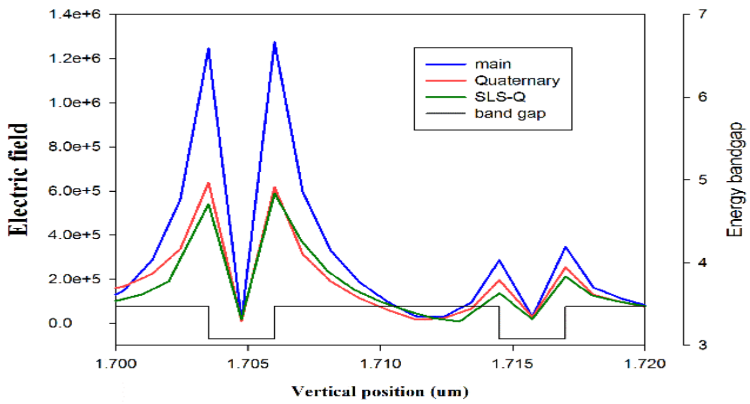

Figure 3. Electric field of InGaN DQW lasers with quaternary and SLS-Q barriers structures

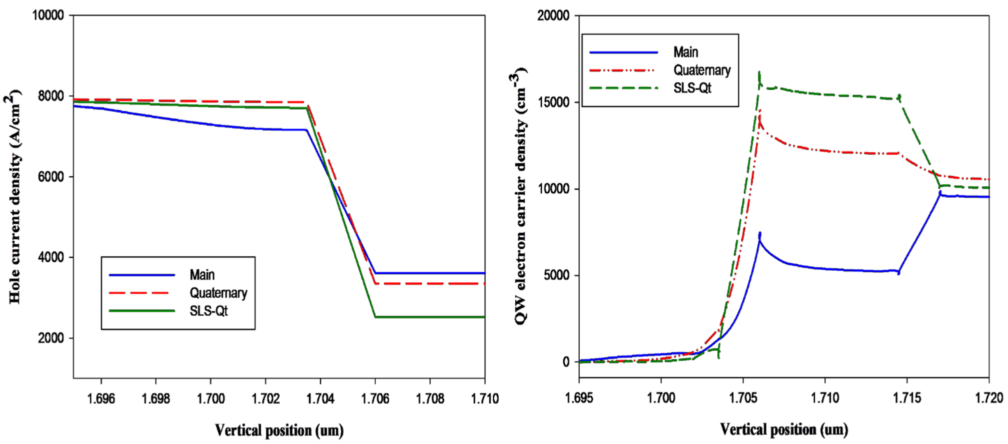

Figure 4. The carrier current density of InGaN DQW lasers with SLS and quaternary barriers structures

The radiative recombination rates of the three considered structures are shown in Figure 5. According to the knowledge that by increasing the carrier concentration, more electrons can remain in the active region which would be recombined with holes. Therefore, the efficiency degradation is reduced due to more quantum wells' contribution to the radiative recombination. As a result, it can be seen that the radiative recombination rate in quaternary and SLS-Q structures is higher than that in the basic structure because the two proposed structures provide greater extensive electron confinement and hole injection.

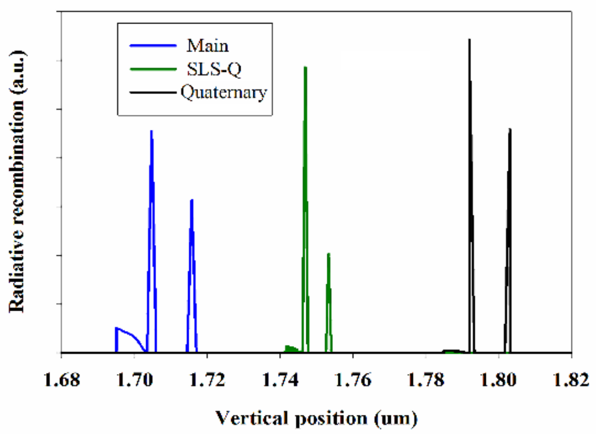

Figure 5. Rate of radiative recombination of the InGaN DQW lasers including quaternary and SLS-Q barriers structures

The optical intensity of the three of the InGaN DQW LDs with three different barriers structures is shown in Figure 6. The presence of more carriers in LDs that are supposed to accumulate in the active region improves the stimulated recombination rate in the active region and results in the enhancement of the optical intensity of LDs. It is observed that the InGaN laser with a quaternary structure has the highest carrier current density and good radiative recombination in the active region that causes the highest optical intensity among all the considered structures.

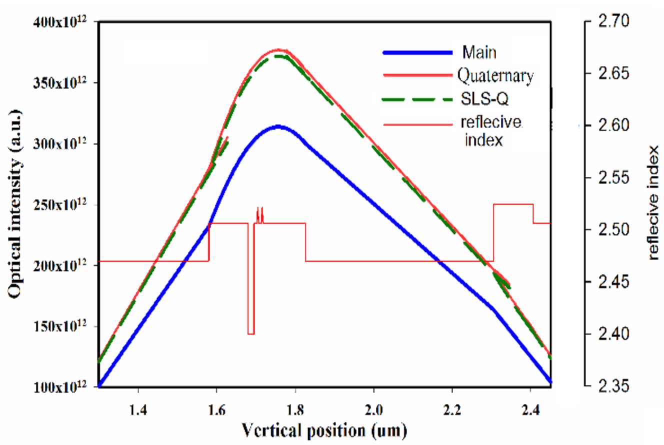

Figure 6. The optical intensity of the three structures of InGaN DQW lasers with quaternary and SLS-Q barriers structures

The light output characteristics of the InGaN DQW LDs with three different barrier structures are shown in Figure 7. As shown in this figure, the LD structures with quaternary and SLS-Q barriers have considerably higher output power than the main LD structures. The output power strongly depends on the photon density inside the cavity. Based on the presented results (Figure 2 & Figure 3), InGaN DQW LDs with quaternary and SLS-Q barriers are of highest current density, which itself indicates the highest amount of output power. The results of output power are completely in good agreement with the previously discussed outcomes and also with the reported experimental results in the literature [15].

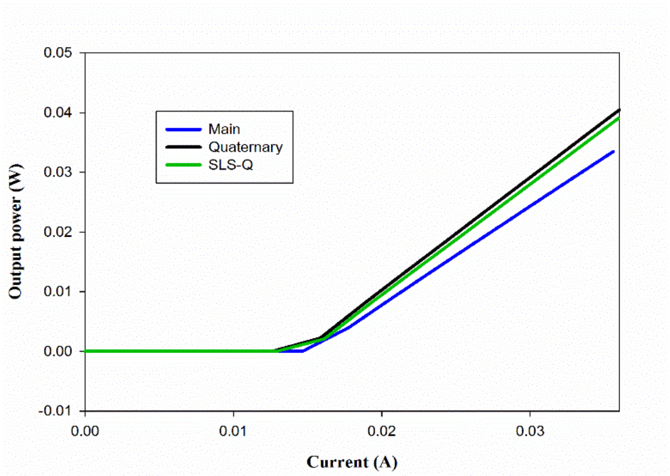

Figure 7. Light output characteristic (L-I) of InGaN DQW lasers with quaternary and SLS-Q barriers structures

4. CONCLUSIONS

To enhance the InGaN DQW LDs characteristics, a different designed LD was proposed with quaternary barriers and AlGaN/AlInGaN quaternary superlattice barriers. The simulation results indicate that the optical properties of the LDs were significantly enhanced in both quaternary and quaternary SLS structures owing to the increase of hole injection, the reduction of electron leakage, and the better radiative recombination in the QWs. Compared with the LDs using GaN, quaternary barriers, the laser with SLS-Q barriers exhibited the lowest threshold current. The reason could be the effects of the lowered generated strong piezoelectric polarization field due to the lattice mismatch between the AlGaN layer and the AlInGaN layer in the SLS structure. The proposed SLS-Q barriers, as the best structure, improved the output power, slope efficiency, and DQE while the threshold current was significantly reduced.

5. ACKNOWLEDGEMENT

The authors are gratefully indebted to Shahid Beheshti University for researching support of this work.

REFERENCES

1. Ohta, H., DenBaars, S.P. and Nakamura, S., "Future of group-III nitride semiconductor green laser diodes", ***Journal of the Optical Society of America B***, Vol. 27, No. 11, (2010), B45-B49. (https://doi.org/10.1364/JOSAB.27.000B45).

2. Huang, C.-Y., Lin, Y.-D., Tyagi, A., Chakraborty, A., Ohta, H., Speck, J.S., DenBaars, S.P. and Nakamura, Sh., "Optical waveguide simulations for the optimization of InGaN-based green laser diodes", ***Journal of Applied Physics***, Vol. 107, No. 2, (2010), 023101-023107. (https://doi.org/10.1063/1.3275325).

3. Nakamura, Sh., Senoh, M., Nagahama, S.-I., Iwasa, N., Matsushita, T. and Mukai, T., "Blue InGaN-based laser diodes with an emission wavelength of 450 nm", ***Applied Physics Letters***, Vol. 76, No. 1, (2000), 22-24. (https://doi.org/10.1063/1.125643).

4. Alahyarizadeh, Gh., Aghajani, H., Mahmodi, H., Rahmani, R. and Hassan, Z., "Analytical and visual modeling of InGaN/GaN single quantum well laser based on rate equations", ***Optics & Laser Technology***, Vol. 44, No. 1, (2012), 12-20. (https://doi.org/10.1016/j.optlastec.2011.05.003).

5. Zhang, Y., Li, P.L., Nie, P.L. and Wu, Y.X., "Effect of ultra-rapid cooling on microstructure of laser cladding IN718 coating", ***Surface Engineering***, Vol. 29, No. 6, (2013), 414-418. (https://doi.org/10.1179/1743294413Y.0000000142).

6. Cheng, L., Li, Z., Zhang, J., Lin, X., Yang, D., Chen, H., Wu, S. and Yao, S., "Advantages of InGaN–GaN–InGaN delta barriers for InGaN-based laser diodes", ***Nanomaterials***, Vol. 11, No. 8, (2021), 2070. (https://doi.org/10.3390/nano11082070).

7. Ghazai, A.J., Thahab, S.M., Abu Hassan, H. and Hassan, Z., "A study of the operating parameters and barrier thickness of $Al_{0.08}In_{0.08}Ga_{0.84}N/Al_xIn_yGa_{1-x-y}N$ double quantum well laser diodes-Alaa", ***Science China Technological Sciences***, Vol. 54, No. 1, (2011), 47-51. (https://doi.org/10.1007/s11431-010-4183-1).

8. Usman, M., Mushtaq, U., Zheng, D.-G., Han, D.-P., Rafiq, M. and Muhammad, N., "Enhanced internal quantum efficiency of bandgap-engineered green W-shaped quantum well light-emitting diode", ***Applied Science***, Vol. 9, No. 1, (2019), 77. (https://doi.org/10.3390/app9010077).

9. Xiong, J.-Y., Zhao, F., Fan, G.-H., Xu, Y.-Q., Liu, X.-P., Song, J.-J., Ding, B.-B., Zhang, T. and Zheng, S.-W., "Efficiency enhancement of an InGaN light-emitting diode with a p-AlGaN/GaN superlattice last quantum barrier", ***Chinese Physics B***, Vol. 22, No. 11, (2013), 118504. (https://doi.org/10.1088/1674-1056/22/11/118504).

10. Hansen, M., Piprek, J., Pattison, P.M., Speck, J.S., Nakamura, S. and DenBaars, S.P., "Higher efficiency InGaN laser diodes with an improved quantum well capping configuration", ***Applied Physics Letters***, Vol. 81, No. 22, (2002), 4275-4277. (https://doi.org/10.1063/1.1524690).

11. Kuo, Y.-K., Chen, F.-M., Chang, J.-Y., Huang, M.-F., Liou, B.-T. and Shih, Y.-H., "Design and optimization of electron-blocking layer in deep ultraviolet light-emitting diodes", ***IEEE Journal of Quantum Electronics***, Vol. 56, No. 1, (2020), 1-6. (https://doi.org/10.1109/JQE.2019.2957575).

12. Alahyarizadeh, Gh., Amirhoseiny, M. and Hassan, Z., "Effect of different EBL structures on deep violet InGaN laser diodes performance", ***Optics and Laser Technology***, Vol. 76, (2016), 106-112. (https://doi.org/10.1016/j.optlastec.2015.08.007).

13. Paliwal, A., Singh, K. and Mathew, M., "Strain-free GaN/InAlN chirped short-period superlattice electron-blocking layer for 450 nm InGaN laser diode", ***Laser Physics***, Vol. 29, No. 5, (2019), 056204. (https://doi.org/10.1088/1555-6611/ab05be).

14. Paliwal, A., Singh, K. and Mathew, M., "Effects of electron blocking layer configuration on the dynamics of laser diodes emitting at 450 nm", ***Laser Physics***, Vol. 30, No. 1, (2020), 016210. (https://doi.org/10.1088/1555-6611/ab5587).

15. Park, S.-H., Kim, H.-M. and Ahn, D., "Optical gain in GaN quantum well lasers with quaternary AlInGaN Barriers", ***Japanese Journal of Applied Physics***, Vol. 44, No. 10R, (2005), 7460. (https://doi.org/10.1088/1555-6611/ab5587).

16. Asif Khan, M., Yang, J.W. and Simin, G., "Lattice and energy band engineering in AlInGaN/GaN heterostructures", ***Applied Physics Letters***, Vol. 76, (2000), 1161. (https://doi.org/10.1063/1.125970).

17. Alahyarizadeh, Gh., Hassan, Z., Thahab, S.M., Amirhoseiny, M. and Naderi, N., "Comparative study of the performance characteristics of green InGaN SQW laser diodes with ternary AlGaN and quaternary AlInGaN electron blocking layer", ***Digest Journal of Nanomaterials and Biostructures***, Vol. 7, No. 4, (2012), 1869-1880. (https://chalcogen.ro/index.php/journals/digest-journal-of-nanomaterials-and-biostructures/8-djnb/29-volume-7-number-4-october-december-2012), (Accessed: 4 February 2022).

18. Schubert, M.F., Xu, J., Kim, J.K., Schubert, E.F., Kim, M.H., Yoon, S., Lee, S.M., Sone, Ch., Sakong, T. and Park, Y., "Polarization-matched GaInN/AlGaInN multi-quantum-well light-emitting diodes with reduced efficiency droop", ***Applied Physics Letters***, Vol. 93, (2008), 041102. (https://doi.org/10.1063/1.2963029).

19. Usman, M., Munsif, M. and Anwar, A.-R., "Wedge-shaped electron blocking layer to improve hole transport and efficiency in green light-emitting diodes", ***Optics Communications***, Vol. 464, (2020), 125493. (https://doi.org/10.1063/1.2963029).

20. Usman, M., Munsif, M., Anwar, A.-R., Jamal, H., Malik, Sh. and Islam, N.U., "Quantum efficiency enhancement by employing specially designed AlGaN electron blocking layer", ***Superlattices and***

Microstructures, Vol. 139, (2020), 106417. (https://doi.org/10.1016/j.spmi.2020.106417).

21. Yang, W., Li, D., He, J. and Hu, X., "Advantage of tapered and graded AlGaN electron blocking layer in InGaN-based blue laser diodes", ***Physics Status Solidi C***, Vol. 10, No. 3, (2013), 346-349. (https://doi.org/10.1002/pssc.201200637).

22. Tzou, A.-J., Lin, D.-W., Yu, C.-R., Li, Z.-Y., Liao, Y.-K., Lin, B.-C., Huang, J.-K., Lin, C.-C., Kao, T. S., Kuo, H.-C. and Chang, C.-Y., "High-performance InGaN-based green light-emitting diodes with quaternary InAlGaN/GaN superlattice electron blocking layer", ***Optics Express***, Vol. 24, No. 11, (2016), 11387-11395. (https://doi.org/10.1364/OE.24.011387).

23. Alahyarizadeh, Gh., Hassan, Z., Thahab, S.M., Yam, F.K. and Ghazai, A.J., "Numerical study of performance characteristics of deep violet InGaN DQW laser diodes with AlInGaN quaternary multi-quantum barrier electron blocking layer," ***Optik***, Vol. 124, No. 24, (2013), 6765-6768. (https://doi.org/10.1016/j.ijleo.2013.05.080).

24. Xiong, J.-Y., Xu, Y.-Q., Zheng, S.W., Zhao, F., Ding, B.-B., Song, J.-J., Yu, X.-P., Zhang, T. and Fan, G.-H., "Advantages of GaN-based light-emitting diodes with p-AlGaN/InGaN superlattice last quantum barrier", ***Optics Communications***, Vol. 312, (2013), 85-88. (https://doi.org/10.1016/j.optcom.2013.08.053).

25. Alahyarizadeh, Gh., Hassan, Z., Thahab, S.M., Yam, F.K. and Ghazai, A.J., "Performance characteristics of deep violet InGaN DQW laser diodes with InGaN/GaN superlattice waveguide layers", ***Optik***, Vol. 125, No. 1, (2014), 341-344. (https://doi.org/10.1016/j.ijleo.2013.06.059).

26. Alahyarizadeh, Gh., Hassan, Z. and Yam, F.K., "Improvement of the performance characteristics of deep violet InGaN multiquantum-well laser diodes using step-graded electron blocking layers and a delta barrier", ***Journal of Applied Physics***, Vol. 113, (2013), 123108. (https://doi.org/10.1063/1.4798388).

27. Alahyarizadeh, Gh., "Improved performance characteristics of violet InGaN MQW LDs through asymmetric W-shaped quantum wells", ***Physics E***, Vol. 127, (2021), 114570. (https://doi.org/10.1016/j.physe.2020.114570).

ABSTRACTS

Sensitivity Analysis for 3E Assessment of BIPV System Performance in Abadan in Southwestern Iran

Sepideh Rahmati Dehkordi [a], Mehdi Jahangiri [b*]

[a] *Department of Architecture and Urbanism, Central Tehran Branch, Islamic Azad University, Tehran, Iran.*
[b] *Department of Mechanical Engineering, Shahrekord Branch, Islamic Azad University, Shahrekord, Iran.*

PAPER INFO

Paper history:
Received: 16 December 2020
Revised in revised form: 07 February 2021
Scientific Accepted: 16 February 2021
Published: 22 August 2021

Keywords:
BIPV,
HOMER,
CO_2 Emission,
Photovoltaic,
3E Analysis

ABSTRACT

In Iran, due to the problems and constraints of fossil fuels and the need to maximize the use of solar potential, one of the best ways is the application of photovoltaic systems integrated with buildings. Due to the significant dependence of solar cell performance on the availability of radiation, it is necessary for architects to have an accurate assessment of the amount of electricity produced in different conditions. Therefore, in the present work, using HOMER software, the energy-econo-Enviro (3E) potential of a Building Integrated Photovoltaic (BIPV) in Abadan was studied. The effect of slope and azimuth of solar cells as well as cloudiness and system losses were investigated using sensitivity analysis. The results showed that the PV-grid system was the most economical option and after the azimuth angle of zero degree, the positive azimuth angle was the most economical. The results also showed that the slope of 30 degree and the angle of azimuth equal to zero was appropriate, for which the price per kWh of generated electricity was calculated to be $0.09. For the use of solar cells in the vertical wall of the building, the southwest direction was the most suitable and based on the results, it was suggested that the western wall of the building should be in the form of "inclined PVs with windows". The authors of this paper hope that the results of the present work can be used by architects and energy decision-makers as a guide in developing the BIPV use in Iran.

https://doi.org/10.30501/jree.2021.262420.1173

چکیده

در ایران به سبب مشکلات و محدودیت‌های سوخت‌های فسیلی و ضرورت بهره‌برداری حداکثری از پتانسیل خورشیدی، امروزه یکی از بهترین راه‌ها، بکارگیری سیستم‌های فتوولتاییک به‌صورت ساختمان یکپارچه با فتوولتاییک است. بدلیل وابستگی زیاد عملکرد سلول‌های خورشیدی به در دسترس بودن تابش، لازم است تا معماران اطلاعات دقیقی از میزان برق تولیدی در شرایط مختلف داشته باشند. لذا در کار حاضر، با استفاده از نرم‌افزار HOMER به پتانسیل‌سنجی فنی-اقتصادی-زیست‌محیطی یک BIPV در شهر آبادان پرداخته شده است. تأثیر شیب و جهت‌گیری سلول‌های خورشیدی و همچنین تلفات ابرناکی و افت سیستم، بوسیله آنالیز حساسیت مورد بررسی قرار گرفتند. نتایج نشان دادند که سیستم هیبریدی سلول خورشیدی-شبکه برق سراسری، اقتصادی‌ترین گزینه برای تمام حالات مورد بررسی بوده و پس از ازیموث صفر، ازیموث مثبت، اقتصادی‌ترین حالت می‌باشد. همچنین نتایج، حاکی از مناسب بودن شیب ۳۰ درجه و زاویه ازیموث صفر بودند که برای این حالت، قیمت هر کیلووات ساعت برق تولیدی برابر ۰/۰۹ دلار محاسبه شد. برای استفاده از سلول‌های خورشیدی در دیواره عمودی ساختمان، جهت جنوب‌غربی مناسب‌ترین بود و براساس نتایج، پیشنهاد شد تا جداره غربی ساختمان به فرم inclined PVs with windows باشد. نویسندگان مقاله حاضر امیدوارند تا نتایج کار حاضر بتوانند به‌عنوان یک راهنما در توسعه استفاده از BIPV در ایران، به کار معماران و تصمیم‌گیران حوزه انرژی بیایند.

Investigation and Ranking of the Effect of Biodiesel Produced from Safflower Oil by the Hydrodynamic Method in Diesel Generator Engine Using TOPSIS Method

Marziyeh Gharibian [a], Bahram Hosseinzadeh Samani [a*], Alireza Shirneshan [b,c], Sajad Rostami [a]

[a] *Department of Mechanical Engineering of Biosystems, Shahrekord University, Shahrekord, Chaharmahal and Bakhtiari, Iran.*
[b] *Department of Mechanical Engineering, Najafabad Branch, Islamic Azad University, Najafabad, Iran.*
[c] *Aerospace and Energy Conversion Research Center, Najafabad Branch, Islamic Azad University, Najafabad, Iran.*

P A P E R I N F O

Paper history:
Received: 27 February 2021
Revised in revised form: 10 April 2021
Scientific Accepted: 15 April 2021
Published: 30 October 2021

Keywords:
Biodiesel,
Hydrodynamic Reactor,
Diesel Generator,
Performance Indices,
Pollution Indicators

A B S T R A C T

To investigate the possibility of using fuel for plant origin in a diesel generator, safflower methyl ester was prepared and used as a biodiesel. In this research, biodiesel was produced through a transesterification reaction using a hydrodynamic reactor, which increased the reaction efficiency and reduced fuel production time. Upon increasing the reaction time from 30 seconds to 60 seconds, the reaction performance increased by 5.5 %. Then, its important features complied with ASTM D-6751 standard. The performance and pollution indices of the diesel generator engine were tested with compounds B0, B20, B50, B80 and B100. The results of short-term engine tests showed that by increasing the share of biodiesel to 20 %, CO emissions were reduced by 21 % compared to pure diesel fuel, but the amount of NO_X increased by 0.82 % compared to diesel. Also, the use of 20 % volume of biodiesel in the fuel composition increased the thermal efficiency of braking, braking power, and braking torque of fuel, compared to diesel. Also, the specific fuel consumption of B20 was reduced by 2 %, which is very important economically. Finally, the TOPSIS analysis illustrated that B50 fuel outperformed pure diesel fuel and other listed fuel combinations.

https://doi.org/10.30501/jree.2021.272074.1186

چکیده

به منظور بررسی امکان استفاده از سوخت‌های با منشأ گیاهی در موتور دیزل ژنراتور، متیل‌استر گلرنگ به عنوان بیودیزل تهیه و به‌کار گرفته شد. در این تحقیق، سوخت بیودیزل با استفاده از واکنش ترانس استریفیکاسیون به کمک راکتور کاویتاسیون هیدرودینامیکی با متانول در حضور هیدروکسید پتاسیم به عنوان کاتالیست، تولید شد که این راکتور باعث افزایش بازده و کاهش زمان فرایند تولید بیودیزل شد. به طوری‌که با افزایش زمان واکنش از ۳۰ ثانیه به ۶۰ ثانیه، عملکرد واکنش ۵/۵ ٪ افزایش یافت. در انتها، ویژگی‌های مهم سوخت با استاندارد ASTM D-6751 تطبیق داده شد. سپس شاخص‌های عملکردی و آلایندگی موتور دیزل ژنراتور با ترکیبات B0، B20، B50، B80 و B100 مورد آزمایش قرار گرفت. نتایج آزمون‌های کوتاه مدت موتور نشان داد که با افزایش مقدار بیودیزل در ترکیب سوخت تا ۲۰ ٪ حجمی ، انتشار آلاینده کربن مونواکسید (CO) نسبت به سوخت دیزل خالص، ۲۱ ٪ کاهش می‌یابد ولی مقدار NO_X تا ۰/۸۲ ٪ نسبت به گازوئیل افزایش می‌یابد. همچنین استفاده از ترکیب B20 باعث افزایش بازده حرارتی ترمزی، توان ترمزی و گشتاور ترمزی سوخت نسبت به گازوئیل می‌شود. دمای گازهای خروجی به مقدار قابل توجهی کاهش یافت. همچنین مصرف سوخت ویژه ترمزی سوخت B20 مقدار ۲ ٪ کاهش یافت که به لحاظ اقتصادی بسیار مهم است. در نهایت، آنالیز به روش TOPSIS نشان داد بهترین سوخت از لحاظ همه جوانب، B50 است.

Assessment of Effect of Different Parameters on Temperature Distribution in Chemical Looping Combustor: Experimental and Numerical Approaches

Mohamed A. Barakat, Tamer Mohamed Ismail, Sayed Ibrahim Abdel-Mageed, Khaled Ramzy *

Department of Mechanical Engineering, Faculty of Engineering, Suez Canal University, Ismailia, Egypt.

PAPER INFO

Paper history:
Received: 26 January 2021
Revised in revised form: 15 March 2021
Scientific Accepted: 12 April 2021
Published: 07 November 2021

Keywords:
CO_2 Capture,
Chemical Looping Combustion,
Solid Fuel,
Gaseous Fuel,
Nickel Powder,
Modelling

ABSTRACT

The greenhouse problem has a significant effect on our communities, health, and climate. So, the capturing techniques for CO_2 remain the focus of attention these days. In this work, a Chemical Looping Combustor (CLC) was designed and fabricated with the major geometric sizes at the Faculty of Engineering, Suez Canal University. The system involves two interconnected fluidized beds. Nickel powder with 150 µm diameter as well as brown coal and liquefied petroleum gas were used as oxygen carrier, solid fuel, and gaseous fuel, respectively. The temperature distributions along the fuel reactor for LPG flow rates of 11 and 18 LPM with and without using nickel powder as well as using preheated reactor were discussed and evaluated. The effects of brown coal diameter change with and without using nickel powder were studied. The CO and CO_2 concentrations at combustion gases with and without using nickel powder were conducted for LPG and brown coal fuels. A mathematical model was used to simulate the combustion in CLC using combustion and energy code. The obtained results showed that using nickel powder improved the combustion process and in case of using LPG, the flame color changed to blue which is the color of the complete combustion flame. The CO was reduced by 48.4 % and CO_2 was augmented by 66.5 %. In case of using brown coal as solid fuel, CO was reduced by 53.7 % and CO_2 was increased by 71.9 %. Finally, there is good agreement between the experimental and numerical results based on the determination coefficient.

https://doi.org/10.30501/jree.2021.269946.1182

چکیده

مشکل گلخانه تأثیر قابل توجهی بر جوامع، سلامت و آب و هوای ما دارد. بنابراین، تکنیک‌های جذب CO_2 این روزها همچنان مورد توجه است. در این کار، یک احتراق چرخشی شیمیایی (CLC) با اندازه‌های هندسی عمده در دانشکده مهندسی دانشگاه کانال سوئز طراحی و ساخته شد. این سیستم شامل دو بستر سیال متصل به هم است. از پودر نیکل با قطر ۱۵۰ میکرومتر و زغال‌سنگ قهوه ای و گاز مایع (LPG) به‌ترتیب به‌عنوان حامل اکسیژن، سوخت جامد و سوخت گازی استفاده شد. توزیع دما در طول راکتور سوخت برای دبی LPG ۱۱ و ۱۸ لیتر در دقیقه با و بدون استفاده از پودر نیکل و همچنین با استفاده از راکتور پیش‌گرم شده مورد بحث و بررسی قرار گرفت. اثرات تغییر قطر زغال‌سنگ قهوه ای با و بدون استفاده از پودر نیکل مورد مطالعه قرار گرفت. غلظت CO و CO_2 در گازهای احتراق با و بدون استفاده از پودر نیکل برای LPG و سوختهای زغال‌سنگ قهوه ای انجام شد. یک مدل ریاضی برای شبیه‌سازی احتراق در CLC با استفاده از کد احتراق و انرژی استفاده شد. نتایج بدست آمده نشان داد که استفاده از پودر نیکل روند احتراق را بهبود بخشیده و در صورت استفاده از LPG، رنگ شعله به آبی که رنگ شعله کامل احتراق است، تغییر کرده است. میزان کربن دی اکسید کربن ۴۸/۴ درصد کاهش یافته و میزان کربن دی اکسید کربن ۶۶/۵ درصد افزایش یافته است. در صورت استفاده از زغال‌سنگ قهوه ای به عنوان سوخت جامد، CO به میزان ۵۳/۷ درصد کاهش و CO_2 به میزان ۷۱/۹ درصد افزایش می‌یابد. در نهایت، بین نتایج تجربی و عددی بر اساس ضریب تعیین، توافق خوبی وجود دارد.

Trends of Progress in Setting up Biorefineries in Developing Countries: A Review of Bioethanol Exploration in Nigeria

Toyese Oyegoke [a,b*], Emo Obadiah [a], Francis Adah [c], John E. Oguche [a], Geoffrey T. Timothy [d], Ismail A. Mantu [e], Abubakar D. Ado [a]

[a] *Department of Chemical Engineering, Ahmadu Bello University, Zaria, Nigeria.*
[b] *Laboratoire de Chimie, École Normale Supérieure de Lyon, Lyon, France.*
[c] *Department of Water Resources & Environmental Engineering, Ahmadu Bello University, Zaria, Nigeria.*
[d] *Department of Biochemistry, Federal University, Dutsinma, Nigeria.*
[e] *Department of Political Science, Federal University, Dutsinma, Nigeria.*

P A P E R I N F O

Paper history:
Received: 27 March 2021
Revised in revised form: 14 June 2021
Scientific Accepted: 19 July 2021
Published: 20 November 2021

Keywords:
Biofuels,
Biomass,
Biorefinery,
Bioethanol,
Renewable Fuels,
Nigeria

A B S T R A C T

In recent times, limitations and adverse effects of fossil fuels have significantly attracted researchers' attention to green fuels worldwide, especially in developed nations. As a way of assessing this actualization of biorefineries establishment in developing nations, this report surveys the works done by various researches towards this great course in terms of promoting and gaining the attention of both government and private investors about the technical and economic feasibility of embracing the use of biofuels, a case of bioethanol in Nigeria. Different classes of feedstocks were reviewed for the laboratory-scale, process scale-up, pilot plant, and techno-economic studies regarding ascertaining the technical and economic feasibility of local setup of a functional biorefinery in Nigeria, which would be beneficial environmentally and economically. The literature survey unveiled that the Bioethanol yield obtained from sugarcane-juice (72.7 %), banana-stems (84.0 %), and cassava (92.0 %) were found to be of highest potential amongst other sugar-based, lignocellulosic, and starch-based feedstock, respectively. The survey further unveils that the volume of process scale-up and economic feasibility studies does not correlate well with the laboratory-scale studies. The bulk of the research works on bioethanol has given preferential attention to laboratory studies. Only a few studies have looked into the commercialization (i.e., scale-up) of the laboratory findings and the economic implications. Presently, only sugarcane and a few cassavas are reported in the literature so far. It is, therefore, necessary for further studies to give attention to the investigation of the commercializing locally developed technologies and the exploration of their economic benefits.

https://doi.org/10.30501/jree.2021.278037.1197

چکیده

اخیراً محدودیت‌ها و اثرات نامطلوب سوخت‌های فسیلی به طور قابل توجهی توجه محققان را به سوخت‌های سبز در سراسر جهان به‌ویژه در کشورهای توسعه‌یافته جلب کرده است. این گزارش به عنوان روشی برای ارزیابی واقعیت تأسیس پالایشگاه‌های زیستی در کشورهای در حال توسعه، به بررسی کارهای مختلف انجام شده توسط محققان در جهت ارتقاء و جلب توجه سرمایه گذاران دولتی و خصوصی در مورد امکان فنی و اقتصادی استفاده از سوخت‌های زیستی، از جمله اتانول زیستی در نیجریه می‌پردازد. انواع مختلف مواد اولیه برای بررسی مقیاس آزمایشگاهی، افزایش مقیاس فرآیند، پایلوت و مطالعات فنی-اقتصادی با توجه به امکان‌سنجی فنی و اقتصادی راه‌اندازی محلی یک پالایشگاه زیستی کاربردی در نیجریه، که از نظر زیست‌محیطی و اقتصادی مفید است، بررسی شدند. مطالعات مختلف نشان داد که بازده بیواتانول بر اساس مواد اولیه، به ترتیب حاصل از عصاره نیشکر (۷۲/۷ درصد)، ساقه موز (۸۴/۰ درصد) و کاساوا (۹۲/۰ درصد) در بین سایر مواد قندی، لیگنوسلولزی و نشاسته ای دارای بالاترین پتانسیل است. مطالعات بیشتر همچنین نشان می‌دهد که حجم مقیاس‌پذیری فرآیند و مطالعات امکان‌سنجی اقتصادی با مطالعات آزمایشگاهی همبستگی خوبی ندارد. بخش عمده ای از کارهای تحقیقاتی روی بیواتانول ترجیحاً به مطالعات آزمایشگاهی اختصاص داده شده است. تنها چند مطالعه به تجاری‌سازی (به عنوان مثال، افزایش مقیاس) یافته‌های آزمایشگاهی و پیامدهای اقتصادی آن پرداخته اند. در این مقاله تنها نیشکر و تعدادی کاساوا گزارش شده است. بنابراین، لازم است مطالعات بیشتری درباره بررسی تجاری‌سازی فناوری‌های توسعه‌یافته محلی و اکتشاف منافع اقتصادی آنها انجام پذیرد.

The Effect of Roof Integrated Photovoltaic (RIPV) on Building Indoor Air in African Tropical Climate

Aloys Martial Ekoe A. Akata*

Department of Physics, Faculty of Science, University of Douala, P. O. Box: 2701, Douala, Cameroon.

P A P E R I N F O

Paper history:
Received: 28 November 2020
Revised in revised form: 21 February 2021
Scientific Accepted: 12 March 2021
Published: 21 November 2021

Keywords:
Building Integrated Photovoltaic (BIPV),
Thermal Comfort,
Heat Transfer,
Indoor Air Temperature,
Photovoltaic,
Solar Roof

A B S T R A C T

Photovoltaic energy has the potential to become one of the major energy sources used in the households in the tropical region of Africa, where the solar radiation intensity is abundant and almost constant over the year. Solar photovoltaic systems present many advantages when they are integrated in the building structure envelope and have a significant influence on the indoor air temperature of dwelling buildings due to the thermal resistance modification. In this paper, a simplified model of the photovoltaic system integrated on the roof of a residential building according to the building construction customs and materials has been designed and modeled. The heat transfer is studied in several situations: with and without a Building Integrated Photovoltaic (BIPV) system and for a building with and without false ceiling. The BIPV system installed over an effective area of 35 m^2 increases the building indoor air temperature of approximately 5 °C which is corrected by the heat insulation optimization of the false ceiling made up with building local materials. The final indoor air temperature obtained is in good agreement with the ASHRAE standards and can, therefore, be applied to tropical regions.

https://doi.org/10.30501/jree.2021.259138.1166

چکیده

انرژی فتوولتائیک این پتانسیل را دارد که به یکی از منابع اصلی انرژی مورد استفاده در خانوارهای منطقه گرمسیری آفریقا تبدیل شود، جایی‌که شدت تابش خورشیدی در طول سال فراوان و تقریباً ثابت است. سیستم‌های فتوولتائیک خورشیدی هنگامی که با پوسته ساختمان ادغام می‌شوند، مزایای زیادی داشته و به دلیل اصلاح مقاومت حرارتی تأثیر قابل توجهی بر دمای هوای داخلی ساختمان‌های مسکونی دارند. در این مقاله، یک مدل ساده از سیستم فتوولتائیک ادغام شده بر روی پشت‌بام یک ساختمان مسکونی با توجه به مصالح ساختمانی به‌کار رفته شده، طراحی و مدل‌سازی شده است. انتقال حرارت در چندین موقعیت مورد مطالعه قرار می‌گیرد: با یا بدون سیستم فتوولتائیک یکپارچه ساختمان (BIPV) و برای یک ساختمان با داشتن و یا بدون داشتن سقف کاذب. سیستم BIPV نصب شده در مساحت مؤثر ۳۵ متر مربع، دمای هوای داخل ساختمان را تقریباً ۵ درجه سانتیگراد افزایش می‌دهد که با بهینه‌سازی عایق حرارتی سقف کاذب ساخته شده با مصالح محلی ساختمان اصلاح می‌شود. دمای نهایی هوای داخلی به‌دست آمده با استانداردهای ASHRAE مطابقت مطلوبی دارد و بنابراین می‌توان آن را در مناطق گرمسیری اعمال کرد.

Surface Modification of Copper Current Collector to Improve the Mechanical and Electrochemical Properties of Graphite Anode in Lithium-Ion Battery

Mohsen Babaiee *, Mohammad Zarei-Jelyani *, Shaghayegh Baktashian, Rahim Eqra

Department of Energy Storage, Institute of Mechanics, Shiraz, Iran.

P A P E R I N F O

Paper history:
Received: 20 June 2021
Revised in revised form: 17 August 2021
Scientific Accepted: 30 August 2021
Published: 05 December 2021

Keywords:
Li-Ion Battery,
Current Collector,
Surface Modification,
Cu Foil,
Graphite

A B S T R A C T

A mechanical technique was applied to the copper current collector of lithium-ion battery anode to improve interface adhesion between Cu foil and anode film. The mechanical and electrochemical performances of graphite anodes coated on Bare Cu Foil (BCF) and Modified Cu Foil (MCF) were evaluated. The BCF and MCF anodes exhibited adhesion strengths of 1.552 and 1.617 MPa, respectively. The electrochemical studies of BCF and MCF anodes showed that the initial discharge capacity of graphite anode coated on the MCF (323.6 mAh g^{-1}) was about 8 % higher than the BCF anode (299.9 mAh g^{-1}). The BCF anode capacity reached 227.9 mAh g^{-1} after 100 charge/discharge cycles at 0.5C rate, while this value was 247.7 mAh g^{-1} for MCF anode. The results of electrochemical impedance spectra demonstrated that the diffusion coefficient of lithium-ion for MCF anode was about 56 % higher than that for BCF anode. On the other hand, the surface modification of the copper current collector reduced the charge transfer resistance of anode from 28.5 Ω to 23.2 Ω.

https://doi.org/10.30501/jree.2021.290435.1219

چکیده

اصلاح سطحی جمع‌کننده جریان مسی در آند باتری لیتیوم-یون به روش مکانیکی انجام شده است تا خواص چسبندگی بین جمع‌کننده جریان و فیلم آندی بهبود یابد. عملکرد مکانیکی و الکتروشیمیایی آندهای گرافیتی پوشش داده‌شده روی ورق مسی اولیه (BCF) و ورق مسی اصلاح‌شده (MCF) مورد ارزیابی قرارگرفته است. نتایج نشان می‌دهد که آند BCF و MCF به ترتیب دارای استحکام چسبندگی ۱/۵۵۲ و ۱/۶۱۷ MPa می‌باشند. بررسی رفتار الکتروشیمیایی آندهای BCF و MCF نشان می‌دهد که ظرفیت دشارژ اولیه آند پوشش داده‌شده روی جمع‌کننده جریان MCF (۳۲۳/۶ mAh g^{-1}) حدود ۸ ٪ بیشتر از آند BCF (۲۹۹/۹ mAh g^{-1}) می‌باشد. پس از صد سیکل شارژ/ دشارژ در نرخ جریان ۰/۵C مقدار ظرفیت آند BCF به ۲۲۷/۹ mAh g^{-1} می‌رسد، درحالی‌که این مقدار برای آند MCF برابر با ۲۴۷/۷ mAh g^{-1} است. نتایج طیف‌های امپدانس الکتروشیمیایی نیز بیان‌گر این است که ضریب نفوذ یون لیتیوم برای آند MCF حدود ۵۶ ٪ بیشتر از آند BCF است. از طرفی اصلاح سطحی جمع‌کننده جریان مسی باعث شده است که مقاومت انتقال بار آند از Ω ۲۸/۵ به Ω ۲۳/۲ کاهش یابد.

A New Interleaved ZVT High Step-Up Converter with Low Count Elements for Photovoltaic Applications

Babak Tohidi, Majid Delshad *, Hadi Saghafi

Department of Electrical Engineering, Isfahan (Khorasgan) Branch, Islamic Azad University, P. O. Box: 81551-39998, Isfahan, Isfahan, Iran.

PAPER INFO

Paper history:
Received: 27 April 2021
Revised in revised form: 06 August 2021
Scientific Accepted: 22 August 2021
Published: 11 December 2021

Keywords:
High Step-Up,
Zero Voltage Transition,
Interleaved,
Current Ripple Cancelation

ABSTRACT

A new interleaved high step-up converter with Zero Voltage Transition (ZVT) is proposed for operation in this paper. The main advantages of the proposed converter are low input current ripple and low voltage stress on the power switches, high efficiency, low total component count, and eliminating reverse recovery problem of power diodes. Due to the soft switching operation of the switches and diodes in the converter, the efficiency has been enhanced. Also, the switches do not have capacitive turn on loss due to ZVT operation. The proposed converter uses only one power switch to provide ZVT conditions for all switches and the clamp capacitor transfers its energy to the lifting capacitor, which causes increase in voltage gain of the converter. Because of the interleaved structure, the converter has a low input ripple current and this advantage makes it very suitable for solar applications. The proposed converter is analysed and a 580W prototype is made to verify theoretical analyses.

https://doi.org/10.30501/jree.2021.279818.1198

چکیده

در این مقاله، یک مبدل بسیار افزاینده درهم‌تنیده با کلیدزنی در گذار ولتاژ صفر پیشنهاد شده است. مزایای اصلی مبدل پیشنهادی پایین بودن مقدار ریپل جریان ورودی و استرس ولتاژ سوئیچ‌ها، راندمان بالا، تعداد المان کم و حذف مشکل بازیابی معکوس دیودها است. به دلیل عملکرد کلیدزنی نرم سوئیچ‌ها و دیودهای مبدل، راندمان بهبود یافته است. همچنین، سوئیچ‌ها تلفات روشن شدن خازنی ندارند. مبدل پیشنهادی فقط از یک سوئیچ قدرت به منظور فراهم کردن شرایط گذار ولتاژ صفر برای همه سوئیچ‌ها استفاده کرده است، و خازن کلمپ، انرژی آن را به خازن لیفت منتقل می‌کند که باعث می شود بهره ولتاژ مبدل افزایش پیدا کند. به خاطر ساختار درهم‌تنیده این مبدل، ریپل جریان ورودی مبدل پایین می‌باشد و این مزیت، مبدل را برای استفاده در سیستم‌های سلول خورشیدی، مناسب می‌سازد. مبدل پیشنهادی بررسی شده و یک نمونه ۵۸۰ وات برای تصدیق محاسبات تئوری ساخته شده است.

Performance Evaluation and Optimization of a Solar-Assisted Multi-Belt Conveyor Dryer Based on Response Surface Methodology

Hemad Zareiforoush*, Adel Bakhshipour, Iraj Bagheri

Department of Biosystems Engineering, Faculty of Agriculture, University of Guilan, P. O. Box: 41635-1314, Rasht, Guilan, Iran.

P A P E R   I N F O

Paper history:
Received: 08 June 2021
Revised in revised form: 25 August 2021
Scientific Accepted: 25 September 2021
Published: 29 December 2021

Keywords:
Drying,
Specific Energy,
Energy Efficiency,
Solar-Assisted Dryer,
Solar Water Heater

A B S T R A C T

Drying process is an important post-harvest stage of food crops production which accounts for about 20 % of the world's energy consumption in the industrial sector. One of the effective ways to reduce the share of fossil fuel consumption in the food drying process is to develop new drying systems based on the use of renewable energy sources. In this research, a novel solar-assisted multi-belt conveyor dryer was developed and its performance was analysed. The required thermal energy for drying process was supplied by the combination of solar-gas water heaters and four solar-powered infrared (IR) lamps. The experimental factors included the speed and temperature of the drying air and the power of IR lamps. The performance characteristics were drying time, Overall Specific Energy (OSE), Non-Solar Specific Energy (NSE), Overall Energy Efficiency (OEE), and Solar-Assisted Energy Efficiency (SEE). The optimization process of the drying system was carried out using Response Surface Methodology (RSM) by defining two general modes for the energy sources of the drying system, namely overall mode and solar-assisted mode. Based on the results, the lowest OSE (17.30 MJ/kg water evaporated) was obtained when the speed and temperature of the drying air were equal to 7 m/s and 40 °C, respectively, without using IR power. The lowest NSE (2.71 MJ/kg water evaporated) was achieved by applying the treatment of 7 m/s * 40 °C * 300 W. The maximum OEE was equal to 13.92 % whilst the maximum SEE was obtained as 88.71 %. Both of the mentioned maximum values were obtained at the speed and temperature combination of 7 m/s and 40 °C and their difference was applying 300 W IR power to gain maximum SEE and no IR utilization for the maximum OEE. According to RSM analysis, the optimum working conditions for the drying system included the treatment of 7 m/s * 39.96 ºC * 300 W. Under this condition, the drying time, NSE, and SEE values were equal to 180.95 min, 1.062 MJ/kg water evaporated, and 84.63 %, respectively.

https://doi.org/10.30501/jree.2021.285697.1203

چکیده

فرآیند خشک کردن یک مرحله مهم پس از برداشت در تولید محصولات غذایی است که حدود ۲۰ درصد از انرژی مصرفی جهان در بخش صنعت را تشکیل می‌دهد. یکی از راه‌های مؤثر برای کاهش سهم مصرف سوخت‌های فسیلی در فرآیند خشک‌کردن مواد غذایی، توسعه سیستم‌های خشک‌کن جدید مبتنی بر استفاده از منابع انرژی تجدیدپذیر است. در این پژوهش، یک خشک‌کن چندتسمه نقاله‌ای جدید با کمک انرژی خورشیدی توسعه داده شد و عملکرد آن مورد تجزیه و تحلیل قرار گرفت. انرژی حرارتی مورد نیاز برای فرآیند خشک کردن با ترکیب آبگرمکن‌های گازی-خورشیدی و چهار لامپ مادون قرمز با بهره‌گیری از انرژی خورشیدی تأمین شد. عوامل آزمایشی شامل سرعت و دمای هوای خشک شدن و توان لامپ‌های مادون قرمز بود. ویژگی‌های عملکردی مورد بررسی عبارت بودند از: زمان خشک کردن، انرژی ویژه کلی (OSE)، انرژی ویژه غیر خورشیدی (NSE)، بازده انرژی کلی (OEE)، و بازده انرژی کمک-خورشیدی (SEE). فرآیند بهینه‌سازی سامانه خشک‌کن با استفاده از روش سطح پاسخ (RSM) با تعریف دو حالت کلی برای منابع انرژی سامانه خشک‌کن، یعنی حالت کلی و حالت کمک-خورشیدی انجام شد. بر اساس نتایج، کمترین مقدار OSE (۱۷/۳۰ مگاژول بر کیلوگرم آب تبخیر شده) زمانی به‌دست آمد که سرعت و دمای هوای خشک‌کن بدون استفاده از توان مادون قرمز به ترتیب برابر با ۷ متر بر ثانیه و ۴۰ درجه سانتی‌گراد بود. کمترین مقدار NSE (۲/۷۱ مگاژول بر کیلوگرم آب تبخیر شده) با اعمال تیمار ۷ m/s، ۳۰۰ W و ۴۰ ºC به دست آمد. حداکثر مقدار OEE برابر با ۱۳/۹۲ درصد بود در حالی‌که حداکثر مقدار SEE برابر با ۸۸/۷۱ درصد به دست آمد. هر دو مقدار بیشینه مورد اشاره در ترکیب سرعت و دمای ۷ متر بر ثانیه و ۴۰ درجه سانتی‌گراد به دست آمدند و تفاوت آنها استفاده از توان مادون قرمز ۳۰۰ W برای دستیابی به بیشینه SEE و عدم استفاده از توان مادون قرمز برای بیشینه OEE بود. بر اساس تجزیه و تحلیل RSM، شرایط کاری بهینه برای سامانه خشک‌کن شامل سرعت هوای ورودی ۷ m/s، دمای هوای ورودی ۳۹/۹۶ ºC و توان مادن قرمز ۳۰۰ W بود. در این شرایط، مقادیر زمان خشک کردن، NSE و SEE به ترتیب برابر با ۱۸۰/۹۵دقیقه، ۱/۰۶۲ مگاژول بر کیلوگرم آب تبخیر شده و ۸۴/۶۳ درصد بود.

Chlorella vulgaris Cultivation Using Triangular External Loop Airlift Photobioreactor: Hydrodynamic and Mass Transfer Studies

Shiva Shadpour [a], Ali Pirouzi [a*], Mohsen Nosrati [b], Hoda Hamze [c]

[a] *Department of Chemical Engineering, University of Science and Technology of Mazandaran, P. O. Box: 48518-78195, Behshahr, Mazandaran, Iran.*
[b] *Biotechnology Group, Faculty of Chemical Engineering, Tarbiat Modares University, P. O. Box: 14115-143, Tehran, Tehran, Iran.*
[c] *Chemistry and Chemical Engineering Research Center of Iran (CCERCI), P. O. Box: 14335-186, Tehran, Tehran, Iran.*

PAPER INFO

Paper history:
Received: 13 June 2021
Revised in revised form: 04 August 2021
Scientific Accepted: 10 August 2021
Published: 08 January 2022

Keywords:
Airlift Photobioreactor,
Chlorella vulgaris,
Hydrodynamics,
Mass Transfer,
Mixing Time

ABSTRACT

Long mixing time, high power consumption, and small mass transfer coefficients are common problems in the photobioreactor design for microalgae culture which have a great effect on system efficiency and performance, CO_2 stabilization, and biomass production. In this study, a special design of the triangular external loop airlift photobioreactor was studied. The bioreactor's geometry was such that the angle between hypotenuse and the horizontal side (α) could vary. This configuration created an effective gas-liquid countercurrent flow in the downcomer section. In the present research, hydrodynamic and mass transfer of the reactor were investigated on the microalgae productivity under different design and operating parameters. The optimum conditions for the enhancement of *Chlorella vulgaris* productivity were explored by analyzing the mixing time (t_m), volumetric power consumption (P/V), mass transfer coefficients (k_La), bubble diameter (d), and gas holdup (ε) as responses. The results showed that the hypotenuse angle of $\alpha = 59^o$ and the superficial gas velocities of the $V_{gs1} = 0.0050$ m.s^{-1} for the downcomer and $V_{gs2} = 0.008$ m.s^{-1} for the riser of the reactor were the best conditions to achieve the highest biomass productivity. The responses' values obtained in the optimum condition were as follows: $k_La_R= 19.67$ (h^{-1}), $k_La_D = 23.79$ (h^{-1}), $k_La_S = 23.76$ (h^{-1}), $\theta_m = t_m/t_c= 0.41$, and $P/V = 62.83$ W/m^3, which had a smaller deviation than the actual values. The highest concentration of *Chlorella vulgaris* ($X_{max} = 1.4$ g.L^{-1}) achieved in this work was obtained in a shorter span of time (11th day of cultivation) based on the growth curve in optimized conditions.

https://doi.org/10.30501/jree.2021.290449.1216

چکیده

زمان‌های اختلاط طولانی، توان مصرفی زیاد و ضرایب انتقال جرم کوچک، از مشکلات معمول در طراحی فتوبیوراکتورهای کشت ریزجلبک‌هاست که اثر زیادی بر بازدهی و عملکرد سامانه، در تثبیت CO_2 و تولید زیست‌توده دارند. در این مطالعه، طرح خاصی از فتوبیوراکتور مثلثی قائم‌الزاویه‌ی هواراند با حلقه‌ی خارجی مورد مطالعه قرار گرفت. هندسه‌ی این فتوبیوراکتور به گونه‌ای است که قابلیت تغییر زاویه‌ی میان وتر و ضلع افقی (α) وجود دارد. این ساختار، سبب ایجاد جریان مؤثر ناهمسوی گاز-مایع در وتر فتوبیوراکتور می‌شود. در پژوهش حاضر، هیدرودینامیک و انتقال جرم راکتور با بررسی اثرات پارامترهای مختلف عملیاتی و طراحی بر بازدهی تولید میکروجلبک مورد بررسی قرار گرفت. شرایط بهینه به منظور افزایش میزان تولید *کلرلا ولگاریس* با تجزیه و تحلیل پاسخ های زمان اختلاط (t_m)، مصرف توان حجمی سامانه (P/V)، ضریب انتقال جرم حجمی (k_La)، اندازه‌ی حباب (d) و نگه‌داشت گاز (ε) مورد بررسی قرار گرفت. نتایج نشان داد که زاویه وتر برابر با $\alpha = 59^o$ و سرعت خطی گاز برابر با $V_{gs1} = 0.0050\ m.s^{-1}$ برای بخش پایین رو و سرعت خطی گاز برابر با $V_{gs2} = 0.008\ m.s^{-1}$ برای بخش بالارو، بهترین شرایط برای دستیابی به بالاترین میزان تولید زیست‌توده بودند. مقادیر پاسخ های بدست آمده در شرایط بهینه بدست آمده عبارتند از: $k_La_R = 19.67$ (h^{-1})، $k_La_D = 23.79$ (h^{-1})، $k_La_S = 23.76$ (h^{-1})، $\theta_m = t_m/t_c = 0.41$ و $P/V = 62.83\ W/m^3$ که انحراف خیلی کمی با مقادیر واقعی پاسخ ها داشت. افزون بر این، میزان تولید بالای زیست‌توده در شرایط بهینه (X_{max} =۱/۴ g. L^{-1}) در زمان کوتاهتر (یازدهمین روز کشت) نسبت به سایر پژوهش های مشابه مؤید نتایج بدست آمده از تحلیل ها است.

Performance Enhancement of Deep Violet InGaN Double Quantum Wells Laser Diodes with Quaternary Superlattice Barriers Structure

Ghasem Alahyarizadeh [a], Maryam Amirhoseiny [b], Majid Khorsandi [c*]

[a] Faculty of Engineering, Shahid Beheshti University, P. O. Box: 1983969411, Tehran, Tehran, Iran.
[b] Buin Zahra Higher Education Center of Engineering and Technology, Imam Khomeini International University, P. O. Box: 3451745346, Qazvin, Qazvin, Iran.
[c] Radiation Application Department, Shahid Beheshti University, P. O. Box: 1983969411, Tehran, Tehran, Iran.

P A P E R   I N F O

Paper history:
Received: 07 September 2021
Revised in revised form: 31 October 2021
Scientific Accepted: 14 November 2021
Published: 11 January 2022

Keywords:
InGaN Quantum Well Laser,
Superlattice Barriers,
Electrical and Optical Properties,
Numerical Simulation

A B S T R A C T

The performance characteristics of InGaN Double-Quantum-Well (DQW) Laser Diodes (LDs) with different barrier structures were studied numerically by Integrated System Engineering Technical Computer-Aided Design (ISE TCAD) software. Three different kinds of structures of barriers including quaternary AlInGaN and AlInGaN/AlGaN superlattice barriers were used and compared with conventional GaN in InGaN-based laser diodes. Replacing the traditional GaN barriers with quaternary AlInGaN increased holes and electrons flowing in the active region and thus, the radiative recombination enhanced the output power. However, it did not reduce the threshold current due to hole and electron overflowing. To investigate the ways of greatly reducing the threshold current, the structure consisting of AlInGaN/AlGaN superlattice barriers was proposed. The simulation showed that electrical and optical characteristics such as output power, Differential Quantum Efficiency (DQE), and slop efficiency were significantly enhanced for LDs containing superlattice barriers compared to the basic structure. This is while the threshold current was considerably reduced. The enhancement was mainly attributed to the improvement of hole injection and also the blocking hole and electron overflowing caused by the reduction of polarization charges at the interface between the barriers, the well, and the Electron Blocking Layer (EBL).

https://doi.org/10.30501/jree.2021.300112.1246

چکیده

کارایی لیزرهای دیودی چاه کوانتومی دوتایی ایندیوم گالیوم نیتراید (InGaN) با ساختارهای مختلف دیواره کوانتومی با استفاده از نرم‌افزار عددی ISE-TCAD مورد مطالعه قرار گرفت. سه نوع ساختار مختلف برای دیواره‌های کوانتومی اعم از ساختار حجمی چهارتایی آلومینیوم ایندیوم گالیوم نیتراید (AlInGaN)، ساختار ابرشبکه AlInGaN/AlGaN و ساختار مرسوم حجمی GaN مورد مقایسه قرار گرفتند. با استفاده از ساختار حجمی چهارتایی AlInGaN شارش حفره‌ها درون منطقه فعال افزایش یافته و متعاقب آن بازترکیب تابشی که نتیجه در افزایش توان خروجی دارد، افزایش می‌یابد. به‌دلیل وجود شارش زیادی الکترون‌ها از منطقه فعال، کاهش قابل توجهی در جریان آستانه لیزر دیود رخ نمی‌دهد. برای فراهم آوردن راهی برای کاهش جریان آستانه، دراین مقاله ساختار ابرشبکه AlInGaN/AlGaN پیشنهاد شده است. نتایج شبیه‌سازی دلالت براین دارد که ویژگی‌های الکتریکی و اپتیکی لیزر دیودها با ساختار دیواره‌های ابرشبکه، درمقایسه با ساختار دیواره حجمی بطور قابل توجهی بهبود می‌یابد. علاوه براین، جریان آستانه لیزر نیز بطور قابل توجهی کاهش می‌یابد. افزایش ویژگی‌های کارایی منجر به افزایش تزریق حفره‌ها به منطقه فعال و جلوگیری از فرار شارشی الکترون‌ها به بیرون منطقه فعال می‌شود که موجب کاهش بارهای فضایی ناشی از پلاریزاسیون سطح مشترک میان دیواره‌ها و چاه‌های کوانتومی و همچنین لایه بازدارنده الکترونی می‌شود.

CONTENTS

Journal Homepage: www.jree.ir